12-1959

An Investigation of the Effect of High Temperature on the Schumann-Runge Ultraviolet Absorption Continuum of Oxygen

John Stanton Evans
University of Tennessee - Knoxville

To the Graduate Council:

I am submitting herewith a thesis written by John Stanton Evans entitled "An Investigation of the Effect of High Temperature on the Schumann-Runge Ultraviolet Absorption Continuum of Oxygen." I have examined the final electronic copy of this thesis for form and content and recommend that it be accepted in partial fulfillment of the requirements for the degree of Doctor of Philosophy, with a major in Physics.

Dr. Edward G. Harris, Major Professor

We have read this thesis and recommend its acceptance:

Accepted for the Council:
Carolyn R. Hodges

Vice Provost and Dean of the Graduate School

(Original signatures are on file with official student records.)

December 7, 1959

To the Graduate Council:

I am submitting herewith a thesis written by John Stanton Evans entitled "An Investigation of the Effect of High Temperature on the Schumann-Runge Ultraviolet Absorption Continuum of Oxygen." I recommend that it be accepted in partial fulfillment of the requirements for the degree of Doctor of Philosophy, with a major in Physics.

Edward D. Harris
Major Professor

We have read this thesis and recommend its acceptance:

A. Busemann

Alvin H. Nilsen

Robert D. Lorell

W. E. Deeds

D. D. Millican

Accepted for the Council:

Dale Hawthorne
Dean of the Graduate School

AN INVESTIGATION OF THE EFFECT OF HIGH TEMPERATURE ON THE SCHUMANN-RUNGE ULTRAVIOLET ABSORPTION CONTINUUM OF OXYGEN

A THESIS

Submitted to
The Graduate Council
of
The University of Tennessee
in
Partial Fulfillment of the Requirements
for the degree of
Doctor of Philosophy

---

by

John Stanton Evans

December 1959

ACKNOWLEDGEMENTS

The author wishes to express his appreciation to the many people at the Langley Research Center of the National Aeronautics and Space Administration who contributed to the successful completion of the research reported here. Among these are: Dr. Adolf Busemann, who gave freely of his time in order to discuss the problems which arose from time to time; Mr. Charles J. Schexnayder, who shared the day-by-day routine of the shock tube laboratory; and Mrs. Edna Bartlett, who spent many hours operating a desk computer and tabulating data.

The author is also grateful to those professors from the University of Tennessee who visited the laboratory while the work was in progress and made several helpful suggestions. These are: Dr. John D. Trimmer*, Dr. Alvin H. Nielsen, and Dr. Edward G. Harris.

*Dr. Trimmer is now head of the physics department of the University of Massachusetts.

TABLE OF CONTENTS

CHAPTER PAGE

LIST OF FIGURES

FIGURE PAGE

FIGURE PAGE

LIST OF SYMBOLS

$A_{v''} = \left[\beta(x_e^{-1} - 2v'' - 1)(v'')!/\Gamma(x_e^{-1} - v'')\right]^{1/2}$. Normalization factor for the Morse eigenfunctions

a — slope of the potential curve for the $B(^3\Sigma_u^-)$ state at r_s, erg(angstrom unit)$^{-1}$

a_I — speed of sound in gas; subscript I refers to gas before the shock wave passes, cm sec^{-1}

$B_e = h/8\pi^2 cM_e$. Rotational constant, cm^{-1}

$B_e' = 1.44567$ cm^{-1}

$B_e'' = 0.819$ cm^{-1}

C_1, C_2, C_3, C_4 — experimentally determined proportionality constants appearing in equations (8) and (11) and Appendix A.

$c = 2.9979 \times 10^{10}$ cm sec^{-1}. Velocity of light

D = 39.888 cm. Diameter of Rowland circle; equals radius of curvature of diffraction grating, cm

$D_e = 42048$ cm^{-1}. Dissociation energy of the oxygen molecule in the $X(^3\Sigma_g^-)$ state measured from the minimum of the potential curve

d — diffraction angle; see figure 29

E' — vibrational kinetic energy for the $B(^3\Sigma_u^-)$ state, cm^{-1}

E'' — vibrational kinetic energy for the $X(^3\Sigma_g^-)$ state, cm^{-1}

$E^* = h\nu$. Energy of absorbed light quantum, erg

$\tilde{E}$ energy of final state measured from the dissociation level of the $B(^3\Sigma_u^-)$ state, erg

$F^{1/2} = 241.89\tilde{E}^{1/4}a^{-1/6}$. Normalization factor for the u wave function

$G_{v'}$, $G_{v''}$, G_{v_a}, G_{v_b} energy of vibrational levels referred to $v'' = 0$ level as the zero level, cm^{-1}

g = 1.00 for oxygen, 0.21 for air, and 0.1007 for oxygen-argon. Fractional amount of oxygen in the gas mixture

$h = 6.6253 \times 10^{-27}$ erg sec. Planck constant

$\hbar \equiv h/2\pi = 1.05445 \times 10^{-27}$ erg sec

I intensity of transmitted light, erg $cm^{-2}sec^{-1}$

I_o intensity of incident light, erg $cm^{-2}sec^{-1}$

$I_{\tilde{\nu}}$ intensity of transmitted light per unit wave number, erg $cm^{-2}sec^{-1}$ per cm^{-1}

$I^o_{\tilde{\nu}}$ intensity of incident light per unit wave number, erg $cm^{-2}sec^{-1}$ per cm^{-1}

$I_{I,II}$ intensity of light transmitted through absorption path in the shock tube; subscript I refers to gas before the shock wave passes; subscript II refers to gas immediately behind the shock front, erg $cm^{-2}sec^{-1}$

$I^{v'v''}_{abs}$ absorption intensity of a band of the $v'v''$ electronic transition, erg $cm^{-2}sec^{-1}$

i angle of incidence; see figure 29

K rotational quantum number

K', K'', K_a, K_b — rotational quantum number; prime denotes upper state of Schumann-Runge transition; double prime denotes lower state, a denotes $a(^1\Delta_g)$ state; b denotes $b(^1\Sigma_g^+)$ state

k — absorption coefficient, cm^{-1}

$k_{v''}(\lambda)$ — absorption coefficient of molecules in the v'' level as a function of λ, cm^{-1}

$\hat{k}_{v''}(\lambda) \equiv k_{v''}(\lambda)/k_0^m$

$k_T(\lambda) = \sum_{v''=0}^{v''=10} N_{v''}(T) k_{v''}(\lambda)$. Absorption coefficient of oxygen as a function of T and λ, cm^{-1}

$\hat{k}_T(\lambda) \equiv k_T(\lambda)/k_0^m$

$k_T(\tilde{\nu})$ — absorption coefficient of oxygen as a function of T and $\tilde{\nu}$, cm^{-1}

$\hat{k}_T(\tilde{\nu}) \equiv k_T(\tilde{\nu})/k_0^m$

$k_0^m = 400\ cm^{-1}$ — maximum value of the $k_T(\lambda)$ curve at 0° K; equals (essentially) peak value of k at room temperature

l — absorption path length, cm

$M_I \equiv v_I/a_I$ — shock Mach number

$\bar{M}_{II} \equiv v_{II}/a_I$ — dimensionless velocity of flow behind the shock front

$M_e = \mu r_e^2$ — moment of inertia of the molecule, $sec^2 cm^{-1}$

$N_{v''}(T) = (1/S)\exp(G_{v''}hc/\kappa T)$. Weighting factor for $k_{v''}(\lambda)$; represents relative population of ground state vibrational levels at temperature, T

n — diffraction order; see figure 29

$p_{I,II}$ — pressure; subscript I refers to gas before the shock wave passes; subscript II refers to gas immediately behind the shock front, $gm\ cm^{-1} sec^{-2}$

p_e pressure; subscript e refers to gas in thermal equilibrium behind the shock front, gm $cm^{-1}sec^{-2}$

$p_s = 1.013 \times 10^6$ gm $cm^{-1}sec$. One atmosphere

$Q_{v''}$ associated Laguerre polynomial

R gas constant per unit mass, $cm^2sec^{-2}gm^{-1}deg^{-1}$

$R_e(r)$ electronic transition probability for $X(^3\Sigma_g^-) \leftarrow B(^3\Sigma_u^-)$

r distance between the oxygen atoms in the oxygen molecule, angstrom units

r_e value of r corresponding to the minimum of the vibrational potential curve, angstrom units

$r_e' = 1.604$ A value of r at the minimum of the $B(^3\Sigma_u^-)$ curve

$r_e'' = 1.207$ A value of r at the minimum of the $X(^3\Sigma_g^-)$ curve

r_s value of r corresponding to the turning point of the motion in the $B(^3\Sigma_u^-)$ state, angstrom units

$S = \sum_{v''} \exp(-G_{v''}hc/\kappa T) + \sum_{v_a} \exp(-G_{v_a}hc/\kappa T) + \sum_{v_b} \exp(-G_{v_b}hc/\kappa T)$. Partition function for vibrational levels of the the three lowest electronic states of oxygen

$s = 1.693 \times 10^{-4}$ cm. Distance between lines on the diffraction grating; see figure 29

T temperature, ^oK

$T_{I,II}$ temperature; subscript I refers to gas before shock wave passes, subscript II refers to gas immediately behind the shock front, ^oK

T_e temperature; subscript e refers to gas in thermal equilibrium behind the shock wave, ^oK

$T_s = 273.2^{\circ}$ K

u unnormalized vibrational wave function for the $B(^3\Sigma_u^-)$ state

V' vibrational potential energy for the $B(^3\Sigma_u^-)$ state, cm^{-1}

V'' vibrational potential energy for the $X(^3\Sigma_g^-)$ state, cm^{-1}

$v_{I,II}$ gas flow velocity; subscript I refers to gas before the shock wave passes, subscript II refers to gas immediately behind the shock front, cm sec^{-1}

v', v'', v_a, v_b vibrational quantum number; prime denotes upper state of Schumann-Runge transition, double prime denotes lower state, a denotes $a(^1\Delta_g)$ state, b denotes $b(^1\Sigma_g^+)$ state

v_e gas flow velocity; subscript e refers to gas in thermal equilibrium behind the shock wave, cm sec^{-1}

$x_e = \omega_e x_e/\omega_e = 0.0076345$. See definitions of ω_e and $\omega_e x_e$

Δx absorption path length for gas at standard atmospheric temperature and pressure (Herzberg's notation, ref. 11), cm^{-1}

x_1, x_2 distances locating entrance and exit slits; see figure 29

y distance of entrance and exit slits from monochromator center line; see figure 29

α angle between grating normal and monochromator center line; see figure 29

$\beta = 4(0.12177)(2\omega_e x_e)^{1/2} = 2.3935\ A^{-1}$. Morse function constant for the $X(^3\Sigma_g^-)$ state; $\beta = 0.12177\omega_e(\mu/D_e)^{1/2} = 2.6544\ A^{-1}$ is better for plotting the whole Morse curve.

$\eta_{I,II}$ dimensionless enthalpy; enthalpy divided by RT. Subscript I refers to gas before the shock wave passes, subscript II refers to gas immediately behind the shock front

$\gamma_{A,B}$ ratio of specific heat at constant pressure to specific heat at constant volume; subscript A refers to gas in the high pressure chamber of the shock tube, subscript B refers to gas in the low pressure chamber of the shock tube

$\gamma_{I,II}$ ratio of specific heat at constant pressure to specific heat at constant volume; subscript I refers to gas before the shock wave passes, subscript II refers to gas immediately behind the shock front

$\theta = 2260^\circ$ K. characteristic vibrational temperature for $X(^3\Sigma_g^-)$ state

θ angle between the normal to the grating at the point of rotation and the center line of the monochromator; see figure 29

$\kappa = 1.3804 \times 10^{-16}$ erg deg^{-1}, Boltzmann constant

λ wavelength of absorbed light quantum, angstrom units

$\mu = 8.00000$ atomic weight units. Reduced mass of oxygen atom

ν	frequency of absorbed light quantum, sec^{-1}
$\tilde{\nu} = 1/\lambda$	wave number, cm^{-1}
$\tilde{\nu}_m = 69{,}000\ cm^{-1}$	wave number corresponding to the maximum of the $k_T(\tilde{\nu})$ curve at 0° K
$\Delta\tilde{\nu}_o = 6481\ cm^{-1}$	natural half-breadth of the $k_T(\tilde{\nu})$ curve at 0° K
ρ	gas density, $gm\ cm^{-3}$
$\rho_{I,II}$	gas density; subscript I refers to gas before the shock wave passes, subscript II refers to gas immediately behind the shock front, $gm\ cm^{-3}$
$\hat{\rho}_{I,II} \equiv g\rho_{I,II}/\rho_s$	reduced gas density
ρ_e	gas density; subscript e refers to gas in thermal equilibrium behind the shock wave, $gm\ cm^{-3}$
ρ_s	gas density at 273° K and 1 atmosphere, $gm\ cm^{-3}$
$\sigma \equiv \rho_{II}/\rho_I$	density ratio across the shock front
ϕ	normalized Morse vibrational wave function for the $X(^3\Sigma_g^-)$ state
Ψ	normalized vibrational wave function (Herzberg's notation)
$\omega_e = 1580.361\ cm^{-1}$.	Spectroscopic constant of the $X(^3\Sigma_g^-)$ state, vibrational frequency
$\omega_e x_e = 12.0730\ cm^{-1}$.	Spectroscopic constant of the $X(^3\Sigma_g^-)$ state, anharmonicity correction

CHAPTER I

AN INVESTIGATION OF THE EFFECT OF HIGH TEMPERATURE ON THE SCHUMANN-RUNGE ULTRAVIOLET ABSORPTION CONTINUUM OF OXYGEN

INTRODUCTION

The absorption coefficient of a gas for light of a given wavelength is commonly defined by the relation:

$$I = I_o e^{-k\hat{\rho}l} \qquad (1)$$

where I and I_o are the transmitted and incident intensities of the light, k is the absorption coefficient in cm^{-1} and $\hat{\rho}l$ is the thickness in centimeters of the absorbing gas layer reduced to standard density. The absorption coefficient for a given gas is a function of the gas temperature and of the wavelength of the light. Figure 1 is intended to illustrate the general effect of these parameters on an absorption continuum like that found in oxygen. The curves shown were selected from calculations made for this dissertation. The wavelength dependence is such that the absorption coefficient has a maximum value at a particular wavelength and falls off to either side. Increasing temperature has three effects:

(1) the magnitude of the peak decreases,

(2) the position of the peak shifts to shorter wavelengths,

(3) the range over which absorption occurs spreads out to both longer and shorter wavelengths.

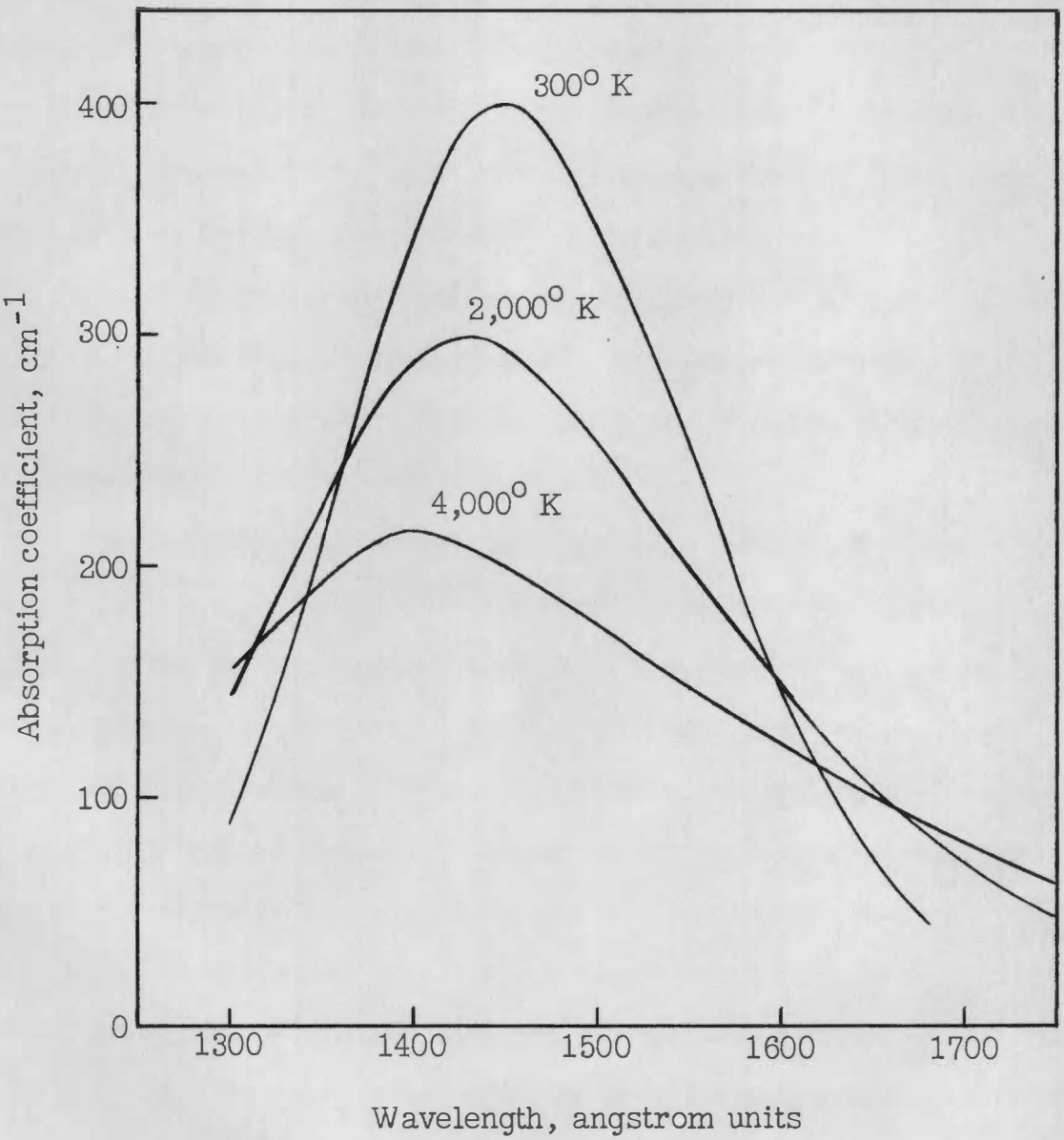

Figure 1.- Absorption coefficient of molecular oxygen: typical curves.

The oxygen continuum with which this dissertation is concerned has a peak between 1400 A and 1500 A and at room temperature extends from 1300 A to 1750 A. One of the chief reasons for attempting a quantitative evaluation of the effect of high temperature on this absorption continuum is that the absorption can be used to follow rapid changes in the concentration of molecular oxygen, such as those which occur in fast chemical reactions behind shock waves.

Since the oxygen involved in these processes is at much higher temperature than that at which presently existing measurements of the absorption coefficient were made, knowledge of the temperature dependence of the absorption coefficient is needed.

Several papers[1] have reported measured values of the absorption coefficient obtained at room temperature. These data are shown on figure 2. The two curves which also appear on figure 2 are the results of two theoretical calculations.[2] Stueckelburg's curve was calculated specifically for oxygen, but the other curve is an application to oxygen of a general formula derived by Sulzer and Wieland for calculating the absorption coefficient of a diatomic gas at any temperature from a knowledge of its absorption at 0° K and its characteristic vibrational temperature.

Apparently no work has been done on the determination of the continuous absorption coefficient of oxygen at elevated temperature. However, Sulzer and Wieland's formula is applicable at high temperature and agrees well with measured values[3] of the continuous absorption coefficients of chlorine, iodine, and bromine at temperatures up to $2{,}000^{\circ}$ K. Some typical curves calculated from their formula and the corresponding experimental data are shown on figures 3 and 4.

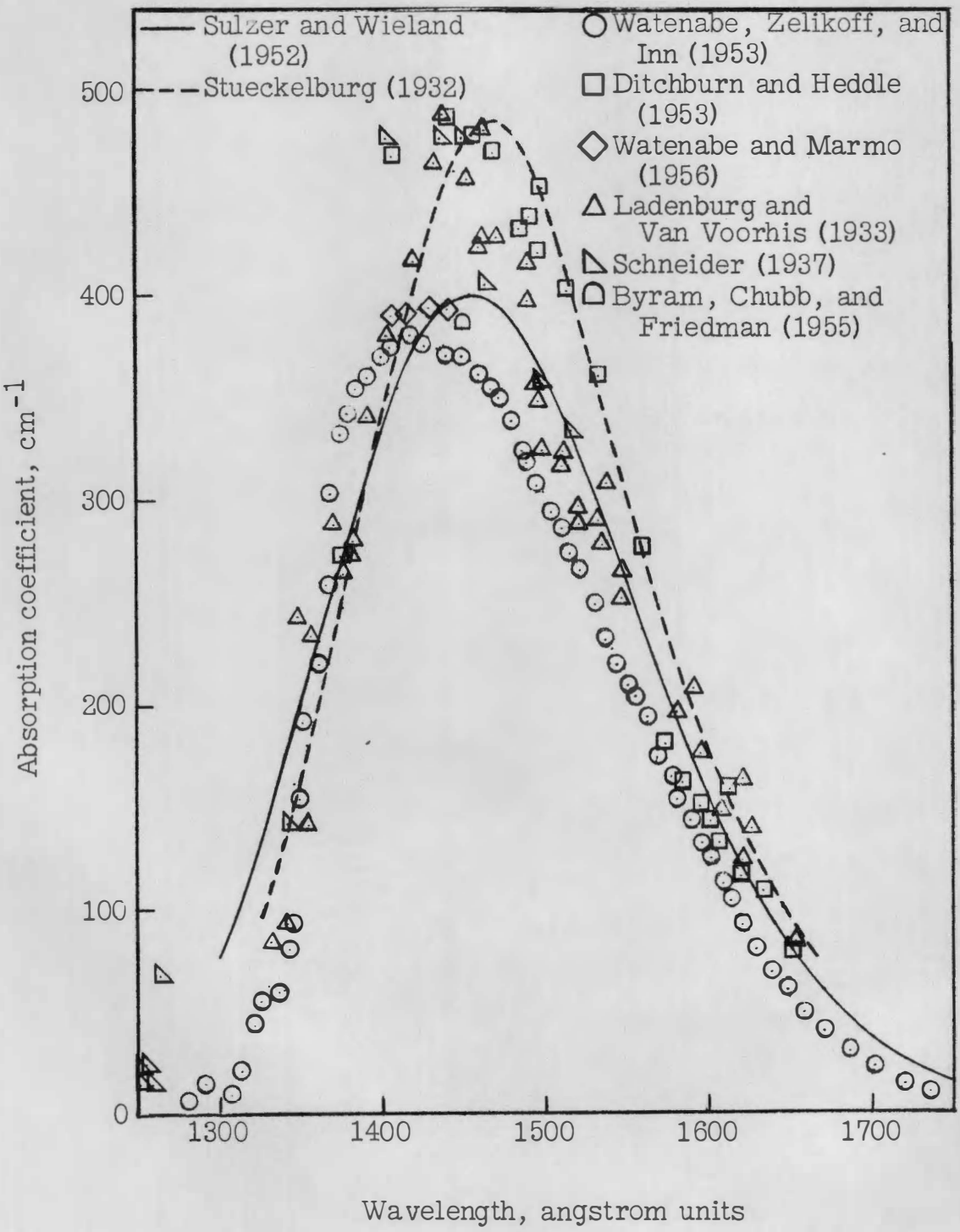

Figure 2.- Absorption coefficient of molecular oxygen; measured values at room temperature.

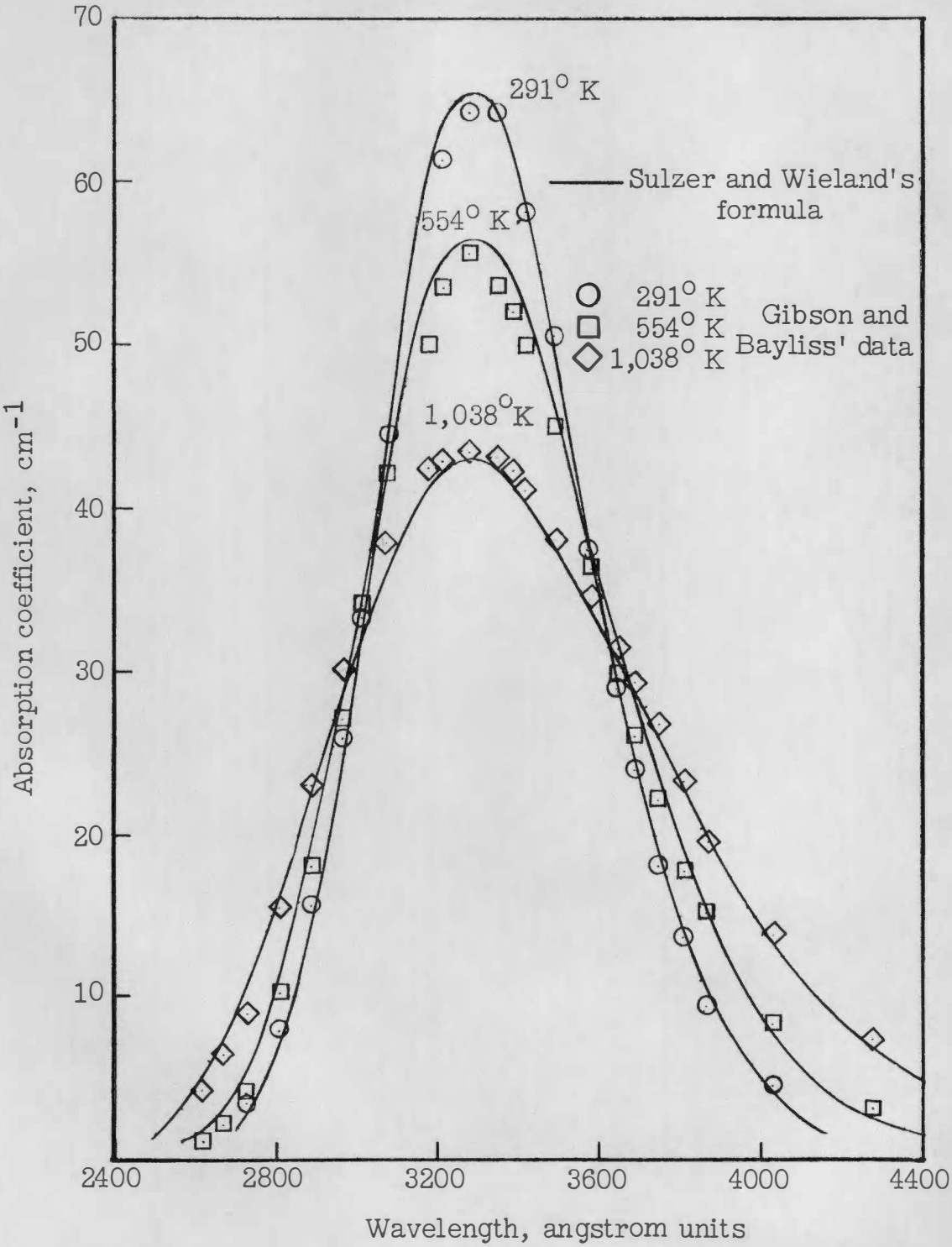

Figure 3.- Absorption coefficient of molecular chlorine.

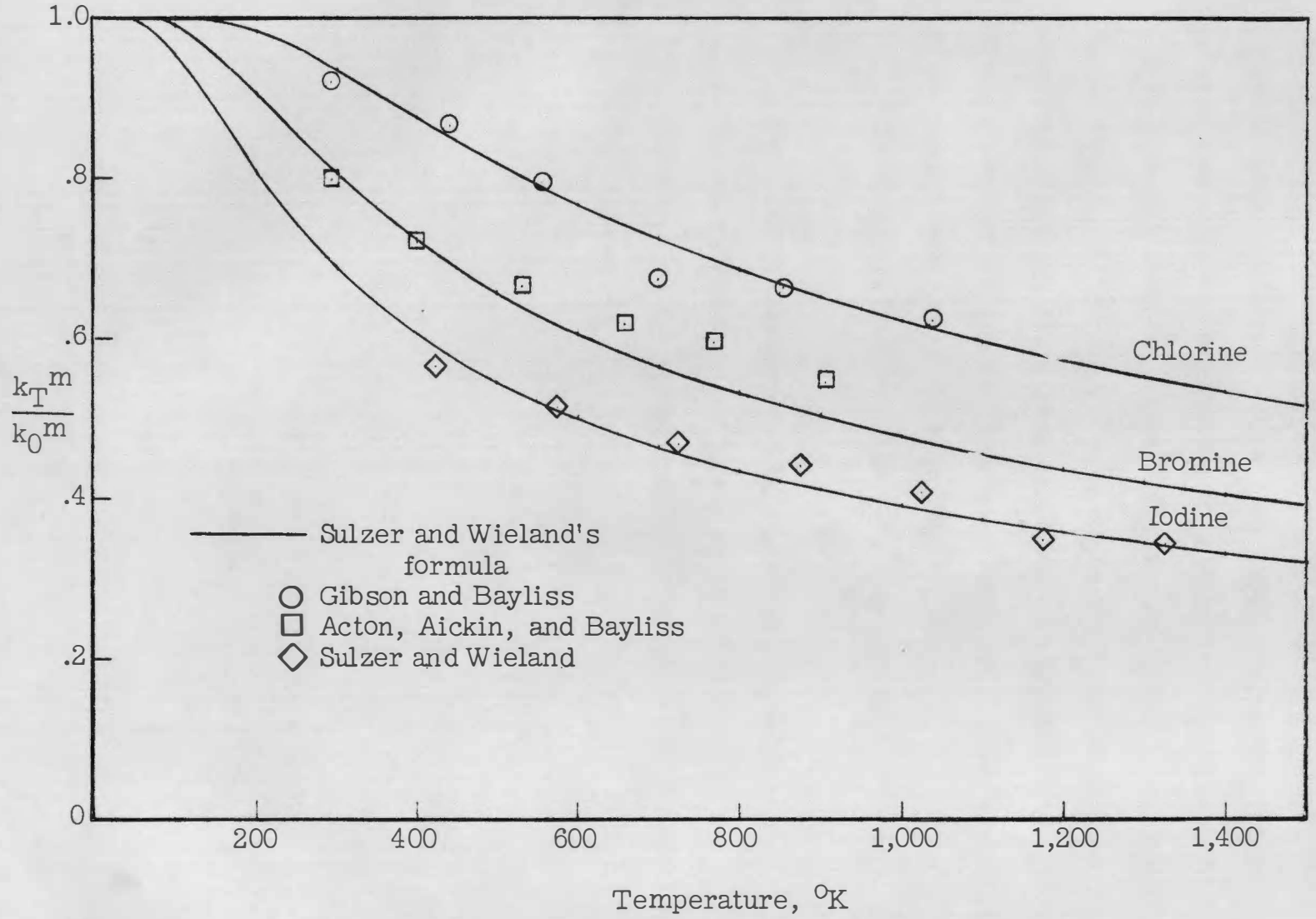

Figure 4.- Temperature dependence of absorption curve peaks.

In this dissertation both experimental and theoretical approaches are made to the problem of determining the absorption coefficient of oxygen at high temperature. High-temperature oxygen was obtained by means of the compression occurring in a shock wave passing through oxygen contained in a steel tube. The gas was heated to temperatures in the range $4{,}000^{\circ}$ to $10{,}000^{\circ}$ K in a time which was short compared to the instrumental resolving time, which was of the order of a few tenths of a microsecond. Light intensity as a function of time was displayed on an oscilloscope screen and photographed.

In the theoretical approach three calculations were made. They were:

(1) substitution into the formula of Sulzer and Wieland,

(2) the "reflection" or "delta function" method,

(3) a more elaborate calculation in which an IBM 704 computer was used.

CHAPTER II

THEORETICAL CALCULATION OF THE ABSORPTION COEFFICIENT

Background Material

1. Discussion of the Molecular State Transitions Responsible for Schumann-Runge Absorption

The absorption continuum under study adjoins the Schumann-Runge molecular band system[4] in oxygen and is due to the same electronic transition. Each electronic state of a diatomic molecule has a characteristic potential energy associated with the vibration of the nuclei along the line joining their centers. The vibrational potential energy curves for the five known electronic states of the O_2 molecule are shown in figure 5. Morse functions[5] were used; the constants were obtained from Herzberg's book[6] except for the dissociation energy, D_e, which was obtained from Brix and Herzberg[7].

Three kinds of molecular energy are involved in the transitions responsible for the Schumann-Runge band system. They are as follows:

a. Electronic energy changes. Electronic energy changes are represented by vertical distances between the potential curves of figure 5. The only transition between the known electronic states of oxygen which is allowed by strict application of the selection rules[8] is the $B(^3\Sigma_u^-) \leftarrow X(^3\Sigma_g^-)$ transition which gives rise to the Schumann-Runge band system. Since the selection rules are not completely obeyed other transitions between these states do occur, but the absorption and emission due to them are weak.

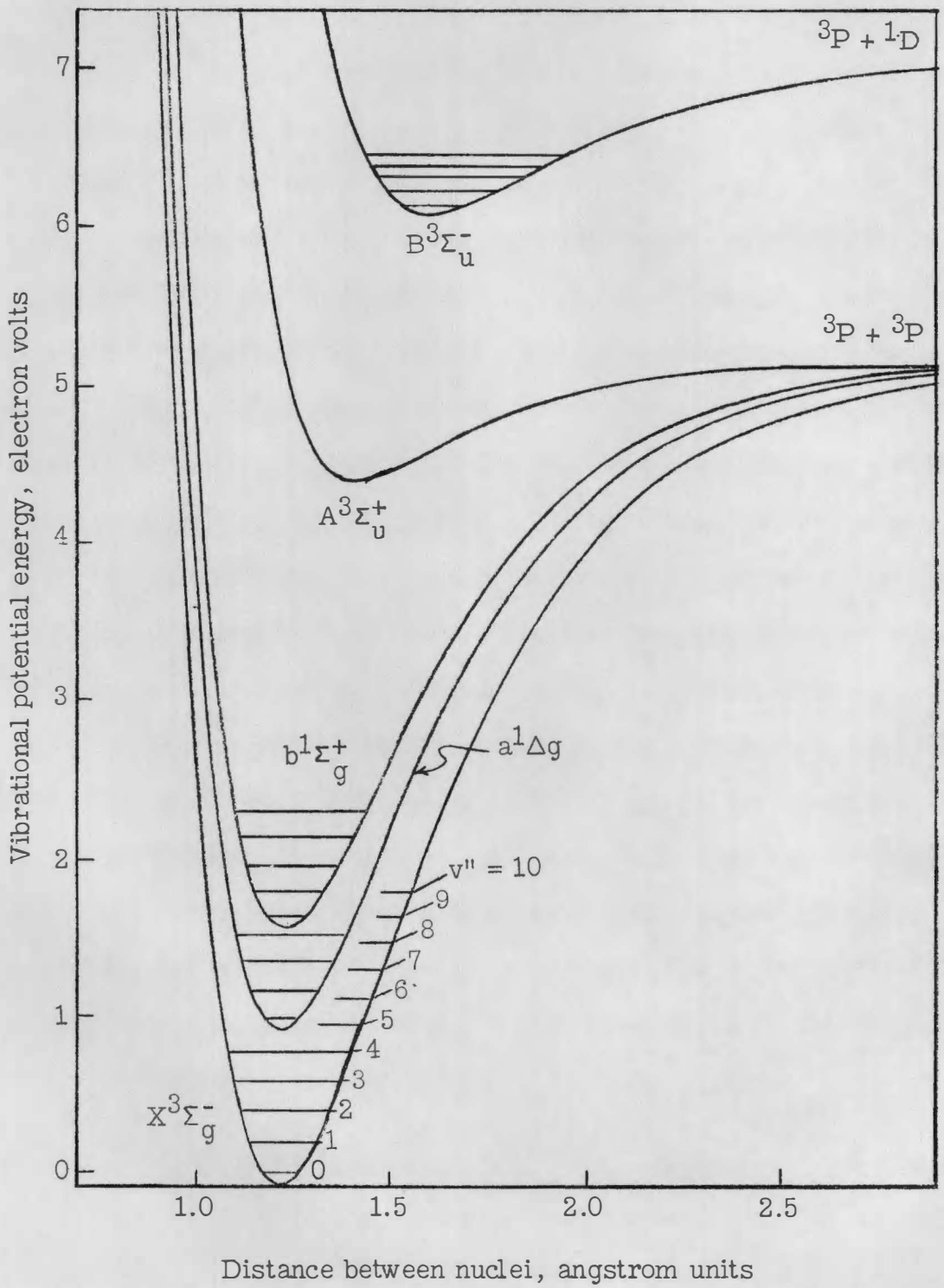

Figure 5.- Vibrational potential energy of the oxygen molecule.

b. Vibrational energy changes. Some of the vibrational energy levels of the states are also shown on figure 5. The individual absorption bands of the Schumann-Runge system are due to transitions which originate in one of the vibrational levels of the $X(^3\Sigma_g^-)$ state and terminate in one of the vibrational levels of the $B(^3\Sigma_u^-)$ state. The absorption continuum is due to the same transitions except that the final state lies above the dissociation limit of the B state. Molecules which have absorbed light in the continuum immediately dissociate into one normal (^3P) and one excited (^1D) atom[9]. In electronic transitions there is no strict selection rule for the vibrational quantum number[10].

c. Rotational energy changes. Examination of the individual bands in a molecular band system with a spectroscope of high resolving power reveals a fine structure which is attributed to rotation of the molecules. Figure 6 shows some of the rotational levels associated with the $v'' = 0$ and $v'' = 10$ vibrational levels of the X state of O_2. The selection rules[11] for rotational transitions limit changes in the rotational quantum number between Σ states to $\Delta K = \pm 1$. This, plus the fact that the rotational energy level spacing is small compared to the spacing of electronic and vibrational levels, made it possible to neglect the effect of the change in rotational energy on the calculation of the absorption coefficient in the continuum.

2. Distribution of Molecules Over Vibrational States

At 0° K all the O_2 molecules in a given sample are in the $v'' = 0$ level of the X state. To calculate the absorption coefficient at 0° K only transitions originating in this lowest state need be considered. At

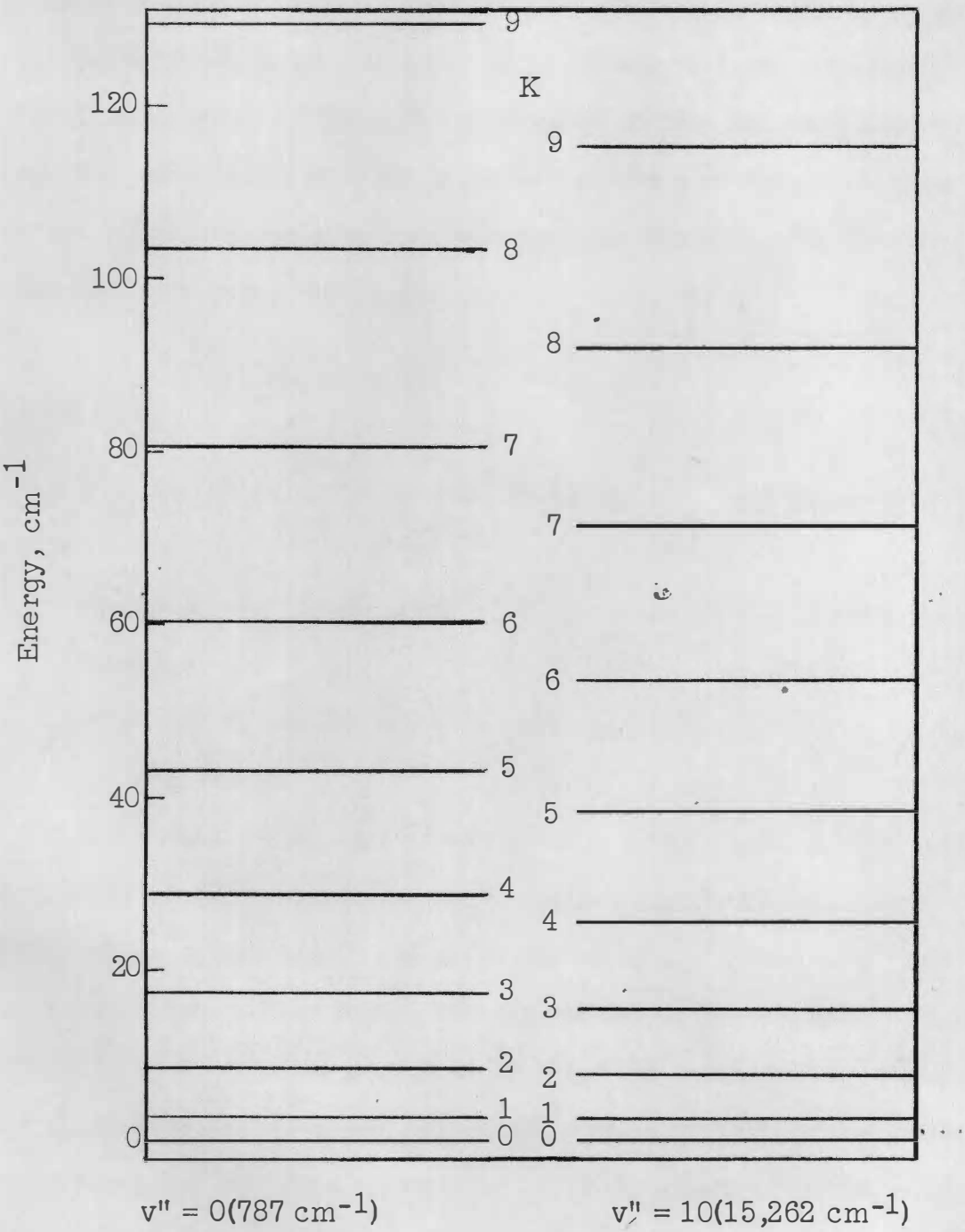

Figure 6.- Rotational energy levels of v" = 0 and v" = 10 vibrational levels. (Term value = $B_v"K(K + 1)$, where $B_0 = 1.438$ cm^{-1} and $B_{10} = 1.280$ cm^{-1}.)

higher temperatures transitions from excited vibrational states have to be taken into account. To do this the absorption coefficient was calculated for each initial state as if it were the only one and the overall absorption coefficient was found by adding the contributions from all the states. Numbers representing the relative populations of the initial levels were used as weighting factors. The expression used for calculating the weighting factors was:

$$N_{v''}(T) = (1/S)\ \exp(-G_{v''}hc/\kappa T) \qquad (2)$$

where

$$S = \sum_{v''} \exp(-G_{v''}hc/\kappa T) + \sum_{v_a} \exp(-G_{v_a}hc/\kappa T) + \sum_{v_b} \exp(-G_{v_b}hc/\kappa T)$$

$G_{v''}$ = energy of v'' level in cm^{-1} (referred to $v'' = 0$ as the zero level),

$G_{v_{a(b)}}$ = energy of $v_{a(b)}$ level in cm^{-1} (referred to $v'' = 0$ as the zero level).

Note that vibrational levels of the $a(^1\Delta_g)$ and $b(^1\Sigma_g^+)$ states were included in the partition function, S. Absorption of light by these states is negligible and it is not necessary to consider them in calculating the overall coefficient except for their appearance in the partition function. The partition function was calculated by summing the terms shown over all the vibrational levels present in the potential--right up to the dissociation energy. S(T) is plotted on figure 7.

The relative population of the vibrational levels of the X, a, and b states is shown on figure 8 for 5,000° and 10,000° K. The population of the rotational states of the $v'' = 0$ and $v'' = 10$ levels of the X state are shown for the same temperatures on figure 9.

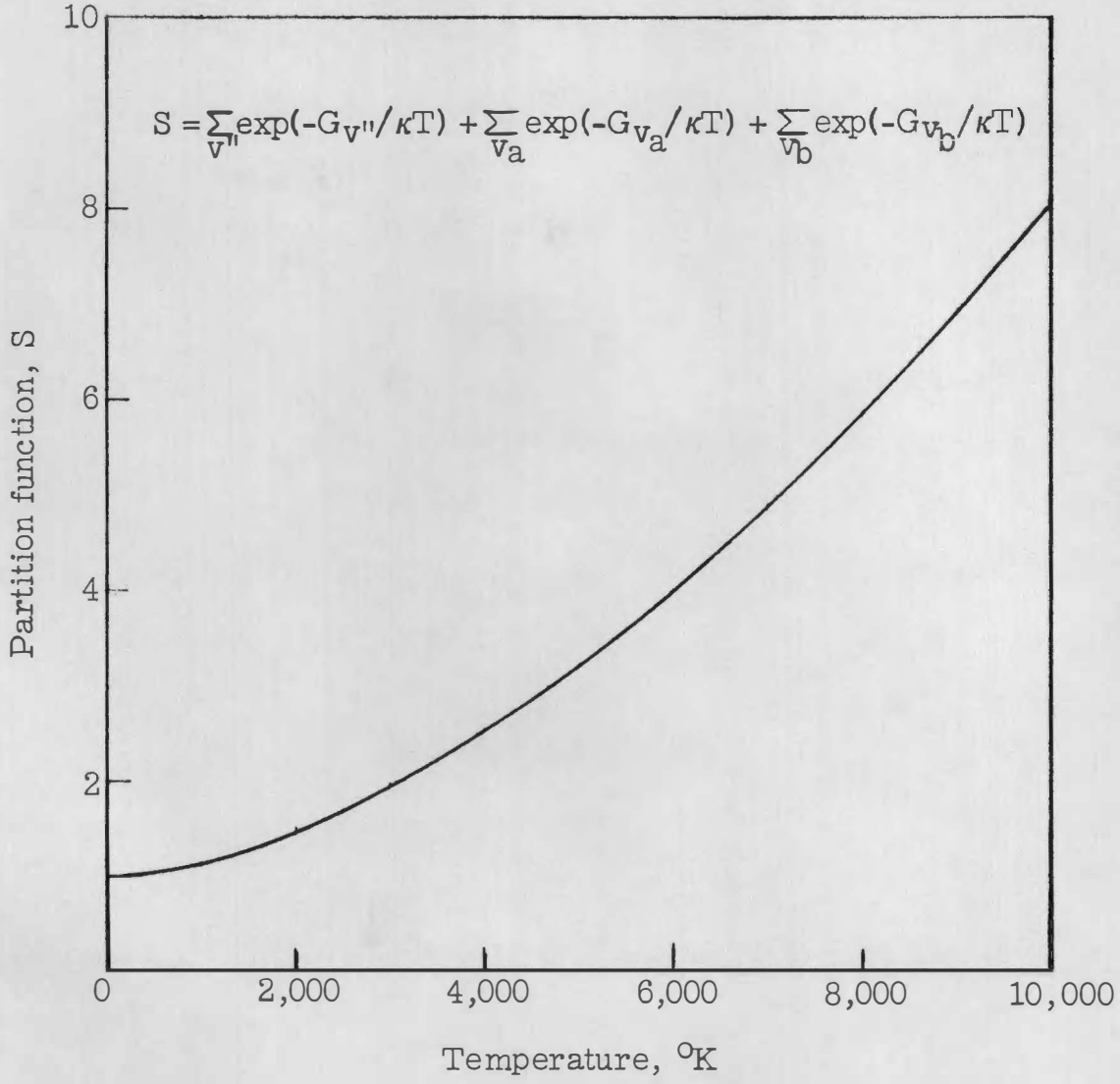

Figure 7.- Vibrational partition function for O_2.

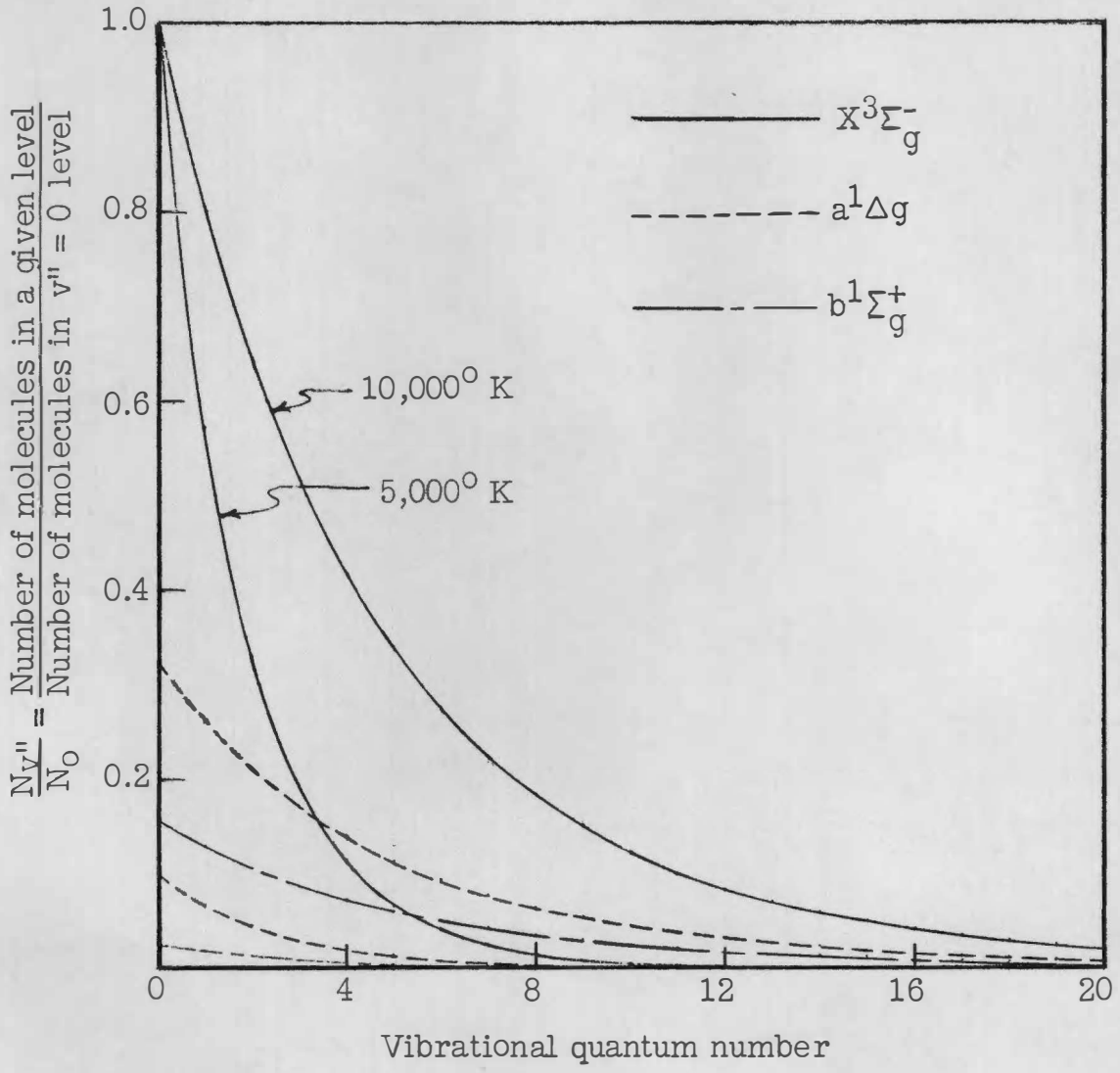

Figure 8.- Relative population of vibrational levels.

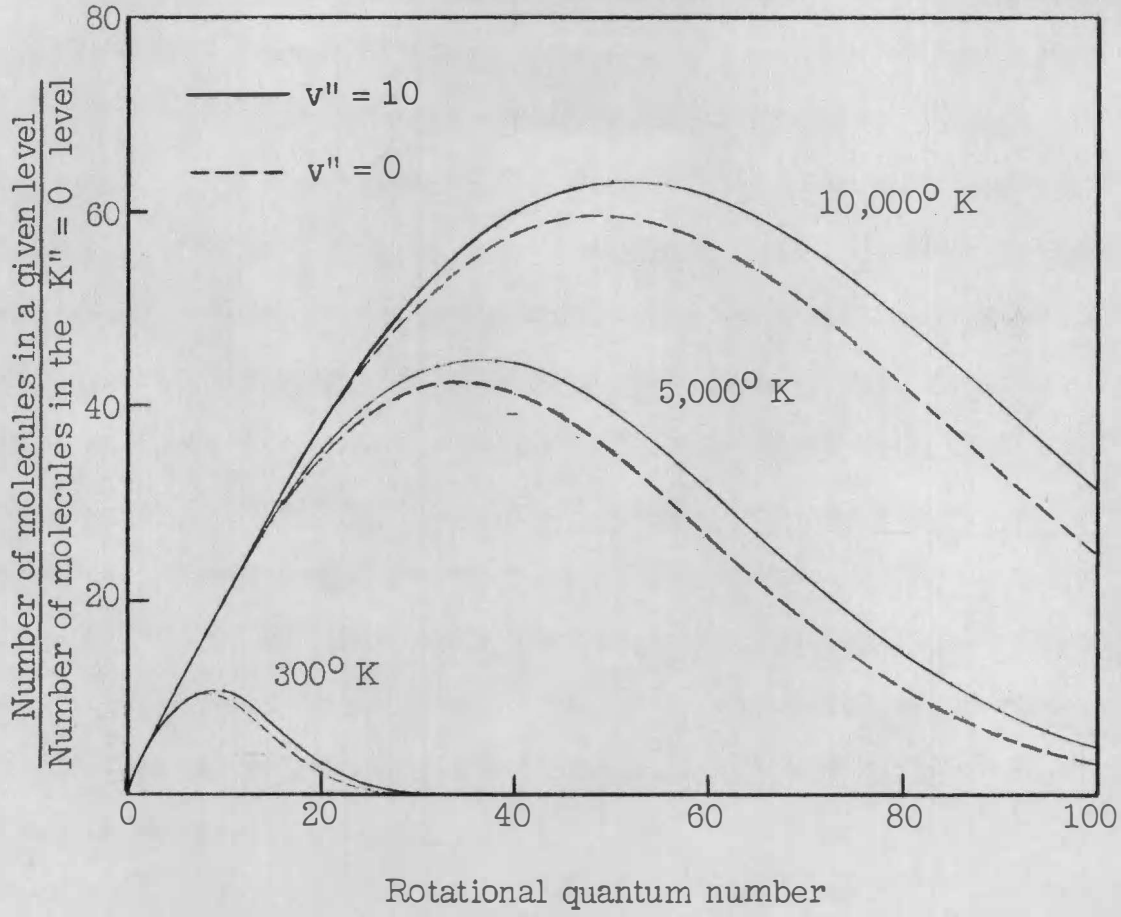

Figure 9.- Relative population of rotational levels.

3. The Franck-Condon Principle

a. Main ideas. The absence of selection rules for vibrational quantum number changes occurring in electronic transitions has already been mentioned. The observed intensity distributions are adequately explained by the quantum mechanical formulation of the Franck-Condon principle. The main idea in this principle is that the electrons move so rapidly compared to the heavy nuclei that the positions and velocities of the nuclei are unchanged in an electronic transition. From the viewpoint of classical mechanics the nuclei spend most of their time near the turning points of the vibrational motion, where they have zero velocity. Thus the most probable transitions are those for which a turning point of the upper state occurs at the same internuclear distance as a turning point of the lower state. The quantum mechanical formulation states that the transition probability is proportional to the square of the vibrational overlap integral,

$$\int_0^\infty \phi(r)u(r)\,dr$$

where $\phi(r)$ is the vibrational wave function for the lower state and $u(r)$ is the vibrational wave function for the upper state. If $\phi(r)$ and $u(r)$ are replaced by delta functions located at the turning points the classical Franck-Condon result is obtained.

b. Expression for the absorption coefficient. Discussions of the quantum mechanical formulation are given in Herzberg's book[12] and by Coolidge, James, and Present[13]. The following expression for the absorption coefficient is essentially the same as equation (VII,1) p. 391, of Herzberg's book:

$$k_{v''}(\lambda) = \text{constant}\ \ E^*(\tilde{E})^{-1/2} f \left[\int_0^\infty \phi_{v''} u\, dr\right]^2 \qquad (3)$$

However, it does differ in some respects. His equation (VII,1) is written as:

$$I_{abs}^{v'v''} \sim \tilde{\nu}\left[\int \psi_{v'}\psi_{v''}\, dr\right]^2$$

where $I_{abs}^{v'v''}$ is the absorption intensity in ergs cm^{-2} sec^{-1} of a band of the $v'v''$ electronic transition. Referring to his equations (VI,62) and (VI,63), p. 383, it can be seen that:

$$I_{abs}^{v'v''} = \int (I_{\tilde{\nu}}^{o} - I_{\tilde{\nu}})d\tilde{\nu} = (I_{\tilde{\nu}}^{o} - I_{\tilde{\nu}}) \cdot 1$$

$$= I_{\tilde{\nu}}^{o}\left(1 - e^{-k_{\tilde{\nu}}\Delta x}\right) \approx I_{\tilde{\nu}}^{o} k_{\tilde{\nu}}\Delta x, \text{ for } \left|k_{\tilde{\nu}}\Delta x\right| \ll 1$$

where $I_{\tilde{\nu}}$ is the intensity of transmitted light per unit wave number interval and $k_{\tilde{\nu}}$ is the absorption coefficient in cm^{-1} at the wave number $\tilde{\nu}$. The integration is justified by the fact that for a continuum $I_{\tilde{\nu}}^{o} - I_{\tilde{\nu}}$ is practically constant over a unit wave number interval. The replacement of $1 - e^{-k_{\tilde{\nu}}\Delta x}$ by $k_{\tilde{\nu}}\Delta x$ is justified because the absorption path length Δx can be made as small as one pleases and still be related to the total path length, l, by the equation $l = \sum_i (\Delta x)_i$. This can be seen from the relation:

$$I_{\tilde{\nu}} = I_{\tilde{\nu}}^{o} e^{-k_{\tilde{\nu}}\Delta x_1} e^{-k_{\tilde{\nu}}\Delta x_2} \ldots e^{-k_{\tilde{\nu}}\Delta x_n} = I_{\tilde{\nu}}^{o} \exp\left[-k_{\tilde{\nu}} \sum_{i=o}^{n} (\Delta x)_i\right]$$

From the above equations it can be seen that:

$$k_{\tilde{\nu}} = I_{abs}^{v'v''} / I_{\tilde{\nu}}^{o}\Delta x \sim I_{abs}^{v'v''}, \text{ since } I_{\tilde{\nu}}^{o}\Delta x = \text{constant}$$

The factor $E^*(= h\nu)$ is the energy of the absorbed quantum and is equivalent to Herzberg's factor $\tilde{\nu}$. The factor F is a normalization factor for the upper state wave function, u. The factor $\tilde{E}$ is the energy of the oxygen molecule in the final state measured from the asymptote of the $B(^3\Sigma_u^-)$ curve. This factor is not present in the expression for $I_{abs}^{v'v''}$ for a discrete line but does appear in the expression for $I_{abs}^{v'v''}$ in a continuum where intensity refers to energy per unit of spectral width. This is pointed out by Coolidge, James, and Present[14] but is not mentioned by Herzberg. This does not mean that Herzberg's treatment is in error, however, because the $\tilde{E}$ factor cancels out when the normalization of the u function is considered.

c. Discussion of the effect of neglecting the variation of electronic transition probability with internuclear distance. Equation (3) makes no allowance for the variation of the electronic transition probability with internuclear distance. Theoretical calculation of this variation is impractical because the necessary electronic wave functions are not known but some empirical treatments[15] have been given. Herzberg[16] points to the excellent quantitative agreement often obtained between theory and experiment as justification for neglecting this factor. Since there is no reason why the electronic transition probability at a given value of r should be a function of temperature, good agreement obtained between theory and experiment at room temperature can be used as a criterion of the adequacy of the assumption. Conversely, by assuming that any discrepancies present are due to this assumption the variation of the electronic transition probability with internuclear distance can be calculated.

d. Discussion of the effect of neglecting the rotation of the molecules. Equation (3) also ignores the rotation of the molecules. This is commonly done in order to cut down on the labor of the computations and for molecules with deep potential wells does not lead to large errors. The following discussion of the considerations involved is similar to one given by Gibson, Rice, and Bayliss[17].

For a rotating vibrator centrifugal forces are acting on the nuclei in addition to the usual restoring forces. The result is that the vibrational motion takes place under the influence of an effective potential[18] given by the equation:

$$V_K(r) = V_0(r) + \left[B_e r_e^2/r^2\right] K(K + 1) \qquad (4)$$

where $V_0(r)$ is the potential curve for the rotationless state, B_e is the rotational constant $h/8\pi^2 c M_e$, and K is the rotational quantum number. M_e is the moment of inertia of the molecule. Figure 10 shows some of these curves for the X and B states of oxygen.

Most of the rotating molecules in the eleven lowest vibrational levels of the X state have rotational quantum numbers of the order of $K = 50$ at a temperature of 10,000° K. (See fig. 9.) For the X state the minimum of the effective potential curve as compared to that of the rotationless state is shifted up by 3458 cm^{-1} and to the right from 1.207 A to 1.234 A. At the left extremity of r values used ($r = 1.08$ A) the curve is shifted up by 4514 cm^{-1} and at the right extremity ($r = 1.32$ A) it is shifted up by 3022 cm^{-1}. The net effect on the shape of the curve when the upward shift of the minimum is subtracted out is an upward shift of 1056 cm^{-1} at the left extremity and a downward shift of

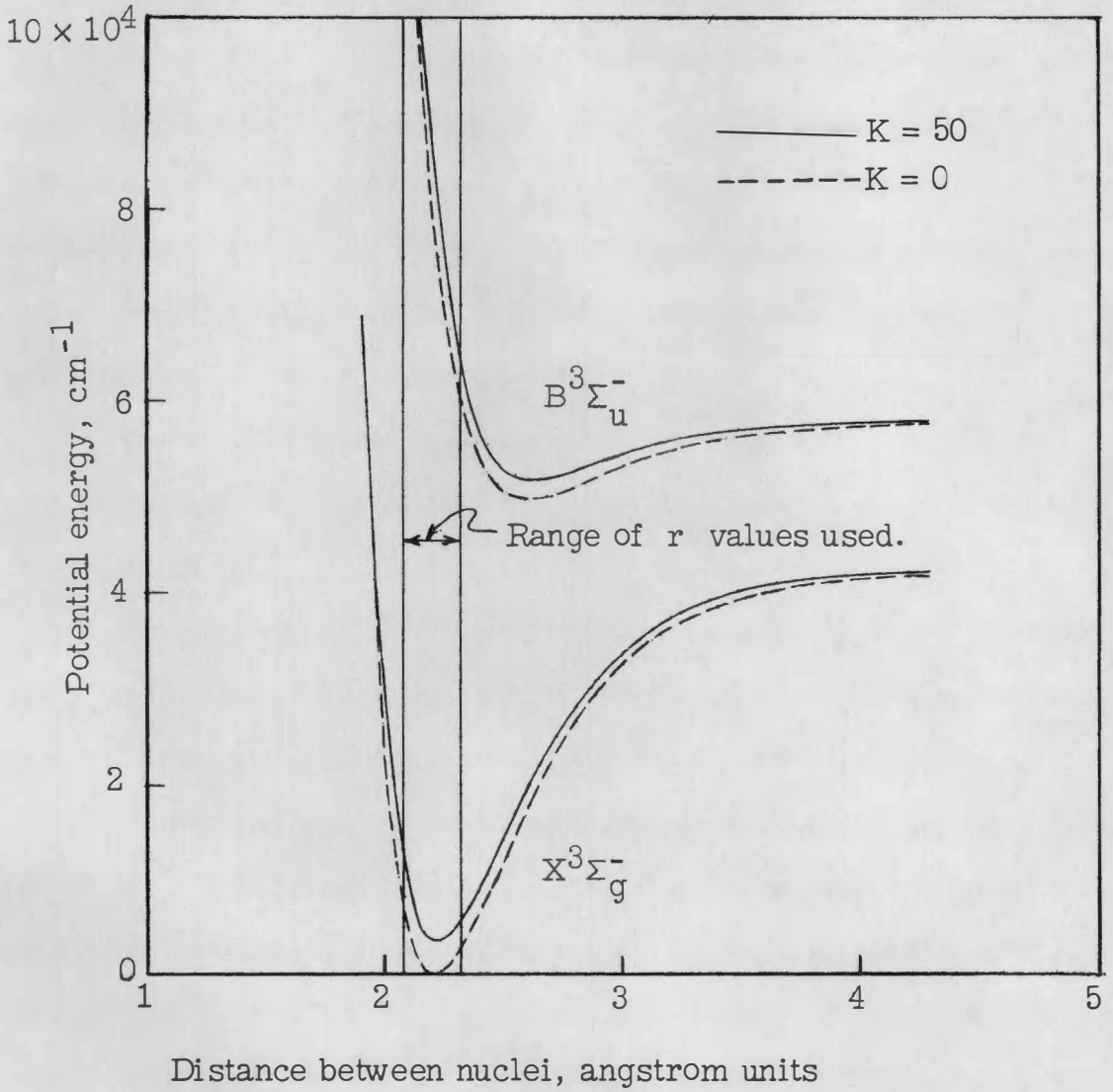

Figure 10.- Effect of rotation on potential curves.

436 cm^{-1} at the right extremity plus a shift to the right of the minimum by 0.027 A. The vertical changes amount to about 2 per cent of the depth of the potential well and the horizontal shift of the minimum to about 11 per cent of the range of r values used. The effect on the B state is almost exactly the same. The left extremity is raised by 4516 cm^{-1} (compared to 4514 cm^{-1} for the X state) and the right extremity by 3024 cm^{-1} (compared to 3022 cm^{-1} for the X state). The minimum of the B state does not fall within the range of r values used. The vibrational energy eigenvalues and eigenfunctions are functions of the shape of the potential and thus are slightly different for each rotational state. These differences were neglected in using equation (3), since only eigenfunctions for the rotationless state were used in performing the calculations.

It should be pointed out that the above effects of rotation on the potential curves were calculated for the worst conditions being considered, that is, at the highest temperature and at the extreme values of r. It is also important to note that, since both curves are affected in almost exactly the same way, the net distortion of the curves is what is really important and not the total energy shifts. In view of the fact that the actual potential curves are not accurately known, the approximately 2 per cent energy shifts are not particularly serious. However, the 11 per cent shift in the minimum of the lower curve may have an appreciable effect on the final results because it probably shifts the peaks of the lower state wave functions by roughly comparable amounts.

A small amount of uncertainty is introduced into the energy change to be associated with a given transition when the rotational energy changes

are lumped together. The change in the rotational quantum number must be plus or minus 1, which means that transitions differing in energy by twice the rotational level spacing in the upper state are counted to be the same. At K = 50 two rotational level spacings in the B state amount to 164 cm^{-1}. This amounts to about 0.3 per cent of a typical total energy change in a Schumann-Runge transition.

Calculation of the Absorption Coefficient Using the "Reflection" or "Delta Function" Method

1. Calculation of the Initial State Wave Functions

The problem of evaluating the absorption coefficient was reduced in equation (3) to the problem of integrating the product of the vibrational wave functions for the initial and final states. For the continuum under study the initial states are bound vibrational levels of the $X(^3\Sigma_g^-)$ state. In this calculation they are represented by normalized Morse wave functions[19]. These are solutions to Schroedinger's equation when a Morse potential is used for the vibrational potential. The following equations put these statements into mathematical form:

$$d^2\phi/dr^2 + (2\mu/\hbar^2)\left[E'' - V''(r)\right]\phi = 0 \qquad (5)$$

$$V'' = D_e\left\{1 - \left[e^{-\beta(r - r_e)}\right]^2\right\} \qquad (6)$$

$$\phi_{v''}(r) = \left[A_{v''}(x_e)^{v''}/A_0\right] \exp\left\{-\left[\frac{1}{2}\, x_e^{-1}e^{-\beta(r - re)} + \frac{1}{2}\,(x_e^{-1} - 2v'' - 1)\beta(r - r_e)\right]\right\} \cdot Q_{v''} \qquad (7)$$

The somewhat simpler harmonic oscillator wave functions[20] could be used, but they neglect the asymmetry of the potential curve and this has an appreciable effect on the higher vibrational wave functions.

Figure 11 compares the Morse potential for the $X(^3\Sigma_g^-)$ state to the parabolic potential (corresponding to harmonic oscillator wave functions) and also to the Dunham[21] and to the Hurlburt-Hirschfelder[22] potentials. Except for the parabolic potential the agreement is good over the range of r values needed (r = 1.08 A to 1.32 A). The Morse potential was chosen not only because it appears to be a fairly good representation of the X state potential but also because, except for the parabolic potential, it is the only one mentioned which leads to solutions of the Schroedinger equation in closed form.

2. Substitution of Delta Functions for the Final State Wave Functions

For the continuum under study the final state lies in a continuum of energy states above the dissociation limit of the $B(^3\Sigma_u^-)$ state and is represented by a wave function which near the turning point resembles a bound state wave function. However, as r approaches infinity the wave function does not vanish but becomes a sine function, as is appropriate for the wave function representing a free particle. Good results can often be obtained by replacing this wave function by a delta function located at the turning point. This substitution is the basic assumption underlying the "reflection" method. Herzberg[23] discusses why this method works. Briefly, it works because the main contribution to the overlap integral comes from the broad maximum near the turning point of the final state wave function. Contributions from the other maxima and minima tend

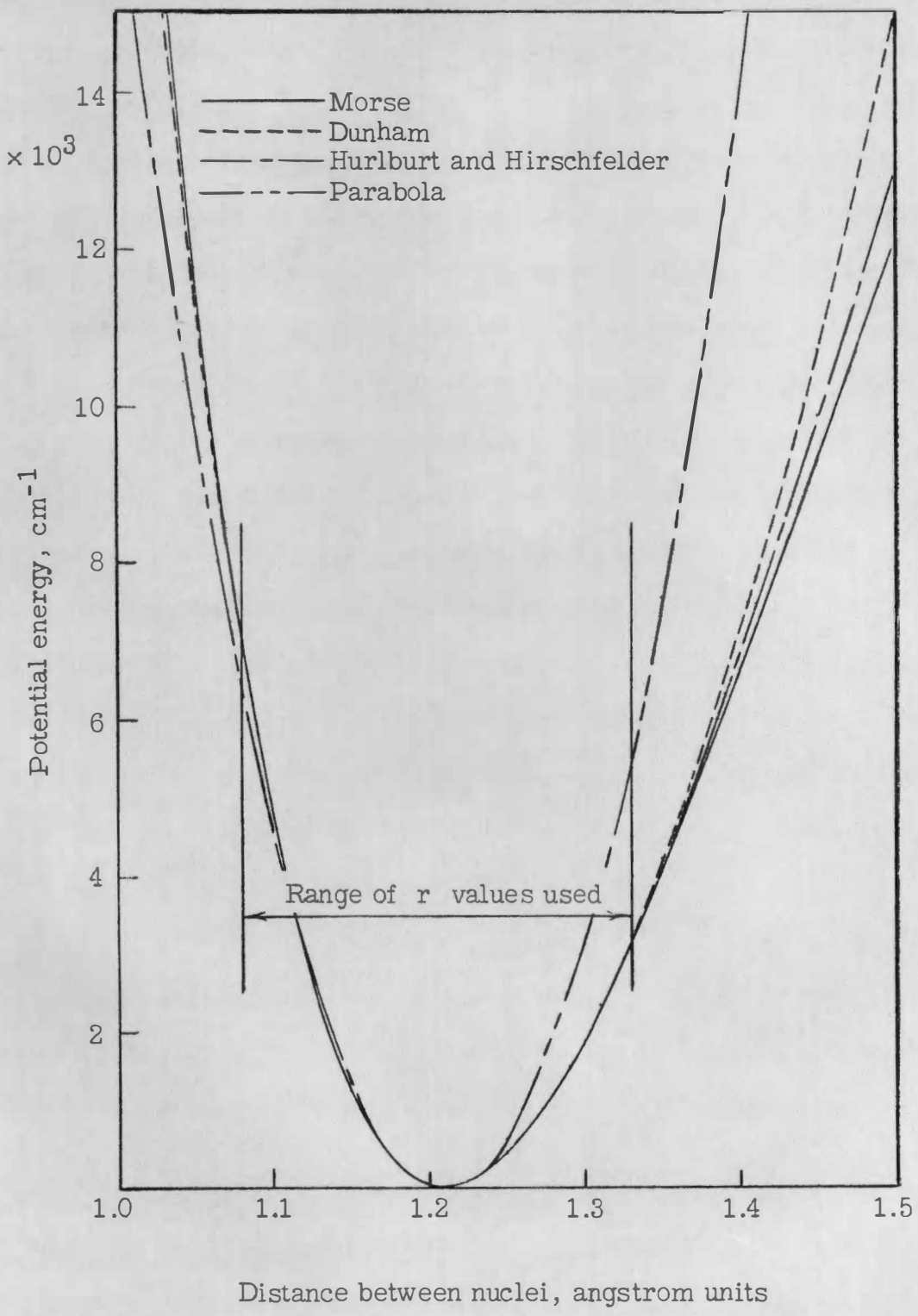

Figure 11.- Comparison of potential curves for the $X^3\Sigma_g^-$ state.

to cancel each other so long as the oscillation frequency of the final state wave function is large compared to the frequency of the initial state wave function.

The Morse, Dunham, Hurlburt-Hirschfelder, and Klein-Rydberg[24] potentials for the B state are shown on figure 12. The Klein-Rydberg potential is derived directly from spectroscopic data and unlike the other potentials, is shown by plotted points. Also shown are a number of calculated points which show where the B state potential should lie in order to give agreement between the absorption predicted by the "reflection" method and the experimental data shown on figure 2. The procedure used to obtain these points is described in Appendix A.

The agreement between the three curves is not good. The points calculated from experimental data show fairly good agreement among themselves even though they are based on three independent investigations and were obtained by two different methods of calculations. Because of this the true course of the potential is probably most nearly represented by a curve drawn through these points. The curve found in this way is shown on figure 13. A detailed discussion of the problem of accurately determining molecular potential curves from spectroscopic data is given by Coolidge, James and Vernon[25]. They do not deal directly with the determination of a curve above the dissociation limit, however.

3. Relation Between the Energy of the Absorbed Light Quantum and the Internuclear Distance at which the Transition Occurs

The energy difference between a given initial state and a given final state is the energy of the absorbed light quantum, E*. The value of r at the turning point of the upper state was uniquely related to

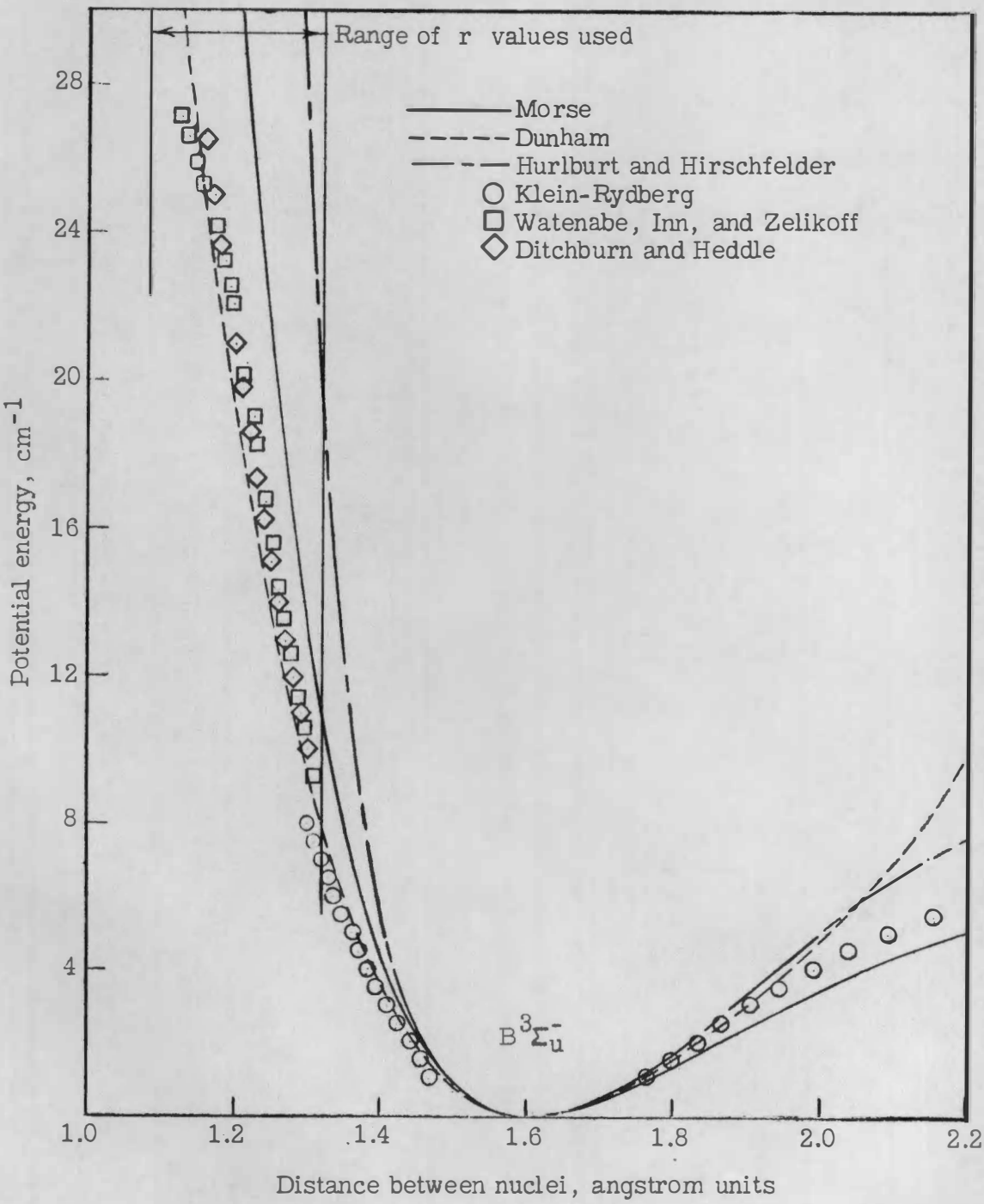

Figure 12.- Comparison of potential curves for the $B^3\Sigma_u^-$ state.

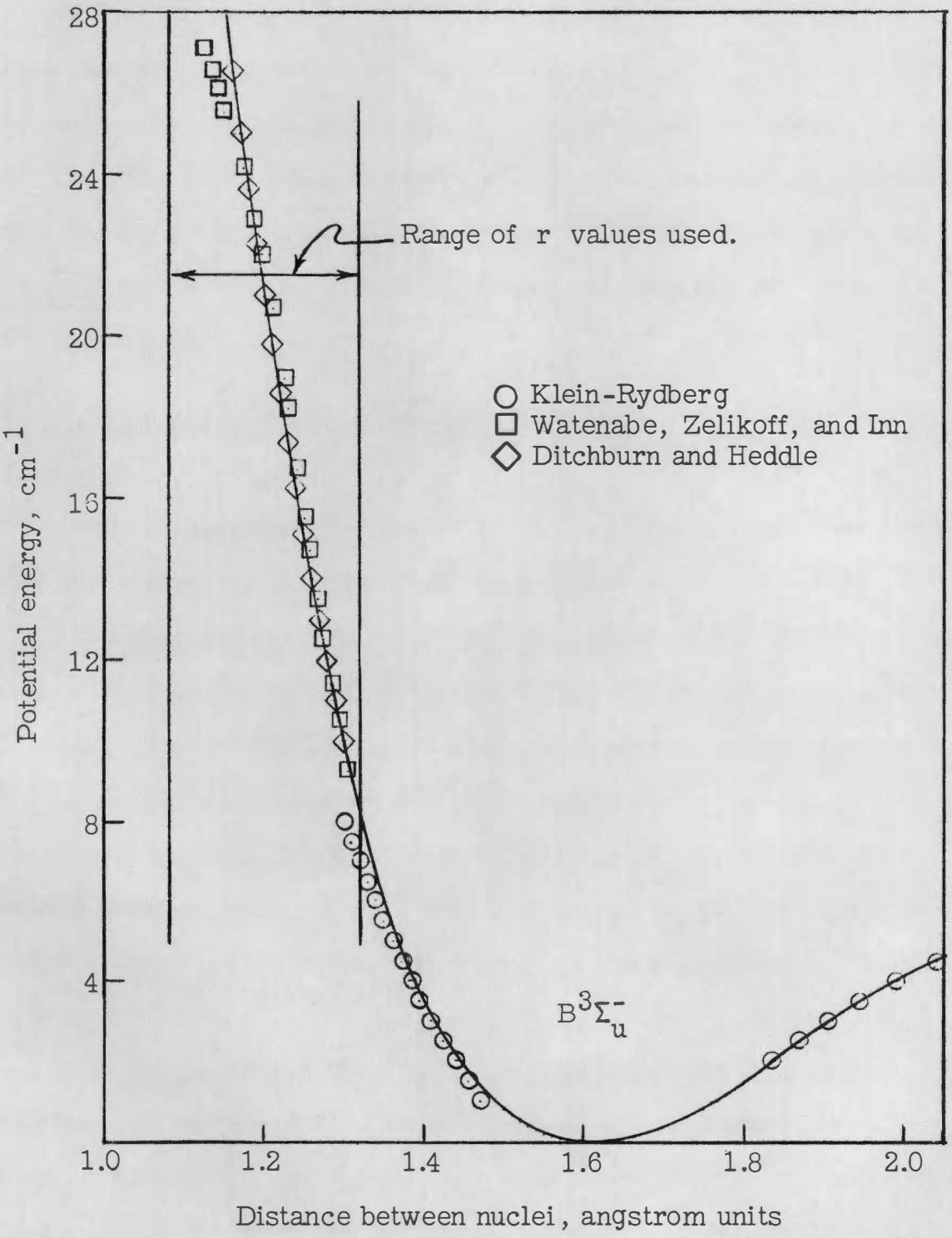

Figure 13.- $B^3\Sigma_u^-$ potential curve used in calculations.

the energy of the final state through the potential curve shown on figure 13. The energies of the discrete initial states were assumed to be the Morse eigenvalues for the X state. Thus, r_s and E* were uniquely related for a given value of v". The relation between r_s and E* for v" = 0 is shown on figure 14. To find the relation between r_s and E* for v" = 1, 2, etc., the energy difference between the level involved and the v" = 0 level was subtracted from the E* value found from the curve.

4. Procedure for Calculating the Absorption Coefficient by the "Reflection" Method

The procedure followed in using the "reflection" method to calculate the absorption coefficient was as follows:

a. Calculation of the Morse wave functions. Morse wave functions were calculated for each of the eleven lowest vibrational levels of the X state. Some difficulty was encountered in evaluating the associated Laguerre polynomials of order four and greater due to the rapidly increasing number of decimal places required to obtain significant differences between the terms. This problem was solved by finding the roots of the polynomials and then expressing the polynomials in factored form.

b. Calculation of the absorption coefficient for each initial state. Equation (3) was used to calculate eleven $\hat{k}_{v"}(\lambda)$ curves, where $\hat{k}_{v"}(\lambda) = k_{v"}(\lambda)/k_0^m$. For these curves each of the eleven lowest vibrational levels of the X state was in turn considered to be the initial state in which absorption takes place. The upper state wave functions were replaced

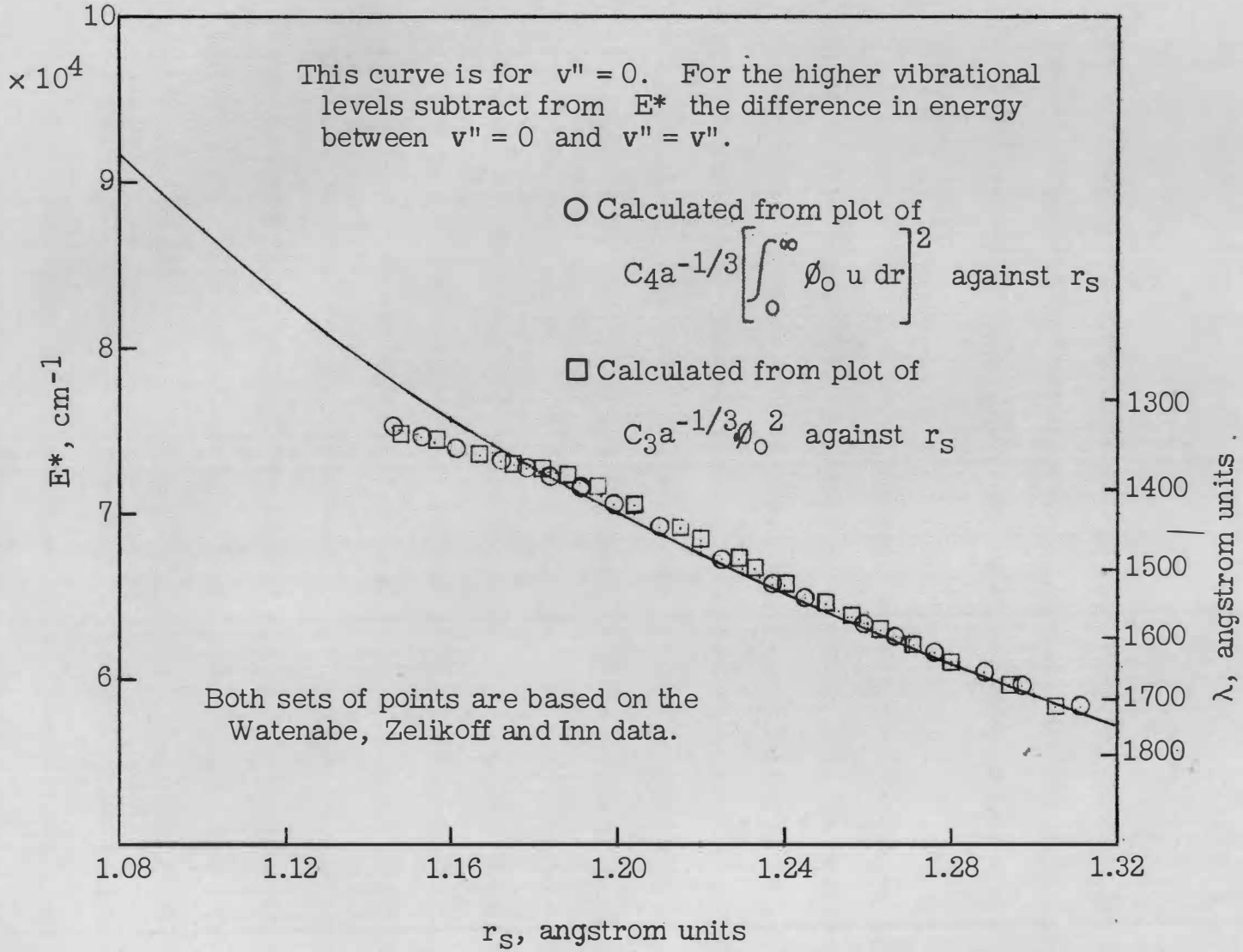

Figure 14.- Relation between E* and r_s.

by properly normalized delta functions located at the turning points. The following formula was the result:

$$\hat{k}_{v''}(\lambda) = \hat{k}_{v''}(r_s) = C_1 a^{-1/3} \overline{B''}^2 \phi_{v''} \qquad (8)$$

where figure 14 was used to relate $k_{v''}(\lambda)$ to $k_{v''}(r_s)$ and C_1 was chosen to make the maximum value of $\hat{k}_0(\lambda) = 1$. The derivation of this formula is given in Appendix B. The $k_{v''}(\lambda)$ curves obtained are shown on figure 15.

Some of the $k_{v''}(\lambda)$ curves were not calculated over the entire range of wavelengths which is available on figure 15. The limits placed on the curves to which this statement applies are indicated on the figure by vertical lines. The long wavelength limits correspond to the convergence limit of the band spectrum, that is, to the dissociation energy of oxygen in the B state, and the short wavelength limits correspond to the arbitrary value, r = 1.08 A, taken for the left extremity of the range of r. Note that the higher the initial vibrational energy level the farther the continuum extends towards longer wavelengths. Thus, the sharp division between continuum and band absorption which occurs at 1750 A for oxygen[26] at room temperature is not present at high temperature. Instead, there is a region of overlapping band and continuum absorption beginning at 1750 A and extending to longer wavelengths. New bands also appear as a result of the population of excited vibrational states of the X state. The wavelengths and relative intensities of the bands overlapping the continuum can be calculated by the Franck-Condon method but were not included in the calculations presented here. Fraser, Jarmain, and Nicholls[27] have tabulated some of the transition probabilities and

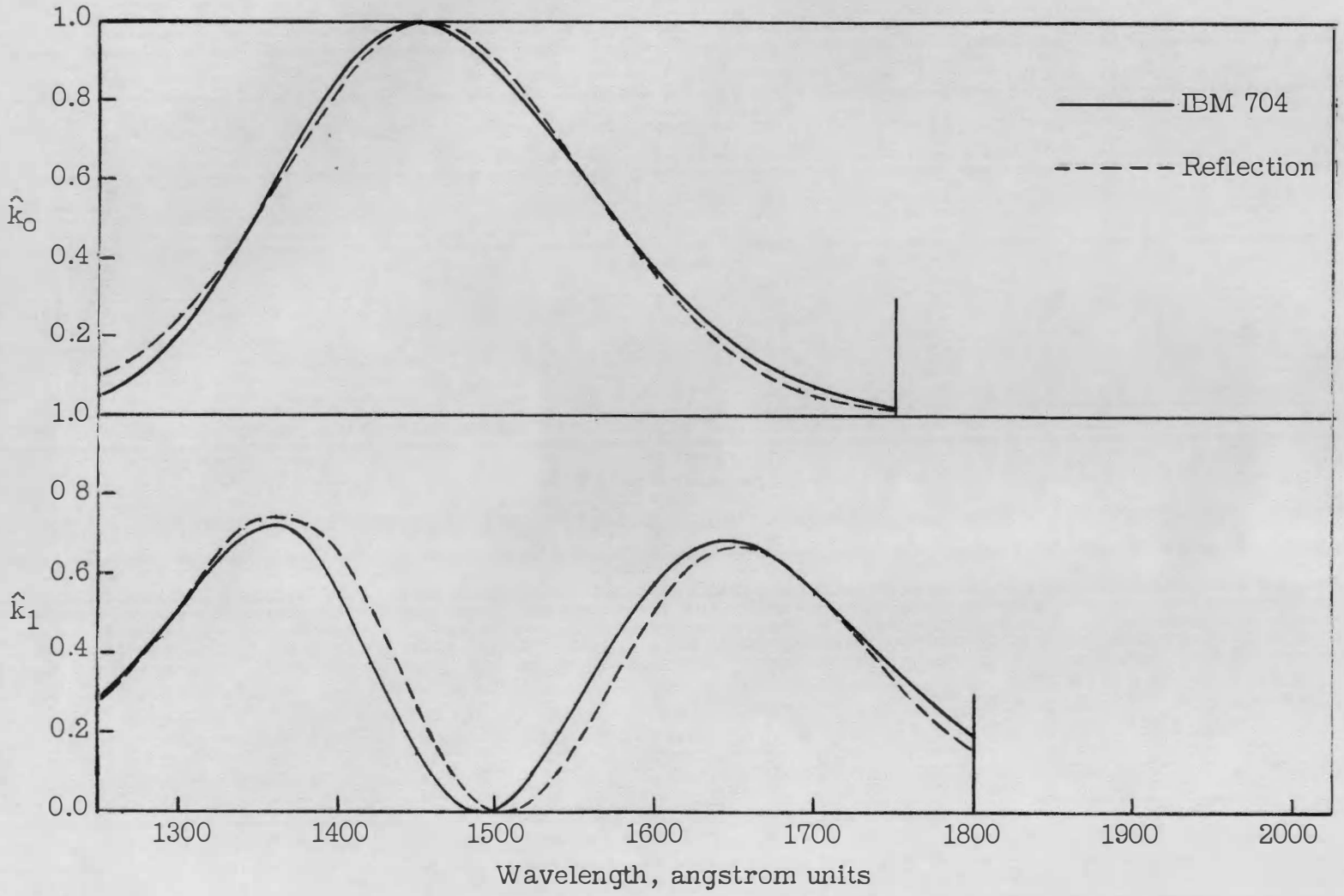

Figure 15(a).- Absorption coefficient of oxygen molecules in each of the 11 lowest vibrational levels.

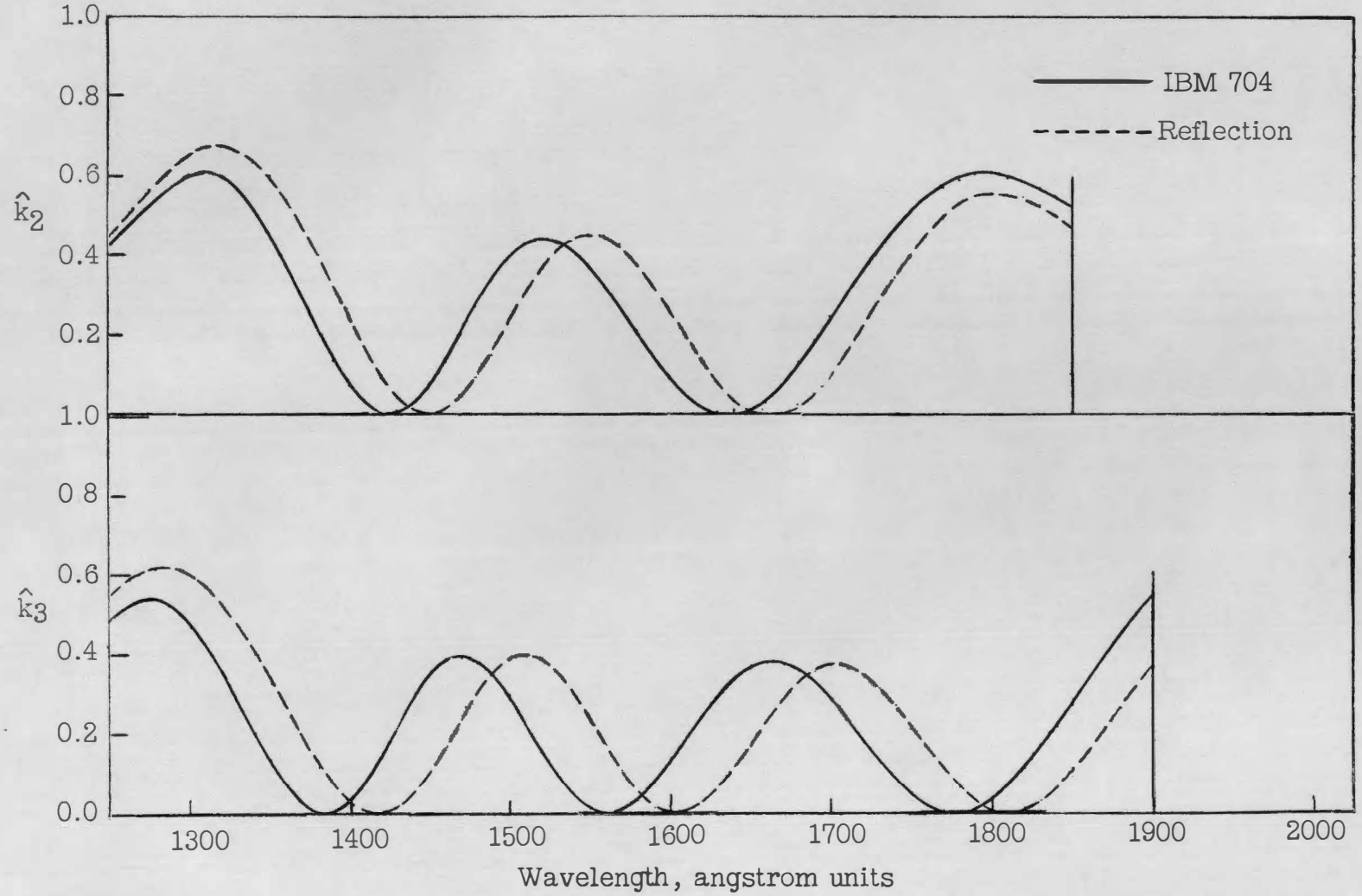
IBM 704
Reflection
$\hat{k}_2$
$\hat{k}_3$
1.0
0.8
0.6
0.4
0.2
1.0
0 8
0.6
0.4
0.2
0.0
1300
1400
1500
1600
1700
1800
1900
2000
Wavelength, angstrom units

Figure 15(b).

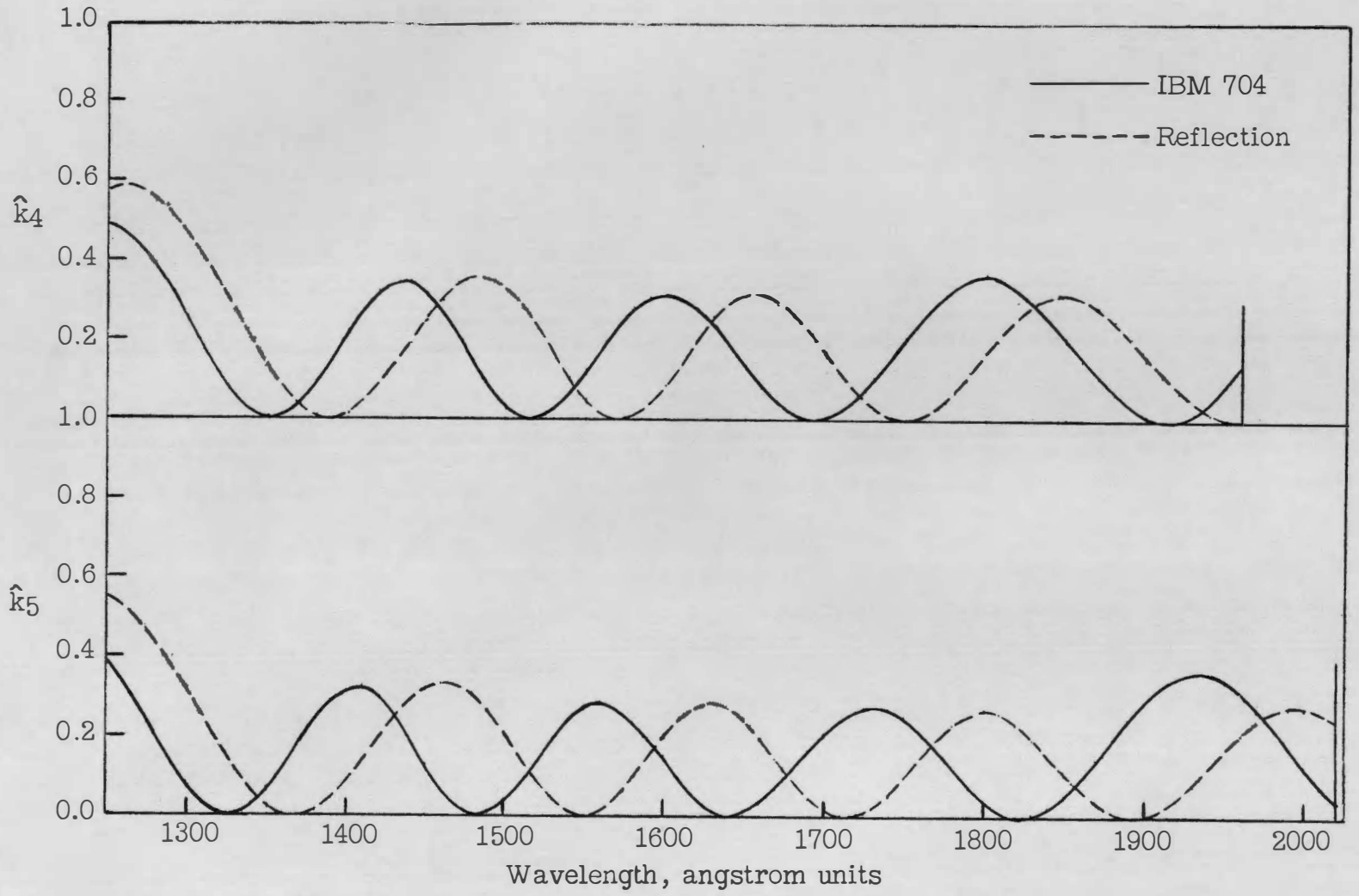
IBM 704
Reflection
$\hat{k}_4$
$\hat{k}_5$
1.0
0.8
0.6
0.4
0.2
0.0
1300
1400
1500
1600
1700
1800
1900
2000
Wavelength, angstrom units

Figure 15(c).

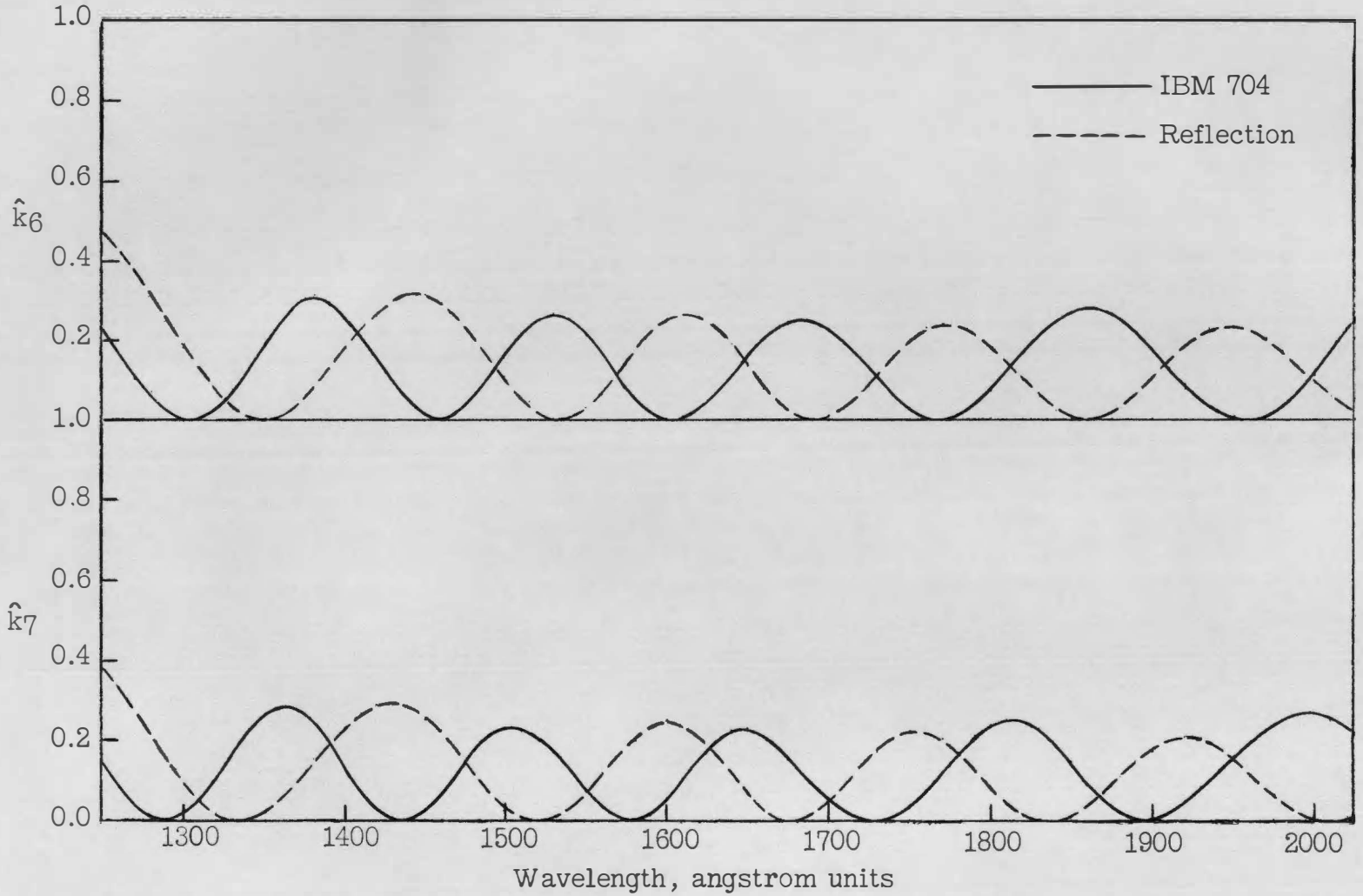
1.0
0.8
0.6
$\hat{k}_6$
0.4
0.2
1.0
0.8
0.6
$\hat{k}_7$
0.4
0.2
0.0
IBM 704
Reflection
1300
1400
1500
1600
1700
1800
1900
2000
Wavelength, angstrom units

Figure 15(d).

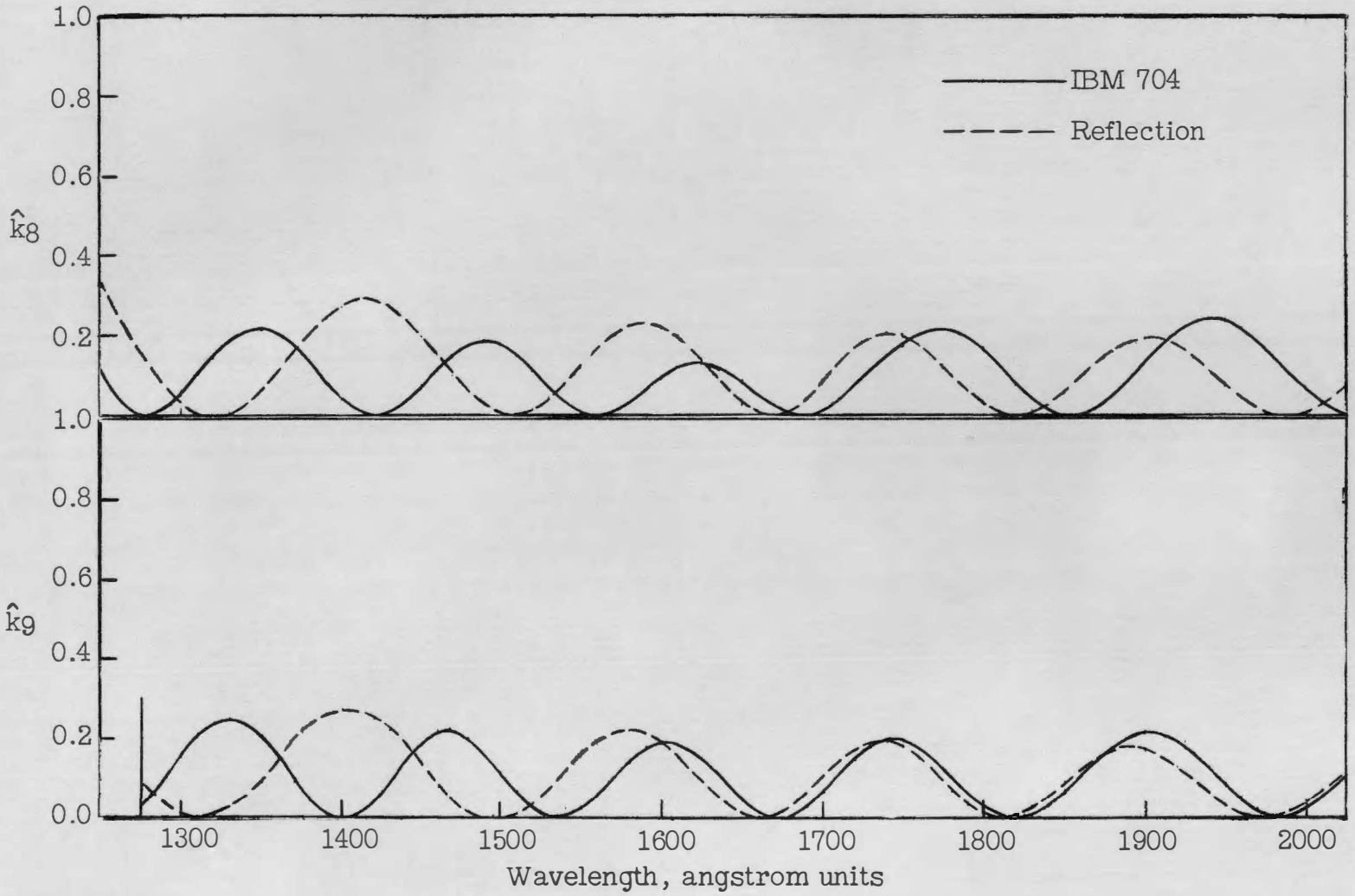
1.0
0.8
0.6
$\hat{k}_8$
0.4
0.2
1.0
0.8
0.6
$\hat{k}_9$
0.4
0.2
0.0
IBM 704
Reflection
1300
1400
1500
1600
1700
1800
1900
2000
Wavelength, angstrom units

Figure 15(e).

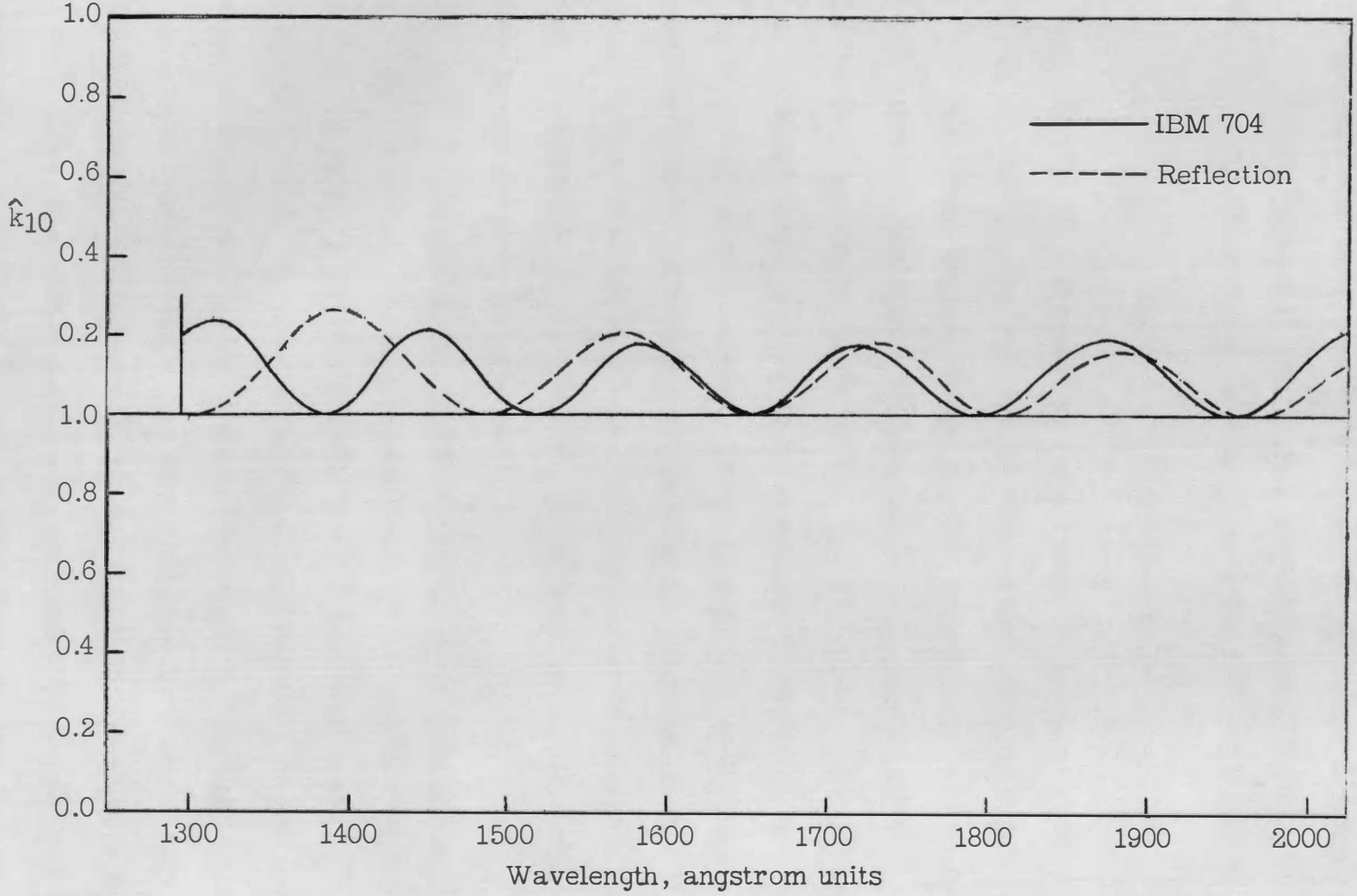
1.0
0.8
0.6
$\hat{k}_{10}$
0.4
0.2
1.0
0.8
0.6
0.4
0.2
0.0
IBM 704
Reflection
1300
1400
1500
1600
1700
1800
1900
2000
Wavelength, angstrom units

Figure 15(f).

Wurster, Treanor, and Glick[28] have observed some of the bands. The extension of the continuum has been observed by Golden and Myerson[29].

c. Calculation of the overall absorption coefficient. The overall absorption coefficient was calculated from the following formula:

$$\hat{k}_T(\lambda) = \sum_{v''=0}^{10} N_{v''}(T)\hat{k}_{v''}(\lambda) \qquad (9)$$

where $N_{v''}(T)$ is the weighting factor based on relative populations of the initial levels. The curves obtained are shown on figure 16.

The limits imposed on the $\hat{k}_{v''}(\lambda)$ curves carry over to the $\hat{k}_T(\lambda)$ curves. The discontinuities on the long wavelength ends correspond to the long wavelength limits of the $\hat{k}_{v''}(\lambda)$ curves. The extent of the curves toward short wavelengths is controlled by the short wavelength limits of the $\hat{k}_{v''}(\lambda)$ curves. It has already been mentioned that the short wavelength limit is due to the arbitrary cut-off at $r = 1.08$ A. To go farther into the short wavelength region would require a rather long extrapolation of the potential curve from the region where it has been determined from measured data.

d. Discussion of the effect of neglecting initial states for which $v'' > 10$. Equation (9) neglects contributions to $\hat{k}_T(\lambda)$ from all initial states for which $v'' > 10$. Figures 7 and 8 show that about $0.125/8.08 = 1.55$ per cent of the oxygen molecules are in the $v'' = 10$ state at 10,000° K. Figure 15 shows that $\hat{k}_{10}(\lambda)$ oscillates somewhat like a sine function with a peak-to-peak amplitude of about 0.2. Thus, the average contribution of $\hat{k}_{10}(\lambda)$ to $\hat{k}_T(\lambda)$ at the highest temperature being considered is about 0.0015 with the actual contribution at a given wavelength varying from 0 to 0.0030. Contributions like this have a very

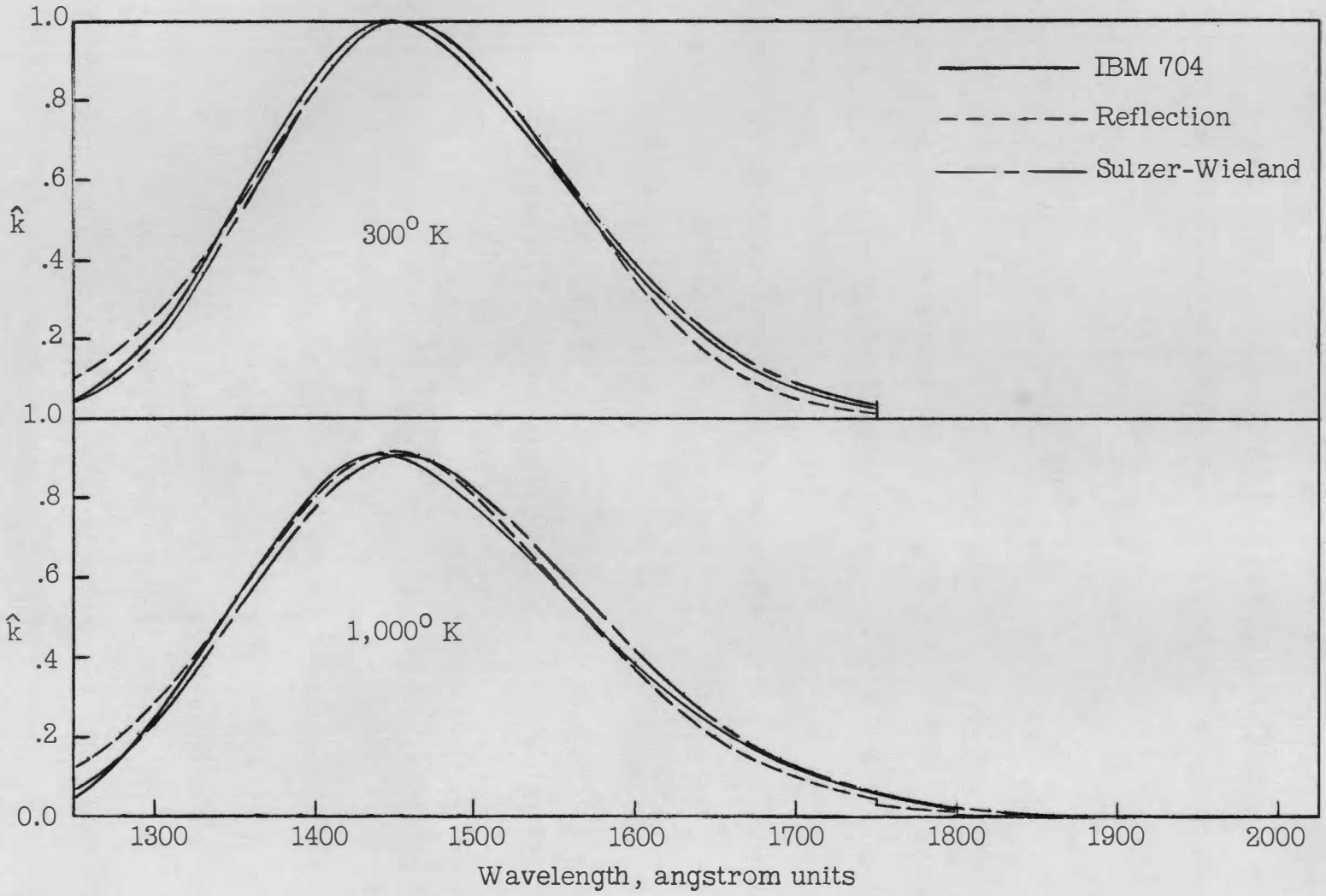

Figure 16(a).- Absorption coefficient of oxygen at temperatures from 300° to 10,000° K.

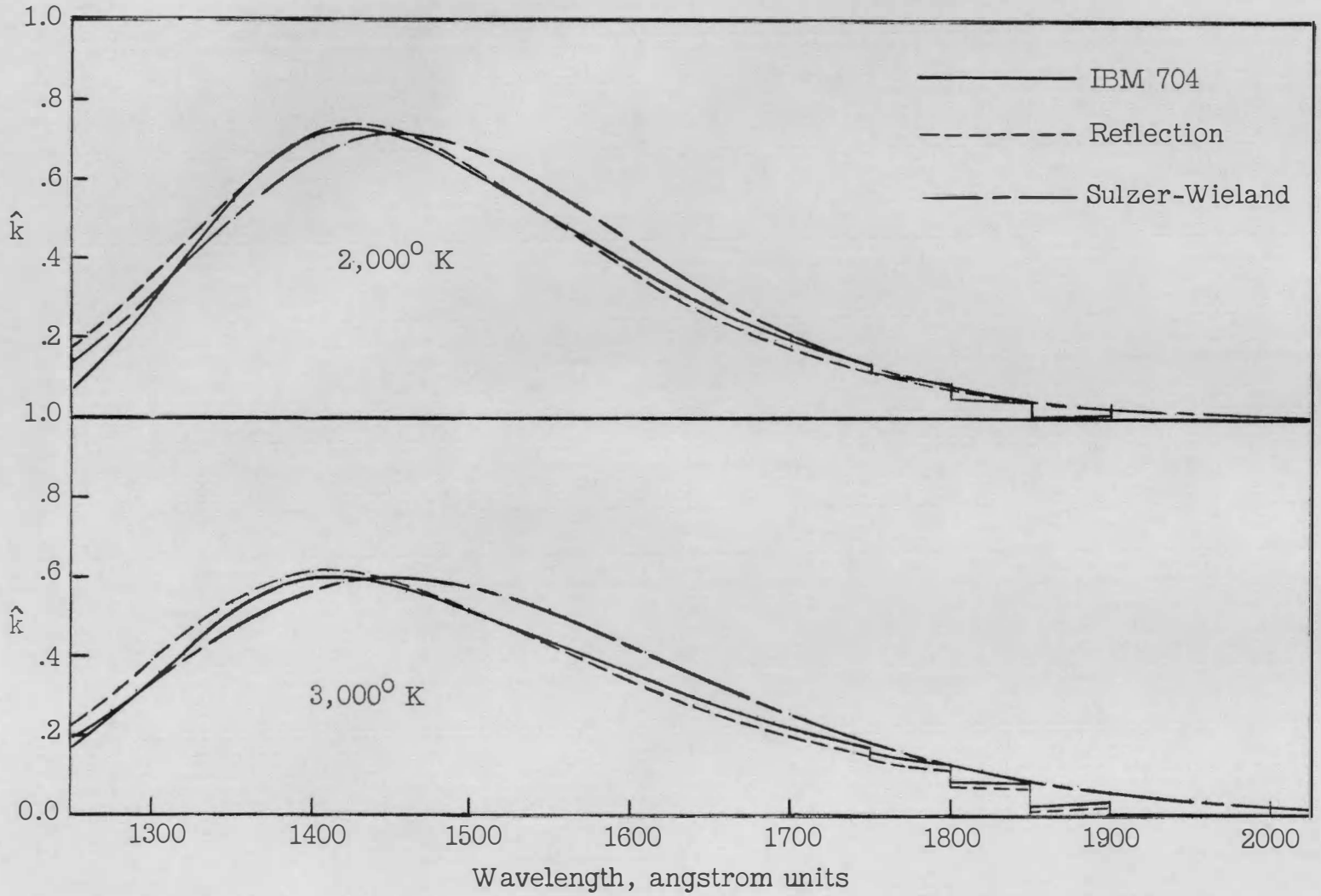
1.0
.8
.6
.4
.2
1.0
.8
.6
.4
.2
0.0
$\hat{k}$
$\hat{k}$
IBM 704
Reflection
Sulzer-Wieland
2,000° K
3,000° K
1300
1400
1500
1600
1700
1800
1900
2000
Wavelength, angstrom units

Figure 16(b).

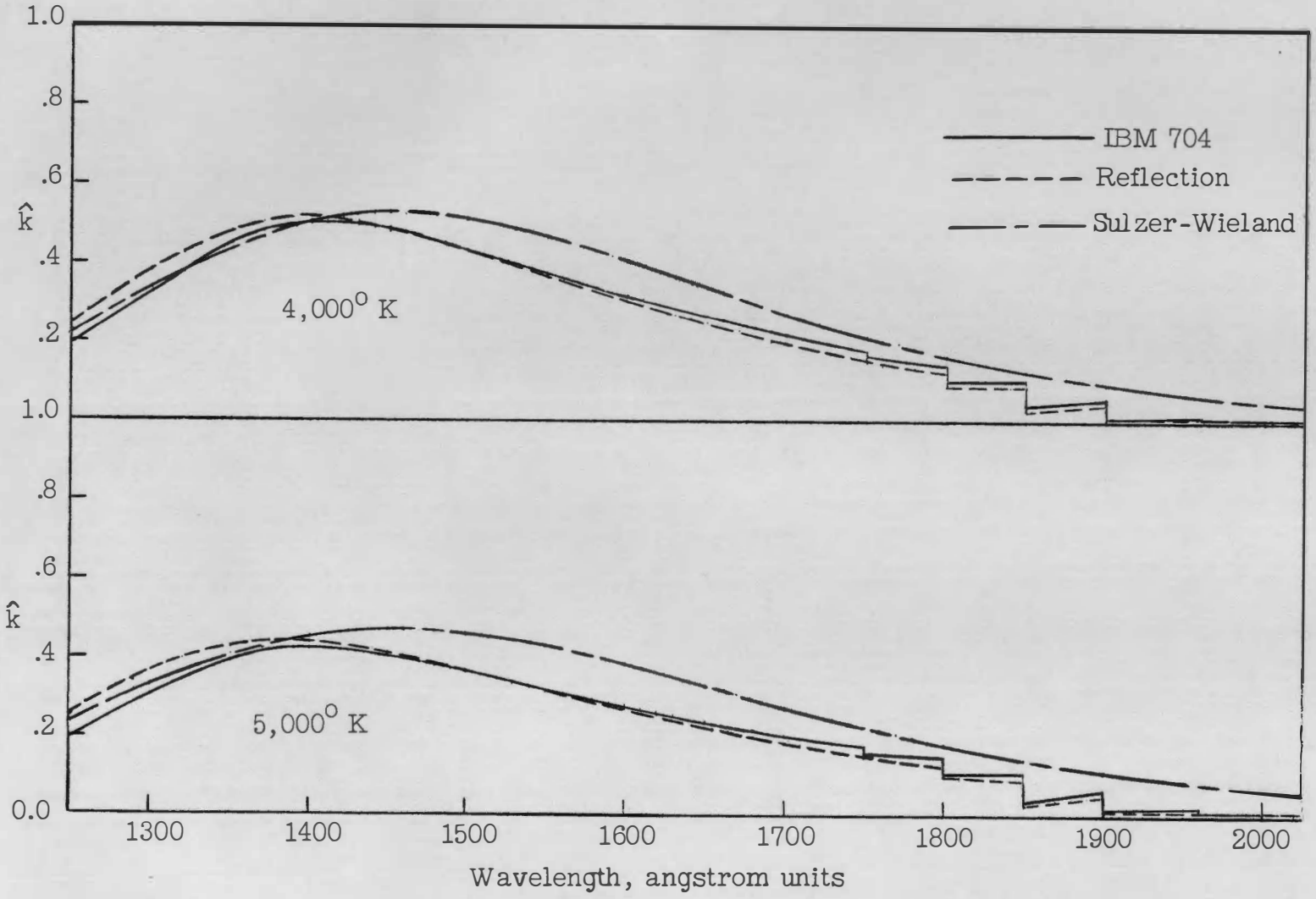
1.0
.8
.6
$\hat{k}$
.4
.2
1.0
.8
.6
$\hat{k}$
.4
.2
0.0
IBM 704
Reflection
Sulzer-Wieland
4,000° K
5,000° K
1300
1400
1500
1600
1700
1800
1900
2000
Wavelength, angstrom units

Figure 16(c).

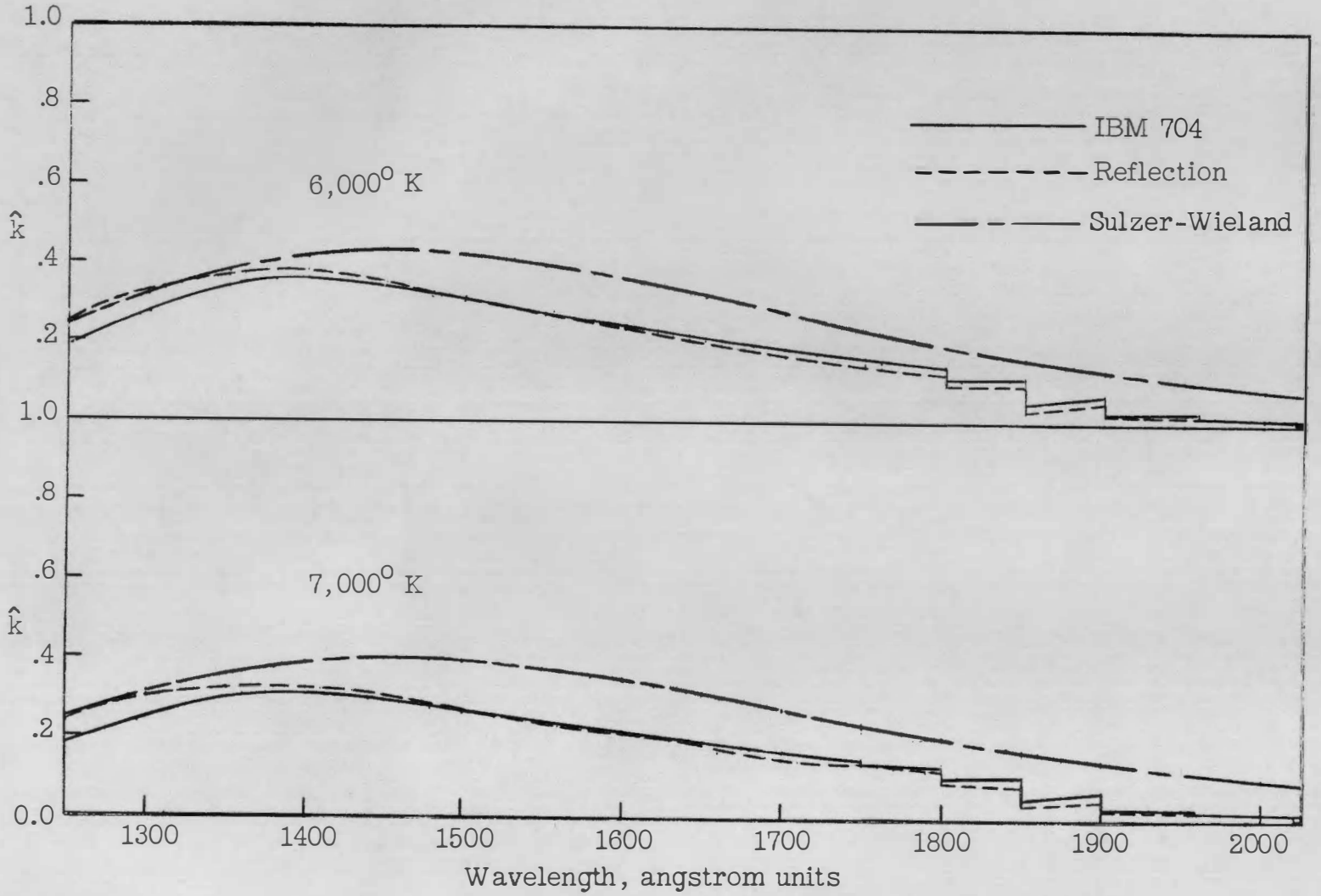
1.0
.8
.6
.4
.2
1.0
.8
.6
.4
.2
0.0
k̂
k̂
6,000° K
7,000° K
IBM 704
Reflection
Sulzer-Wieland
1300
1400
1500
1600
1700
1800
1900
2000
Wavelength, angstrom units

Figure 16(d).

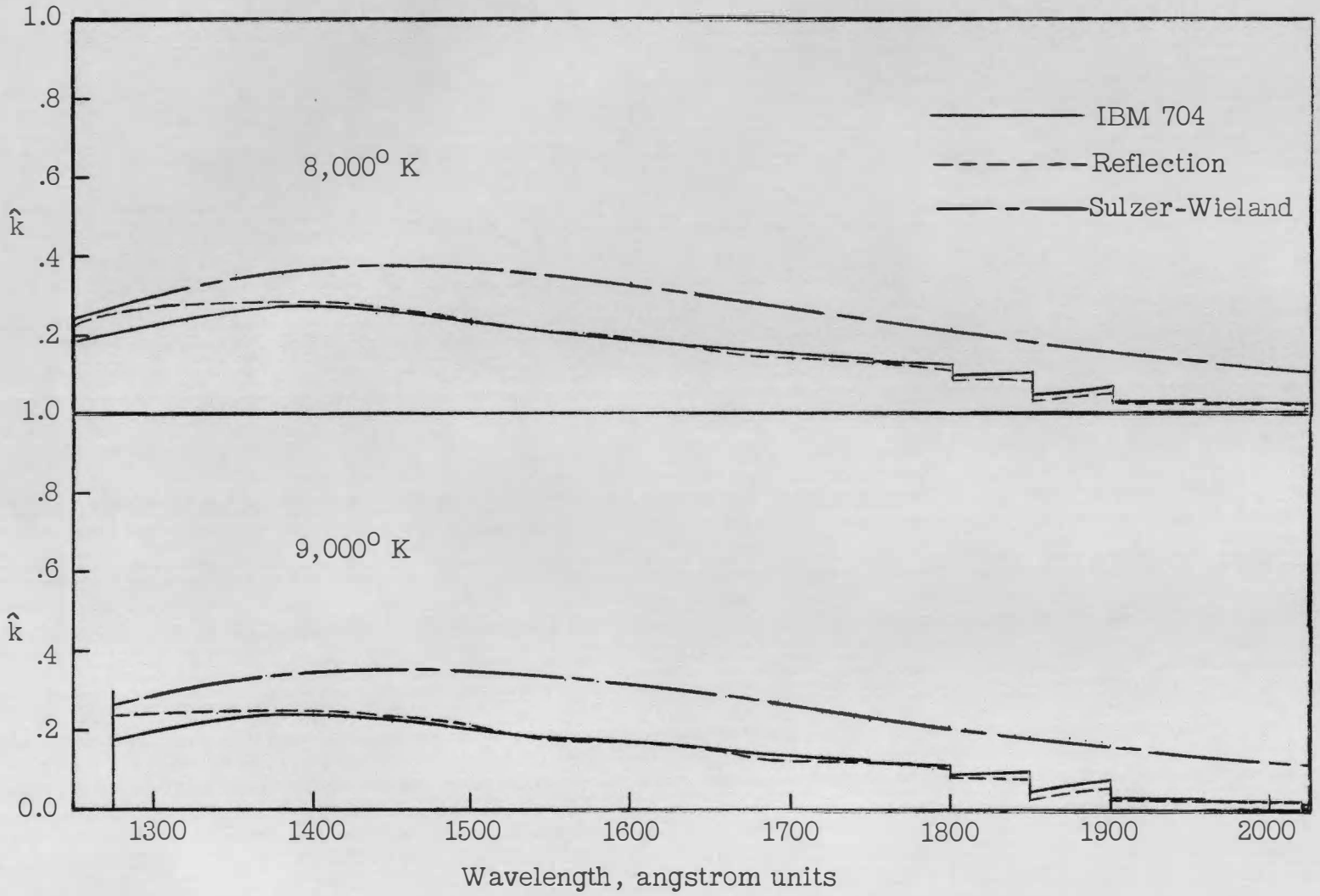
1.0
.8
.6
.4
.2
1.0
.8
.6
.4
.2
0.0
k̂
k̂
8,000° K
9,000° K
IBM 704
Reflection
Sulzer-Wieland
1300
1400
1500
1600
1700
1800
1900
2000
Wavelength, angstrom units

Figure 16(e).

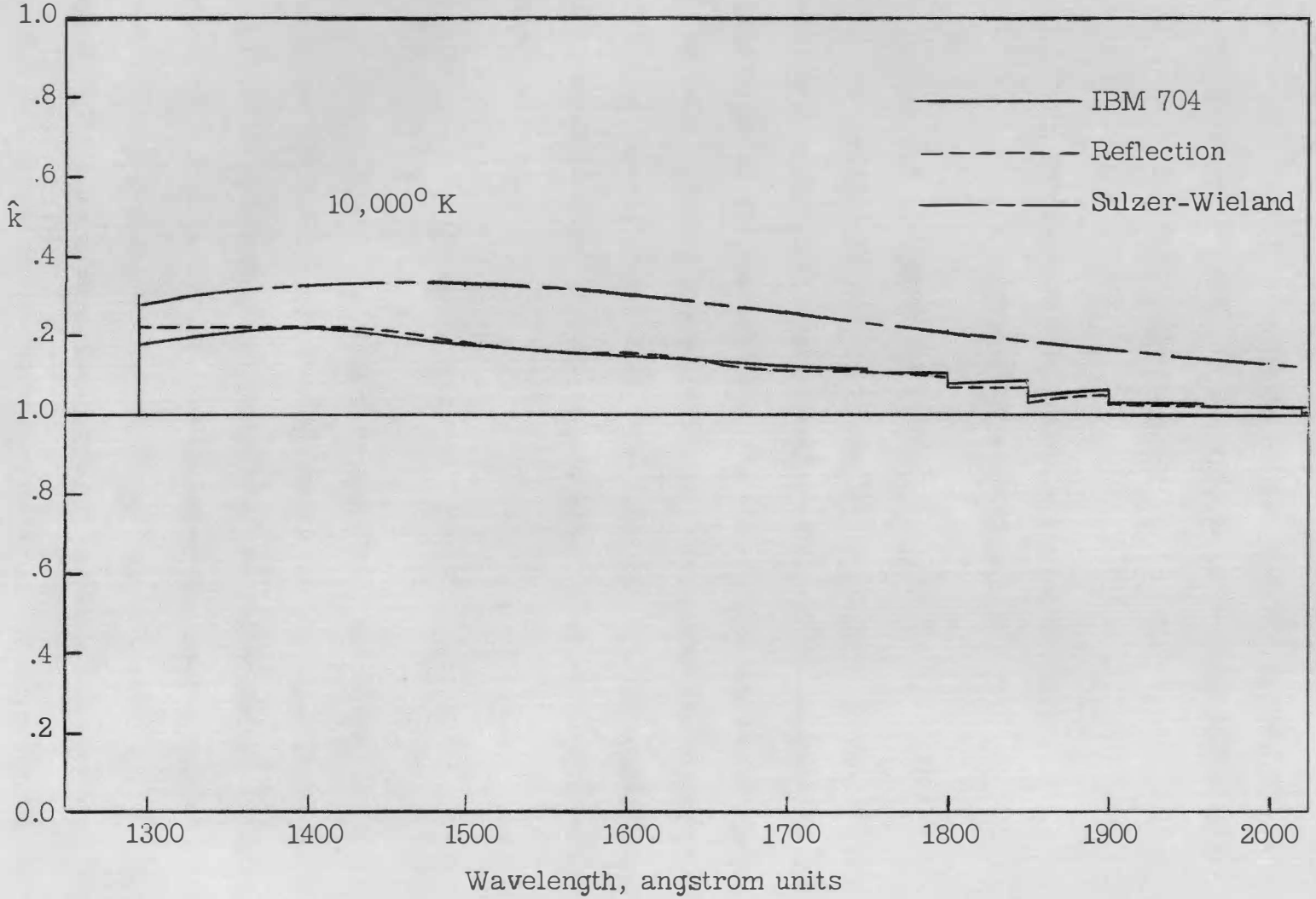
1.0
.8
.6
.4
.2
1.0
.8
.6
.4
.2
0.0
$\hat{k}$
10,000° K
IBM 704
Reflection
Sulzer-Wieland
1300
1400
1500
1600
1700
1800
1900
2000
Wavelength, angstrom units

Figure 16(f).

small effect on the shape of the distribution curve. Contributions from the higher states are even smaller and are more or less randomly distributed over the wavelength range. Thus the cutting off of the calculations at $v'' = 10$ is believed to have a negligible effect on the shape of the distribution curve.

Calculation of the Absorption Coefficient Using an IBM 704 Computer

1. Description of Method and Procedures

a. Machine evaluation of overlap integrals. As has already been mentioned, equation (3) reduces the problem of calculating the absorption coefficient to the evaluation of the vibrational overlap integral, $\int_0^\infty \phi_{v''} u dr$. For the digital computer calculations Morse eigenfunctions were used for the ground state wave functions and the excited state wave functions were found by using the computer to solve the Schroedinger equation:

$$d^2u/dr^2 + 2\mu/\hbar^2\left[E' - V'(r)\right]u = 0 \qquad (10)$$

The solution was started by specifying the values of u and du/dr at the turning point of the motion in the upper state and was continued by the Runge-Kutta procedure[30] as far as needed into the region where $E' - V' > 0$. The machine evaluated the overlap integral at the same time and the value read out at the end of the run was $\int_{r_s}^\infty \phi_{v''} u dr$, where r_s is the internuclear distance corresponding to the starting point. It was only necessary to integrate out to r values where the integral

attained a constant value since the integrand vanishes when ϕ_V'' vanishes. Runs were made in the opposite direction (i.e., into the region where $E' - V' < 0$) from the same starting point to evaluate $\int_0^{r_s} \phi_V'' u dr$ and the two parts were added to obtain $\int_0^{\infty} \phi_V'' u dr$. The machine results in the region where $E' - V' < 0$ were not satisfactory. The trouble was due to the fact that $d^2u/dr^2 > 0$ in this region -- making the solution unstable. Coolidge, James, and Present[31] reported similar difficulty. The problem could have been solved by adjusting du/dr at r_s slightly so as to obtain positive diverging and negative diverging u's for nearly identical values of du/dr at r_s. However, the required integrals were computed instead with a desk integrator using Hankel functions for the u functions. Schiff[32] points out that Hankel functions are solutions of equation (10) when V' is a linear function of r. The tangent to the potential curve was used for V' in the Hankel solutions.

b. Checking the machine results. The following checks were made on the machine results:

(1) For a few runs Hankel solutions were computed over the whole range of r values necessary using the tangent to the potential curve as the potential function. The observed deviations from the machine computed u functions were in the correct directions and vanished as the point of tangency was approached.

(2) Plots of the integrand were made over the range of r values used. The junction of the two parts at the starting point was smooth in every case.

(3) Spot checks of the value of $\int_0^\infty \phi_{v''} u dr$ were made with a desk integrator and were in satisfactory agreement with the machine results.

c. Normalization of the wave functions. The numerical values of the vibrational overlap integrals are properly related to each other only when normalized wave functions are used. The Morse wave functions used were normalized but the u functions obtained from the IBM machine were not. The necessary normalization factor is shown in Appendix C to be $F^{1/2}$ = constant times $a^{-1/6}g^{1/4}$, where a is the slope of the potential curve at r_s.

d. Formula for calculating the absorption coefficient. When $F^{1/2}$ was substituted in equation (3) the result was:

$$\hat{k}_{v''}(\lambda) = \hat{k}_{v''}(r_s) = C_2 a^{-1/3} E^* \left[\int_0^\infty \phi_{v''} u dr\right]^2 \qquad (11)$$

Equation (11) is comparable to equation (8) of the previous section on the "reflection" method. Figure 14 was used to relate $\hat{k}_{v''}(\lambda)$ to $\hat{k}_{v''}(r_s)$ and C_2 was chosen to make the peak value of $\hat{k}_0(\lambda) = 1$.

2. Calculation of the Absorption Coefficient From the Machine Results

The procedure followed in calculating the absorption coefficient was exactly the same as was used for the "reflection" method except that equation (11) was used to calculate the values of $\hat{k}_{v''}$ in place of equation (8). The $\hat{k}_{v''}(\lambda)$ curves are shown on figure 15 and the $\hat{k}_T(\lambda)$ curves are shown on figure 16.

Calculation of the Absorption Coefficient Using Sulzer and Wieland's Formula

1. Statement of the Formula and Calculation of the Absorption Coefficient

The formula[33] given by Sulzer and Wieland is written in terms of the wave number, $\tilde{\nu}$, and is as follows:

$$k_T(\tilde{\nu}) = k_0^m \left[\tanh (\Theta/2T)\right]^{1/2} \exp\left\{-\tanh (\Theta/2T)\left[(\tilde{\nu} - \tilde{\nu}_m)/\Delta\tilde{\nu}_o\right]^2\right\} \qquad (12)$$

where k_0^m is the maximum value of $k_T(\tilde{\nu})$ at 0° K, Θ is the characteristic temperature which appears in the vibrational partition function for the X state, $\tilde{\nu}_m$ is the wave number for which $k_T(\tilde{\nu})$ has its maximum value, and $\Delta\tilde{\nu}_o$ is the natural half-breadth of the $k_0(\tilde{\nu})$ curve, that is, $\Delta\tilde{\nu}_o$ is the difference between the two values of $\tilde{\nu}$ for which $k_0(\tilde{\nu}) = e^{-1}k_0^m$.

In order to use equation (12) k_0^m, $\tilde{\nu}_m$, and $\Delta\tilde{\nu}_o$ must be evaluated from experimental measurements of the absorption at a temperature low enough so that $k_T(\tilde{\nu})$ is for all practical purposes identical to $k_0(\tilde{\nu})$. Room temperature measurements are adequate for oxygen, since practically all oxygen molecules are in the lowest vibrational state at room temperature.

The following values were used for calculating the absorption coefficient for oxygen:

$$k_0^m = 400 \text{ cm}^{-1}$$

$$\tilde{\nu}_m = 69{,}000 \text{ cm}^{-1}$$

$$\Delta\tilde{\nu}_o = 6481 \text{ cm}^{-1}$$

$$\Theta = 2{,}260^\circ \text{ K}$$

The resulting $\hat{k}_T(\lambda)$ curves are shown on figure 16.

2. Underlying Assumptions and the Resulting Limitations

a. Statement of the assumptions. The assumptions underlying Sulzer and Wieland's approach are as follows:

(1) Harmonic oscillator wave functions[34], which are solutions of Schroedinger's equation for a parabolic potential, were assumed for the initial state functions

(2) The upper state potential was assumed to be a straight line

(3) The upper state eigenfunctions were replaced by delta functions as in the "reflection" method

(4) The electronic transition probability was assumed to be independent of r

(5) The expression, $\int_0^\infty \left[k/\tilde{\nu}\right] d\tilde{\nu} = \text{constant}$[35], was replaced by $\int_0^\infty k\,d\tilde{\nu} = \text{constant}$. This is equivalent to omitting E^* from equations (8) and (11) or to omitting $\tilde{\nu}$ from Herzberg's equation for $I_{abs}^{v'v''}$.

(6) The effect of molecular rotation was neglected

b. Limitations due to the assumptions. With the assumptions mentioned the calculation was simplified enough to permit summation of the equations over all the initial vibrational states to obtain the result given in equation (12). The result is symmetrical about $\tilde{\nu}_m$ and thus is incapable of showing any shift of the peak position with temperature such as appears on figure 1. Equation (12) is similar to the equation for the normal curve of error, $y = (2\pi)^{-1/2}\exp(-x^2/2)$, since it can be written as $y = \text{constant}\ \exp(-\tanh ax^2)$ and the hyperbolic tangent does not differ much from its argument for small values of the argument.

The Sulzer-Wieland equation is applicable to any diatomic molecule for which the necessary constants can be evaluated and is formally applicable at any temperature. In practice, it has been found to agree well with measured absorption coefficients for the halogens at temperatures up to 2,000° K. (See figs. 3 and 4 and refs. 3(a) to 3(g).) Because of the rather drastic assumptions made in order to simplify the theory enough to permit the result to be written in the form of a single simple equation it is necessary to guard against using it without making some sort of evaluation of its probable range of validity for the molecule in question and for the temperature range needed. As will appear later in this dissertation, the Sulzer-Wieland formula is not adequate for calculation of the absorption coefficient of oxygen up to 10,000° K.

Calculation of the Absorption Coefficient Including an Empirical Correction for the Variation of the Electronic Transition Probability With Internuclear Distance

1. Determination and Discussion of the Correction Factor

a. Method for determination of the correction factor. The discussion following equation (3) mentioned that an empirical evaluation of the variation of the electronic transition probability, $R_e(r)$, with internuclear distance could be obtained by comparing experimental values of the absorption coefficient to the theoretical values calculated from equation (3). Since the electronic transition probability was assumed to be constant in

the derivation of equation (3), the factor required to make the theory agree with experiment can be interpreted as being proportional to $R_e^2(r)$.

b. Variation of the correction factor with wavelength. Figure 17 shows the variation with wavelength of the factor mentioned. It was derived from a comparison of the smooth, self-consistent data of Watenabe, Zelikoff, and Inn to the IBM results. The variation is slow and smooth from 1750 A down to 1375 A. At 1375 A the slope suddenly changes sign and the factor drops sharply to zero at 1300 A.

c. Discussion of a possible cause of the disturbance at 1375 A. The sharp drop-off mentioned above is particularly interesting and significant, since it indicates the presence of an additional factor affecting the absorption coefficient. Watenabe, Zelikoff, and Inn[36] suggested that another potential interacts with the $B(^3\Sigma_u^-)$ potential to cause this disturbance. Evidence[37] has been cited for the existence of a potential in addition to the five well-established ones shown on figure 5. It is designated as $^3\pi_u^-$ and transitions to it from the $X(^3\Sigma_g^-)$ ground state are allowed by the selection rules[38]. Figure 18 shows that the $^3\pi_u^-$ curve which was proposed by Flory[39] and later substantiated by Volman[40] could be reasonably extrapolated to cross the $B(^3\Sigma_u^-)$ curve at the point required to cause the disturbance noted at 1375 A. On the other hand, Wilkinson and Mulliken[41] gave some good arguments for believing that the $^3\pi_u^-$ curve takes a different course. Their curve is also shown on figure 18. Perhaps two new curves are involved, only one of which is the $^3\pi_u^-$ curve.

d. Comparison to literature results. Nicholls[42] reported a determination of the variation of $R_e(r)$ from the Schumann-Runge bands.

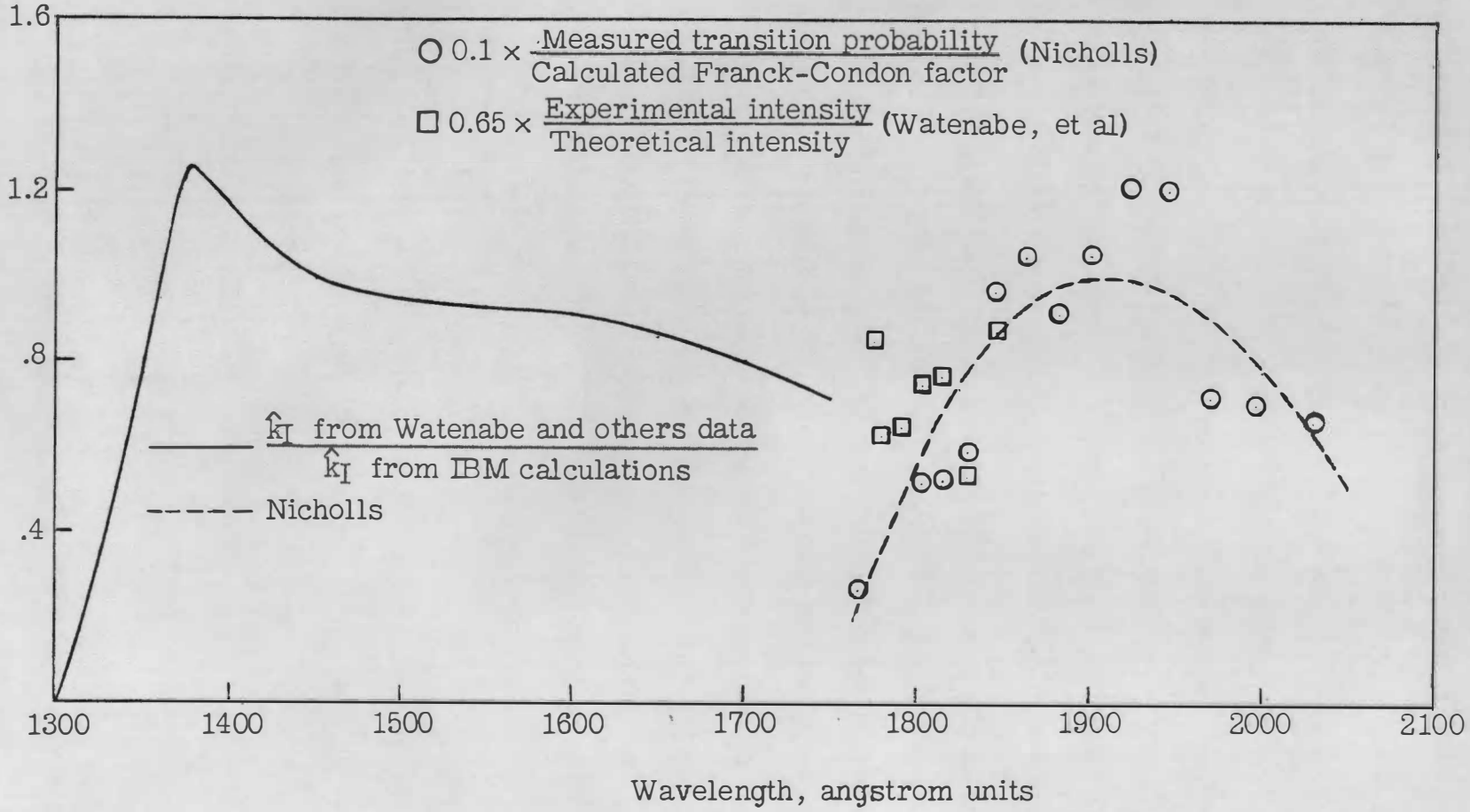

Figure 17.- Ratio of experimental to theoretical absorption coefficient at 300° K.

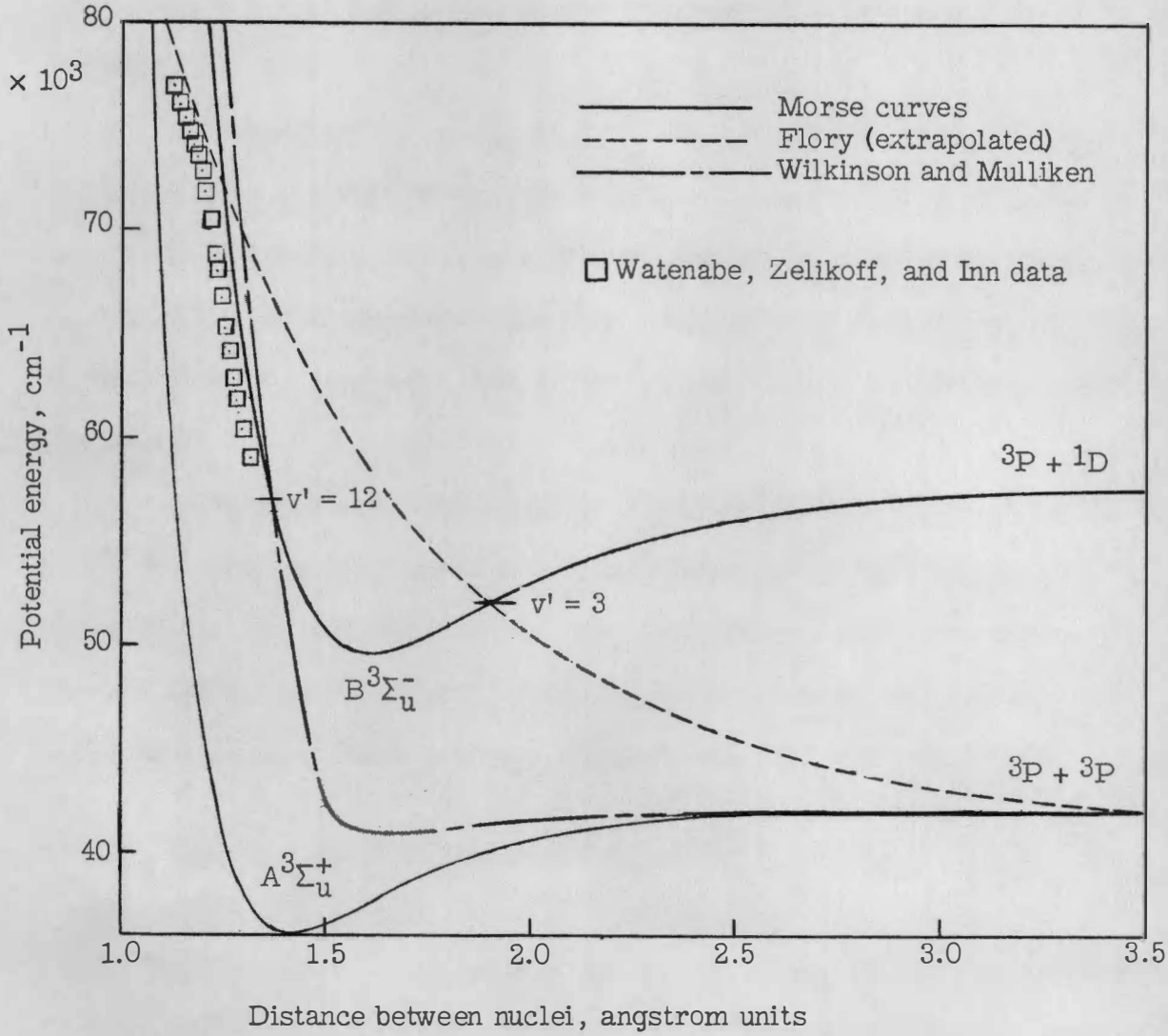

Figure 18.- Illustration of two suggested new potential curves for O_2.

His results, which are based on calculated Franck-Condon factors and absorption measurements by Ditchburn and Heddle[43], are shown on figure 17. Also shown are some additional points prepared from data given by Watenabe, Zelikoff, and Inn[44].

The variation of $R_e(r)$ as defined by Nicholls' curve is quite different from the variation derived here. Since there is no reason to expect the electronic transition probability to be affected by the change from band to continuum absorption, the two curves ought to join smoothly to each other and ought to look as if one were just a continuation of the other.

The variation derived from the continuum absorption is believed to be the more reliable since the experimental scatter of the data used was much smaller than that of the data available in the band region. This is illustrated on figure 17, where both continuum and discrete spectrum data from the Watenabe, Zelikoff, and Inn paper were used.

2. Application of the Correction Factor to the Calculation of the Absorption Coefficient

In the preceding paragraphs and on figure 17 $R_e(r)$ was treated as though it were a function of wavelength. Because λ and r_s are uniquely related for a given initial vibrational level room temperature data can be treated this way. At high temperature, however, several initial vibrational states are present and the fact that $R_e(r)$ is basically a function of r rather than λ must be kept in mind.

The empirical correction factor shown on figure 17 was plotted as a function of r_s and was applied to the $\hat{k}_{v''}(\lambda)$ curves of figure 15

by using the λ, r_s relations defined in the discussion of the "reflection" method. The new $\hat{k}_{v''}(\lambda)$ curves are not shown but the resulting new $\hat{k}_T(\lambda)$ curves for the IBM calculations are shown on figure 19.

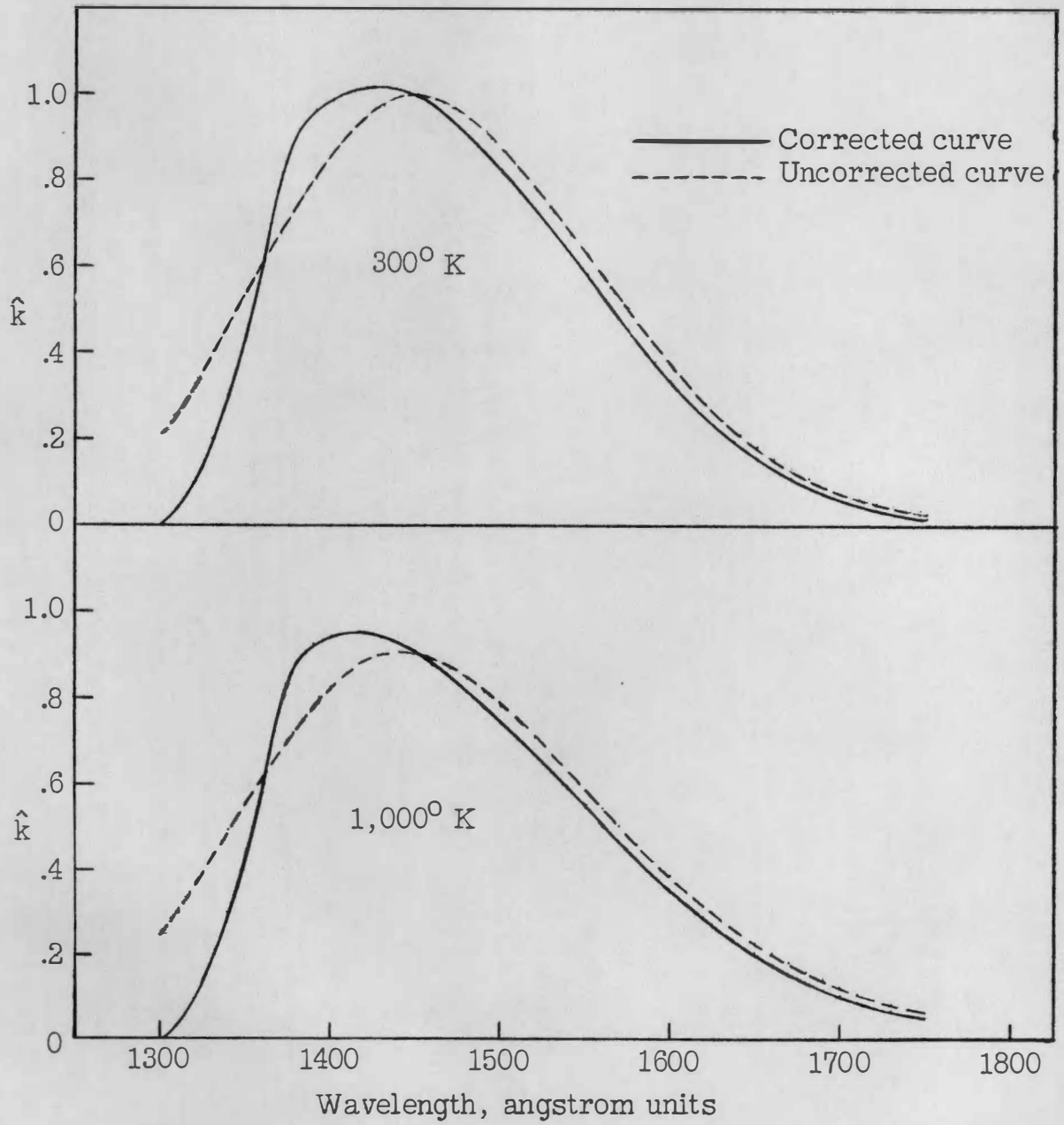

Figure 19(a).- Corrected absorption coefficient of oxygen at temperatures from 300° to 10,000° K.

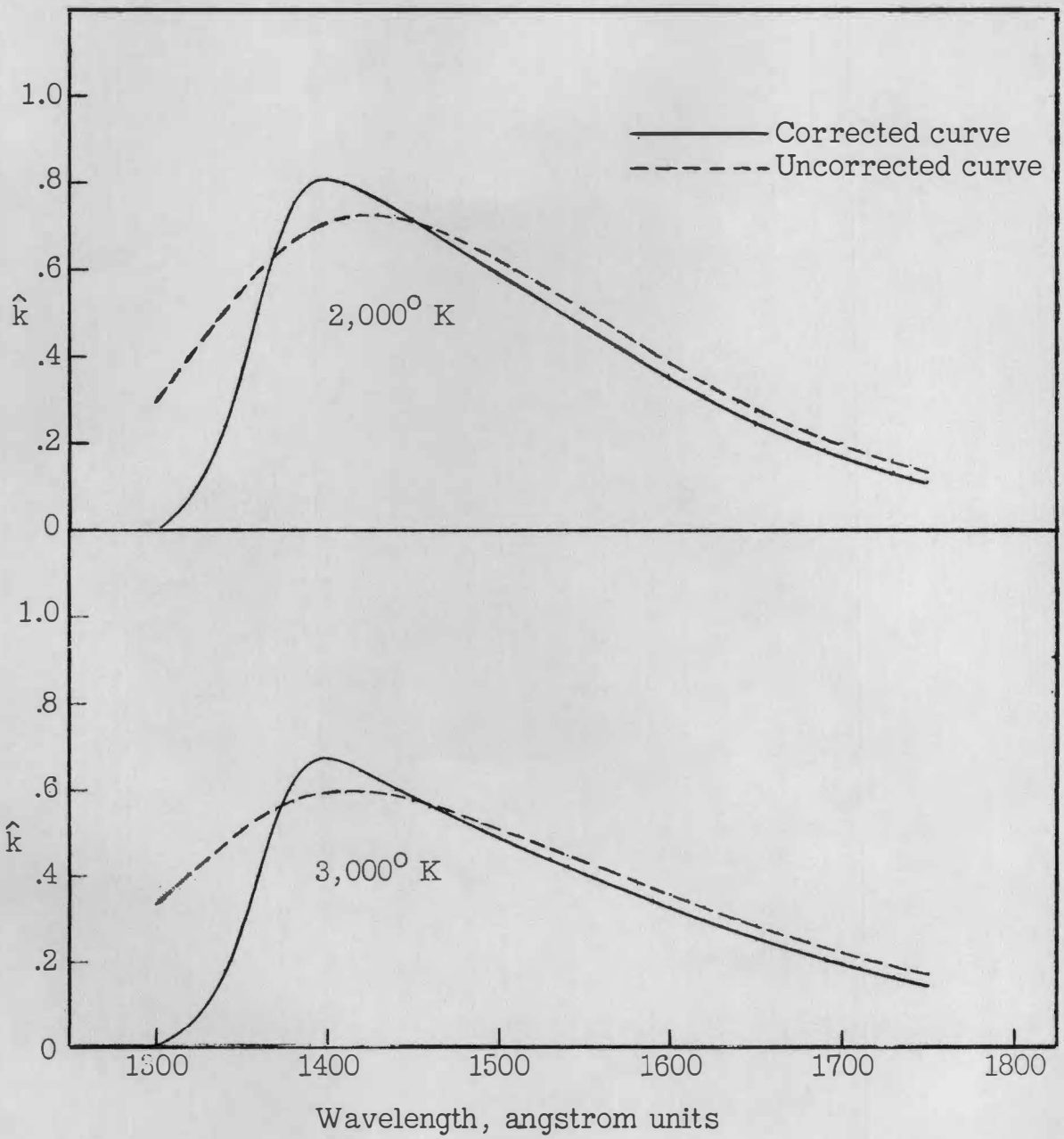
1.0
.8
.6
.4
.2
0
k̂
Corrected curve
Uncorrected curve
2,000° K
1.0
.8
.6
.4
.2
0
k̂
3,000° K
1300
1400
1500
1600
1700
1800
Wavelength, angstrom units

Figure 19(b).

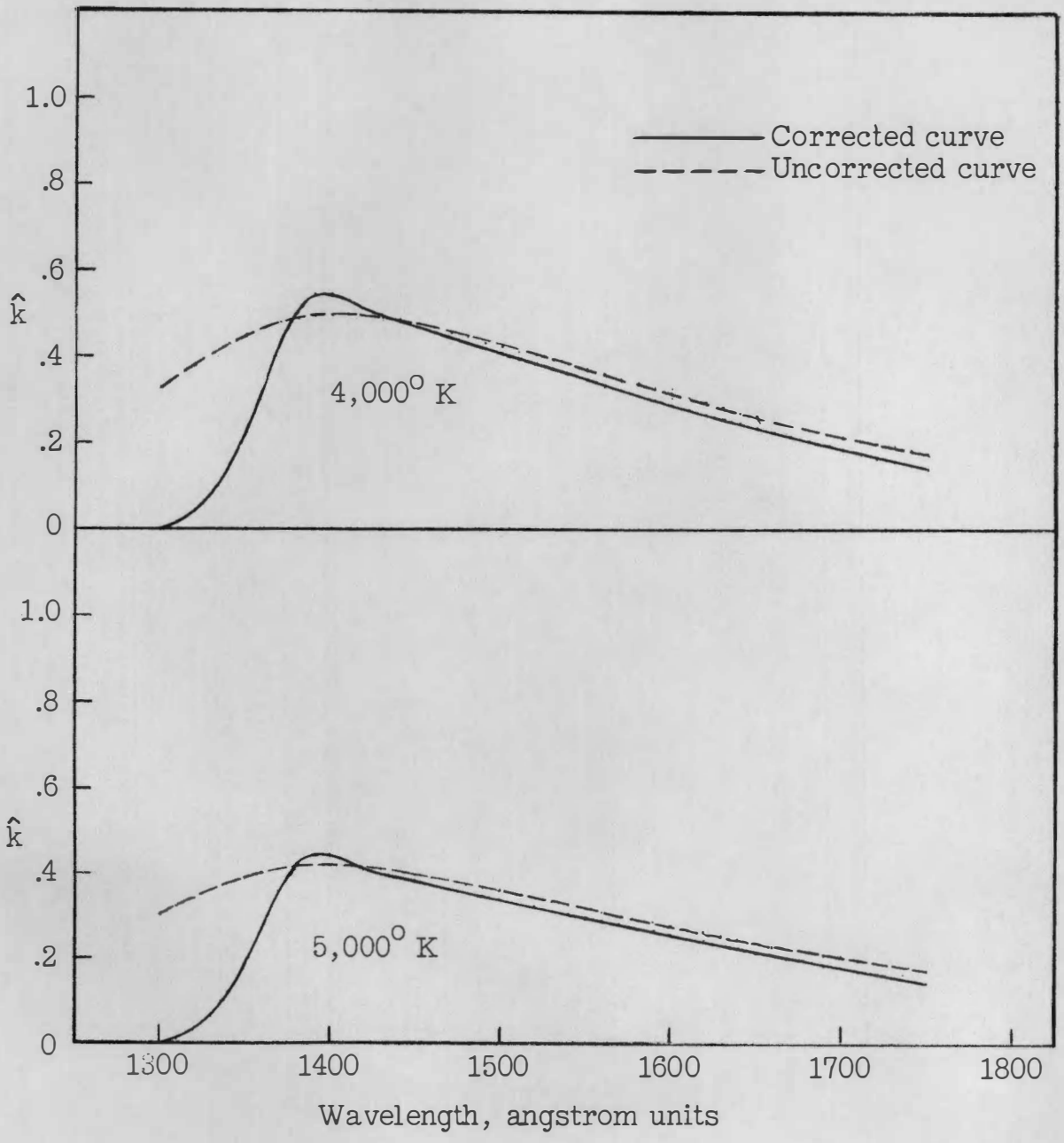
1.0
.8
.6
.4
.2
0
k̂
Corrected curve
Uncorrected curve
4,000° K
1.0
.8
.6
.4
.2
0
k̂
5,000° K
1300
1400
1500
1600
1700
1800
Wavelength, angstrom units

Figure 19(c).

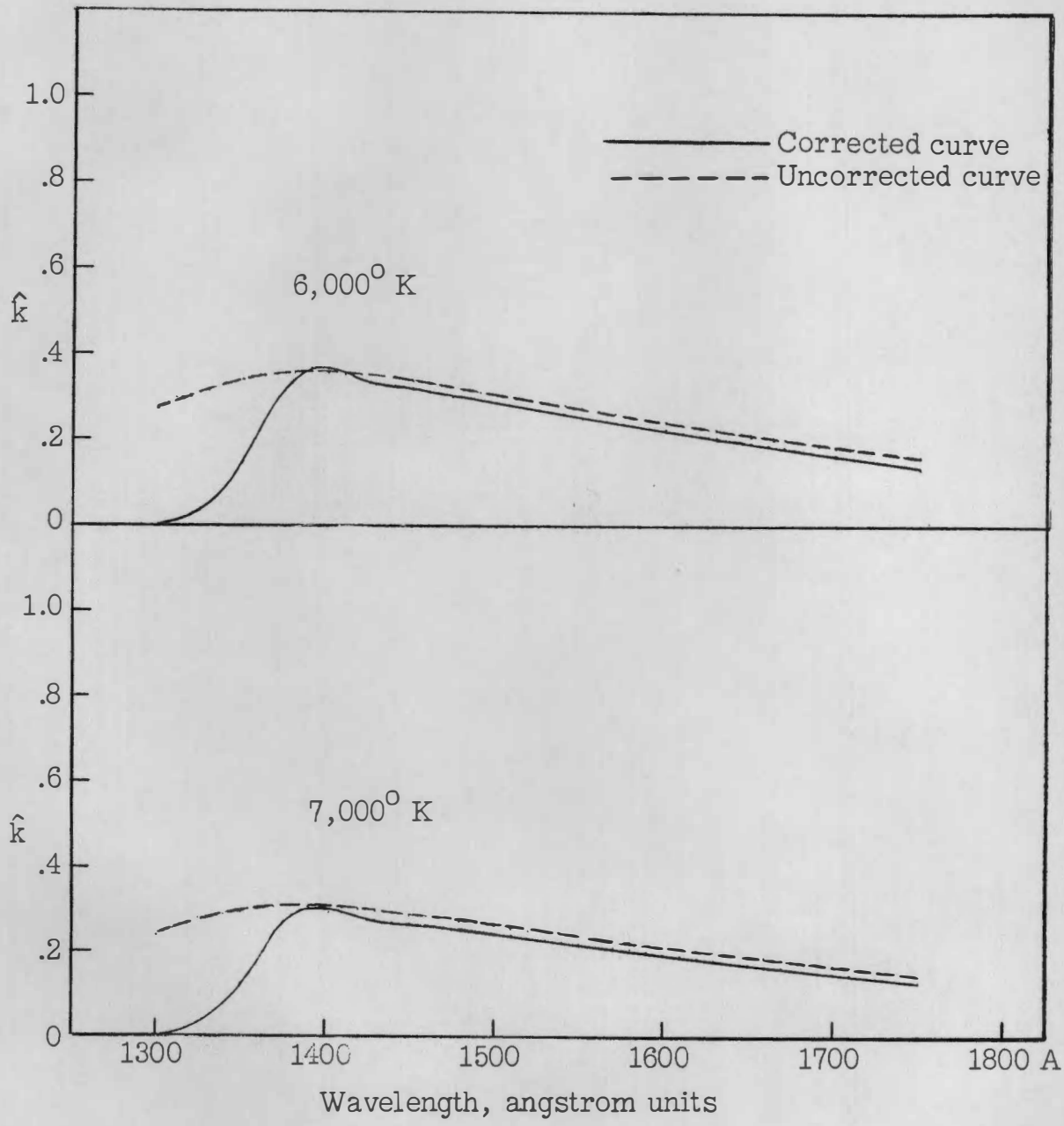
Corrected curve
Uncorrected curve
6,000° K
7,000° K
k̂
1.0
.8
.6
.4
.2
0
1300
1400
1500
1600
1700
1800 A
Wavelength, angstrom units

Figure 19(d).

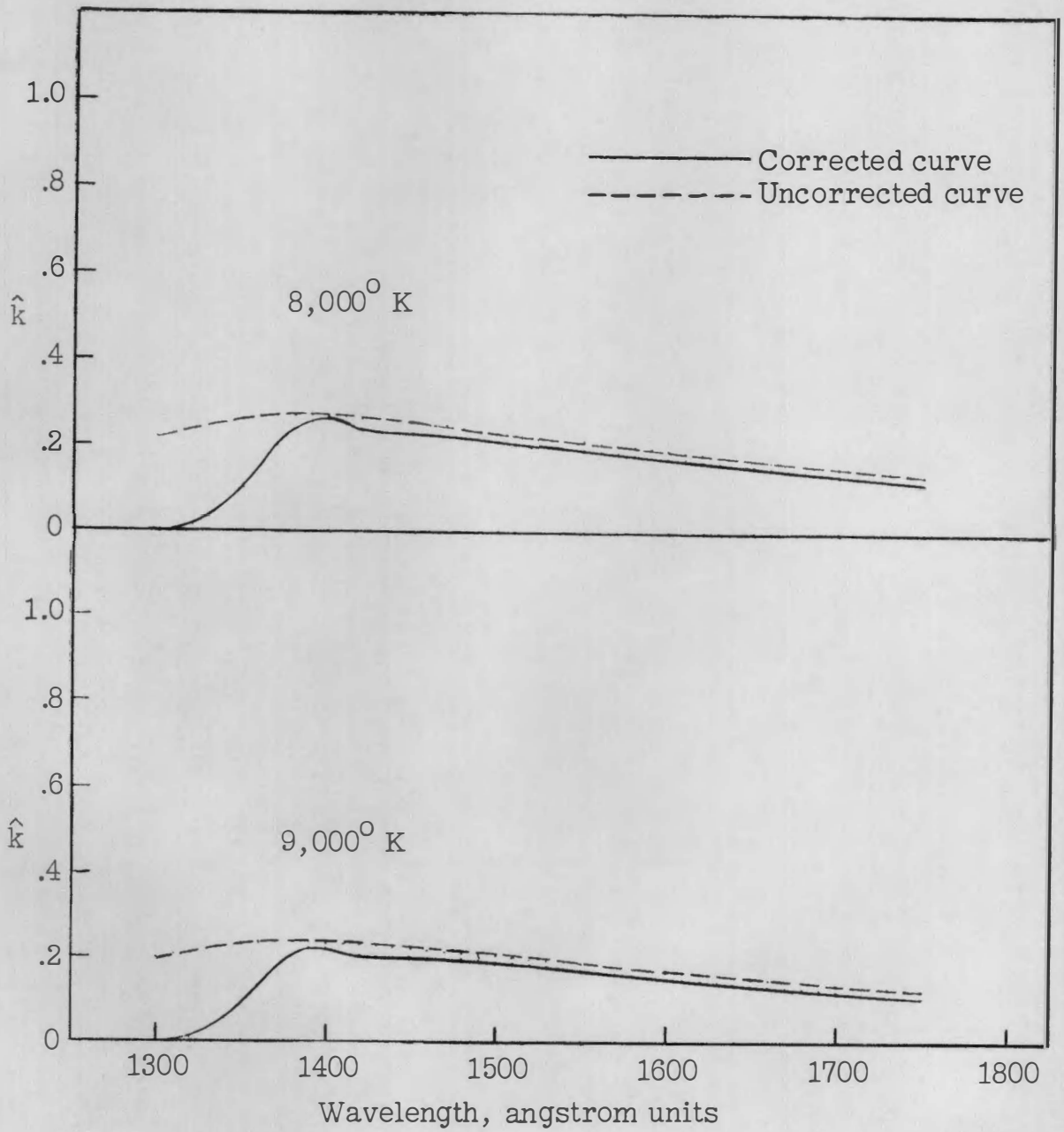
Corrected curve
Uncorrected curve
8,000° K
9,000° K
$\hat{k}$
1.0
.8
.6
.4
.2
0
1300
1400
1500
1600
1700
1800
Wavelength, angstrom units

Figure 19(e).

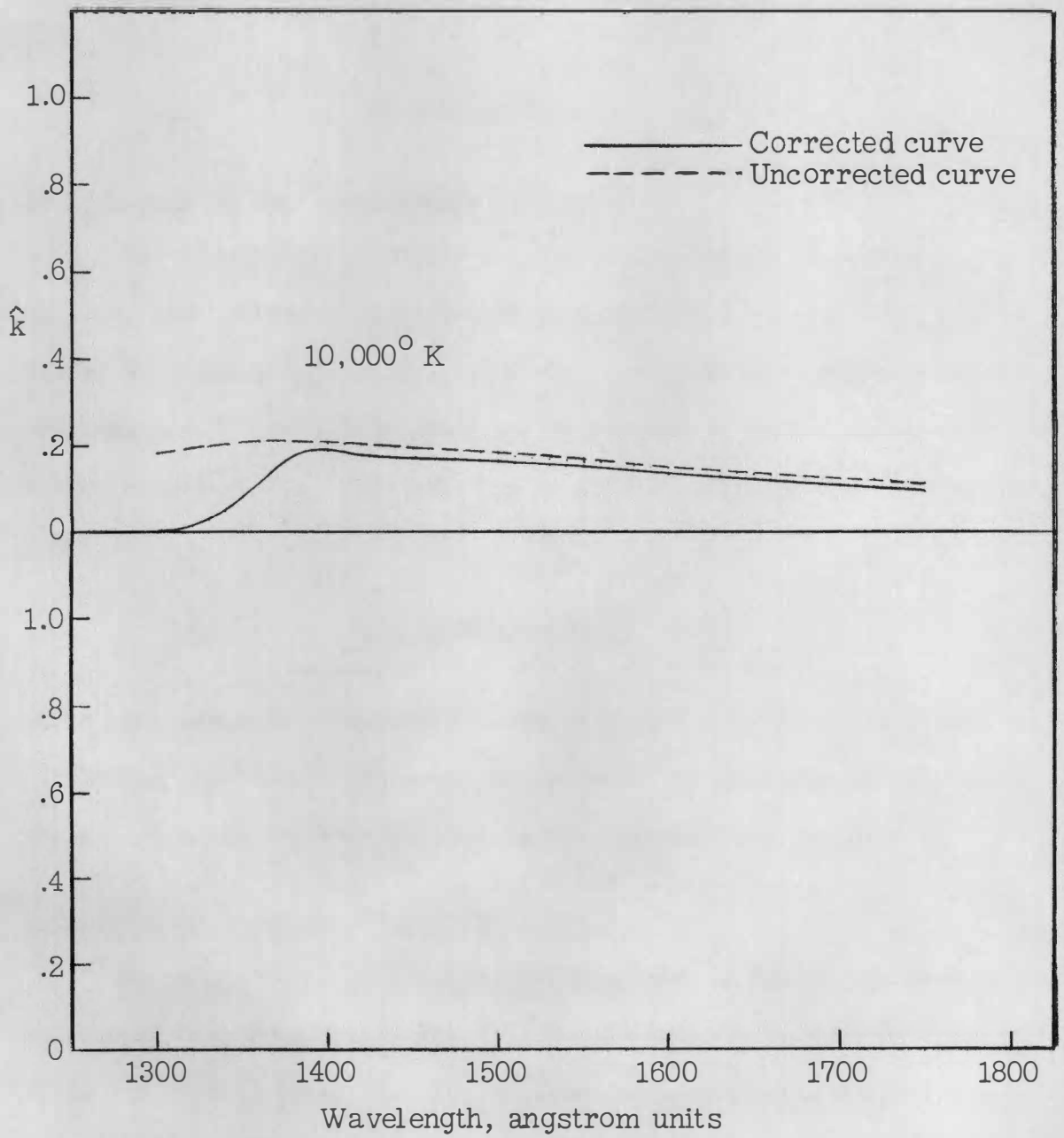
1.0
.8
.6
$\hat{k}$
.4
.2
0
1.0
.8
.6
.4
.2
0
Corrected curve
Uncorrected curve
10,000° K
1300
1400
1500
1600
1700
1800
Wavelength, angstrom units

Figure 19(f).

CHAPTER III

EXPERIMENTAL DETERMINATION OF THE ABSORPTION COEFFICIENT

Background Material

1. Statement of the Experimental Problem

The experimental problem was the determination at several selected wavelengths of the absorption coefficient, k, for molecular oxygen at temperatures up to 10,000° K. Since k is a function of wavelength and temperature these quantities had to be well defined during a measurement. The solution of equation (1) for the absorption coefficient

$$k = -(1/\hat{\rho}l)\ln(I/I_o) \tag{13}$$

shows that the data necessary for the determination of k at given wavelength and temperature were the ratio of the emergent to incident light intensity, the reduced gas density and the path length.

2. Problem of Obtaining Heated Gas Samples

a. Direct approach versus shock heating. A direct approach to the problem of obtaining heated gas samples was made in references 2(a), 3(a), 3(b), and 3(c) by using electric heaters. A more novel, and for some purposes more satisfactory, way of heating the gas samples was used in references 3(d), 3(e), 3(f), and 3(g), where shock waves were used to compress and heat the gases. Since molecular oxygen dissociates into atoms at temperatures above a few thousand degrees Kelvin, the almost

instantaneous heating provided by the shock heating method was necessary for the study of the absorption of oxygen up to 10,000° K. Oxygen persists in the molecular form for a short time behind a shock front because more molecular collisions are required for dissociation of the oxygen molecule than for the excitation of its translational, rotational, and vibrational degrees of freedom[45].

b. Advantages of shock heating. The advantages of using shock waves to heat the gas samples were:

(1) The containing vessel was not appreciably heated. This was very important since the two materials which transmit light well in the vacuum ultraviolet, namely lithium fluoride and calcium fluoride, lose their transparency as temperature increases[46] and break easily under the mechanical stresses imposed by temperature gradients[47]. Even if these obstacles could have been overcome no containing walls would have long withstood temperatures up to 10,000° K, gas purity and high vacuum would have been difficult to maintain at high temperature and temperature gradients between heat sources and surroundings would have caused considerable trouble.

(2) The intensity of the light source did not have to be steady since the transmitted light intensity changed at the shock front in a fraction of a microsecond.

(3) The temperature produced was uniform along the path length.

c. Disadvantages of shock heating. The disadvantages of using shock waves to heat the gas samples were:

(1) The temperature had to be calculated from the thermodynamic properties of the gas and the measured shock velocity.

(2) An intense ultraviolet source was required to maintain a useful signal-to-noise ratio in the fast responding light detector required.

3. Discussion of the Terms "Shock Wave", "Shock Front", and "Shock Tube"

Since terms like "shock wave", "shock front", and "shock tube" will be used frequently in the remainder of the dissertation a slight digression at this point for the purpose of discussing and defining their meaning is in order.

a. Shock waves and shock fronts. Figure 20 illustrates the essential characteristics of a normal shock wave, where "normal" indicates that the disturbance is moving perpendicular to the plane which contains the shock front. The coordinate system for the figure was chosen stationary relative to the shock front in order to illustrate the velocity vectors conveniently. To an observer in the laboratory, however, the shock wave shown in the figure is advancing to the right with the velocity, v_I. It is moving into a stationary gas with pressure p_I, density, ρ_I, and temperature, T_I. For a short distance behind the shock front the pressure, density, velocity, and temperature are functions of the distance from the shock front due to the finite time required to attain thermal equilibrium. After that these quantities take on the steady

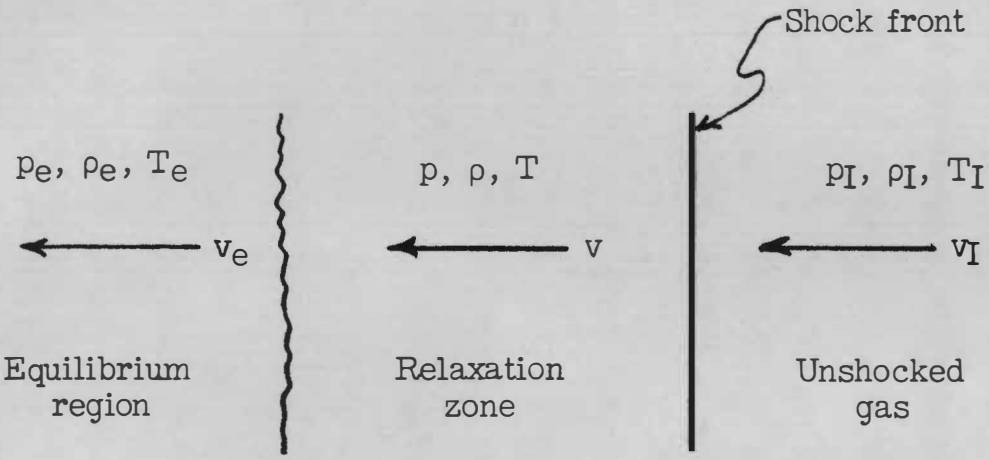

Figure 20.- Flow properties associated with a normal shock wave.

values p_e, ρ_e, v_e, and T_e, where the subscript e indicates the equilibrium state. There is a discontinuous change (or at least an extremely rapid change) in the above quantities at the shock front, whereas everywhere else the changes are smooth and continuous. Except across the shock front the flow is isentropic. Detailed discussions of shock waves can be found in the books by Courant and Friederichs[48] and Ferri[49]. For the purpose of this dissertation it is enough to know that the density and temperature changes across a shock front can be calculated[50] and that the corresponding changes in ultraviolet light absorption can be measured.

b. Shock tubes. Shock waves which compress and heat gases to temperatures well above 10,000° K are easily produced in shock tubes. Since a great deal of detailed information about the construction, operation and theory of shock tubes exists in the literature[51] a complete description of their nature is not necessary here. The following description of the essential parts of a shock tube and of the sequence of events when it is operated has been deliberately kept simple.

The diagrams shown on figure 21 illustrate the basic parts. It is an enclosed space separated into two parts by a thin diaphragm. A pressure difference is established across the diaphragm and then the diaphragm is suddenly removed; that is, the diaphragm breaks. The second diagram on figure 21 shows what happens when the diaphragm breaks. A shock wave travels into the low pressure chamber and a rarefaction wave travels into the high pressure chamber. Figure 22 is a distance-time diagram of the events occurring after a diaphragm break. Note that the rarefaction wave is represented by an expansion fan which as it passes

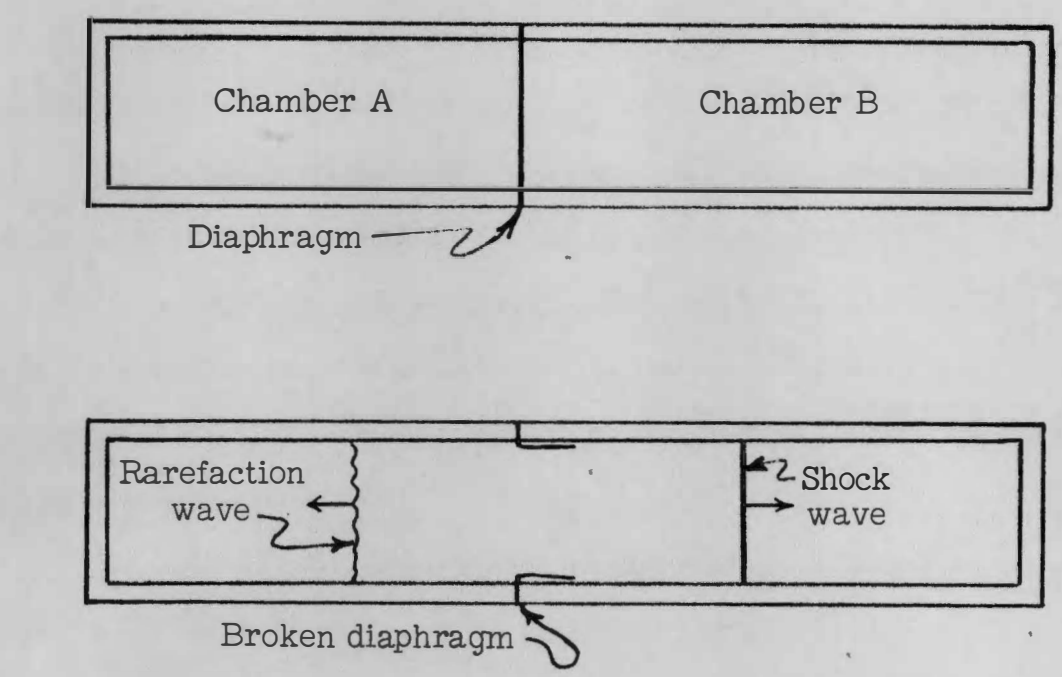

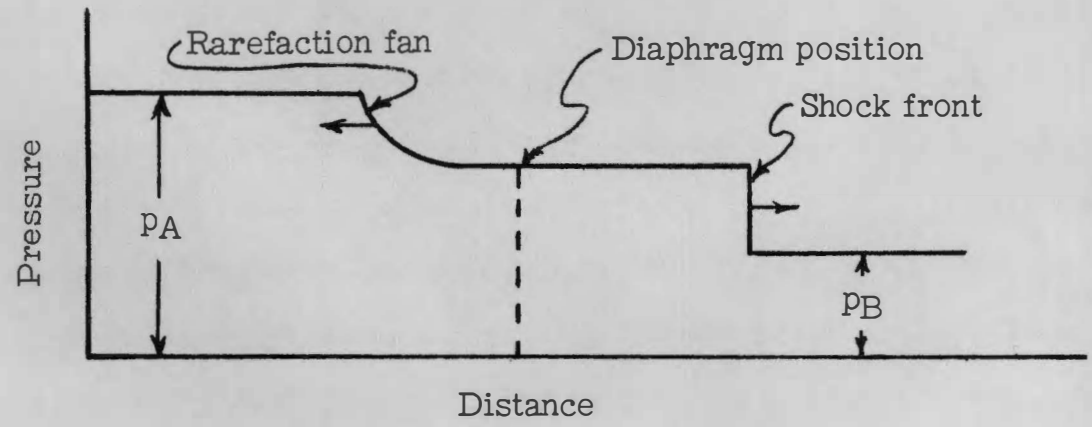

Figure 21.- Diagrams illustrating a simple shock tube.

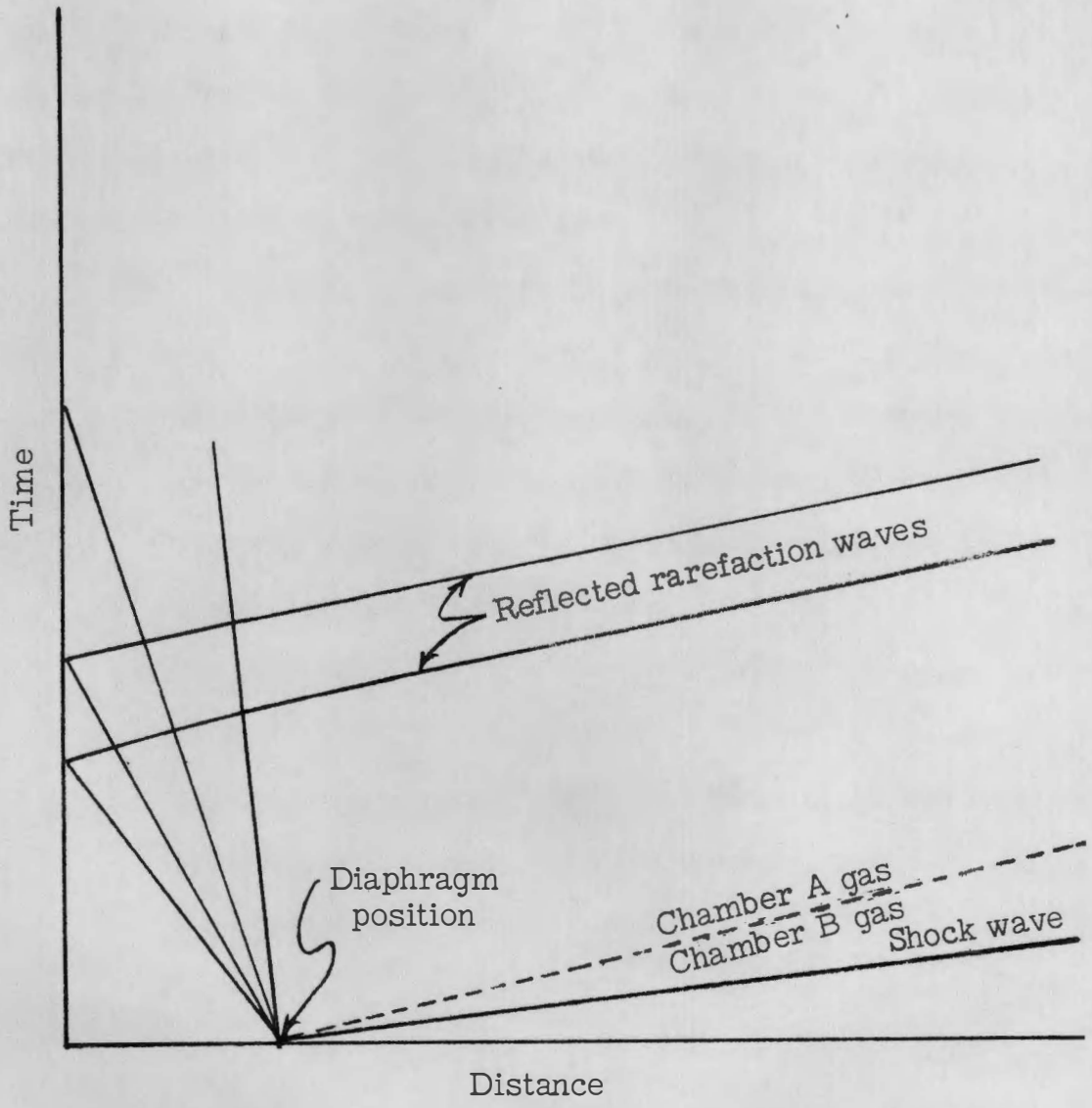

Figure 22.- Distance-time diagram for a simple shock tube.

over the gas in chamber A reduces the high pressure initially present to a value intermediate between the initial pressure in chamber A and the initial pressure in chamber B. At the same time the shock wave is compressing the gas in chamber B to the same intermediate pressure. The last diagram on figure 21 illustrates a typical instantaneous pressure distribution in the shock tube.

The description of simple shock tubes is completed by the following statements:

(1) The shock Mach number, $M_I \equiv v_I/a_I$, is an increasing function of the initial pressure ratio across the diaphragm. The limiting value of M_I for infinite pressure ratio[52] is $\left[(\gamma_B + 1)/(\gamma_A - 1)\right](a_A/a_B)$.

(2) The quantities T/T_I, p/p_I, ρ/ρ_I are all increasing functions of M_I[53].

(3) The following devices[54] have been shown to be effective for producing higher shock Mach numbers than would be obtained from the description given above:

(a) Increasing the ratio of the sound speed in the driver gas to that in the driven gas by using a low molecular weight driver or by heating the driver. Sometimes a hot driver gas is obtained by igniting a combustible mixture, such as hydrogen and oxygen.

(b) Using two or more driver sections in cascade.

(c) Making the driver section larger in cross-sectional area than the driven section.

A recent experimental paper by Duff[55] reported that the flow behind shock waves in small diameter shock tubes operated at low pressure departs markedly from the ideal flow described above. The conditions cited are precisely those present in the shock tube used for the work reported here. Before the paper appeared the following puzzling facts had been noted: The distance between the shock front and the contact surface between driven and driver gases was noticed to be far shorter than predicted by shock tube theory. It was also noticed that this distance, which measures the length of the hot gas region behind the shock front, did not increase as the shock wave progressed down the tube. This also conflicted with the usual shock tube theory. Both these effects were reported by Duff and were attributed along with certain other effects to the formation of a laminar boundary layer behind the shock front. While this disturbance to the otherwise easily calculated thermodynamic properties in the hot flow region complicates the task of those interested in studying relaxation rates behind shock waves, it does not affect the thermodynamic calculation of temperature and density immediately behind the front, and these are the only ones required here.

4. Problems Peculiar to the Vacuum Ultraviolet Spectral Region

Spectral measurements at wavelengths shorter than about 2000 A are considerably more difficult than they would be in the visible spectrum because of the following items:

a. Few materials are transparent to ultraviolet light. There are only a few materials[56] which are transparent in this region. Quartz becomes opaque at about 1500 A, sapphire at about 1425 A, barium fluoride

at about 1350 A, calcium fluoride at about 1225 A, and lithium fluoride at about 1050 A. At wavelengths shorter than 1050 A no windows, prisms or lenses are available. Quartz and sapphire are strong materials and will withstand much thermal and mechanical stress, but calcium fluoride and lithium fluoride are very susceptible to both thermal and mechanical stresses[57].

b. Contamination of optical components is critical. The contamination of the surfaces of mirrors, gratings, lenses and windows by even thin films of oil, water or other substances often results in a great reduction in their efficiency in this spectral range[58].

c. Oxygen in air absorbs ultraviolet light. Since the oxygen present in air absorbs light strongly in this spectral region all light paths must be kept free from oxygen, either by providing an evacuated enclosure or by using nonabsorbing gases in the light paths.

d. Lack of intense light sources. Sources of intense ultraviolet light in the spectral range 1300 A to 1750 A are still in the development stage. In the past the most commonly used sources for studying spectra in this region were as follows:

(1) The positive column discharge in hydrogen[59], which produces a continuum from 1650 A upwards and the many-line molecular hydrogen spectrum below 1650 A.

(2) The continua emitted by the rare gases xenon and krypton under microwave excitation[60]. Xenon emits from 1470 A upwards, with peak emission at 1750 A. Krypton emits from 1236 A upwards, with peak emission at 1500 A.

(3) The Lyman continuum[61] produced by a violent condenser discharge through a narrow-bore tube. This source emits a continuum running from a few hundred angstrom units upwards.

Conventional designs of the first two types mentioned failed to produce adequate intensity of ultraviolet light for the purposes of this research. The Lyman source tried produced intense ultraviolet light, but the material ejected quickly ruined the lithium fluoride window on the shock tube. Additional references[62] are listed in the bibliography which discuss other light sources for the vacuum ultraviolet. All of these were judged to be unsatisfactory for the purposes of this research.

The search for a suitable light source was the greatest obstacle encountered in preparing the experimental equipment. However, suitable sources were finally developed at the Langley Research Center by the author and his co-worker, Mr. Charles J. Schexnayder. Since these sources have not been thoroughly investigated, they probably are not optimum designs. The description of the sources used is given in the section which describes the equipment used in performing the research.

5. Light Detection Problems

a. Fast responding detector needed. A fast responding detector for ultraviolet light was necessary in order to take advantage of the fact that molecular oxygen persists for a short time behind a shock front. Photoelectric detection using a photomultiplier tube was the only solution found.

b. Photomultiplier envelope not transparent to ultraviolet light. Since the glass envelope of a photomultiplier tube does not transmit light in the vacuum ultraviolet, a coating of sodium salicylate was applied to the glass in front of the light sensitive area. Sodium salicylate fluoresces with uniform quantum efficiency[63] over the entire range of wavelengths needed (1300 A to 1750 A). The peak of the emitted light (λ = 4100 A) is close to the sensitivity peak of an S-11 photoelectric surface (λ = 4400 A), which was the type used.

c. Fluorescence decay time of phosphor unknown. No information was available in the literature on the fluorescence decay time of sodium salicylate, but the experience of both Camac and others[64] and the author indicates that it is less than 10^{-7} seconds. The rise time of the signal obtained by coating a 1P21 photomultiplier with some other organic phosphors was measured by Martinson and others[65] and was found to be of the order of 10^{-8} seconds.

Description of Equipment

1. Basic Items

In simplest terms the equipment items needed to measure the absorption coefficient of a sample of gas are a light source, an absorption path of known length, a device to select light of a known wavelength (i.e., a monochromator) and a light detector. The items mentioned will be discussed in the order given. The absorption path is in the shock tube; the description given will include all information pertaining to the shock tube, such as shock velocity measuring equipment and operation

of the shock tube. The description given of the light detector will include information pertaining to the recording as well as the detection of the light signal. Figure 23 illustrates the main items of equipment and how they are related to each other.

2. Detailed Descriptions

a. Light source. As has already been mentioned the ultraviolet light sources used were developed at the Langley Research Center. They are best described as pulsed hydrogen discharge lamps. Figure 24 is a drawing of the first successful lamp built. As indicated on the figure the cathode and most of the glass envelope were taken from a radio transmitter tube (type 872 A). The original intention was to operate it as a hot cathode, continuously operating, hydrogen discharge lamp. While the usual continuum and many-lined molecular spectrum were obtained this way, the intensity was inadequate. When a condenser was discharged through the tube, however, intense ultraviolet light was observed. After a moderate development program the following combination of parts was found to give satisfactory results over at least a portion of the desired spectral range (1550 A to 1750 A):

(1) The lamp as shown on figure 24. The cathode was no longer heated but was merely used as an electrode.

(2) An energy source capable of producing a current pulse of 2000 amperes for 100 microseconds. An artificial transmission line made up of twenty 2 microfarad, 4 kilovolt condensers and ten 5 microhenry, center-tapped coils connected as shown in figure 25 was used for this purpose. The condensers in

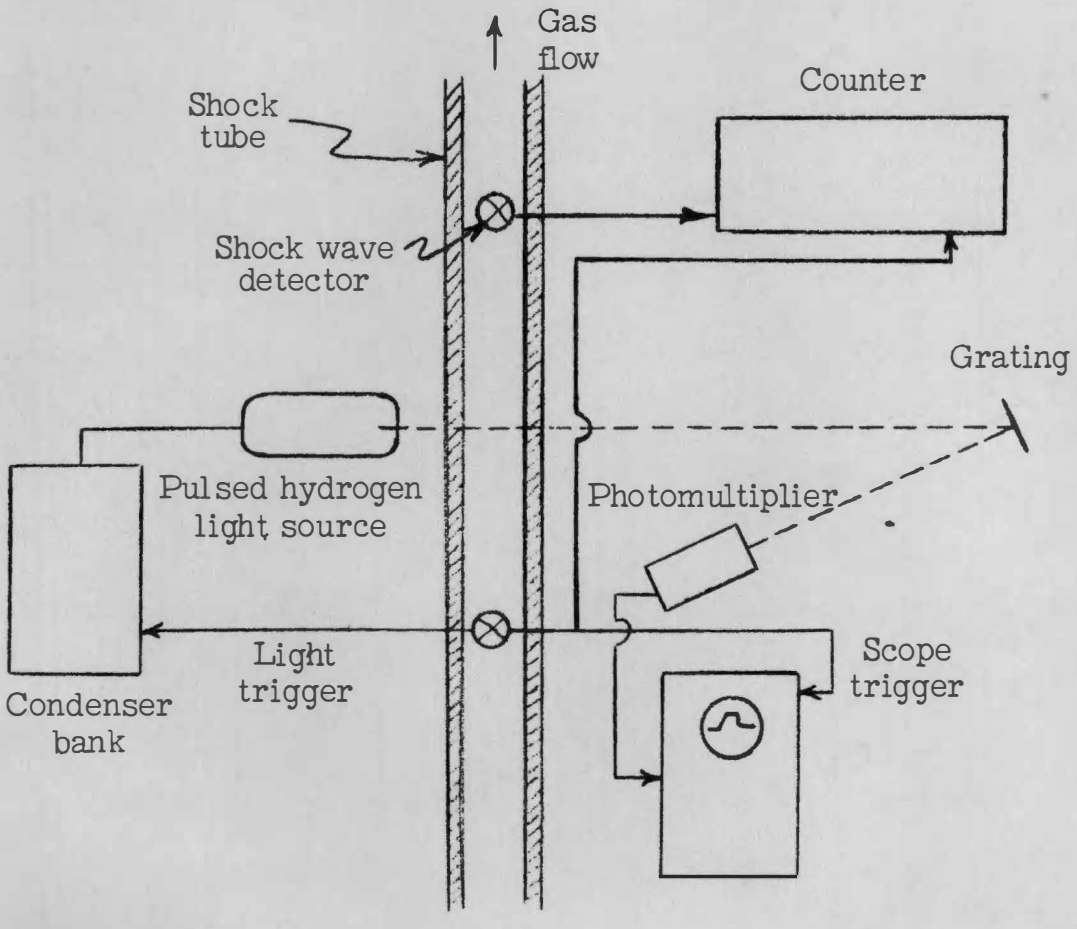

Figure 23.- Schematic diagram of equipment.

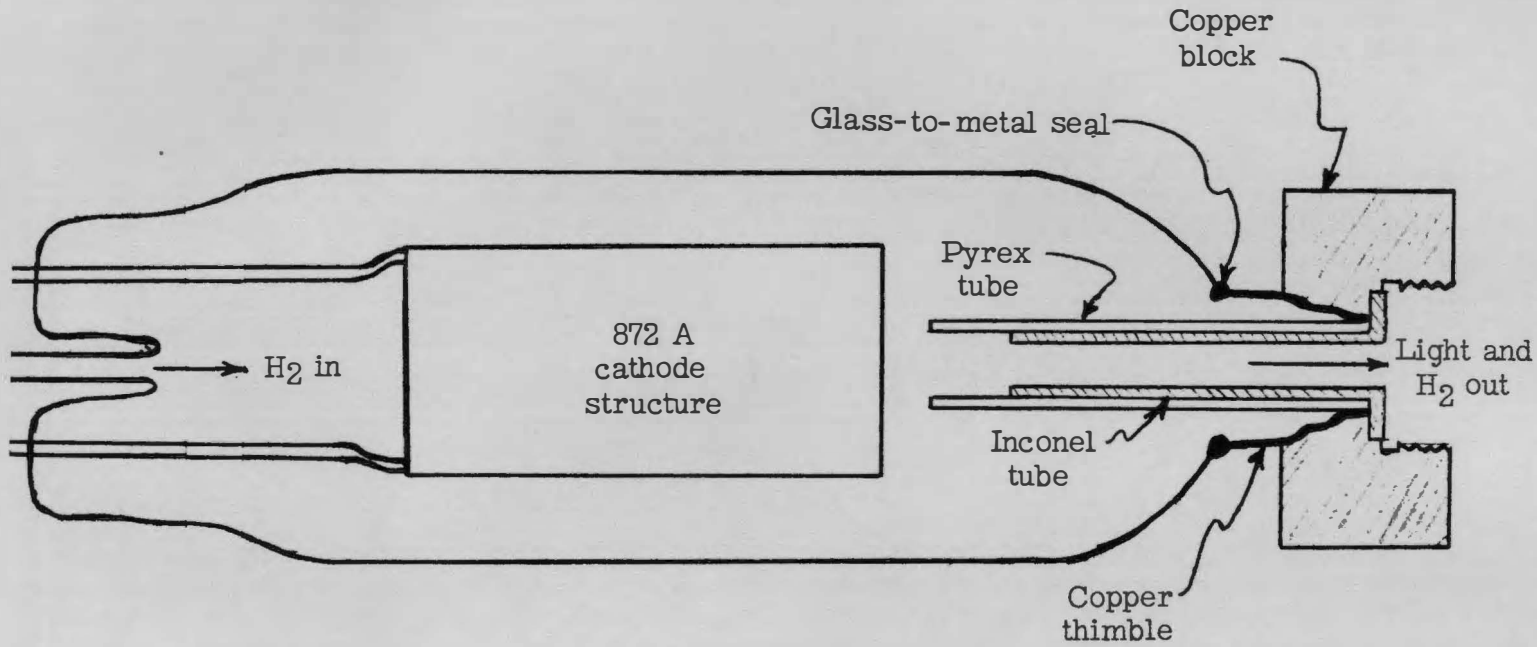

Figure 24.- Light source used for wavelength range 1550 to 1750 A.

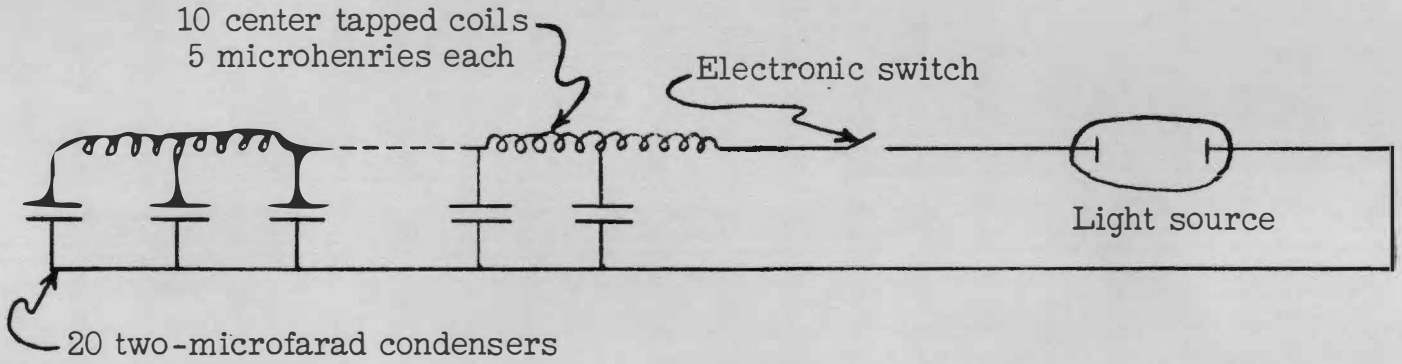

Figure 25.- Artificial transmission line used for energy storage.

the artificial transmission line were charged to about 4 kilovolts. A noninductive series resistance of 0.8 ohms was included to match the load impedance to the output impedance of the line.

(3) An electronic switch. A Kuthe Laboratories hydrogen thyratron tube (type 1754), rated at 1000 amperes peak current and 25 kilovolts peak voltage was used. It applied the voltage to the discharge lamp less than 1 microsecond after being triggered by a pulse on its grid.

(4) A tank of commercial grade hydrogen. This gas was allowed to flow slowly through the discharge tube. The hydrogen pressure was maintained in the discharge region at about 1 millimeter of mercury by continuous pumping.

Figure 26 shows the measured light intensity distribution with wavelength for this light source.

One other light source from the many tried is shown on figure 27. It was used for the shorter wavelengths where the light intensity produced by the first source was low. The intensity distribution with wavelength for this lamp was essentially the same as for the first source but, due to the confinement of the discharge to a smaller space, the intensity was higher.

A pulsed hydrogen discharge lamp was also used by Camac and others. This lamp was described in a private communication to the author as follows: Two hollow cylindrical electrodes were spaced about one-half inch apart and were sealed in a glass tube containing hydrogen at several millimeters pressure. The hydrogen supply was maintained by a small amount

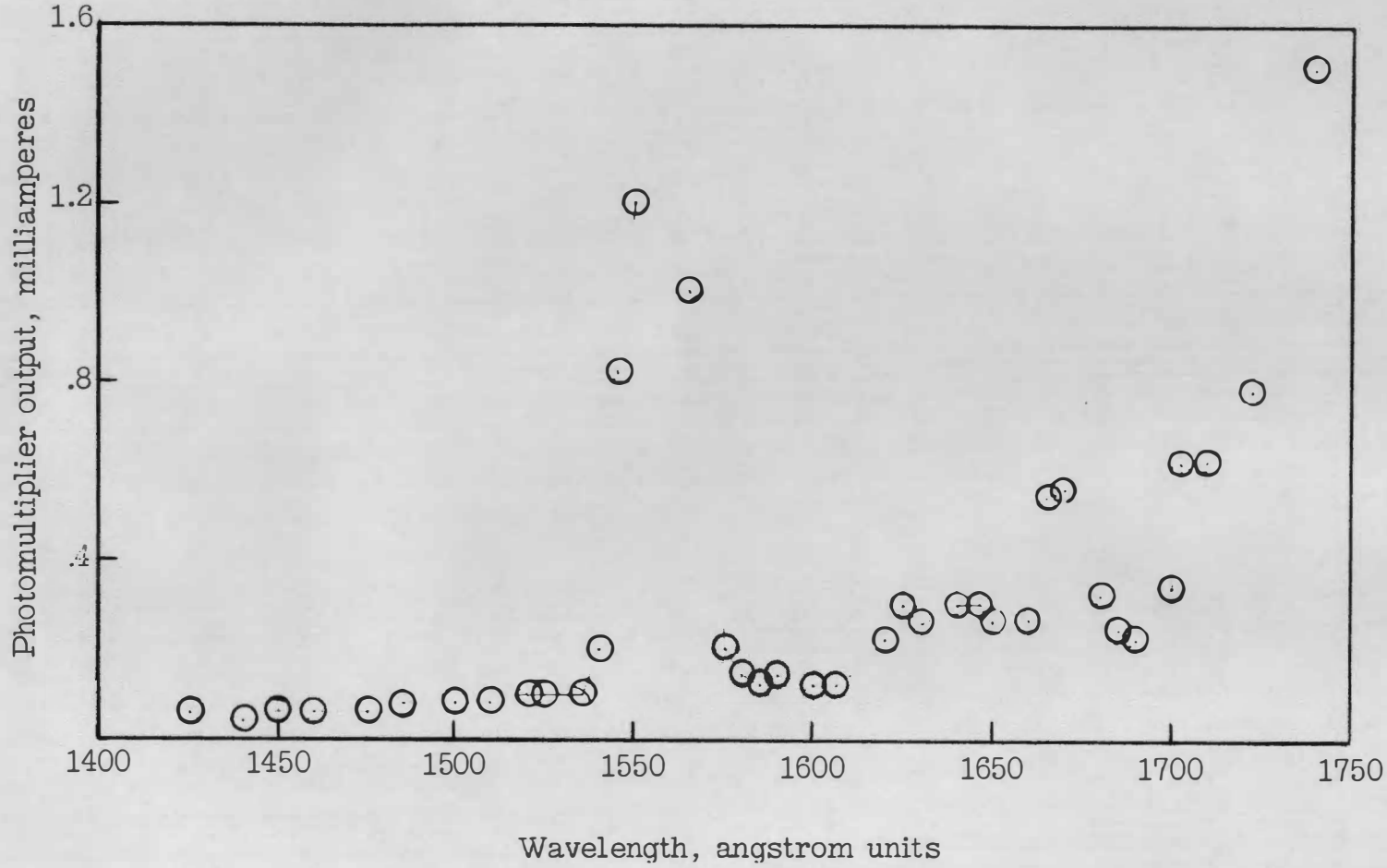

Figure 26.- Measured light intensity distribution for source made from type 872A transmitter tube.

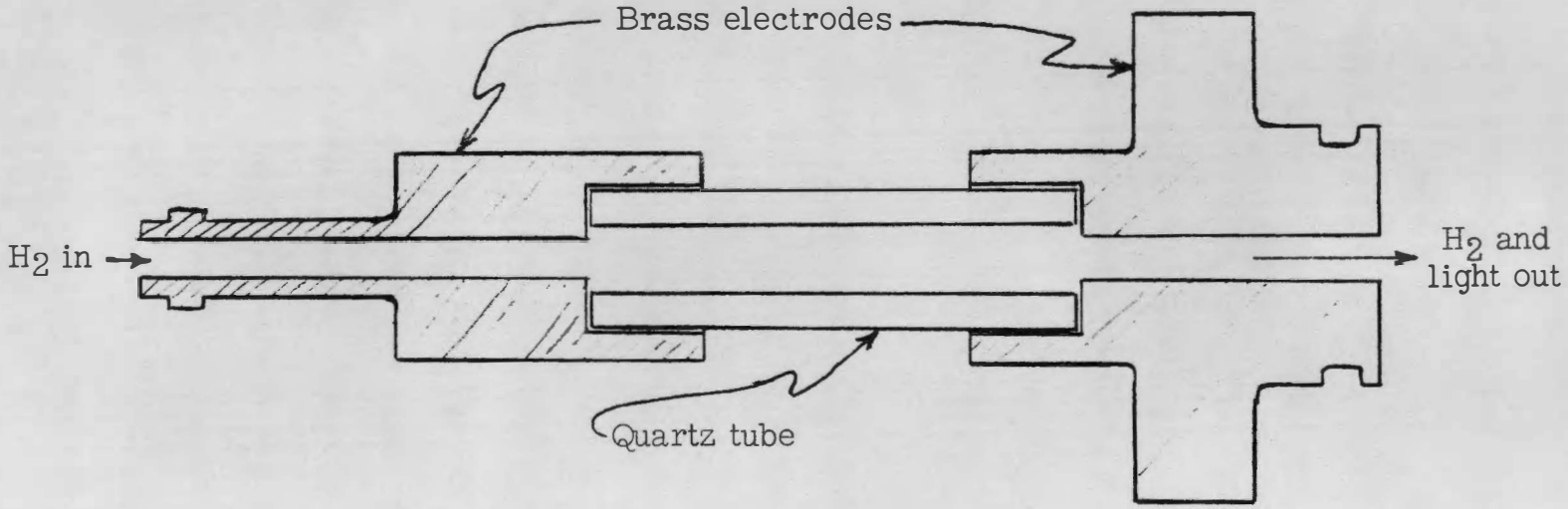

Figure 27.- Light source used for wavelength range 1300 to 1550 A.

of uranium hydride[66], which also served as a getter material for residual impurities. Ultraviolet light from the molecular hydrogen spectrum was produced when the lamp was flashed at about 500 volts and the light left the tube through a calcium fluoride window.

Another flash type ultraviolet source similar to those developed at the Langley Center was reported by Golden and Myerson[67]. Light was produced in their lamp by discharging 120 joules through xenon, argon or krypton contained in a 4 millimeter quartz capillary 15 centimeters long. Continuous emission was reported from 6800 A to 1500 A. The photomultiplier output was 1 volt at 1700 A using a circuit whose response time was less than 1 microsecond. This is about the same magnitude of signal obtained in the present work.

b. Absorption path and description of the shock tube. The absorption path was 1 inch long. This dimension was determined by the inside diameter of the stainless steel tube used for the low pressure section of the shock tube. One-eighth inch diameter lithium fluoride windows approximately 0.5 millimeter thick were set flush with the walls of the tube to permit the light to pass through perpendicular to the direction of motion of the shock wave. Both windows were masked to give apertures 1 millimeter wide by 3 millimeters high. The windows were cemented to the ends of removable plugs so that they could be frequently replaced. They were never polished or cleaned in any way. Replacement windows were always freshly cleaved from a one-eighth inch diameter core of lithium fluoride. After they were cemented in place the edges were smoothed flush with the metal and they were ready to be used.

The shock tube has been described by Schexnayder[68]. It has a double driver section and a sixteen to one area contraction just before the second diaphragm. The middle chamber was filled with helium to about 1 atmosphere pressure and the high pressure chamber was filled with helium or hydrogen to about 100 atmospheres. The high pressure diaphragms were one-sixteenth inch steel plates and two saw cuts about eleven-thousandths of an inch deep were cut on each in the shape of an X to promote easy tearing of the metal and so that the remaining flaps would flatten against the walls out of the way of the flowing gas. Both Mylar film and scribed brass shim stock were used for the second diaphragms. Sometimes the second diaphragm was omitted in order to work in a lower range of shock strengths. In this case the middle chamber gas was the same as the gas under study.

Operation of the shock tube was initiated by building up the pressure in the high pressure chamber until the steel diaphragm ruptured. The shock wave produced in the middle chamber broke the second diaphragm and reflected from the area contraction -- leaving a region of hot, compressed and essentially motionless gas to act as the driver gas for the remainder of the shock tube.

The pressure in the one-inch diameter portion of the shock tube was always determined by the partial pressure of oxygen necessary to give a convenient amount of ultraviolet light absorption. At 1550 A in oxygen this pressure was about 0.3 millimeter of mercury and at the same wavelength in a 10 per cent oxygen in argon mixture was about 3 millimeters. The low pressure section was always pumped to 20 microns of mercury before

filling and was raised to the desired initial pressure by admitting the gas mixture through a leak valve while continuing the pumping. Thus the runs were taken in a slowly flowing gas. The effects of residual vapor pressures and small air leaks were minimized by this procedure. The leak rate of the shock tube when closed off from the pump was 1 or 2 microns per minute.

The data necessary for the determination of the state of the test gas were:

(1) The initial gas temperature. This was taken to be the same as the temperature of the shock tube wall and was measured to $\pm 1^{\circ}$ K with a mercury-in-glass thermometer.

(2) The initial gas pressure. This was measured to ± 0.02 millimeter by two gages, an Alphatron vacuum gage and a 0-20 mm Hg dial gage. Both gages were calibrated against a McLeod gage and always agreed well with each other.

(3) The composition of the gas. Tank oxygen which was guaranteed 99.6 per cent pure was used for the runs in pure oxygen. The percentage of oxygen in the oxygen-argon mixture was measured by the Langley Research Center chemistry section to be 10.07 per cent ± 0.10 per cent. A tank of dry air was used for the runs in air. All gases were passed through an activated alumina filter at tank pressure before entering the shock tube.

(4) The velocity of the shock wave. This was measured by recording the time interval between signals received from ionization probes[69] located 5 inches in front of and 5 inches behind the absorption windows. These probes sensed the small amount of

ionization associated with the shock fronts. The probe signals were applied to the grids of type 2D21 thyratron tubes as shown in the circuit diagram on figure 28. The pulses produced by the thyratrons were fed into a Berkeley counter which recorded the time interval between the pulses to ±1 microsecond. The pulse from the thyratron also triggered the light flash and the horizontal sweep of the Tektronix Model 545 oscilloscope used to display the photomultiplier signal. The ionization probes proved to be unreliable for detecting shock waves which produced temperatures below about 4,000° K. An attempt was made to get data at lower temperatures by using the ionization probes as glow discharge probes in the manner described by Lundquist[70]. This effort was foiled by premature triggering of the thyratron tube associated with the second probe. The trouble was caused by interference produced by the heavy current discharge through the light source. Since lagging adjustment of the vibrational degree of freedom of oxygen would invalidate most, if not all, of the runs below 4,000° K the effort was abandoned.

c. Monochromator. A grating monochromator was used to select a narrow band of wavelengths centered on the wavelength at which the absorption coefficient was to be measured. The monochromator was designed and constructed at the Langley Research Center. It was similar to the instrument described by Parkinson and Williams[71] and like theirs varied

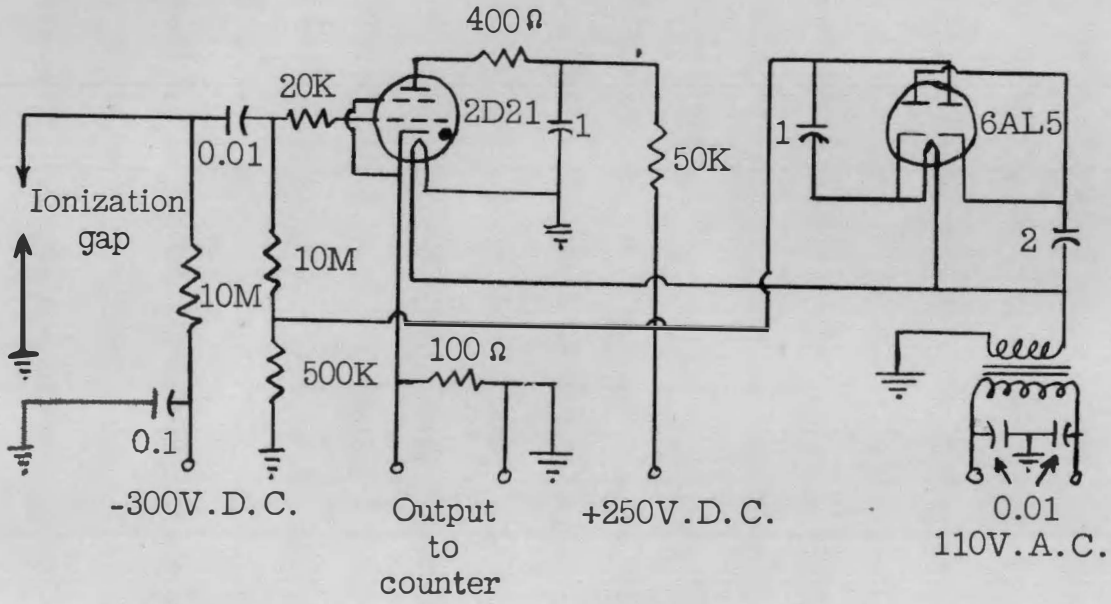

Figure 28.- Single pulse generator triggered by ion probe.

the output wavelength by rotating the grating rather than sliding it along the Rowland circle. The diagram and equation shown on figure 29 give the essential design information.

The 2-inch diameter aluminum-on-glass grating had a radius of curvature of 39.888 ±0.008 centimeters. It was ruled at 15,000 lines per inch over an area of one by three-fourth inch. It was blazed to concentrate most of the light in the first order diffraction pattern. The dispersion was 0.0232 millimeter per angstrom over the wavelength range used.

Both the entrance slit and the exit slit were located 2 inches off the center line and at fixed but unequal distances from the axis of rotation of the grating. The design wavelength was 1590 A. The corresponding values of x_1 and x_2 were 15.524 inches and 15.331 inches, respectively. At 1590 A the image of the entrance slit was focused on the exit slit. When the grating was rotated from the design position the values of x_1 and x_2 mentioned were no longer correct and the image falling on the exit slit was out of focus. Since the defocusing was small over the wavelength range of interest and photomultiplier detection does not require a sharp image the only important effect was a shift of the central wavelength of the transmitted band by about one angstrom unit at the limits of the desired wavelength range.

The widths of the entrance and exit slits were both set at ten-thousandths of an inch. For equal slit widths the distribution of transmitted wavelengths out of a continuum of uniform intensity is triangular in shape. The apex of the triangle represents maximum transmitted intensity and occurs at the central wavelength. For the slit settings

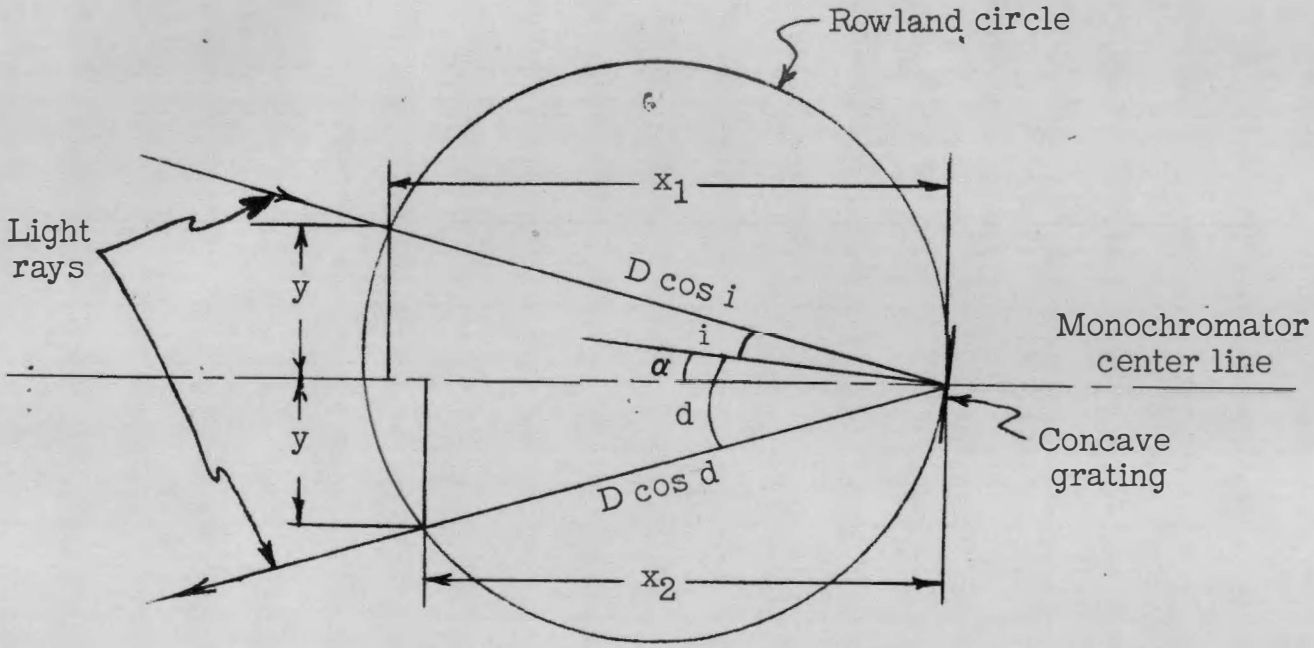

x_1, y - entrance slit position
x_2, y - exit slit position

$$n\lambda = s(\sin d - \sin i)$$

Figure 29.- Design diagram for ultraviolet monochromator.

mentioned the intensity dropped to one half the maximum value at the central wavelength ±5.5 A and to zero at the central wavelength ±11 A.

Selection of a desired wavelength was accomplished by means of a calibrated micrometer screw which moved an arm attached to the grating. The screw was calibrated in terms of wavelength using lines from the spectrum of mercury down to 1849 A and the resonance line of xenon at 1470 A. The calibration points showed excellent agreement with a straight line drawn through the points.

To avoid absorption of the ultraviolet light by the oxygen present in air the monochromator was built in a vacuum-tight enclosure which was maintained at a pressure of 1 micron or less. To illustrate the importance of maintaining such a low pressure consider the calculated absorption at 1450 A in the approximately 45 inches of light path between the shock tube and the photomultiplier. At 1 micron 3 per cent of the light was absorbed, at 10 microns 12 per cent and at 100 microns 72 per cent.

d. Light detector. A Dumont 6292 photomultiplier sensitized for ultraviolet by a coating of sodium salicylate was mounted about an inch from the exit slit of the monochromator. The glass envelope was in vacuum; the base was in air. The vacuum seal was made by means of a neoprene "O" ring at the juncture of the glass envelope and the base. The rise time of the photomultiplier output circuit was about 2×10^{-7} seconds and the rise time of the Tektronix Model 545 oscilloscope used to record the light signal was 10^{-8} seconds. The transit time of the shock wave across the light path was 2×10^{-7} seconds to 5×10^{-7} seconds, depending on the shock velocity. The linearity of the output current as a function of

illumination under the operating conditions used was examined using data published by the manufacturer[72]. The voltage was usually set at 150 volts per stage except for the cathode-first dynode potential which was made twice as high as the interdynode potentials. The signal current was of the order of 2 milliamperes and the voltage divider current was about 6 milliamperes. The last two dynode stages were bypassed to avoid degeneration due to the signal current flowing in the divider. Linearity was better than 1 per cent.

The uniform quantum efficiency of sodium salicylate as a function of wavelength and the belief that its fluorescence lifetime is short enough to permit its use as described above have already been mentioned.

The light intensity as a function of time was displayed on the screen of the oscilloscope and was photographed by a Polaroid Land camera. Figure 30 shows four typical records. The traces marked "Vacuum" show the intensity obtained with vacuum in the shock tube; the traces marked "Initial pressure" show the intensity obtained with the test gas at pressure p_I. The traces marked "Record" correspond to those marked "Initial pressure" but show the shock wave passing through the absorption path. The traces marked "Visible light" were taken with the monochromator filled with air so that a record could be obtained of the amount of visible light getting through the monochromator.

The hot gases behind strong shock waves are known to emit visible light[73], and hot oxygen probably emits some ultraviolet light also. However, the measured absorption coefficients show no trends which could be attributed to emission. Also, two runs for which the ultraviolet light failed to provide the absorption background showed no trace of emitted light at the shock front.

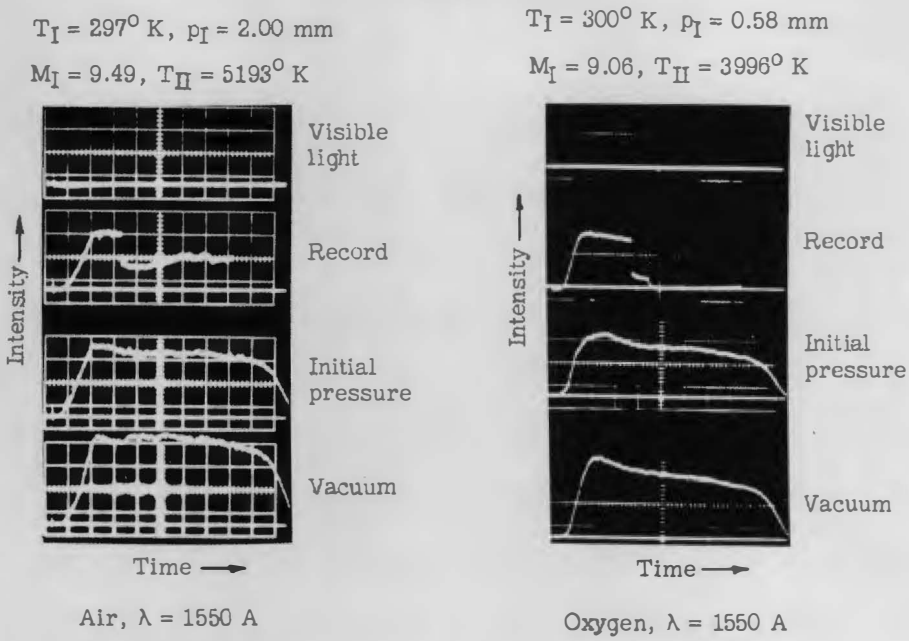

The time base on all the records is 10 microseconds per centimeter.

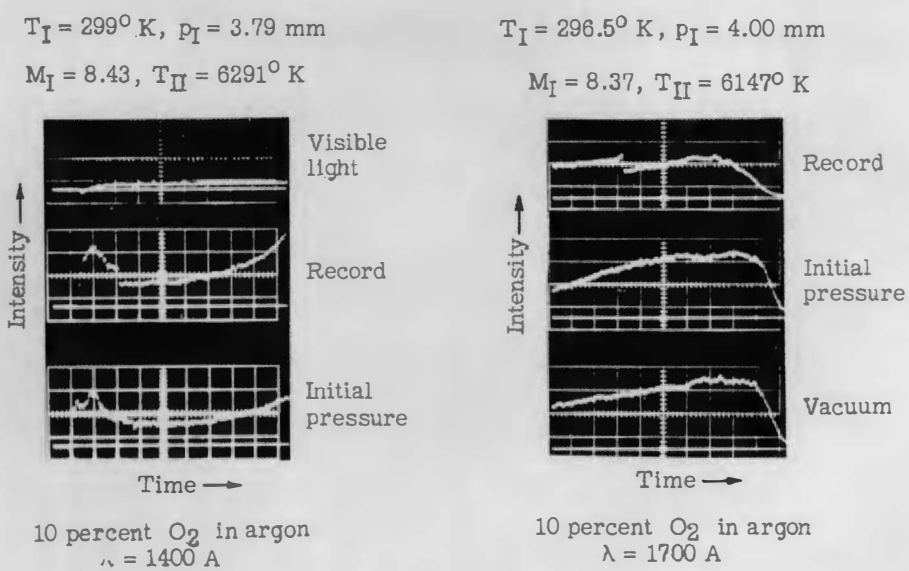

Figure 30.- Typical shock tube records.

Data Analysis

1. Data Needed

Equation (13) showed that the data needed to determine the absorption coefficient at given temperature and wavelength were the ratio of emergent to incident light intensity immediately behind the shock front and the corresponding product of reduced gas density and absorption path length.

2. Description of Analysis Methods

a. Development of a working equation. The diagram on figure 31 illustrates the measurements made on the oscilloscope records. The intensity, I_o, was the intensity which would have been observed if there had been no absorption of ultraviolet light in the shock tube. Because of the lack of reproducibility in the intensity of the source from one flash to another, the values of I_o obtained from the traces corresponding to vacuum in the shock tube were inaccurate. The following equations were set up so that I_o would not be required:

$$\text{Initial transmission ratio} = I_I/I_o = \exp(-k_I\hat{\rho}_I l)$$

$$\text{Transmission ratio after shock compression} = I_{II}/I_o = \exp(-k_{II}\hat{\rho}_{II} l)$$

$$= \exp(-k_{II}\sigma\hat{\rho}_I l)$$

$$I_{II}/I_o = (I_{II}/I_I) \cdot (I_I/I_o) = (I_{II}/I_I)\exp(-k_I\hat{\rho}_I l)$$

$$k_{II} = -(1/\sigma\hat{\rho}_I l)\left[\ln(I_{II}/I_I) - k_I\hat{\rho}_I l\right]$$

$$\hat{k}_{II} = (1/\sigma)\left[\hat{k}_I - \ln(I_{II}/I_I)/k_o^m\hat{\rho}_I l\right] \qquad (14)$$

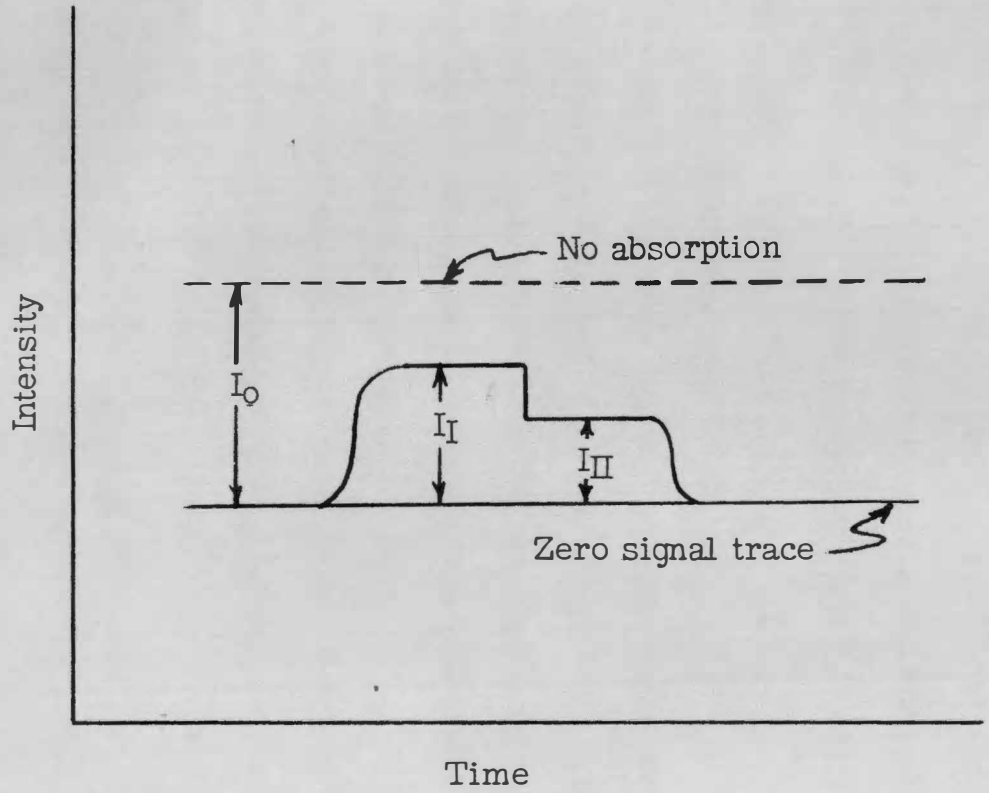

Figure 31.- Diagram illustrating measurements made on records.

The quantities required for the evaluation of the high temperature absorption coefficient, $\hat{k}_{II}$, from equation (14) were:

(1) the shock density,ratio, $\sigma \equiv \rho_{II}/\rho_I$

(2) the room temperature absorption coefficient, $\hat{k}_I$

(3) the maximum value of $k_T(\lambda)$ at 0° K, k_o^m

(4) the light intensity ratio across the shock, I_{II}/I_I

(5) the ratio of the initial oxygen concentration to the concentration of oxygen in the gas at 273° K and 1 atmosphere pressure, $\hat{\rho}_I$

(6) the absorption path length, l

Values for $\hat{k}_I$ were obtained from the corrected IBM calculations shown on figure 19. I_I and I_{II} were taken to be proportional to the distance of the signal trace from the zero signal trace on photographic enlargements of the original records. These distances were of the order of 10 to 50 millimeters ±0.5 millimeter.

Except for the absorption path length, l = 2.54 centimeters ±0.1 centimeter, the remaining items to be evaluated were σ, T_{II}, and $\hat{\rho}_I$. The method for finding these is explained in the next section.

b. Calculation of the gas temperature and the oxygen concentration. The density and temperature behind a normal shock wave can be calculated from a knowledge of the shock velocity and the thermodynamic properties of the gas. Three conservation equations and the equation of state are the starting point:

(1) Conservation of energy

$$\eta_I(p_I/\rho_I) + \frac{1}{2} v_I^2 = \eta_{II}(p_{II}/\rho_{II}) + \frac{1}{2} v_{II}^2 \qquad (15)$$

(2) Conservation of momentum

$$p_I + \rho_I v_I^2 = p_{II} + \rho_{II} v_{II}^2 \tag{16}$$

(3) Conservation of mass

$$\rho_I v_I = \rho_{II} v_{II} \tag{17}$$

(4) Equation of state

$$p = \rho RT \tag{18}$$

From the above equations the following expressions were found:

$$\bar{M}_{II} = \left[1/(2\eta_{II} - 1)\right] \cdot \left[(1 + \gamma_I M_I^2)\eta_{II}/\gamma_I M_I\right] - \left[1/(2\eta_{II} - 1)\right] \cdot \left\{\left[(1 + \gamma_I M_I^2)\eta_{II}/\gamma_I M_I\right]^2 - (2\eta_{II} - 1)\left[M_I^2 + 2/(\gamma_I - 1)\right]\right\}^{1/2} \tag{19}$$

$$\sigma = \rho_{II}/\rho_I = M_I/M_{II} \tag{20}$$

$$T_{II}/T_I = \gamma_I \bar{M}_{II} \left\{\left[(1 + \gamma_I M_I^2)/\gamma_I M_I\right] - \bar{M}_{II}\right\} \tag{21}$$

Equation (21) was solved for $\bar{M}_{II}$ as follows

$$\bar{M}_{II} = (1 + \gamma_I M_I^2)/2\gamma_I M_I - \left\{\left[(1 + \gamma_I M_I^2)/2\gamma_I M_I\right]^2 - T_{II}/\gamma_I T_I\right\}^{1/2} \tag{22}$$

A graphical solution was obtained by plotting equations (19) and (22) against T_{II} at constant M_I. Corresponding values of $\bar{M}_{II}$ and T_{II} were then read off the plots at the intersections of curves of equal M_I. Cross plots of σ and T_{II} as functions of M_I were made from the results and are shown on figure 32.

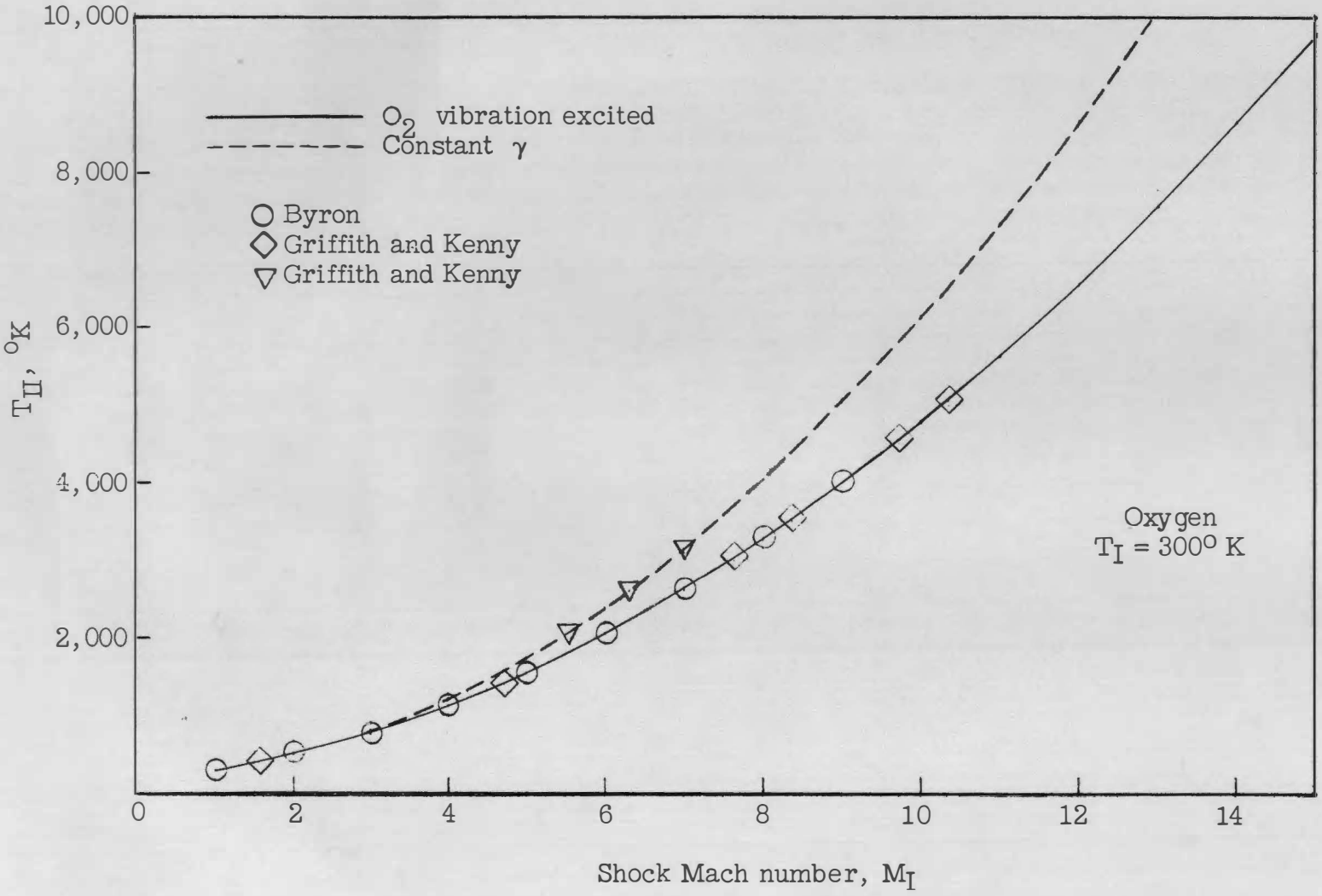

Figure 32(a).- Calculated values of temperature and density behind shock fronts.

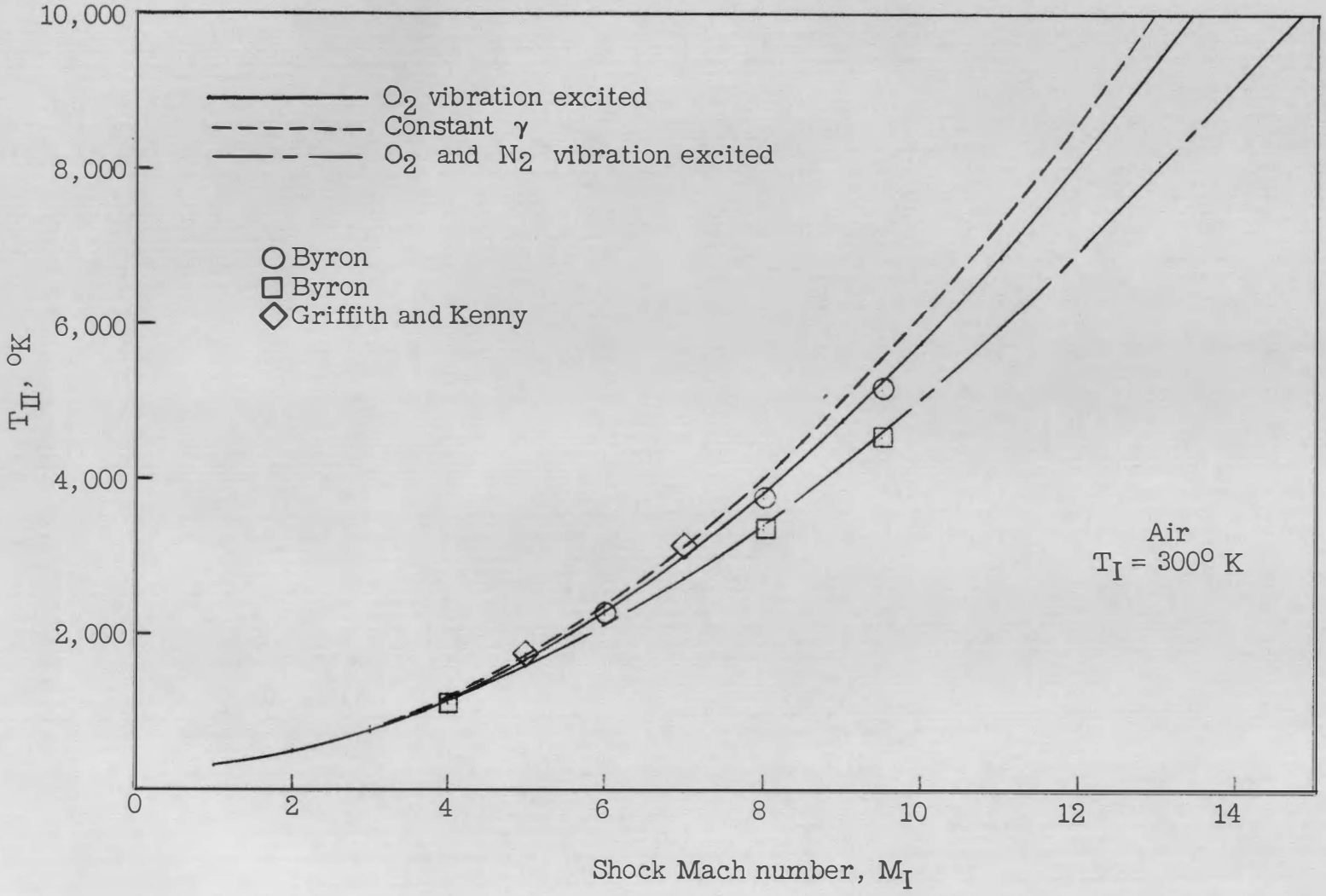
10,000
8,000
6,000
4,000
2,000
0
2
4
6
8
10
12
14
T_{II}, °K
Shock Mach number, M_I
O_2 vibration excited
Constant γ
O_2 and N_2 vibration excited
Byron
Byron
Griffith and Kenny
Air
$T_I = 300^o$ K

Figure 32(b).

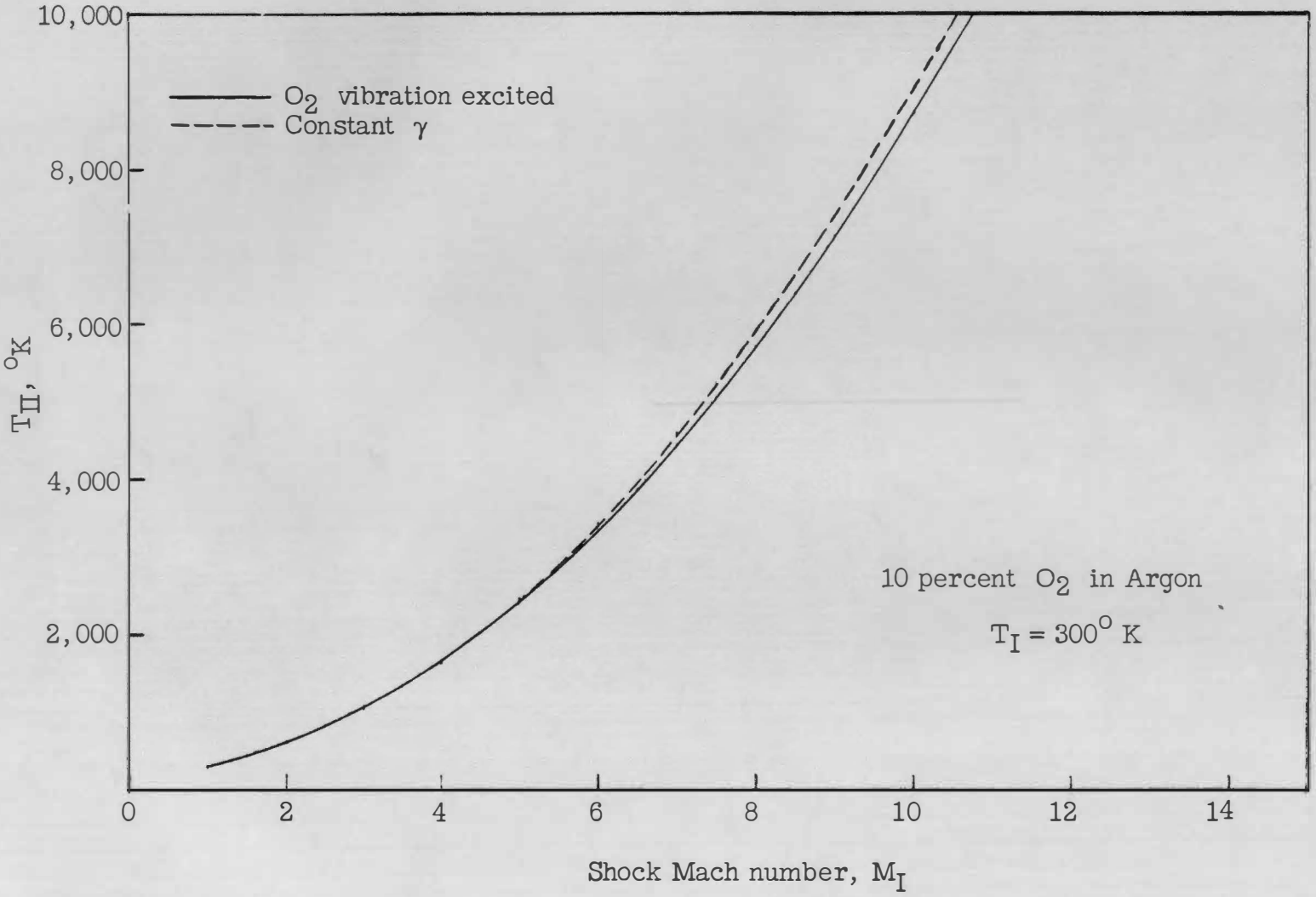
10,000
8,000
6,000
4,000
2,000
T_{II}, °K
O_2 vibration excited
Constant γ
10 percent O_2 in Argon
$T_I = 300^o$ K
0
2
4
6
8
10
12
14
Shock Mach number, M_I

Figure 32(c).

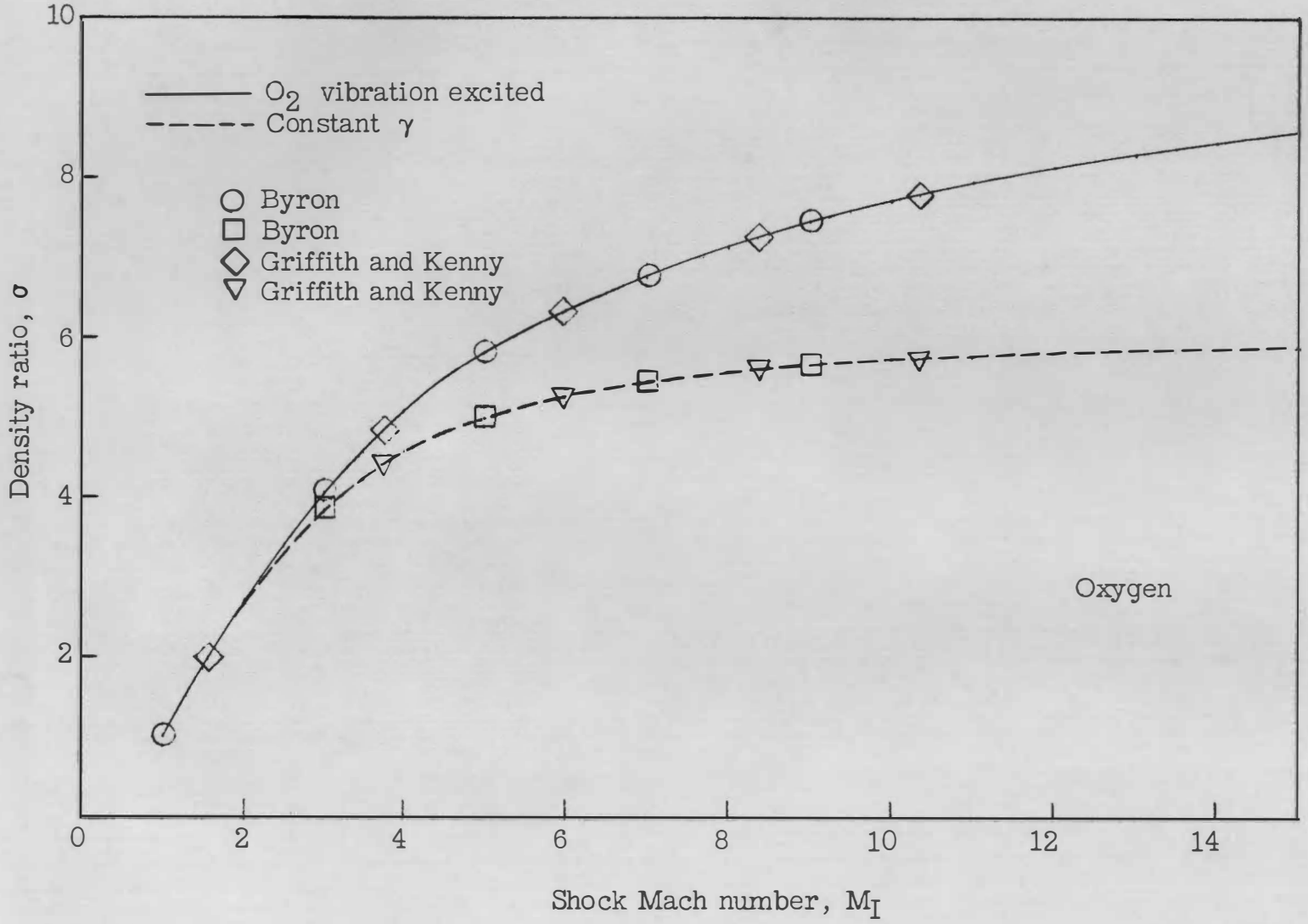
10
8
6
4
2
0
2
4
6
8
10
12
14
Density ratio, σ
Shock Mach number, M_I
O_2 vibration excited
Constant γ
Byron
Byron
Griffith and Kenny
Griffith and Kenny
Oxygen

Figure 32(d).

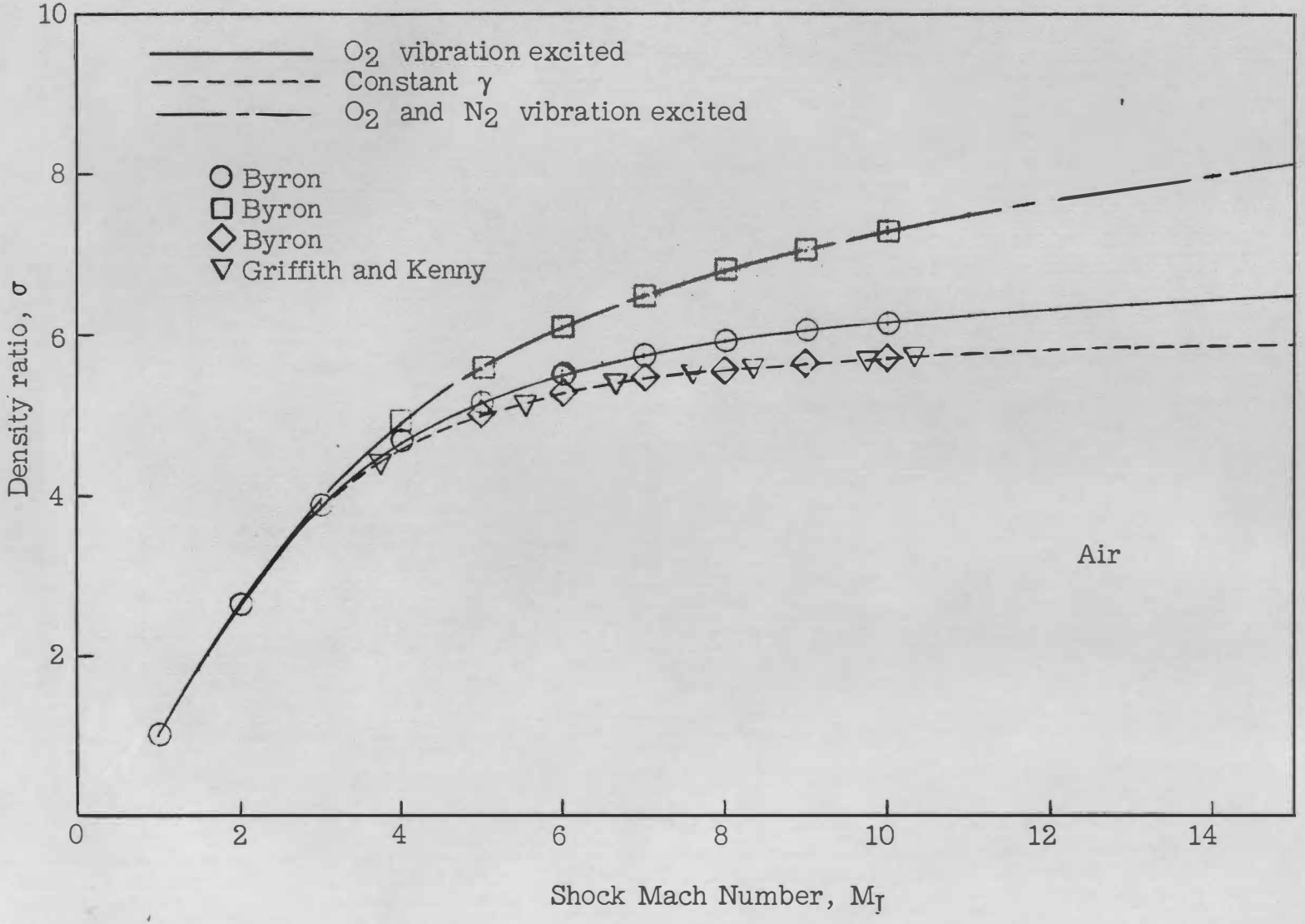
O_2 vibration excited
Constant γ
O_2 and N_2 vibration excited
Byron
Byron
Byron
Griffith and Kenny
Air
Density ratio, σ
Shock Mach Number, M_I
0
2
4
6
8
10
12
14

Figure 32(e).

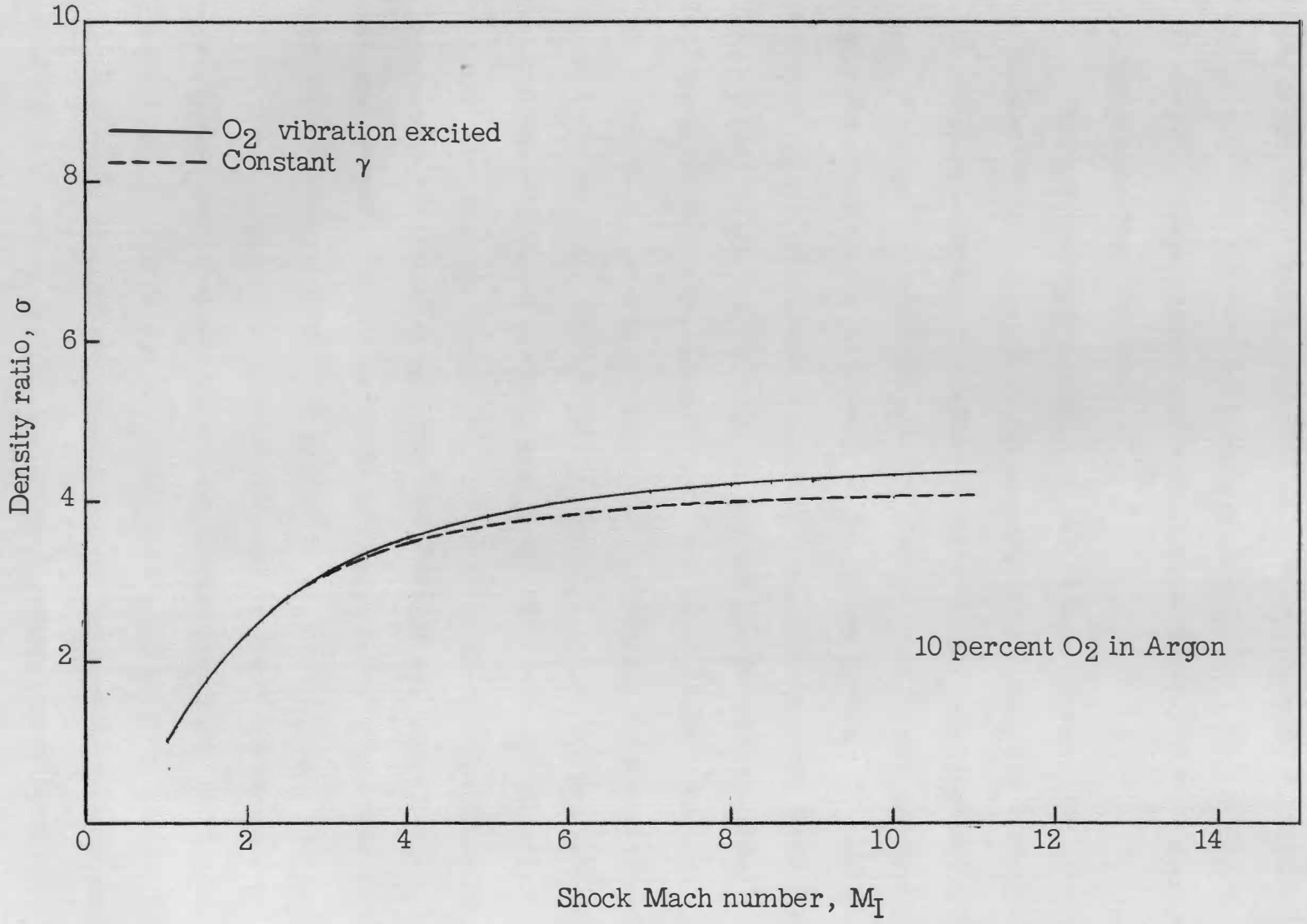
10
8
6
4
2
0
2
4
6
8
10
12
14
O_2 vibration excited
Constant γ
10 percent O_2 in Argon
Density ratio, σ
Shock Mach number, M_I

Figure 32(f).

Plots are shown for the three gas mixtures used. These were air, oxygen and a 10 per cent mixture of oxygen in argon. Calculations of σ and T_{II} for some of these gas mixtures have been published elsewhere[74]. These results are also shown on figure 32 for comparison to the results obtained here.

The curves shown on figure 32 are of three types. One is marked "Constant γ" and is based on the assumption that only the translational and rotational degrees of freedom of the molecules are excited. A second type is marked "O_2 vibration excited" and is based on the assumption that the vibrational degree of freedom of the oxygen molecule is excited in addition to the translational and rotational degrees. The third type applies only to air and is based on the assumption that vibration is fully excited for both oxygen and nitrogen. The above assumptions enter into the solution of equations (19) and (22) through the enthalpy function, η, in equation (19). Vibrationally unexcited oxygen and nitrogen were both assumed to have a specific heat ratio of $\gamma = 1.4$. The value $\gamma = 1.67$ was used for argon. For the cases in which vibrational excitation was assumed for oxygen or nitrogen the enthalpy was taken from a National Bureau of Standards Circular[75] up to 5,000° K and from Fickett and Cowan[76] between 5,000° and 10,000° K.

For a given shock tube run only one of the above assumptions corresponded to the actual conditions present behind the shock. On figures 33, 34, and 35 the transmission of light measured on the records is compared to theoretical curves based on the assumptions mentioned. On figures 33 and 34 the numbers beside the experimental points are oxygen vibrational relaxation times in microseconds and were calculated from

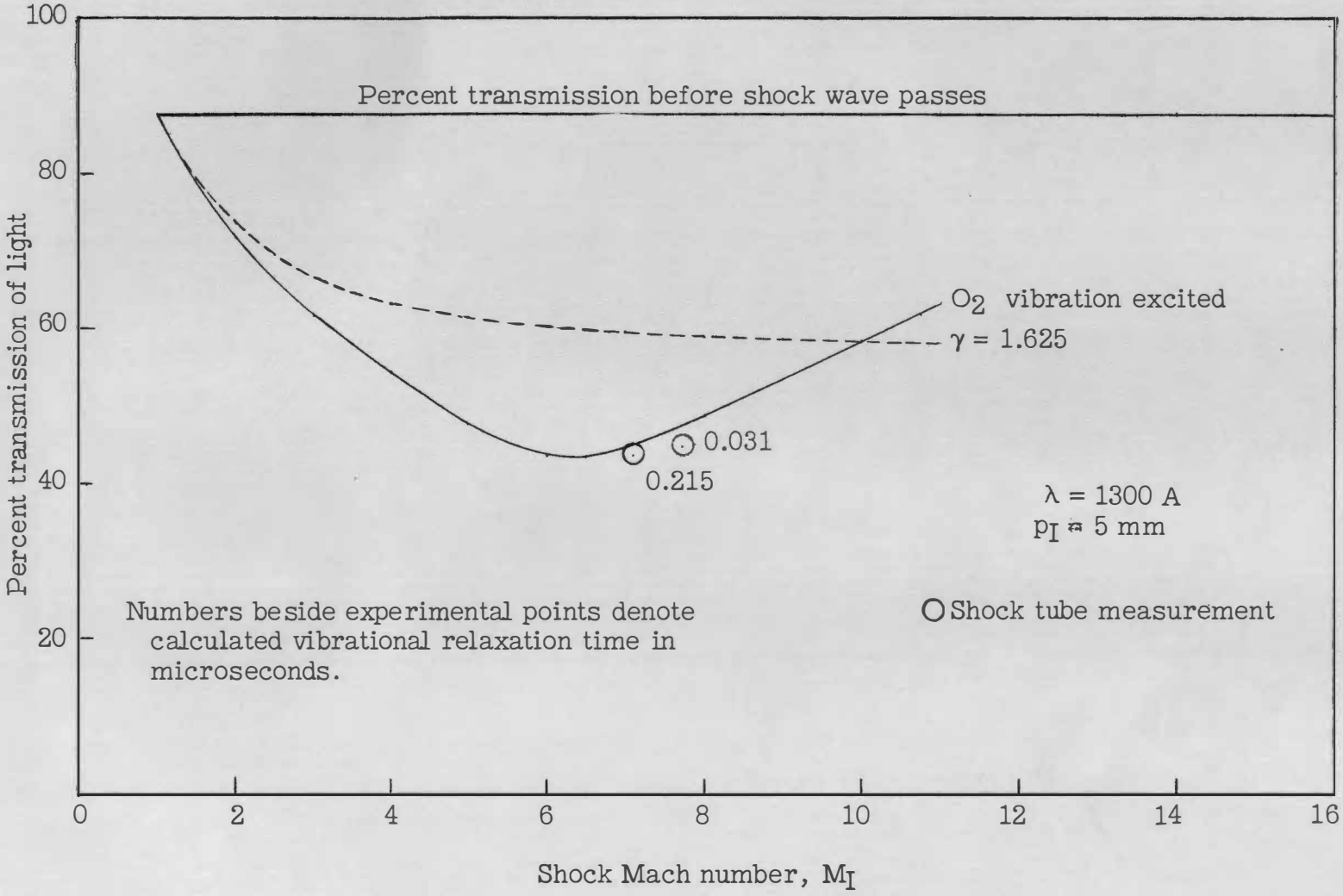

Figure 33(a).- Calculated and observed percent transmission of light for oxygen-argon mixture.

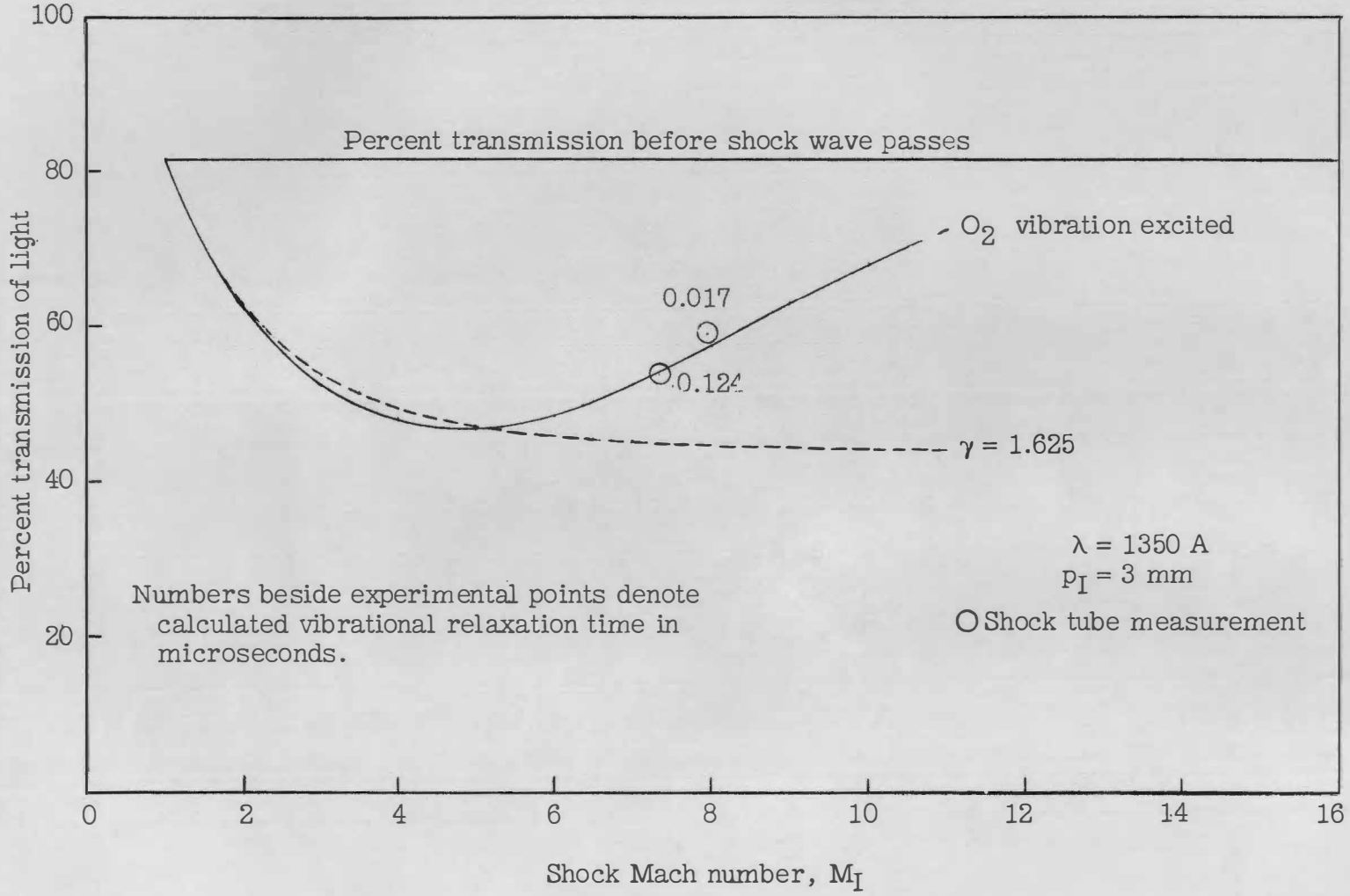
100
80
60
40
20
Percent transmission of light
Percent transmission before shock wave passes
O_2 vibration excited
0.017
0.124
$\gamma = 1.625$
$\lambda = 1350$ A
$p_I = 3$ mm
O Shock tube measurement
Numbers beside experimental points denote calculated vibrational relaxation time in microseconds.
0
2
4
6
8
10
12
14
16
Shock Mach number, M_I

Figure 33(b).

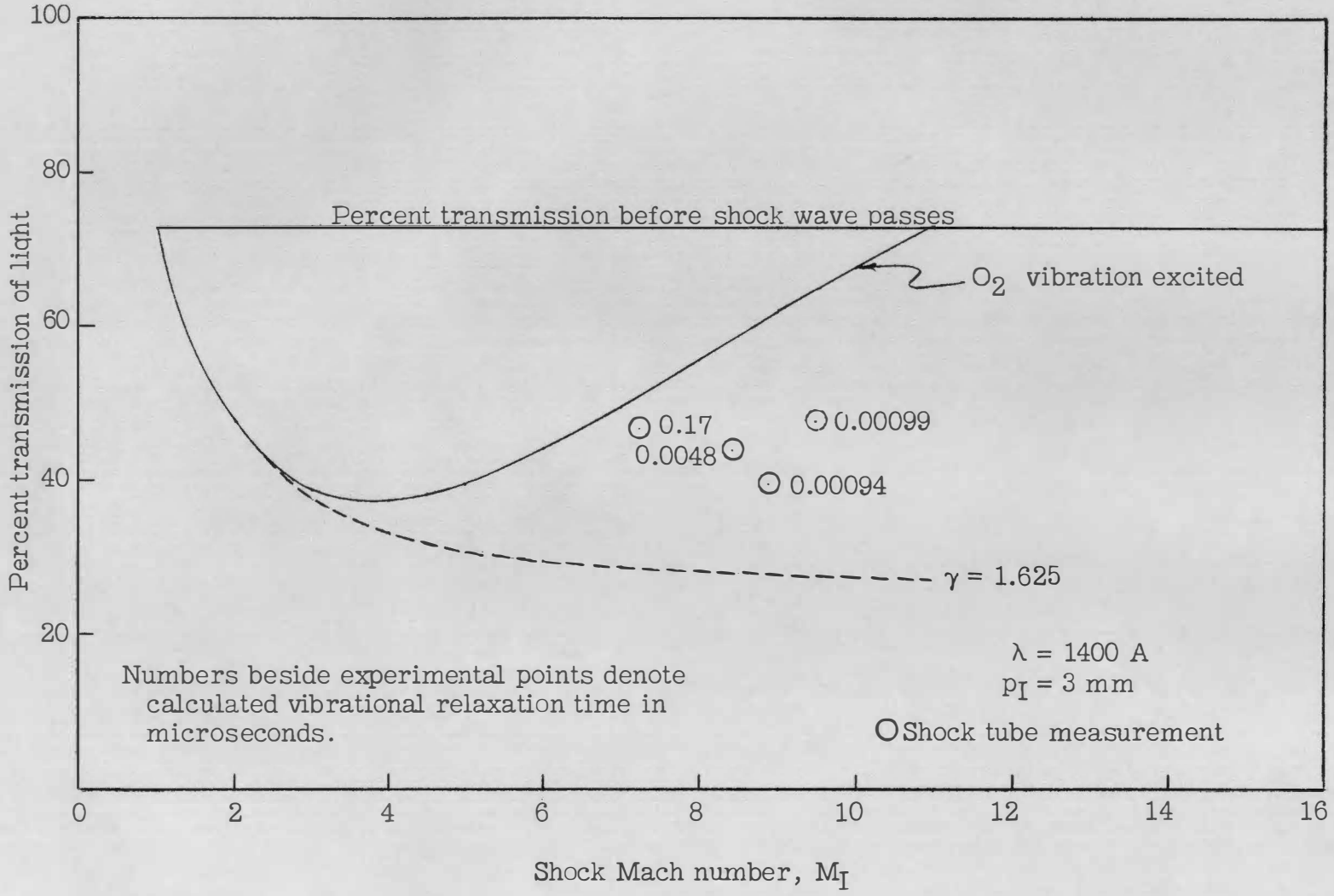
100
80
60
40
20
Percent transmission of light
Percent transmission before shock wave passes
O_2 vibration excited
0.17
0.0048
0.00099
0.00094
$\gamma = 1.625$
Numbers beside experimental points denote calculated vibrational relaxation time in microseconds.
$\lambda = 1400$ A
$p_I = 3$ mm
Shock tube measurement
0
2
4
6
8
10
12
14
16
Shock Mach number, M_I

Figure 33(c).

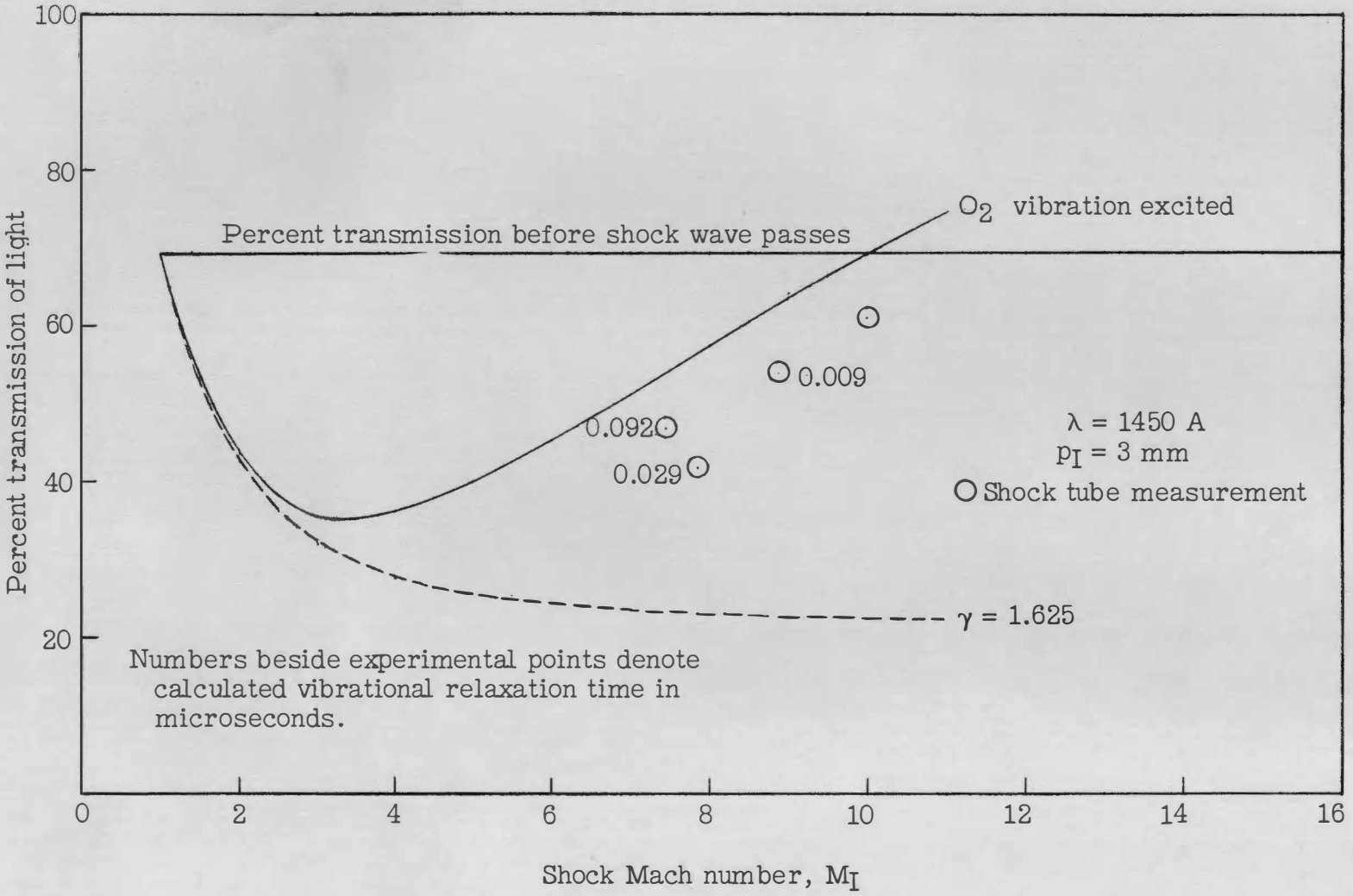
100
80
60
40
20
Percent transmission of light
Percent transmission before shock wave passes
O_2 vibration excited
0.009
0.092
0.029
λ = 1450 A
p_I = 3 mm
Shock tube measurement
γ = 1.625
Numbers beside experimental points denote calculated vibrational relaxation time in microseconds.
0
2
4
6
8
10
12
14
16
Shock Mach number, M_I

Figure 33(d).

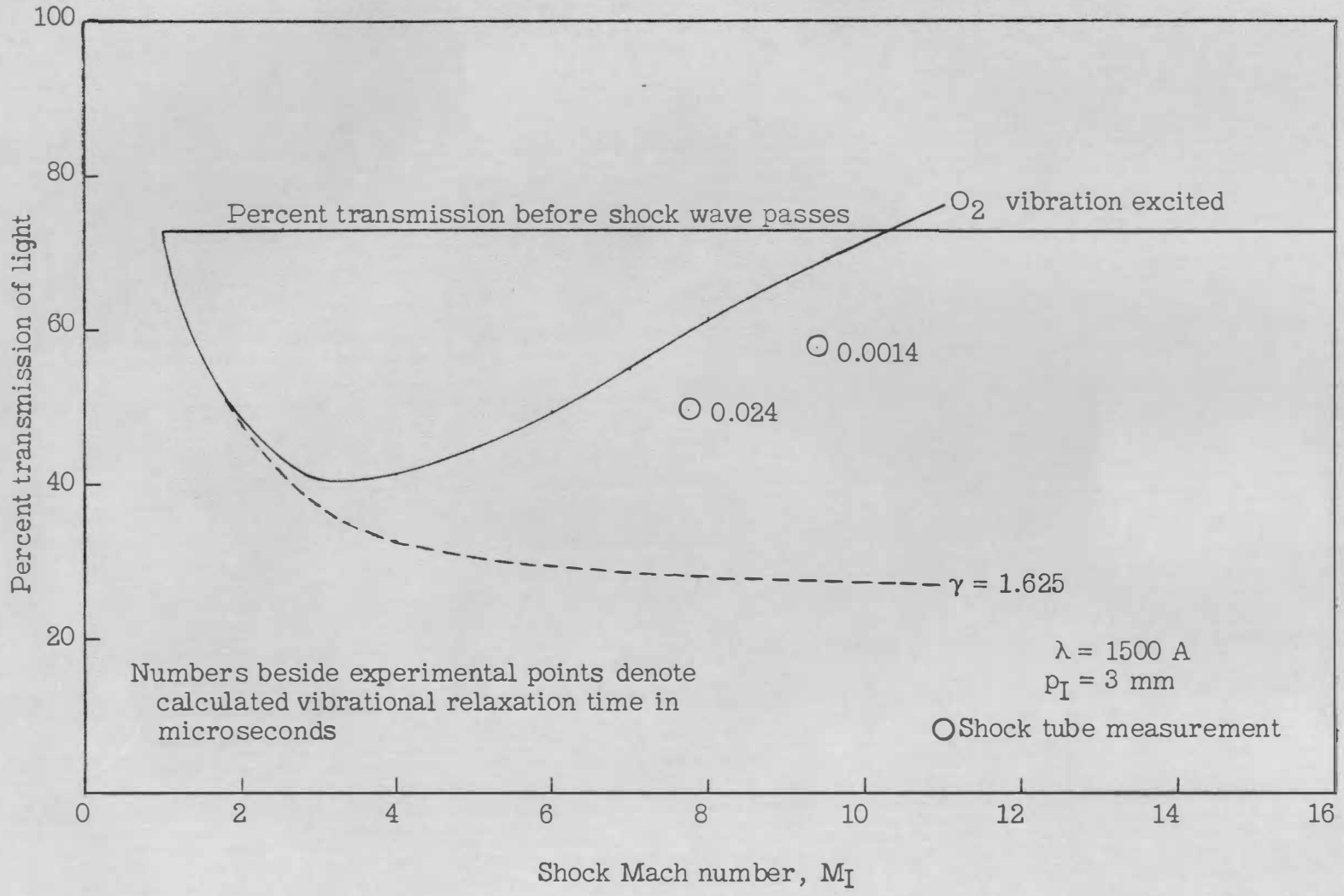
100
80
60
40
20
Percent transmission of light
Percent transmission before shock wave passes
O_2 vibration excited
0.0014
0.024
$\gamma = 1.625$
$\lambda = 1500$ A
$p_I = 3$ mm
Shock tube measurement
Numbers beside experimental points denote calculated vibrational relaxation time in microseconds
0
2
4
6
8
10
12
14
16
Shock Mach number, M_I

Figure 33(e).

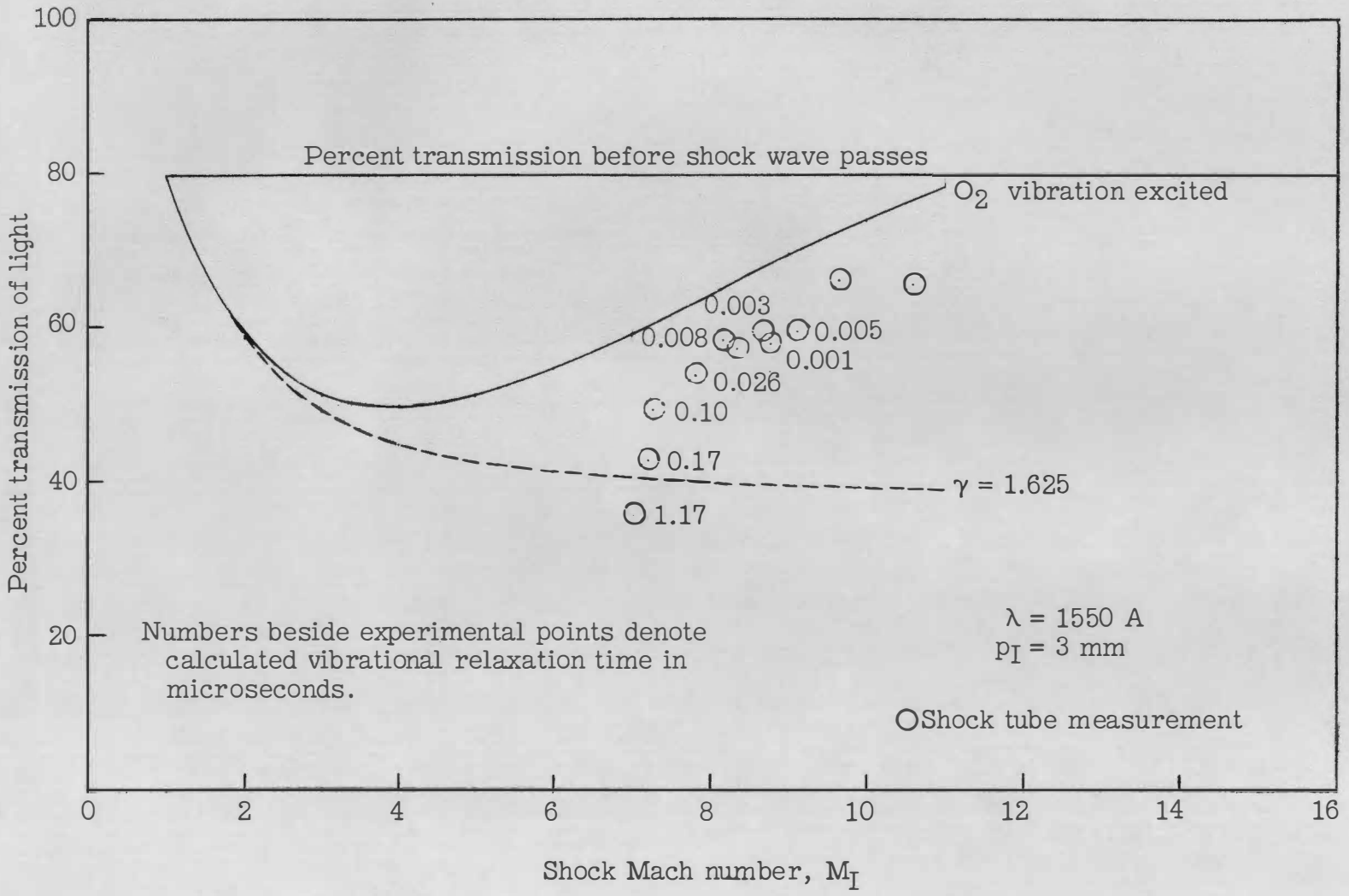
100
80
60
40
20
Percent transmission of light
Percent transmission before shock wave passes
O_2 vibration excited
0.003
0.008
0.005
0.001
0.026
0.10
0.17
1.17
γ = 1.625
Numbers beside experimental points denote calculated vibrational relaxation time in microseconds.
λ = 1550 A
p_I = 3 mm
Shock tube measurement
0
2
4
6
8
10
12
14
16
Shock Mach number, M_I

Figure 33(f).

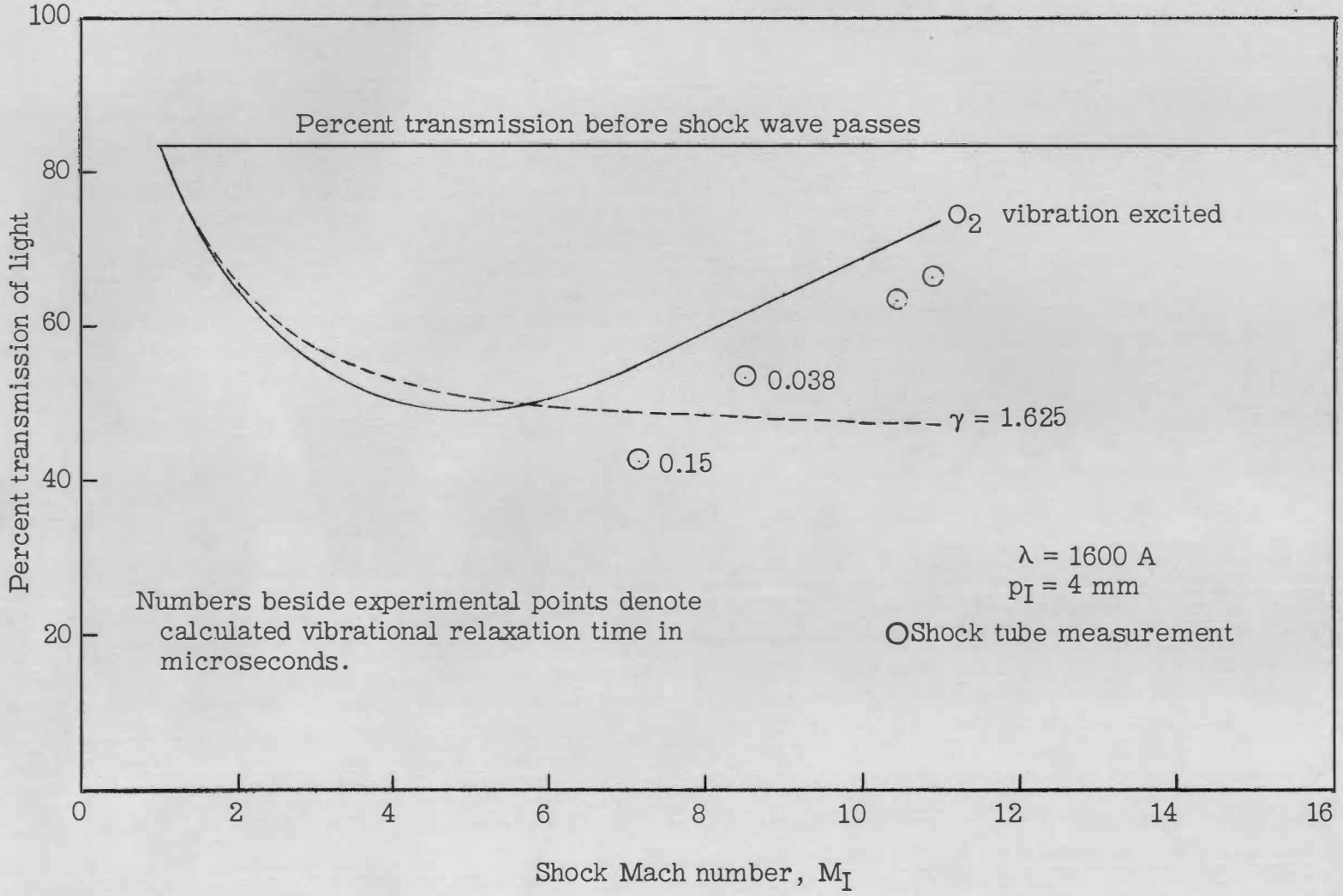
100
80
60
40
20
0
2
4
6
8
10
12
14
16
Percent transmission of light
Shock Mach number, M_I
Percent transmission before shock wave passes
O_2 vibration excited
0.038
0.15
$\gamma = 1.625$
$\lambda = 1600$ A
$p_I = 4$ mm
Shock tube measurement
Numbers beside experimental points denote calculated vibrational relaxation time in microseconds.

Figure 33(g).

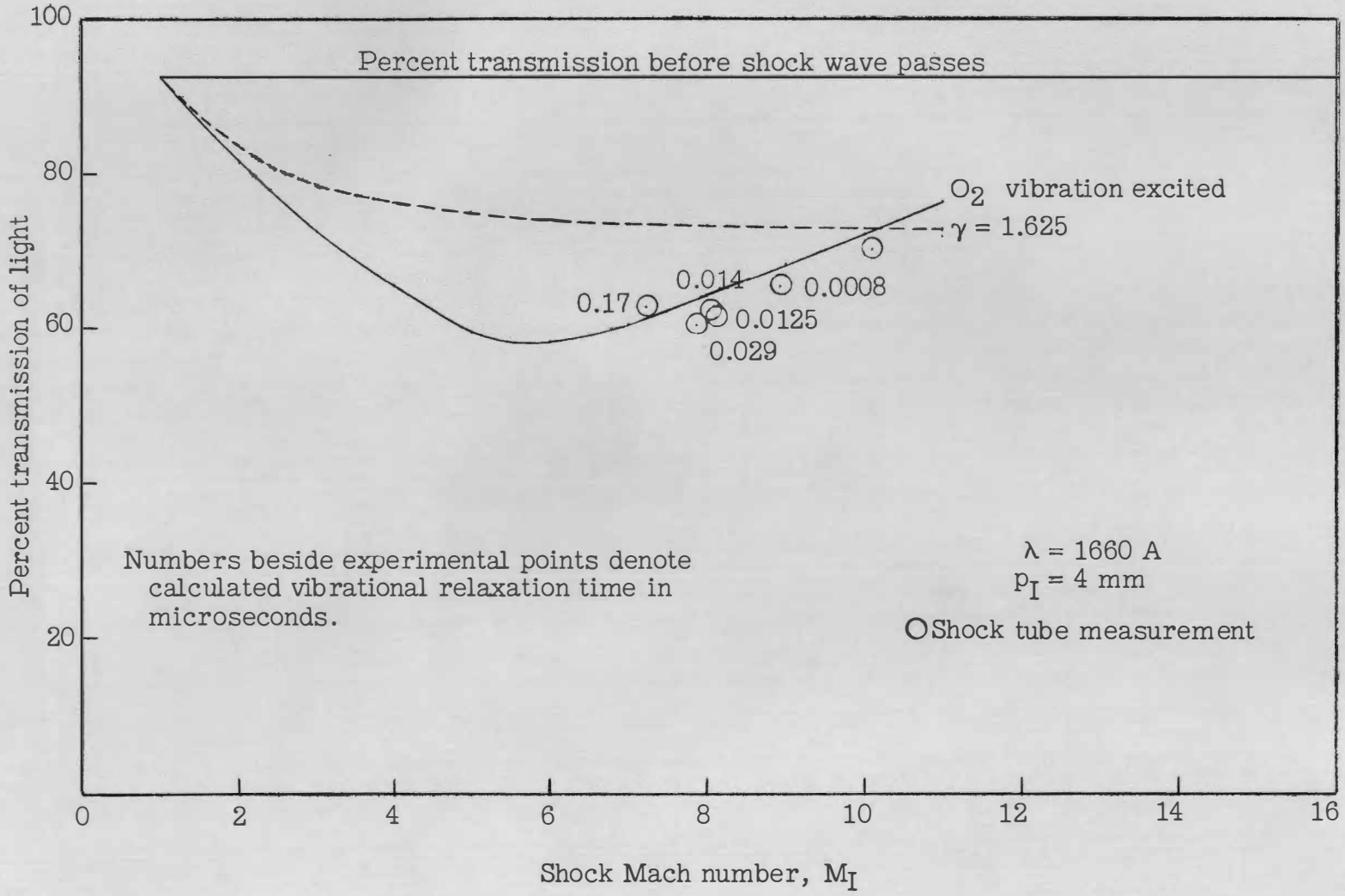
100
80
60
40
20
Percent transmission of light
Percent transmission before shock wave passes
O_2 vibration excited
$\gamma = 1.625$
0.17
0.014
0.0008
0.0125
0.029
Numbers beside experimental points denote calculated vibrational relaxation time in microseconds.
$\lambda = 1660$ A
$p_I = 4$ mm
Shock tube measurement
0
2
4
6
8
10
12
14
16
Shock Mach number, M_I

Figure 33(h).

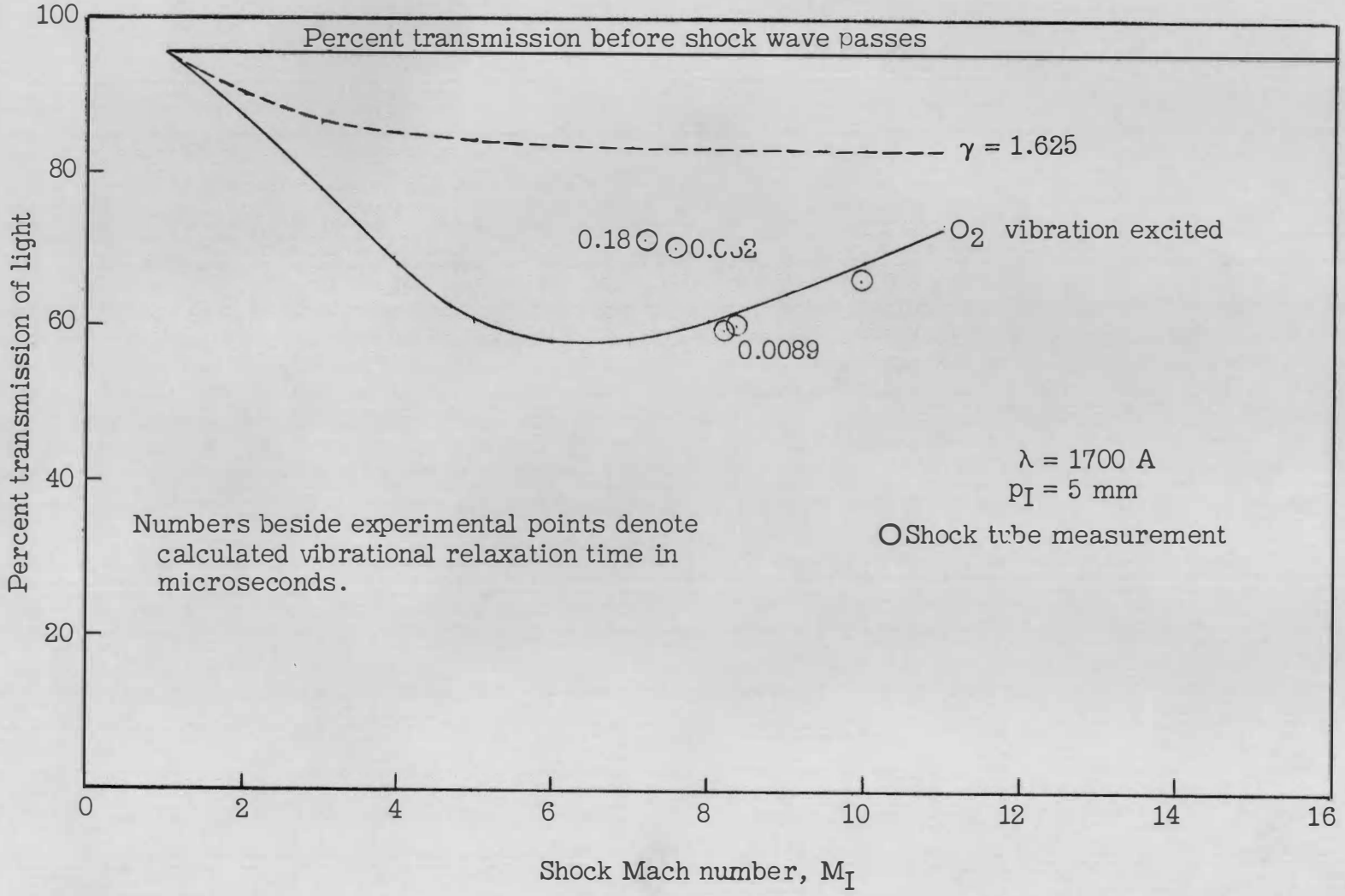
Percent transmission before shock wave passes
γ = 1.625
O2 vibration excited
0.18
0.002
0.0089
λ = 1700 A
pI = 5 mm
O Shock tube measurement
Numbers beside experimental points denote calculated vibrational relaxation time in microseconds.
Percent transmission of light
100
80
60
40
20
0
2
4
6
8
10
12
14
16
Shock Mach number, MI

Figure 33(1).

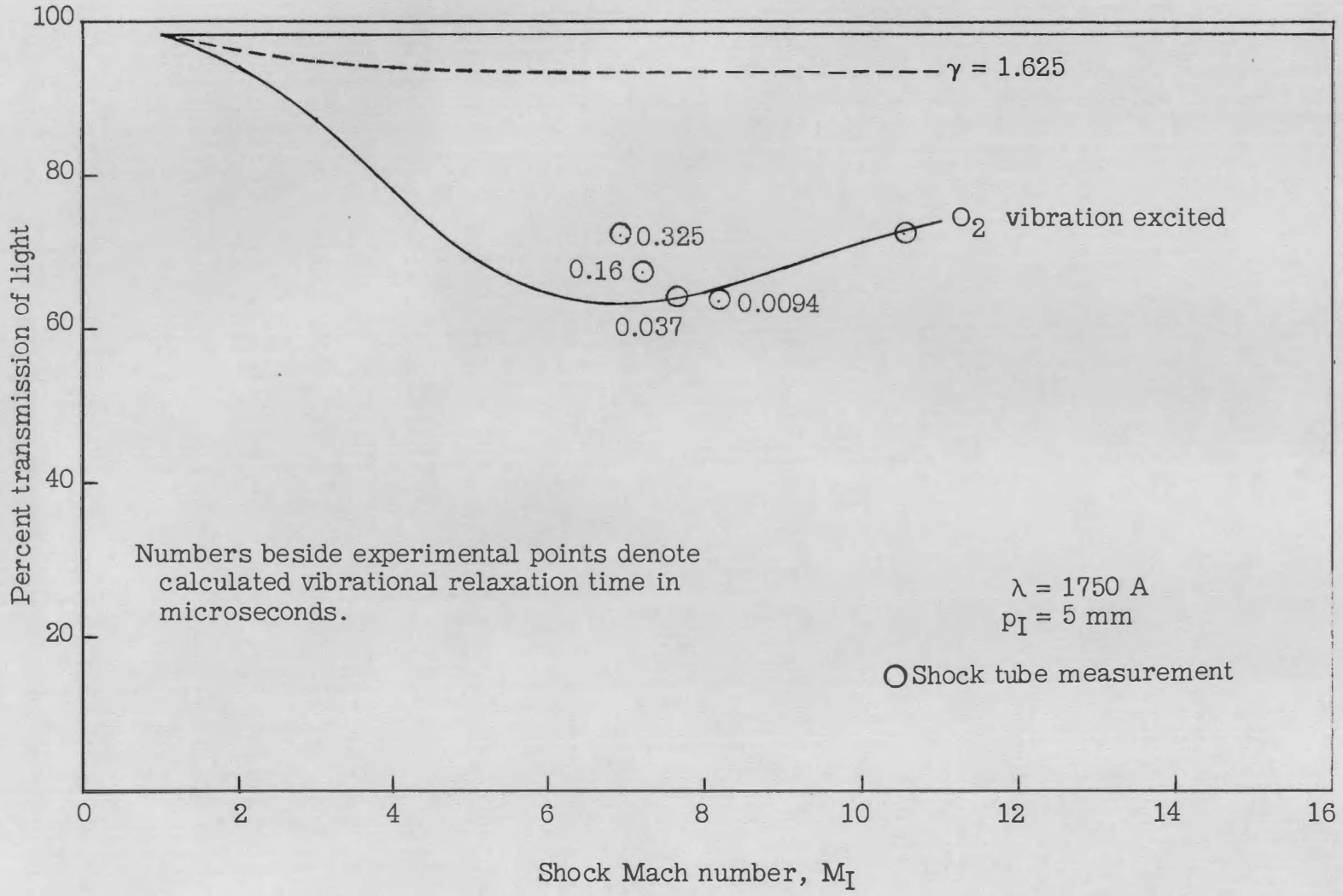
100
80
60
40
20
Percent transmission of light
γ = 1.625
O2 vibration excited
0.325
0.16
0.0094
0.037
Numbers beside experimental points denote calculated vibrational relaxation time in microseconds.
λ = 1750 A
pI = 5 mm
Shock tube measurement
0
2
4
6
8
10
12
14
16
Shock Mach number, MI

Figure 33(j).

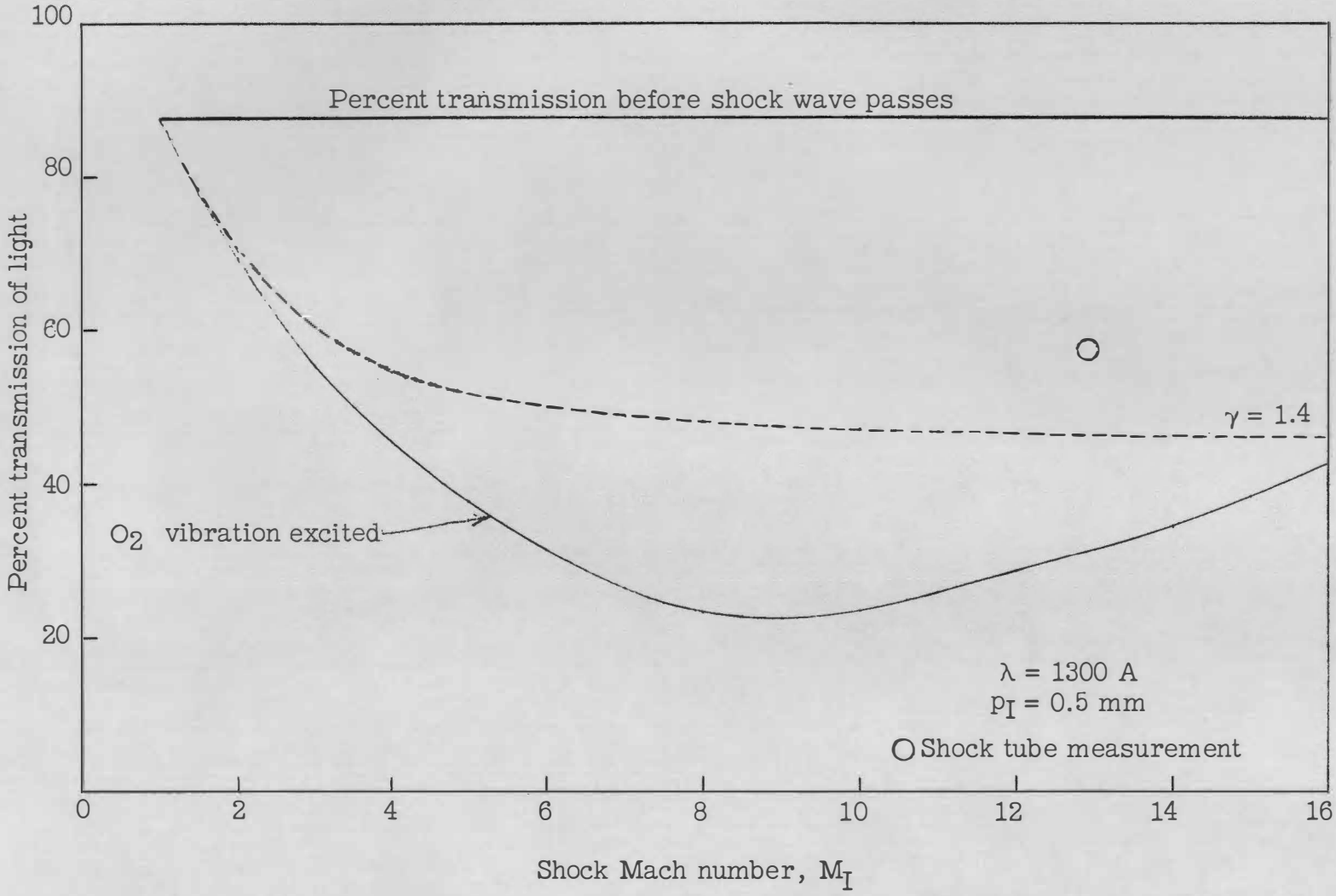

Figure 34(a).- Calculated and observed percent transmission of light for oxygen.

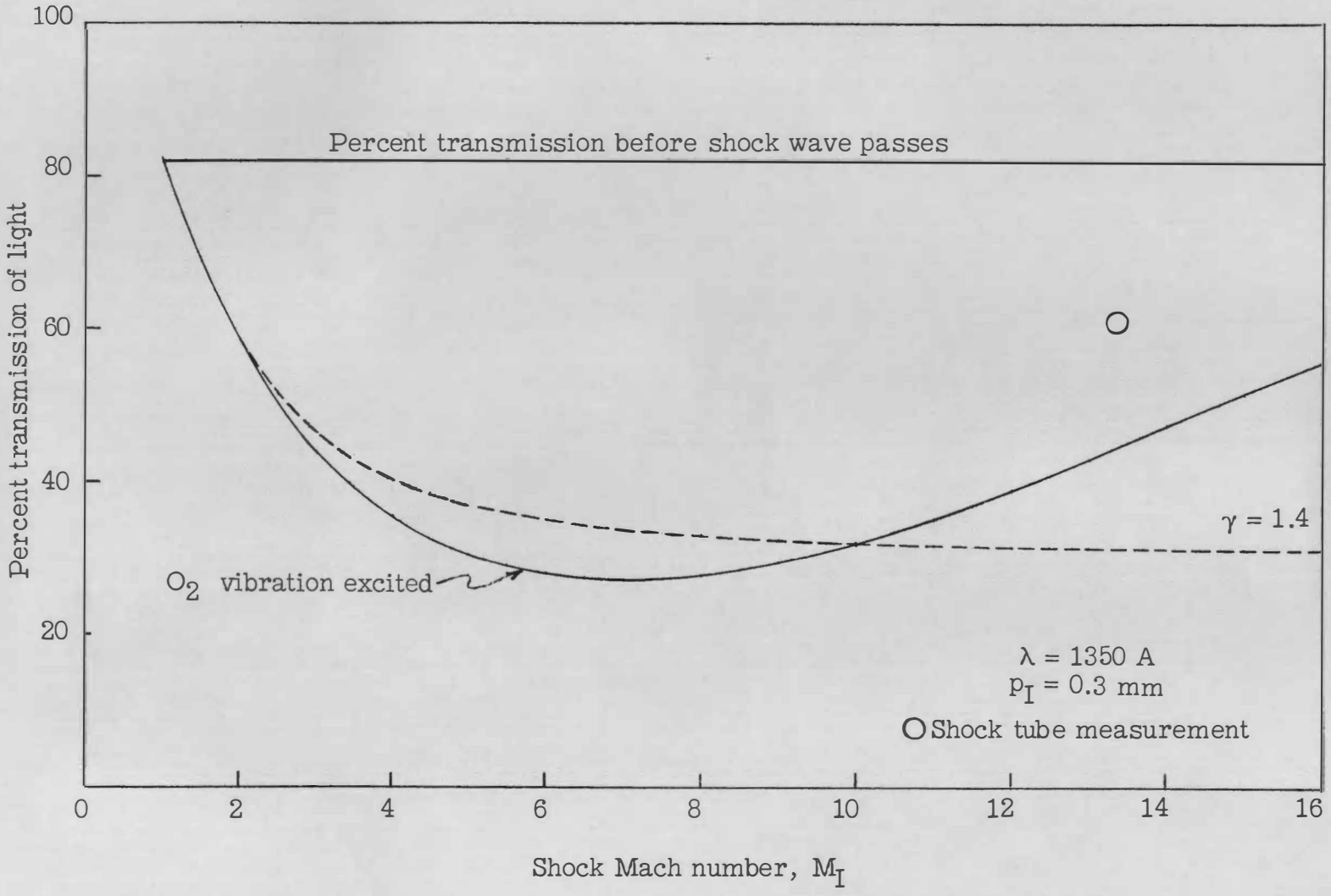
100
80
60
40
20
Percent transmission of light
Percent transmission before shock wave passes
$\gamma = 1.4$
O_2 vibration excited
$\lambda = 1350$ A
$p_I = 0.3$ mm
Shock tube measurement
0
2
4
6
8
10
12
14
16
Shock Mach number, M_I

Figure 34(b).

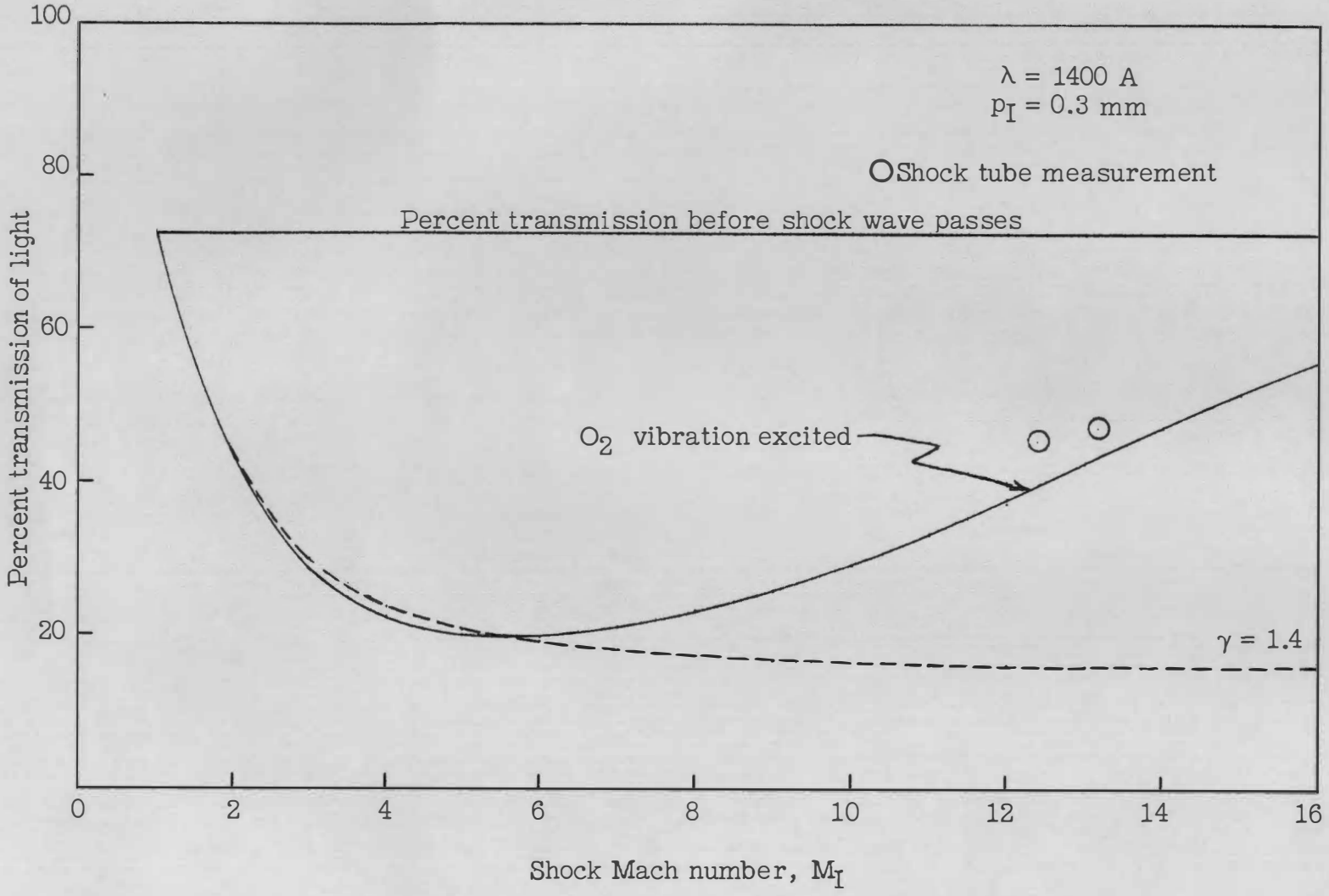
100
80
60
40
20
0
2
4
6
8
10
12
14
16
Percent transmission of light
Shock Mach number, M_I
λ = 1400 A
p_I = 0.3 mm
Shock tube measurement
Percent transmission before shock wave passes
O_2 vibration excited
γ = 1.4

Figure 34(c).

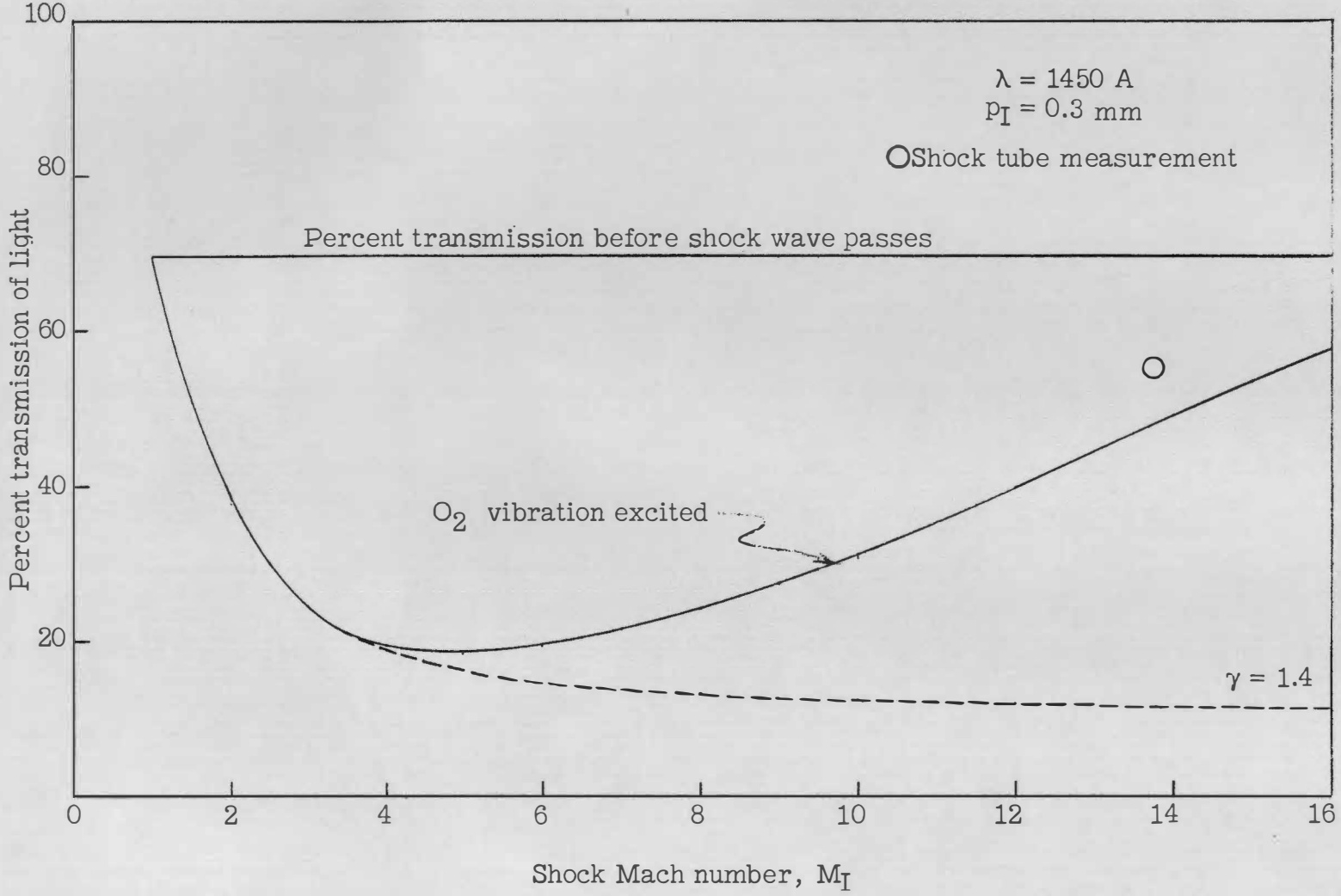
100
80
60
40
20
Percent transmission of light
λ = 1450 A
p_I = 0.3 mm
OShock tube measurement
Percent transmission before shock wave passes
O
O_2 vibration excited
γ = 1.4
0
2
4
6
8
10
12
14
16
Shock Mach number, M_I

Figure 34(d).

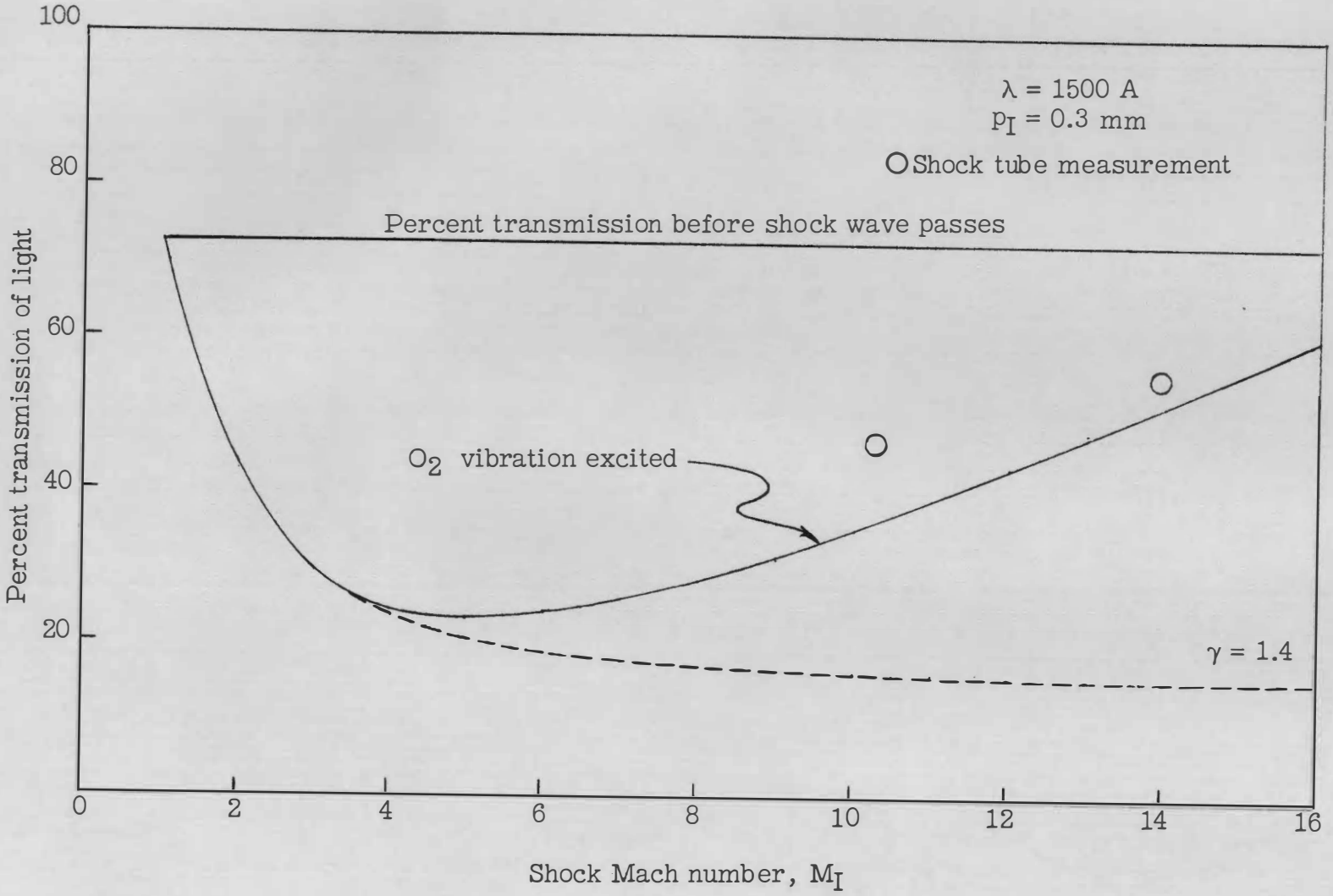
100
80
60
40
20
0
2
4
6
8
10
12
14
16
λ = 1500 A
p_I = 0.3 mm
O Shock tube measurement
Percent transmission before shock wave passes
O_2 vibration excited
γ = 1.4
Percent transmission of light
Shock Mach number, M_I

Figure 34(e).

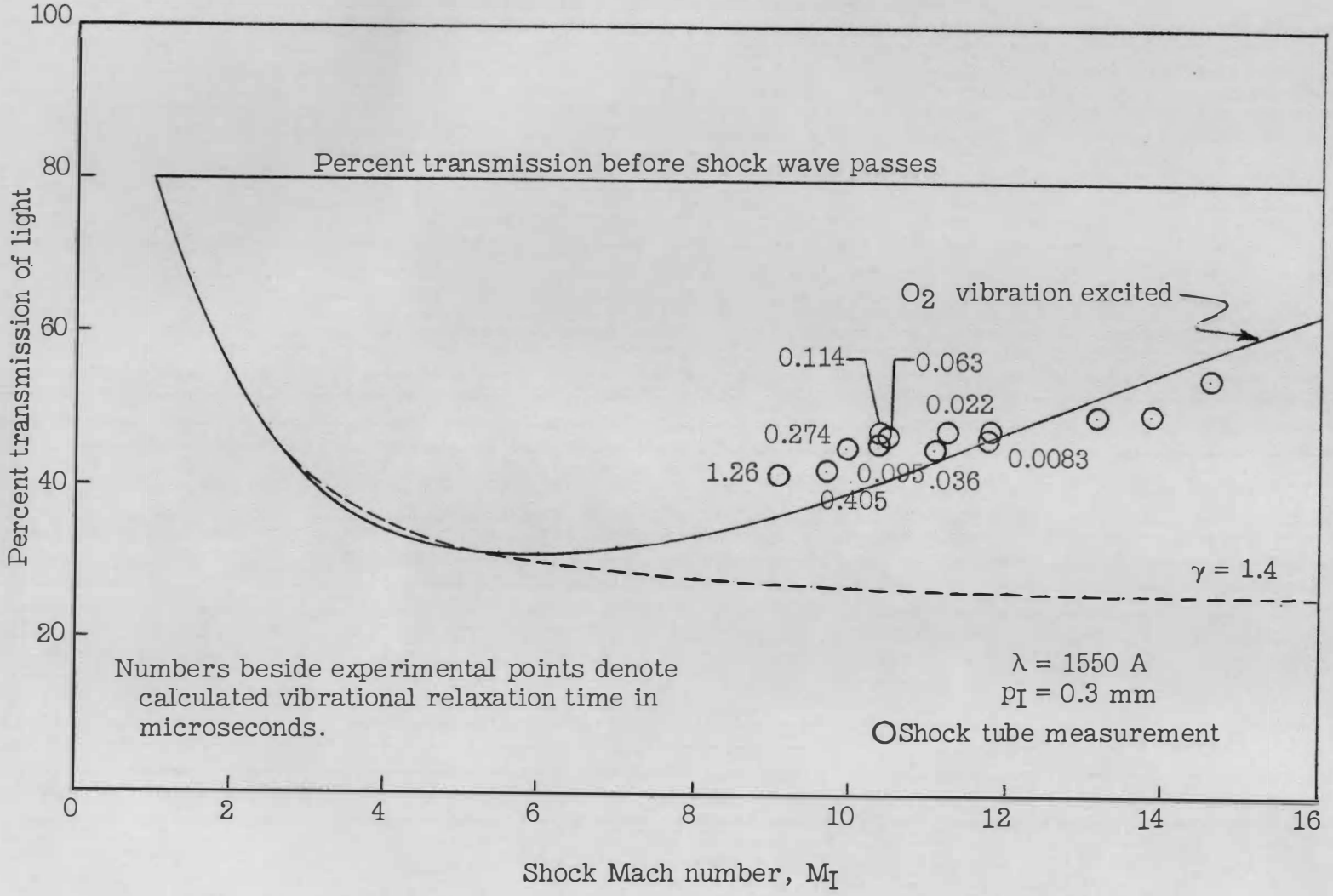
100
80
60
40
20
Percent transmission of light
Percent transmission before shock wave passes
O2 vibration excited
0.114
0.063
0.022
0.274
0.0083
1.26
0.095
.036
0.405
γ = 1.4
Numbers beside experimental points denote calculated vibrational relaxation time in microseconds.
λ = 1550 A
pI = 0.3 mm
Shock tube measurement
0
2
4
6
8
10
12
14
16
Shock Mach number, MI

Figure 34(f).

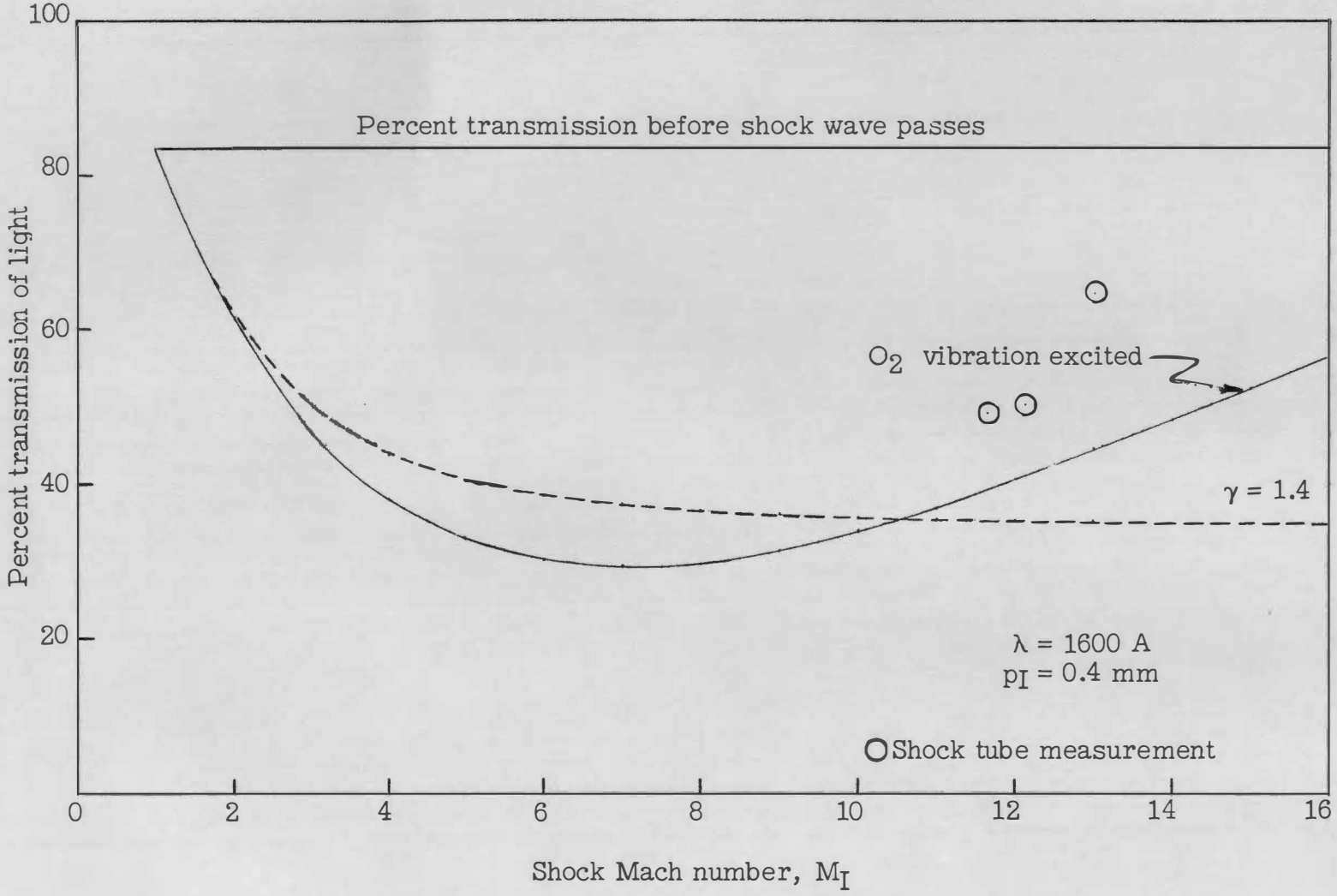
100
80
60
40
20
0
2
4
6
8
10
12
14
16
Percent transmission of light
Shock Mach number, M_I
Percent transmission before shock wave passes
O_2 vibration excited
$\gamma = 1.4$
$\lambda = 1600$ A
$p_I = 0.4$ mm
Shock tube measurement

Figure 34(g).

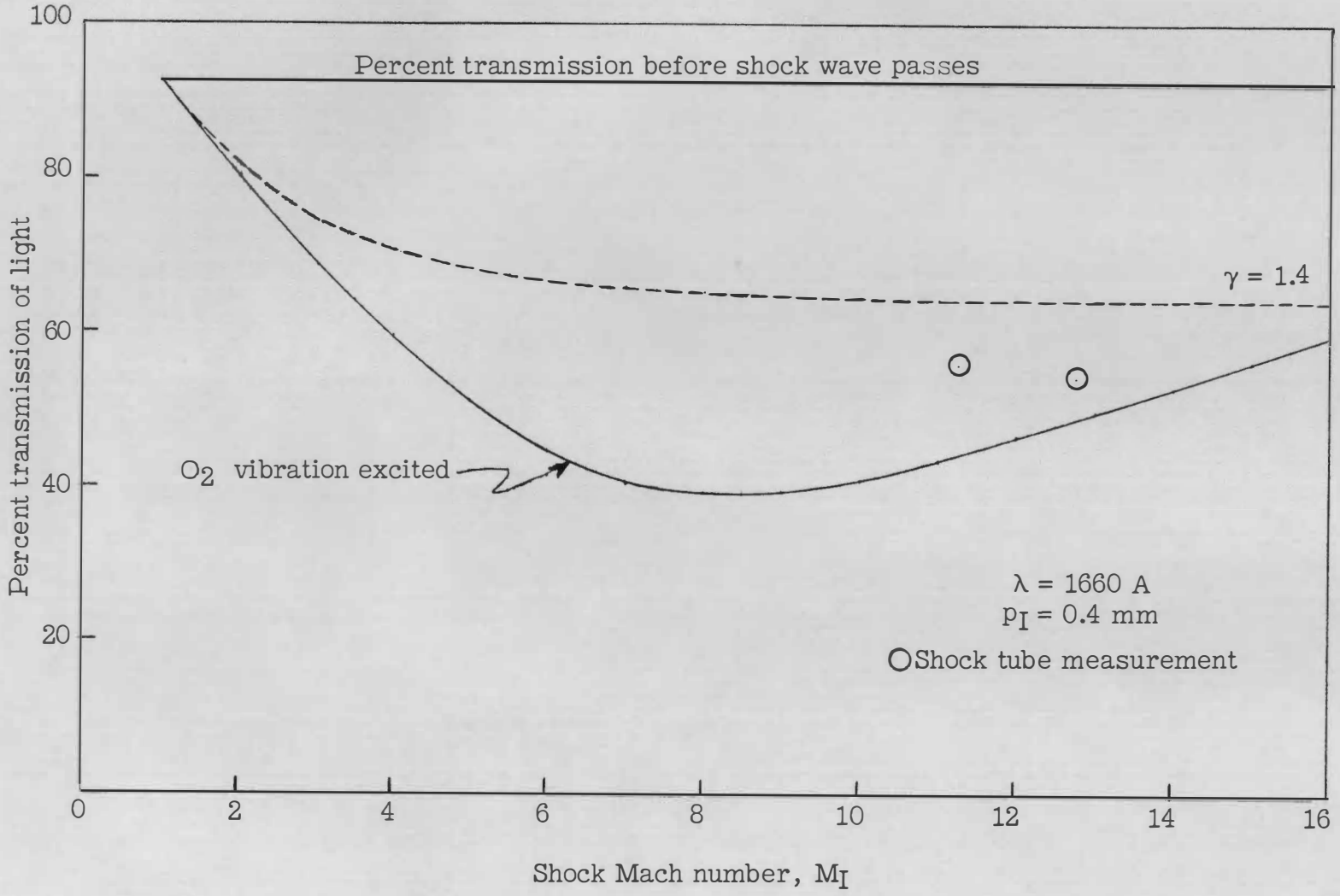
100
80
60
40
20
0
2
4
6
8
10
12
14
16
Percent transmission of light
Shock Mach number, M_I
Percent transmission before shock wave passes
$\gamma = 1.4$
O_2 vibration excited
$\lambda = 1660$ A
$p_I = 0.4$ mm
Shock tube measurement

Figure 34(h).

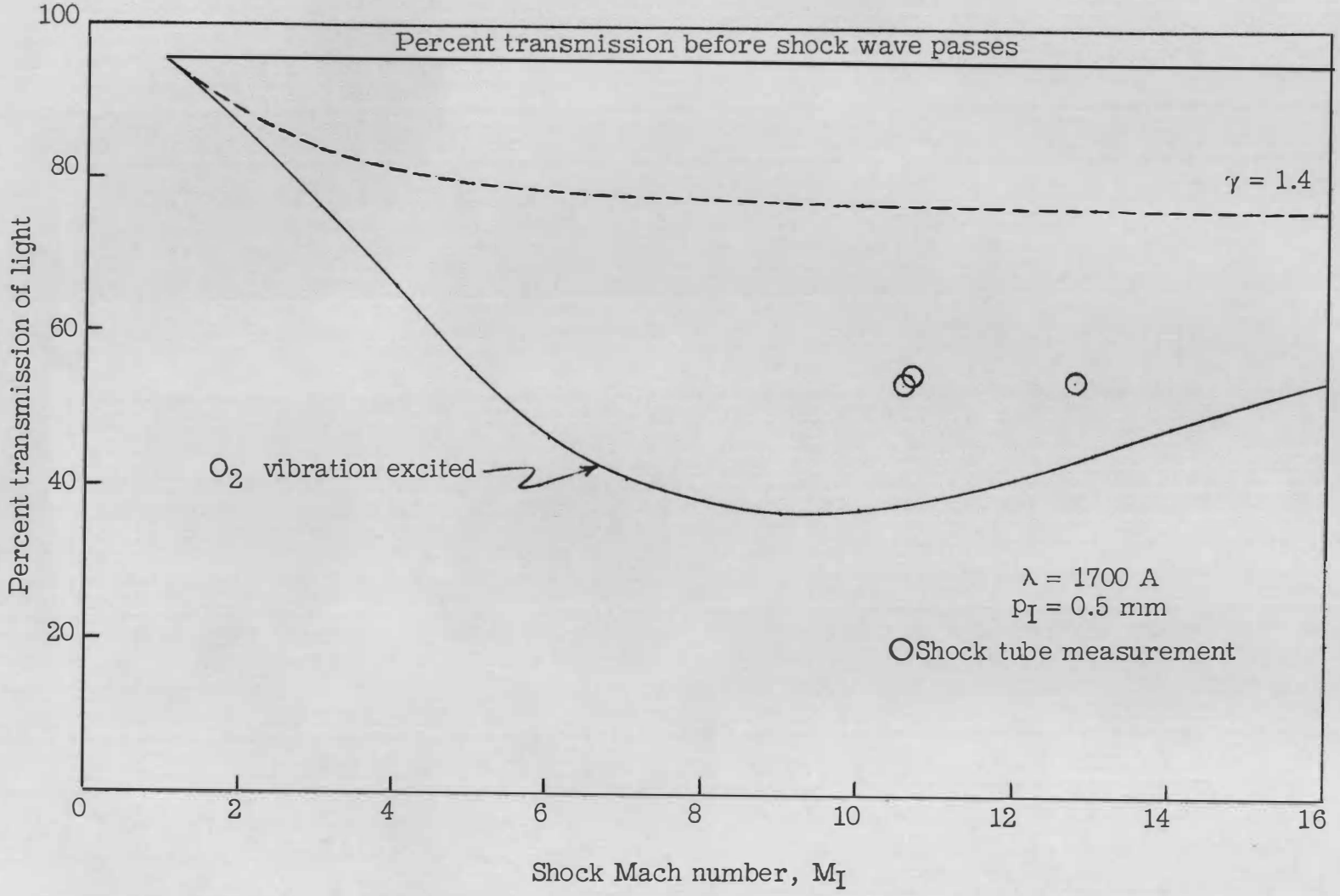
100
80
60
40
20
0
2
4
6
8
10
12
14
16
Percent transmission of light
Shock Mach number, M_I
Percent transmission before shock wave passes
$\gamma = 1.4$
O_2 vibration excited
$\lambda = 1700$ A
$p_I = 0.5$ mm
Shock tube measurement

Figure 34(i).

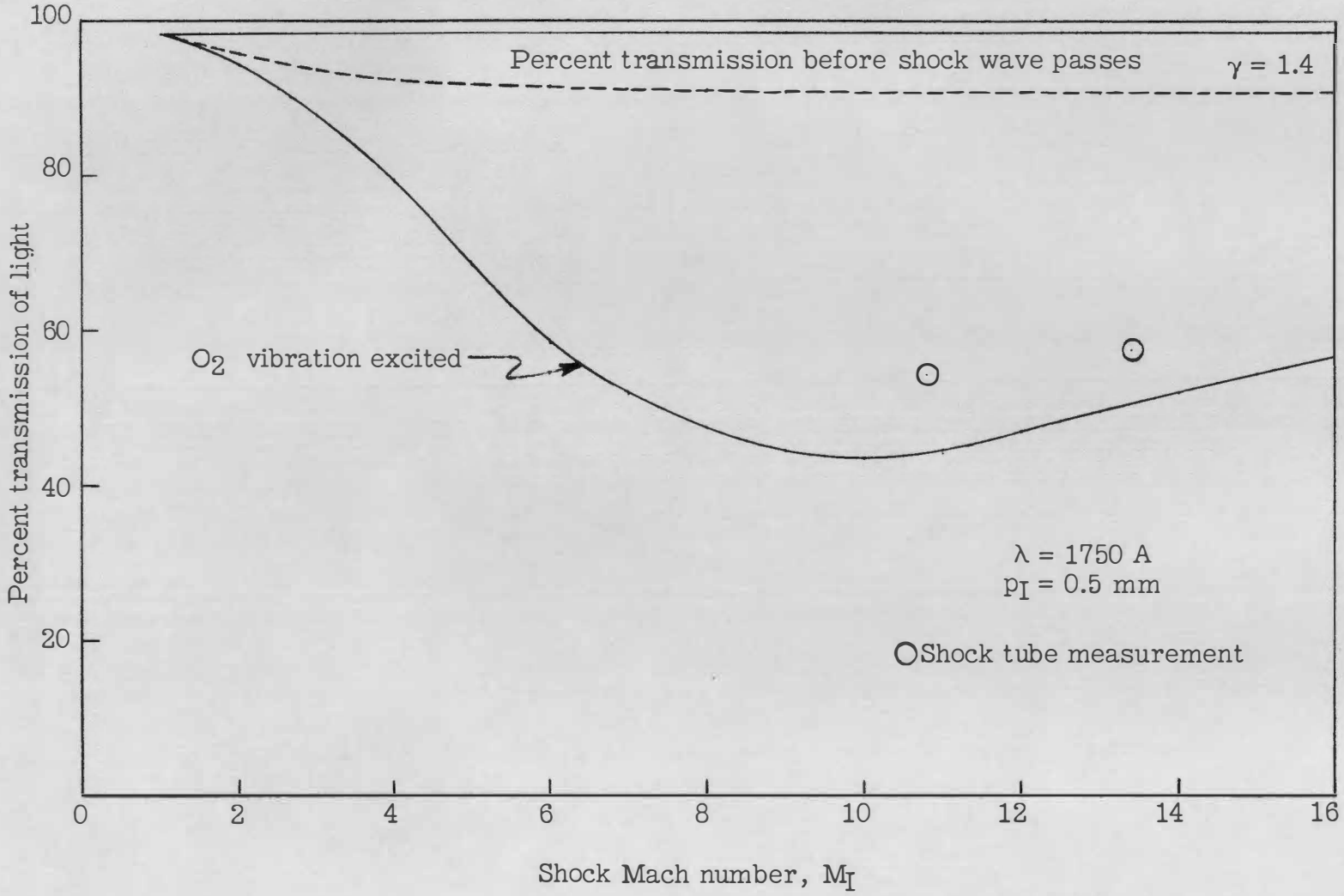
100
80
60
40
20
Percent transmission of light
Percent transmission before shock wave passes
γ = 1.4
O2 vibration excited
λ = 1750 A
pI = 0.5 mm
Shock tube measurement
0
2
4
6
8
10
12
14
16
Shock Mach number, MI

Figure 34(j).

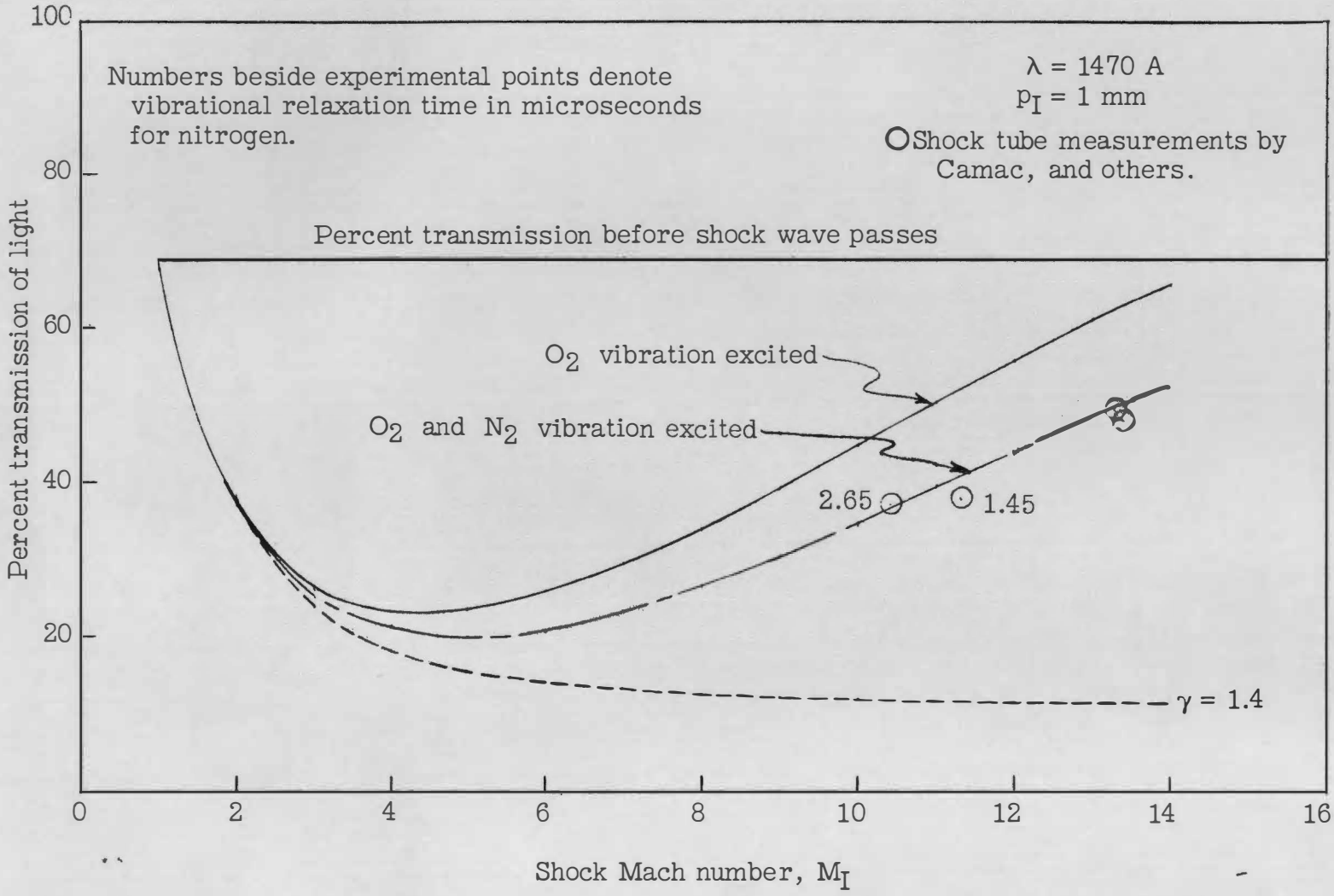

Figure 35(a).- Calculated and observed percent transmission of light for air.

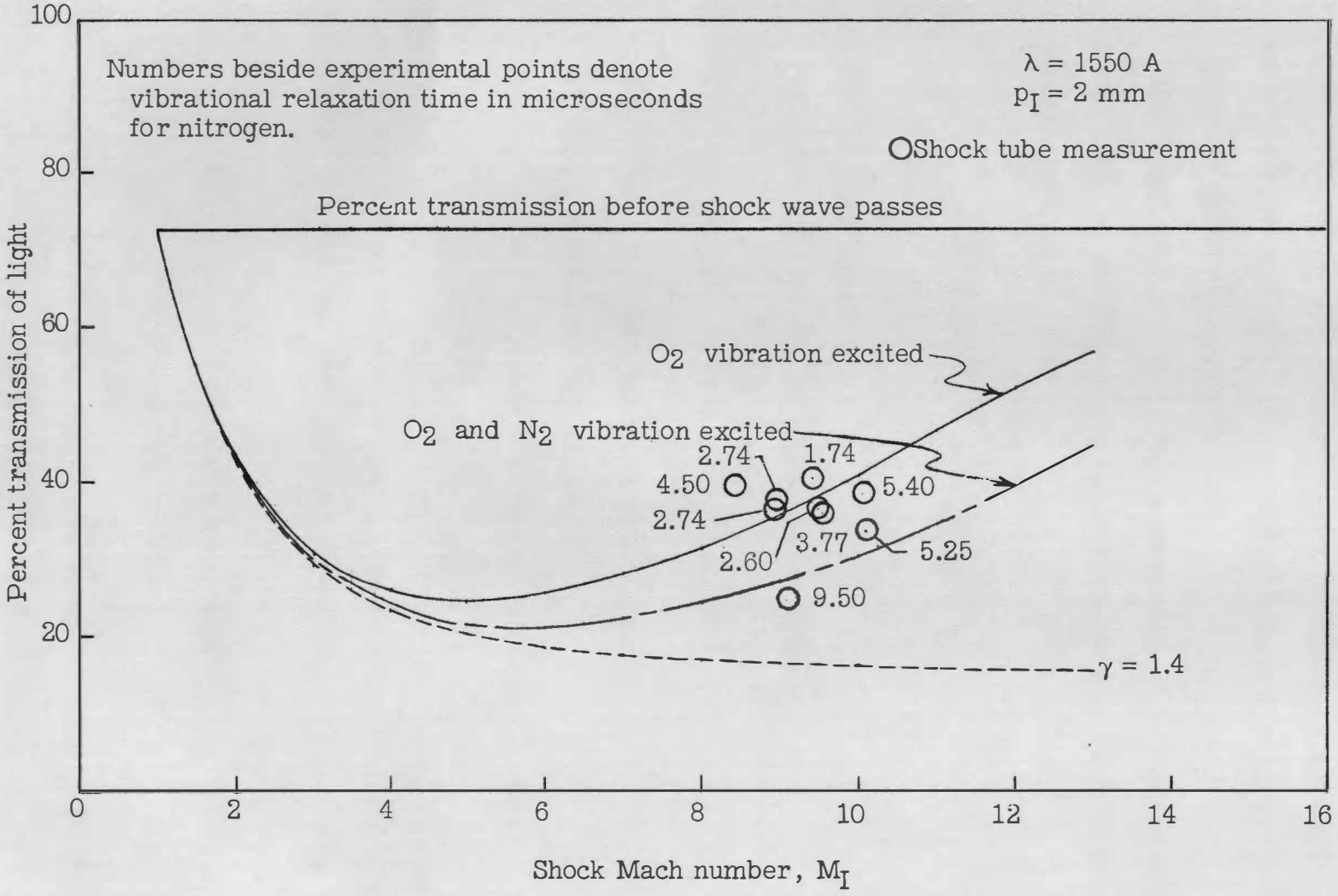
Numbers beside experimental points denote vibrational relaxation time in microseconds for nitrogen.
λ = 1550 A
p_I = 2 mm
Shock tube measurement
Percent transmission before shock wave passes
O_2 vibration excited
O_2 and N_2 vibration excited
2.74
1.74
4.50
5.40
2.74
2.60
3.77
5.25
9.50
γ = 1.4
Percent transmission of light
Shock Mach number, M_I
100
80
60
40
20
0
2
4
6
8
10
12
14
16

Figure 35(b).

Blackman's data[77], using Byron's estimate[78] that argon is one-third as efficient as oxygen for exciting oxygen vibration. On figure 35 the numbers are nitrogen vibrational relaxation times and are based on the results of Camac and others[79].

The remaining quantity to be evaluated was $\hat{\rho}_I$. From equation (18) $p_s = \rho_s R T_s$ and $p_I = \rho_I R T_I$, where the subscript, s, refers to standard atmospheric conditions. Thus

$$\hat{\rho}_I \equiv g\rho_I/\rho_s = (p_I/p_s)(T_s/T_I)g \tag{23}$$

3. Summary of Data Analysis

The data analysis can be summarized as follows:

(1) $$\hat{k}_{II} = (1/\sigma)\left[\hat{k}_I - \ln(I_{II}/I_I)/k_o^m \hat{\rho}_I l\right] \tag{14}$$

(2) σ and T_{II} were obtained from figure 32

(3) $\hat{k}_I$ was obtained from figure 19

(4) I_{II}/I_I was evaluated from the oscilloscope records

(5) $$\hat{\rho}_I = (p_I/p_s)(T_s/T_I)g \tag{23}$$

(6) the absorption path length, l, was always 2.54 centimeters

(7) λ, T_I and p_I were recorded at the time the data were taken

Presentation of Experimentally Measured Absorption Coefficients

Cross plots of $\hat{k}$ as a function of temperature at 1300, 1350,.. 1750 A were prepared from the IBM results shown on figure 19. These

plots are shown on figure 36 and serve as a comparison background for the experimental values of $\hat{k}$, that is, $\hat{k}_{II}$ from equation (14). Each of the experimental points which appear on this figure represents a shock tube run taken under known initial conditions and at the wavelength shown. The results are discussed in chaper IV.

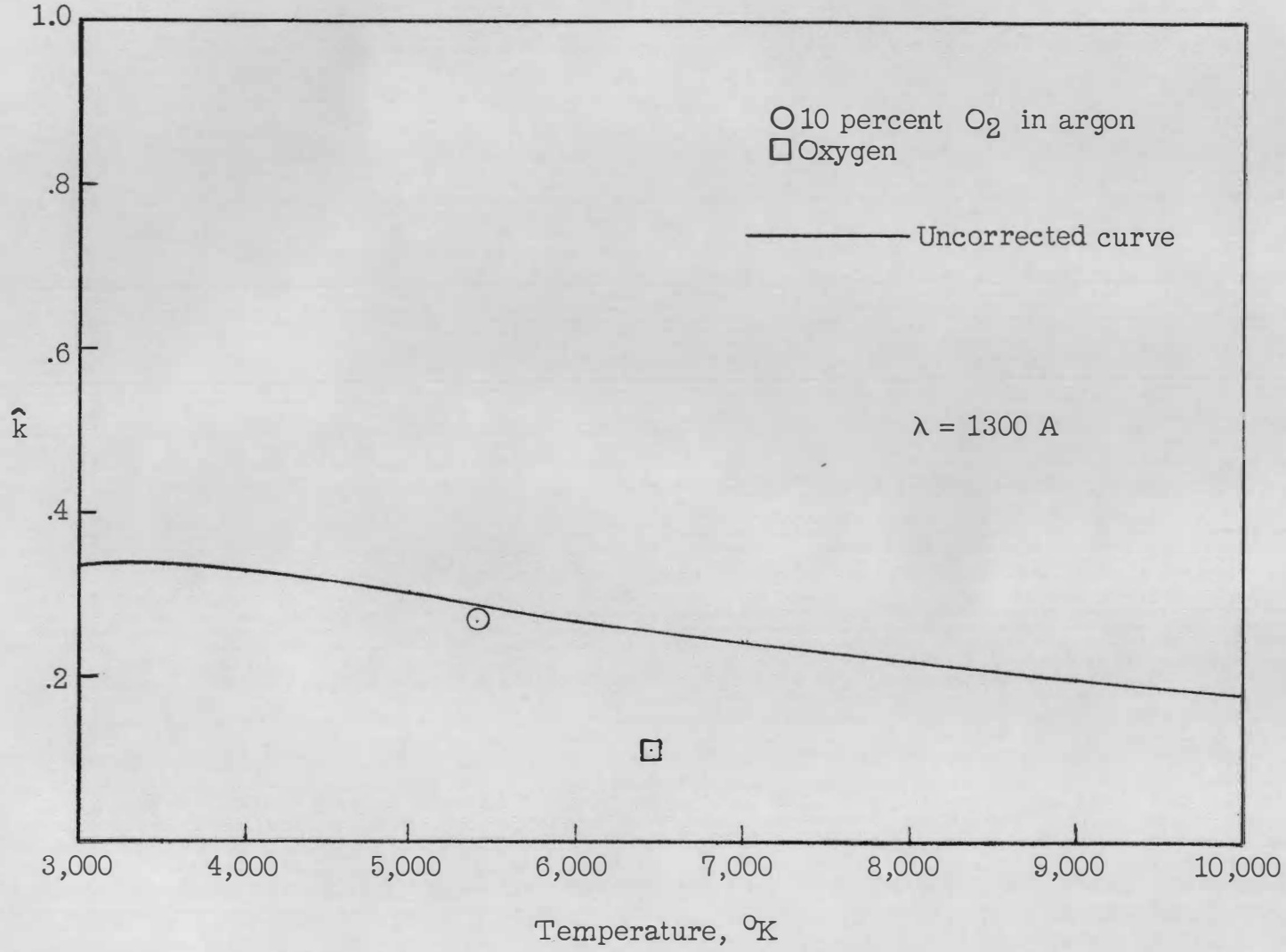

Figure 36(a).- Absorption coefficient of molecular oxygen as a function of temperature at selected wavelengths.

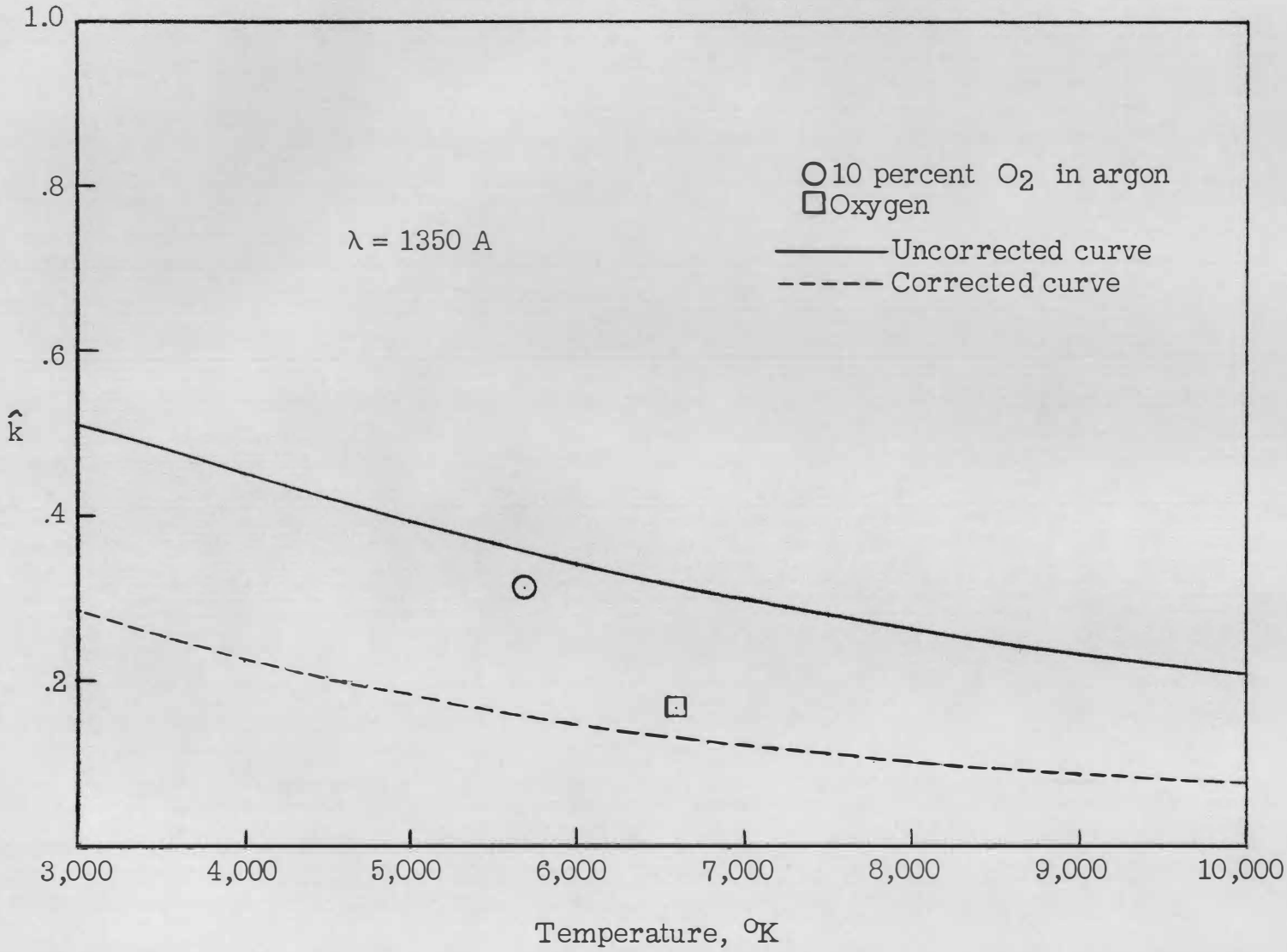
1.0
.8
.6
.4
.2
$\hat{k}$
λ = 1350 A
10 percent O_2 in argon
Oxygen
Uncorrected curve
Corrected curve
3,000
4,000
5,000
6,000
7,000
8,000
9,000
10,000
Temperature, °K

Figure 36(b).

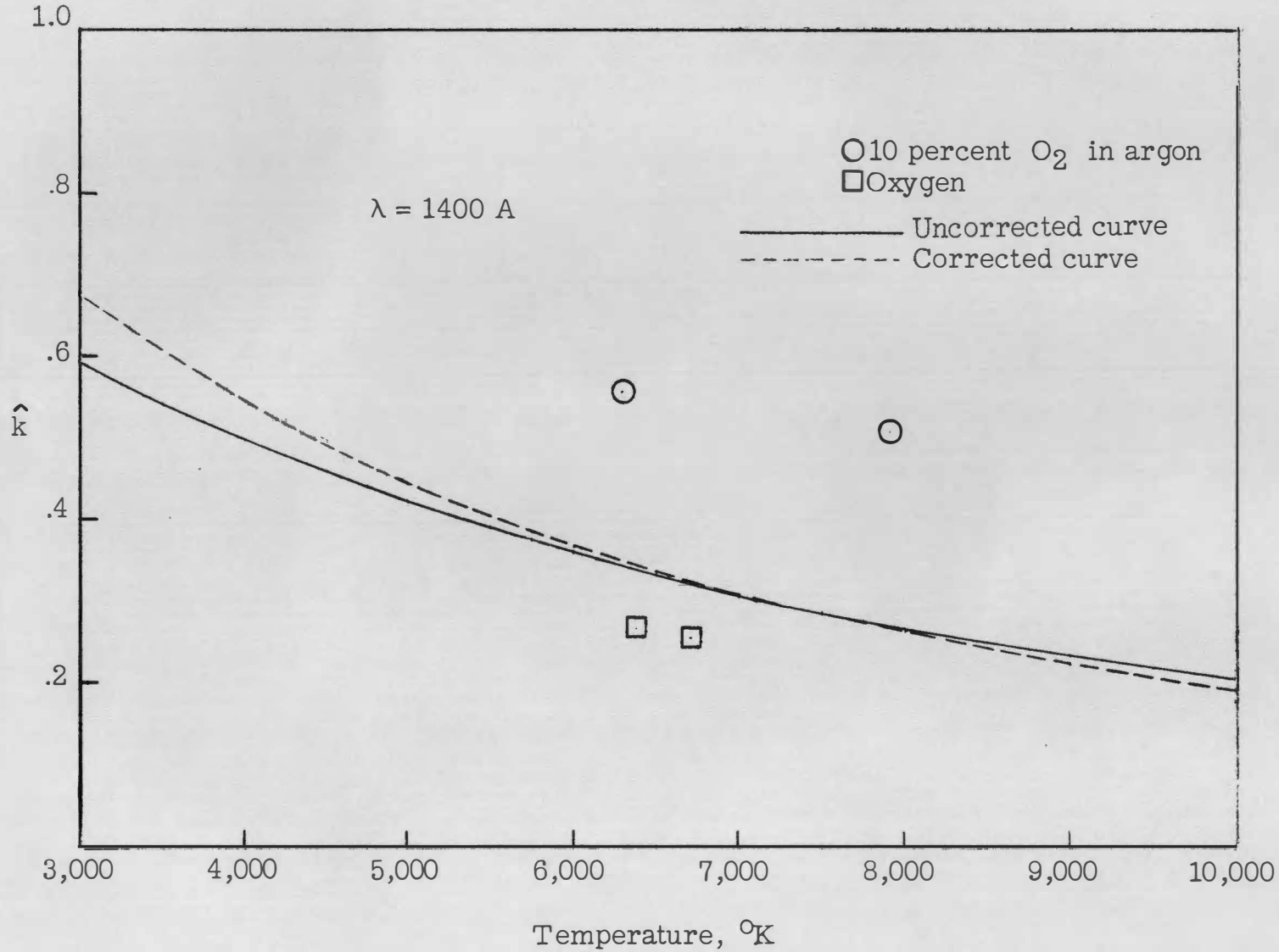
1.0
.8
.6
.4
.2
$\hat{k}$
λ = 1400 A
10 percent O_2 in argon
Oxygen
Uncorrected curve
Corrected curve
3,000
4,000
5,000
6,000
7,000
8,000
9,000
10,000
Temperature, °K

Figure 36(c).

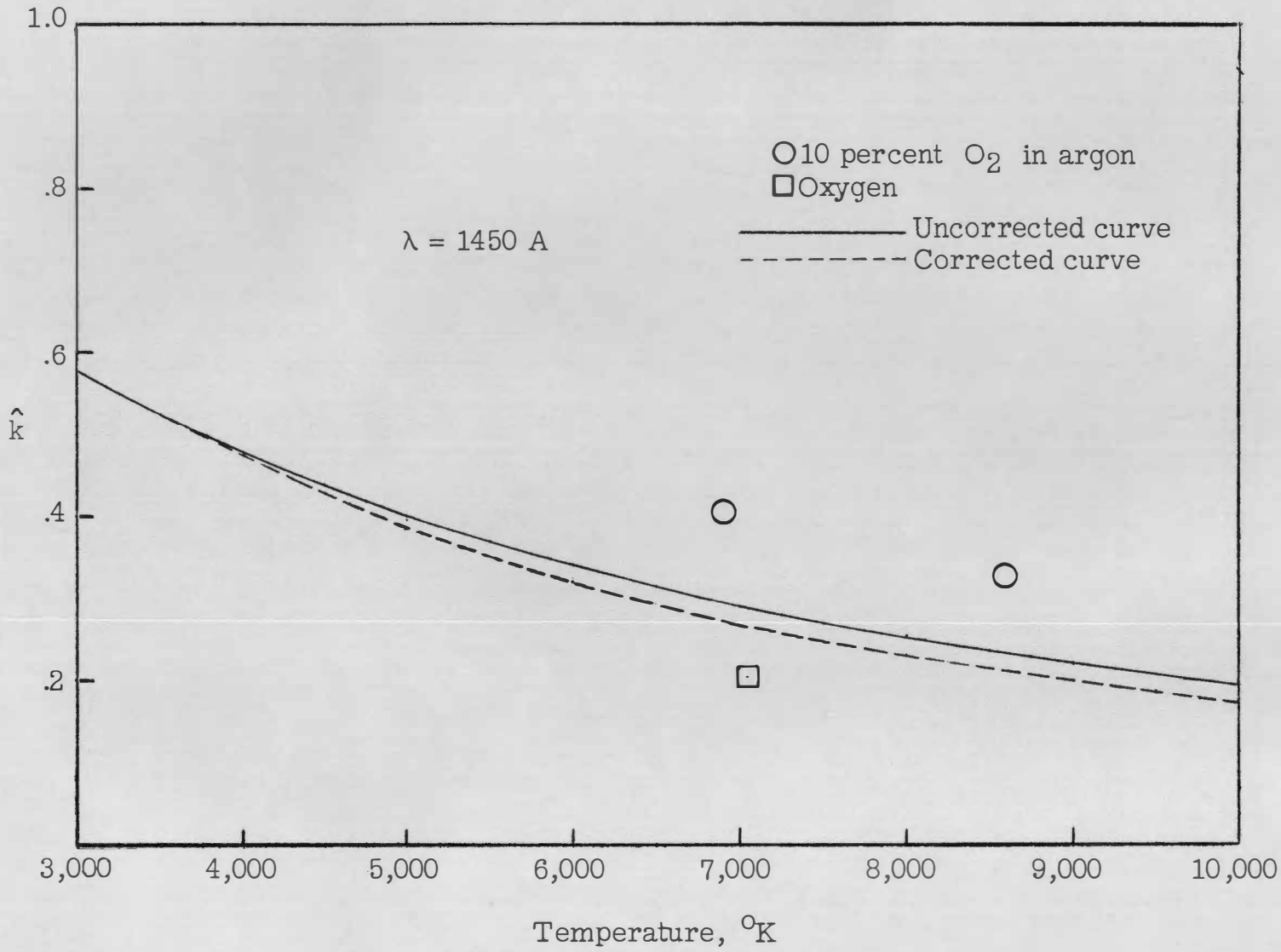
1.0
.8
.6
.4
.2
$\hat{k}$
λ = 1450 A
10 percent O_2 in argon
Oxygen
Uncorrected curve
Corrected curve
3,000
4,000
5,000
6,000
7,000
8,000
9,000
10,000
Temperature, °K

Figure 36(d).

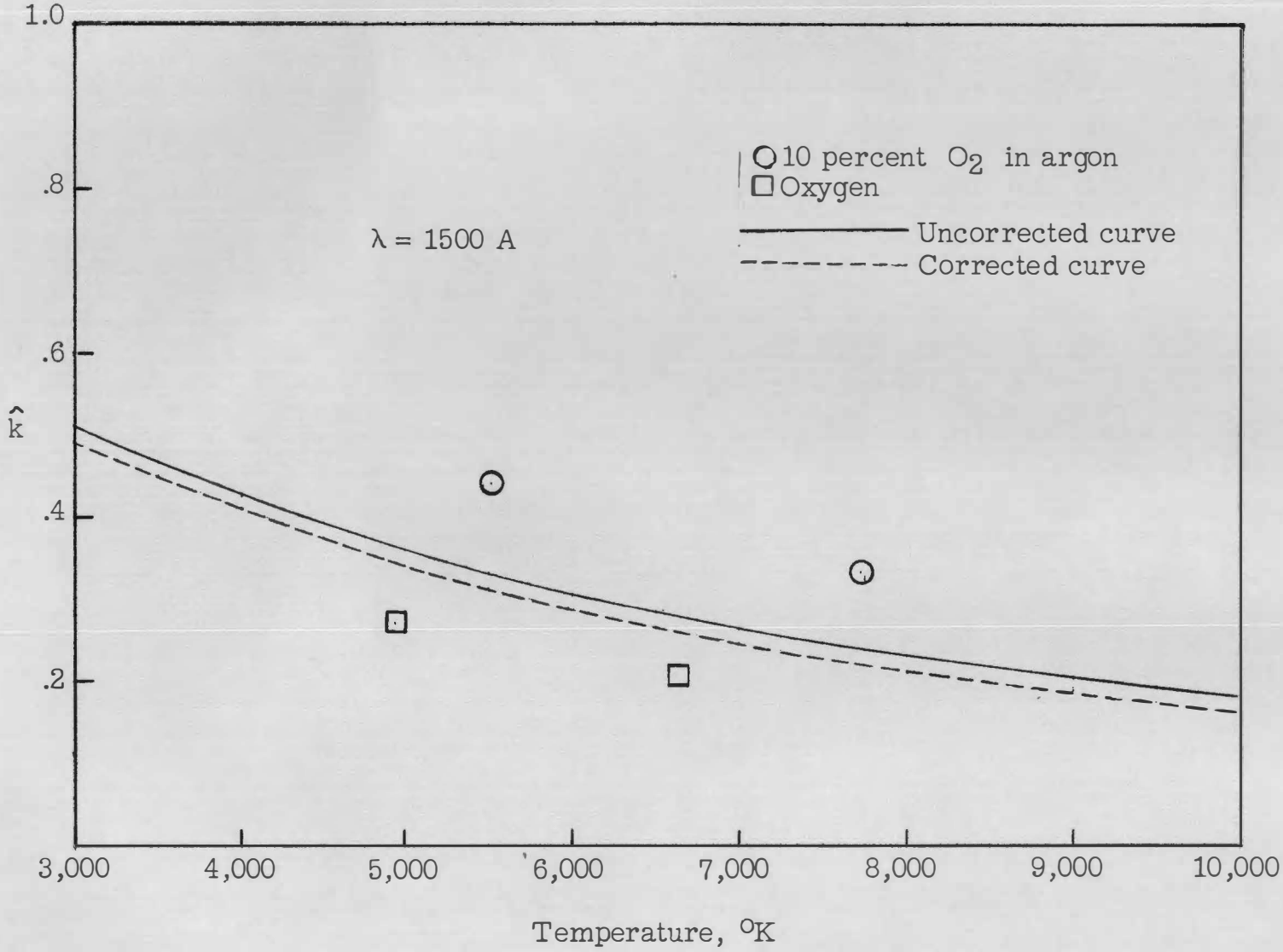
1.0
.8
.6
.4
.2
$\hat{k}$
λ = 1500 A
10 percent O_2 in argon
Oxygen
Uncorrected curve
Corrected curve
3,000
4,000
5,000
6,000
7,000
8,000
9,000
10,000
Temperature, °K

Figure 36(e).

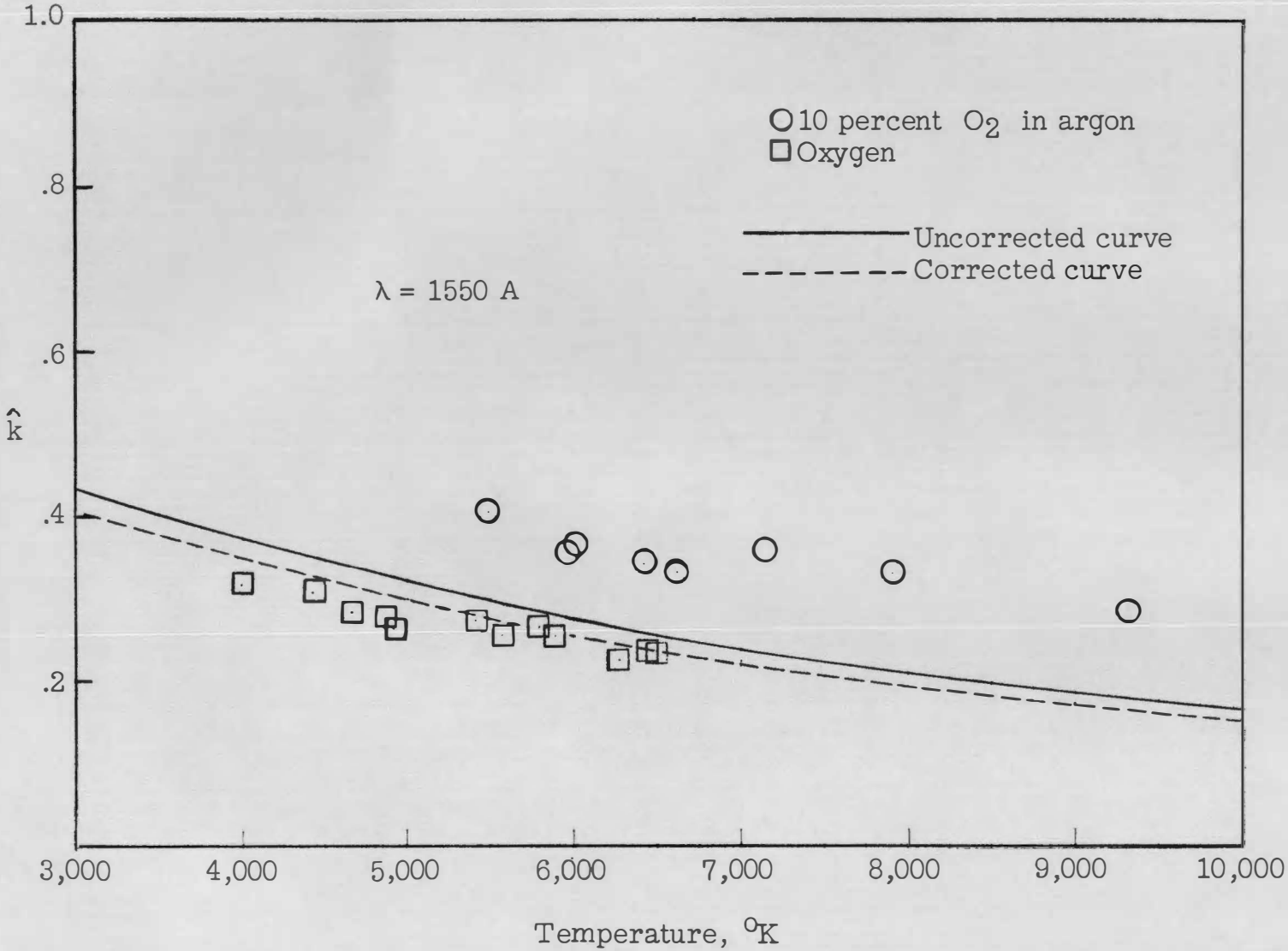
1.0
.8
.6
.4
.2
$\hat{k}$
10 percent O_2 in argon
Oxygen
Uncorrected curve
Corrected curve
λ = 1550 A
3,000
4,000
5,000
6,000
7,000
8,000
9,000
10,000
Temperature, °K

Figure 36(f).

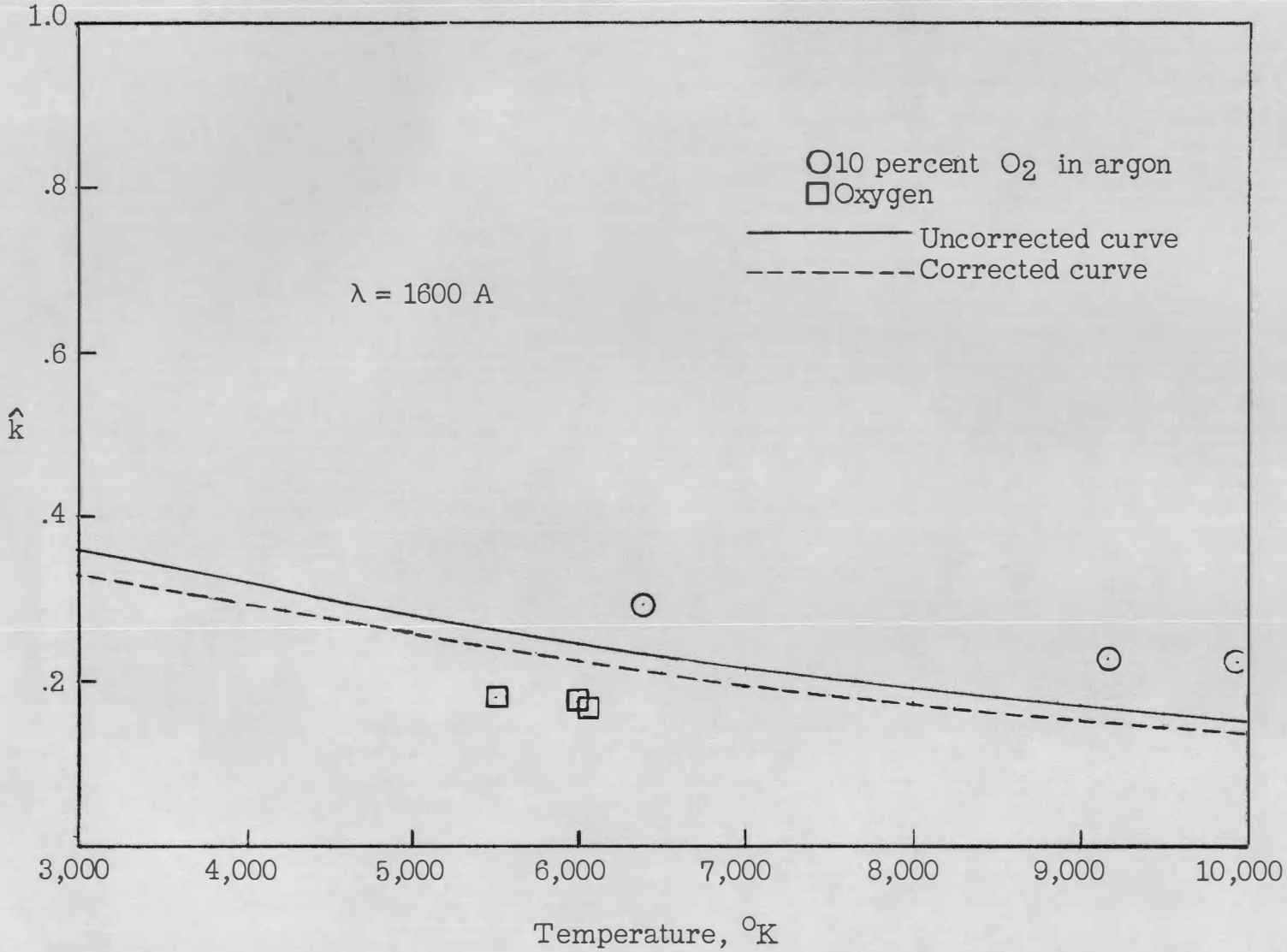
1.0
.8
.6
.4
.2
$\hat{k}$
○10 percent O_2 in argon
□Oxygen
Uncorrected curve
Corrected curve
λ = 1600 A
3,000
4,000
5,000
6,000
7,000
8,000
9,000
10,000
Temperature, °K

Figure 36(g).

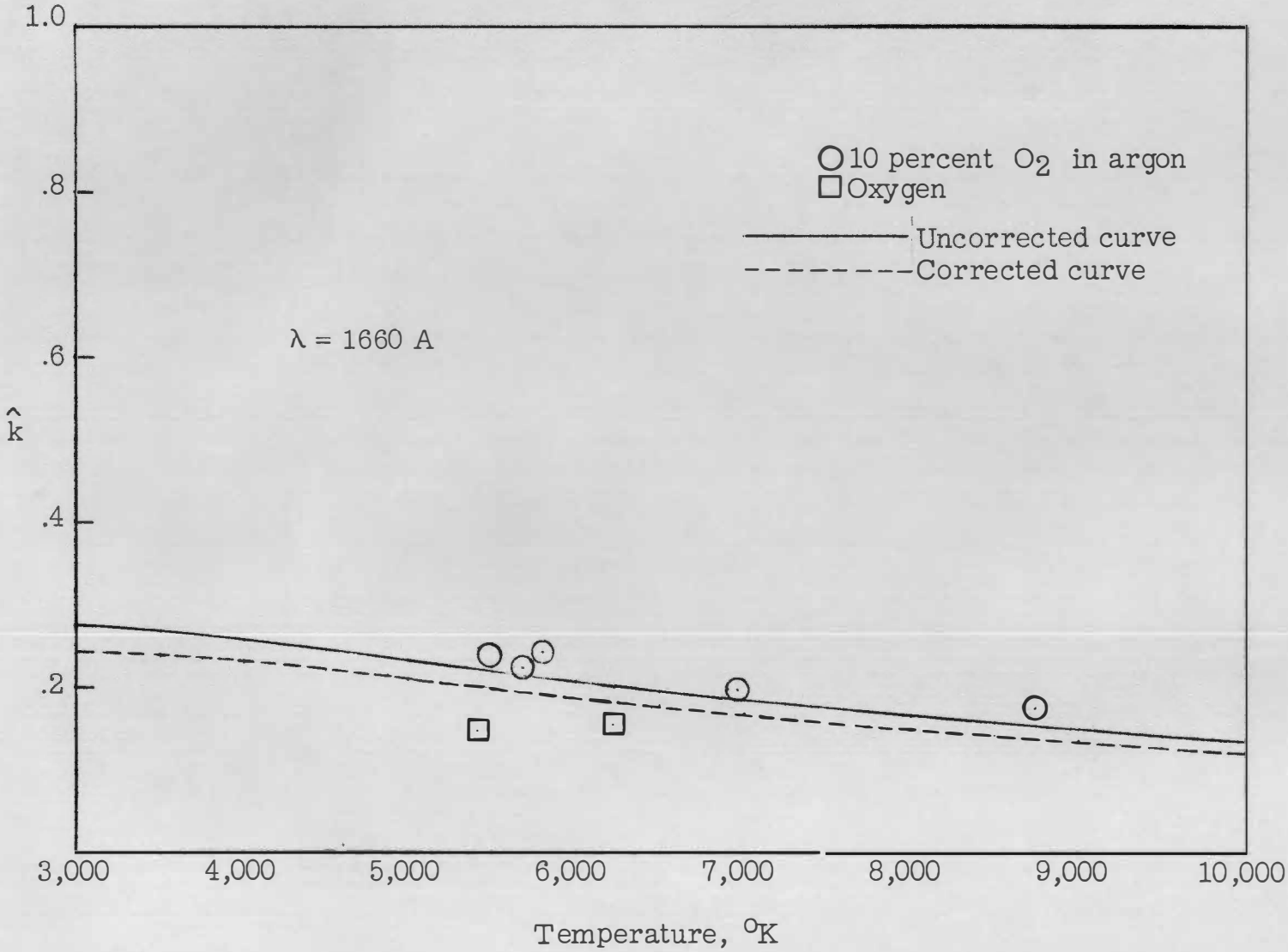
1.0
.8
.6
.4
.2
$\hat{k}$
10 percent O_2 in argon
Oxygen
Uncorrected curve
Corrected curve
λ = 1660 A
3,000
4,000
5,000
6,000
7,000
8,000
9,000
10,000
Temperature, °K

Figure 36(h).

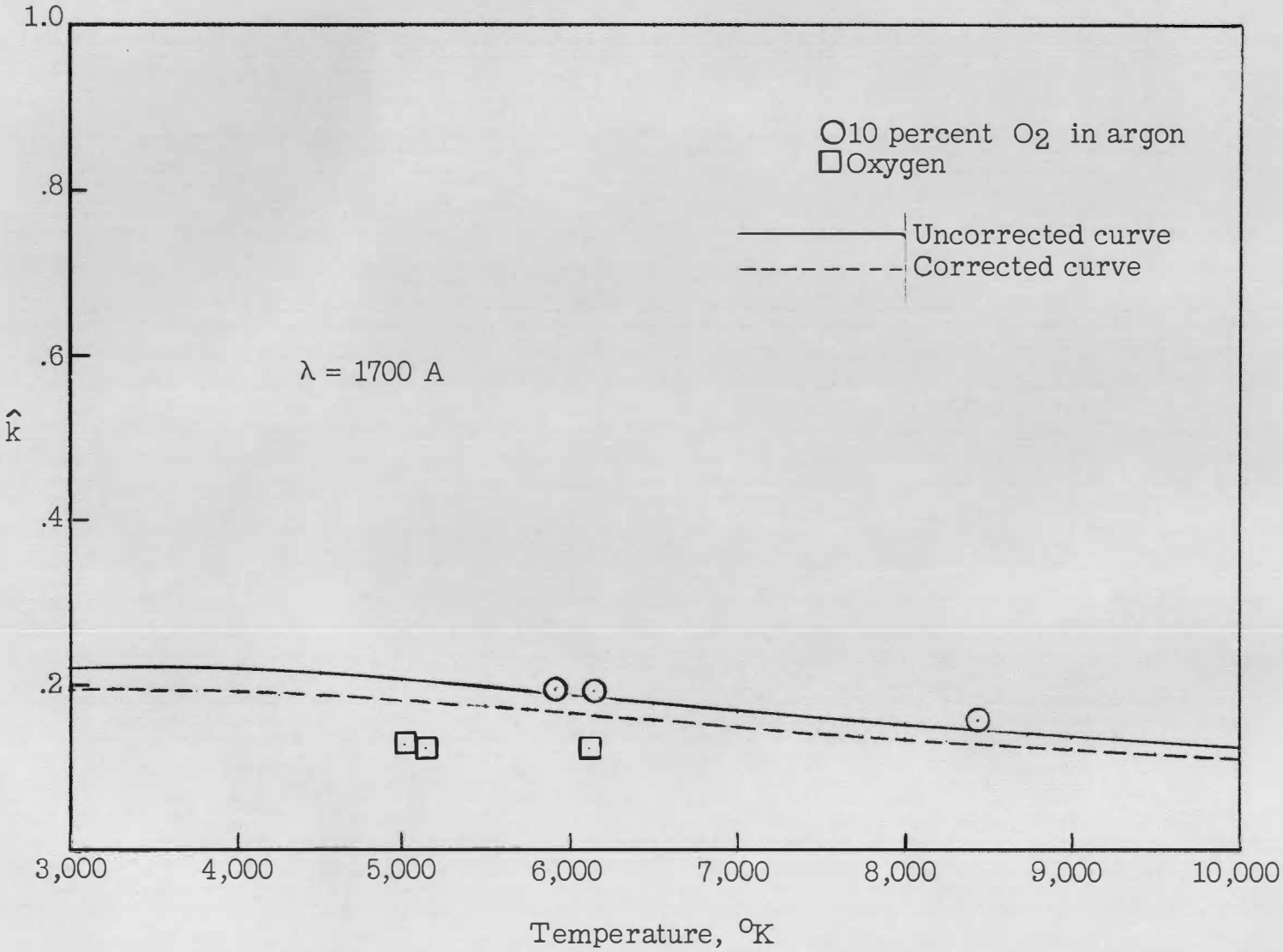
1.0
.8
.6
.4
.2
$\hat{k}$
10 percent O_2 in argon
Oxygen
Uncorrected curve
Corrected curve
λ = 1700 A
3,000
4,000
5,000
6,000
7,000
8,000
9,000
10,000
Temperature, °K

Figure 36(i).

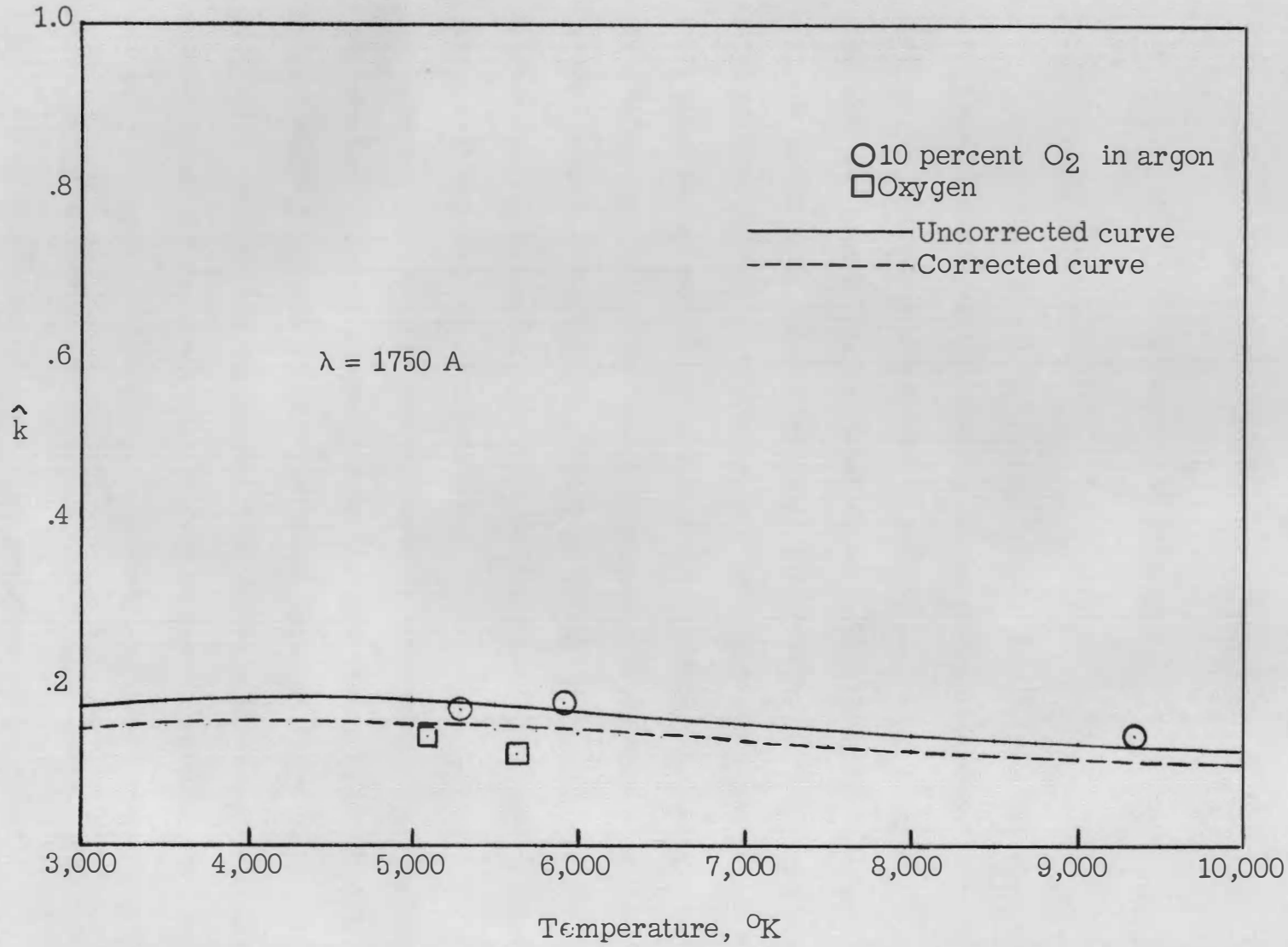
1.0
.8
.6
.4
.2
$\hat{k}$
○10 percent O_2 in argon
□Oxygen
Uncorrected curve
Corrected curve
λ = 1750 A
3,000
4,000
5,000
6,000
7,000
8,000
9,000
10,000
Temperature, °K

Figure 36(j).

CHAPTER IV

DISCUSSION OF RESULTS AND CONCLUSIONS

Discussion of Results

1. Preliminary Remarks

As was pointed out in chapter I, both theoretical and experimental approaches were made to the problem of determining the effect of temperature on the absorption coefficient. The Franck-Condon principle which underlies the theoretical treatment is well established and has proved over the years to be capable of accurate prediction of transition probabilities when all the pertinent factors are known and properly accounted for. From the outset the intention of the present investigation was to discover the general nature of the temperature dependence from the theoretical treatment and then to attempt to verify or to disprove the results by experimental measurement of the absorption in a shock tube. This program was carried out satisfactorily.

At most wavelengths and temperatures the agreement between theory and experiment is good enough to show that the theory is essentially correct and a plausible explanation of the areas of disagreement is available. Because of experimental uncertainties and the possibility of systematic errors the corrected IBM results were selected as the best available estimate of the absorption coefficient except in the areas where experiment showed definite disagreement with theory. Empirical curves based chiefly on the observed absorption were prepared for use in these areas.

2. Comparison of Theory and Experiment at Room Temperature

a. Plotted theoretical and experimental results. The three curves on figure 37(a) show the results of the three theoretical calculations at 300° K. These are the same curves which are shown on figure 16. Since the experimental results did not include any values of the absorption coefficient at room temperature, the literature data shown on figure 2 were replotted on figure 37(a) for comparison to the theory.

On figure 37(b) the literature data are compared to the IBM theoretical curve both with and without the empirical correction for variation of the electronic transition probability with internuclear distance.

b. The wavelength corresponding to maximum absorption. On figure 37(a) the wavelength at which maximum absorption occurs is 1450 A for the IBM curve and is 1455 A for the other two. Figure 37(b) shows that the corrected IBM curve has a very flat peak centered at about 1430 A. The experimental peak lies somewhere between 1400 A and 1475 A and thus does not distinguish between the calculated peak values.

c. The long wavelength side of the curve (1450 A to 1750 A). Theory and experiment agree well in this region. However, the scatter of the experimental points is too great to permit a choice to be made between the various theories.

d. The short wavelength side of the curve (1300 A to 1450 A). Except for the corrected IBM curve theory and experiment do not agree in this region. Note that the absorption coefficients measured by three independent investigators show the rapid drop of the experimental points

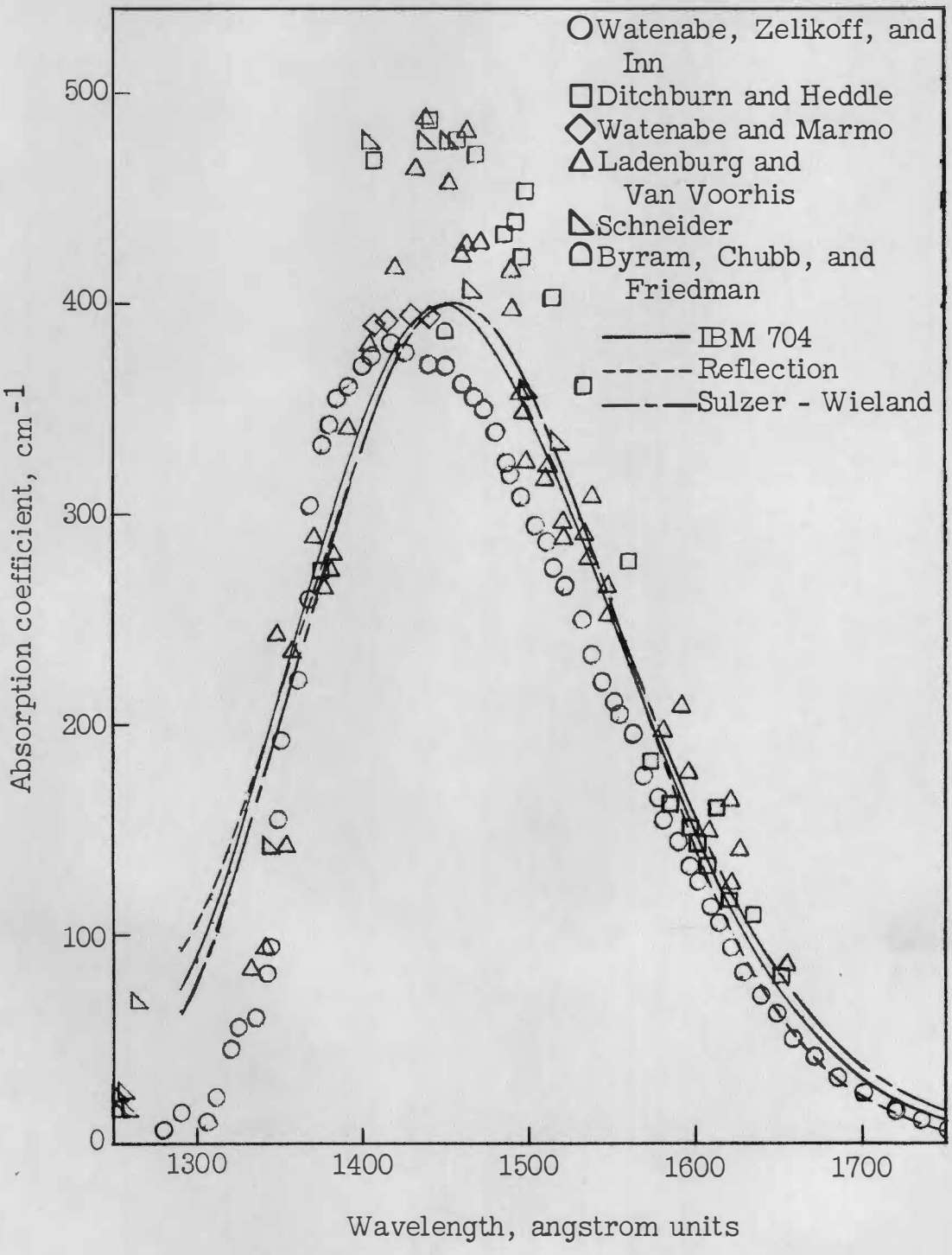

Figure 37(a).- Absorption coefficient of molecular oxygen; comparison of theory and experiment at 300° K.

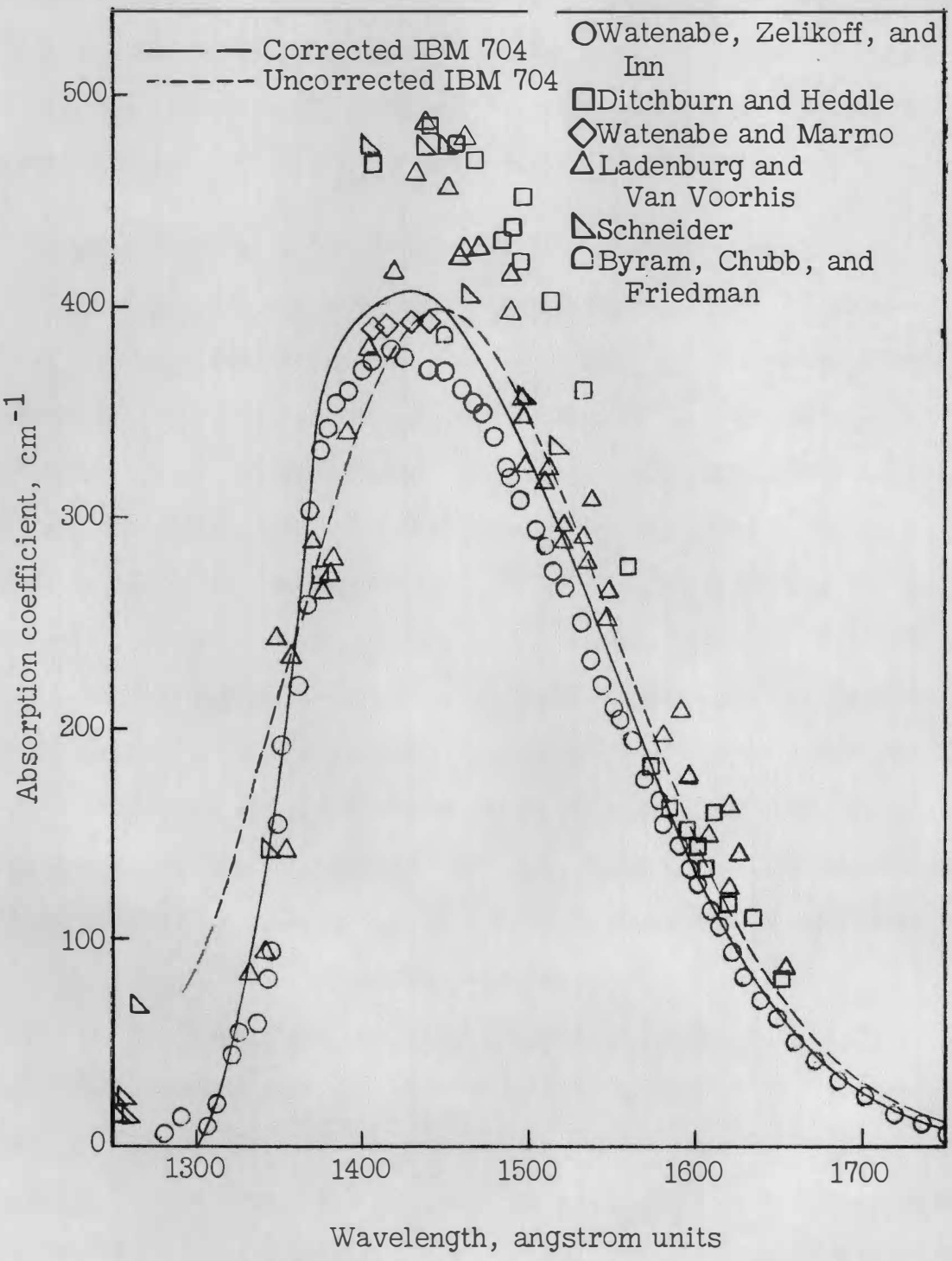
Corrected IBM 704
Uncorrected IBM 704
Watenabe, Zelikoff, and Inn
Ditchburn and Heddle
Watenabe and Marmo
Ladenburg and Van Voorhis
Schneider
Byram, Chubb, and Friedman
Absorption coefficient, cm-1
0
100
200
300
400
500
1300
1400
1500
1600
1700
Wavelength, angstrom units

Figure 37(b).

on the short wavelength side. This is convincing evidence that the deviation from the theoretical curves on figure 37(a) is real.

Little significance can be attached to the agreement on figure 37(b) between the corrected IBM curve and the data because the correction was designed to make the curve fit the room temperature data.

3. Comparison of Theory and Experiment at High Temperature

a. Plotted theoretical and experimental results. The experimental results at high temperature are shown on figure 36. As was mentioned in chapter III, the solid curves are cross plots of $\hat{k}$ against temperature and are based on the uncorrected IBM calculations. The dotted curves are the same except for the application of the empirical correction factor shown on figure 17. No dotted curve is shown on figure 36(a) because the corrected IBM value of $\hat{k}$ is zero at all temperatures for $\lambda = 1300$ A.

Some of the shock tube runs were not suitable for the determination of $\hat{k}$ because molecular vibration was not in equilibrium behind the shock front. Such runs are not shown on figure 36. All runs were plotted on figures 33, 34, and 35, however. The next section explains how the plots on the latter figures were used to determine which runs should be excluded because of the lack of vibrational equilibrium.

b. Determination of which runs have vibrational equilibrium. The description of data analysis procedure given in chapter III pointed out that the σ and T_{II} values appropriate for the calculation of $\hat{k}$ from equation (14) depended upon the state of vibrational excitation of the components of the gas mixture being tested. The comparison of observed light transmission to that expected on the basis of the two or three

possible states of vibrational excitation is the most important single indication of the actual state of the gas but is sometimes ambiguous and misleading when unsupported by additional evidence.

The data on air shown on figure 35 are a good example of this. The four points from the literature plotted on figure 35(a) seem to show that oxygen and nitrogen vibration are both fully excited for all four points but examination of the oscilloscope records revealed relaxation regions behind the fronts of the two slowest shock waves which must be interpreted as nitrogen vibrational relaxation because of the direction of the adjustment[80]. This makes the slight upswing of the low speed points toward the "O_2 vibration excited" curve appear significant. This conclusion is supported by the measured points on figure 35(b). The runs shown there were obtained at $M_I = 10.1$ or below and, as expected, most of them are clustered close to the "O_2 vibration excited" curve. The nitrogen vibrational adjustment was visible on all these records. No values for $\hat{k}$ were obtained from the air records because the state of the gas behind the shock front was not well defined.

Vibrational relaxation of oxygen was observed on only two of the air records. These are the two lowest points on figure 35(b) and are labeled 5.25 and 9.50. Note that these two points lie close to the "O_2 and N_2 excited" curve only by coincidence.

Figure 33(f) shows that between $M_I = 7$ and $M_I = 8$ in oxygen-argon mixtures the points turned toward the constant γ curve, indicating that oxygen vibration was not in equilibrium. The vibrational adjustment was clearly visible on the corresponding records but the observed relaxation times were about three to four times as long as the calculated times.

Camac and others[81] reported that argon was only one tenth as effective as oxygen for exciting oxygen vibration, as compared to the factor one-third[82] used here. Recalculation of the relaxation times using the smaller factor gave better agreement, since it approximately doubled the calculated relaxation times. Thus the observed times support the efficiency factor reported by Camac and others.

Vibrational relaxation was not observed on any of the records taken in pure oxygen. Also the points on figure 34(f) do not turn toward the constant γ curve as they did on figure 33(f). These two statements both indicate that vibrational relaxation of pure oxygen was too fast to observe on the records taken. As was mentioned previously, the inability of the shock detector stations to function properly below about 4,000° K prevented the determination of the region where they bend toward the constant γ curve.

The calculated vibrational relaxation times do not entirely support the above conclusion. In some cases they indicate that the vibrational adjustment should have been visible. For example, at $M_I = 9.06$ on figure 34(f) the calculated time is 1.26 microseconds. In view of the experience gained in interpreting the oxygen-argon records so slow an adjustment should have been detectable. Since it was not, the calculated times were assumed to be in error.

The net effect of the above observations relating to vibrational adjustments was to cause all the air records and all the oxygen-argon records below $M_I = 8$ to be rejected. It was not necessary to reject any of the oxygen runs, although a similar limitation no doubt exists.

c. Correction of data for the presence of dissociation behind the shock front. It was pointed out in chapter III that the transit time of the shock waves over the 1 millimeter width of the ultraviolet light beam was 0.2 to 0.5 microsecond. Unfortunately, these times are long enough to permit some dissociation of molecular oxygen into atomic oxygen, particularly at the higher temperatures. To account for this the calculation of $\hat{k}_{II}$ from equation (14) was modified as follows:

(1) Plots of σ and T_{II} similar to those shown on figure 32 were prepared for partially dissociated mixtures. Oxygen vibration was assumed to be fully excited.

(2) The dissociation rate of oxygen was combined with the σ, T_{II}, and degree of dissociation relations obtained from the plots to calculate the state of the gas as a function of distance from the shock front. The rates used were obtained from a separate investigation in which the same records which were used for the determination of the absorption coefficient were also analyzed for the dissociation rate of oxygen. Comparison of these rates with a rate equation given by Matthews[83] showed satisfactory agreement even at temperatures considerably higher than 5,000° K, which was the upper temperature limit for his experimental determination of the rate.

(3) While the shock wave was passing through the light beam the trace on the oscilloscope rose too rapidly to be recorded. Therefore the observed jump in absorption on the record corresponded to the instant the shock wave left the light beam.

(4) Since the gas behind the shock front was flowing in the direction in which the shock wave was moving and at nearly the same speed, the gas within the 1 millimeter thickness of the light beam was made up not only of the gas originally there but also contained all the gas which was originally in a considerable length of the shock tube preceding the test section. The ratio of these lengths was closely related to, but not quite proportional to, the compression ratio across the shock front.

(5) The 1 millimeter distance immediately behind the shock front was divided into several zones of unequal width. Zone width was determined so that an equal amount of dissociation occurred in each zone.

(6) Corrected IBM values of $\hat{k}$ and appropriate values of σ, T_{II}, and degree of dissociation were used to compute the light transmission in each zone and a weighted average of the calculated light transmission through the shock tube window was obtained by using the zone widths as weighting factors. Below 1375 A uncorrected IBM values were used for $\hat{k}$. Since the temperature dependence of $\hat{k}$ was important to the calculation rather than the magnitude, the uncorrected values were thought to be better suited to the calculation in the wavelength range where the correction factor was considered unreliable.

(7) The weighted average light transmission was compared to transmission calculated for gradually increasing dissociation on

the assumption of uniform gas properties in the volume defined by the beam. The σ, T_{II}, and degree of dissociation values for the uniform sample which gave the same transmission as the weighted average were used for the calculation of $\hat{k}_{II}$ in equation (14).

d. Discussion of the general nature of the high temperature results. Certain general characteristics of the observed data can be brought out more clearly if they are noted before becoming involved in the discussions of the individual mixtures. An examination of figure 36 reveals that:

(1) The values of $\hat{k}$ obtained from the oxygen-argon mixtures are always larger than those obtained from pure oxygen. This follows a definite pattern at all wavelengths and temperatures. The data from either gas are internally consistent but disagree when compared with each other.

(2) The excess of $\hat{k}$ varies with wavelength and is generally larger percentage-wise at the shorter wavelengths.

(3) The excess of $\hat{k}$ varies little, if any, with temperature.

(4) Above 1375 A, which is the wavelength at which the slope of the correction factor changes abruptly, the oxygen points agree reasonably well with the corrected IBM curves. Most of them lie somewhat below the curves, but many of the points at 1550 A, where maximum accuracy was obtained because of the intense ultraviolet light available, agree nicely with the theory.

(5) The corrected IBM theory, which at the higher wavelengths stays quite close to the uncorrected curve, falls far below it at

wavelengths shorter than 1375 A. Both the oxygen and the oxygen-argon points show a tendency to follow this trend but do not go as far. This effect tends to confirm the suspicion voiced earlier that the empirical correction is not valid below 1375 A.

e. Discussion of the oxygen-argon results. The following observations about the oxygen-argon results are based on an examination of figure 36:

(1) The distribution of the points agrees with the shape of the theoretical curves.

(2) With few exceptions the points fall above the theoretical curves, indicating stronger absorption than theory predicts.

(3) This departure is very large in the central range of wavelengths from 1400 A to 1600 A.

(4) The experimental scatter is about ±6 per cent, as judged from the points on figure 36(g).

The departure of the experimental oxygen-argon points from the theoretical curves far exceeds the estimated errors in measurement, which are discussed later in this chapter. Since the oxygen points agree fairly well with theory extra absorption in addition to that due to oxygen is believed to have been present in the oxygen-argon measurements. The cause of this extra absorption was not definitely identified, although it is believed to be due to high temperature argon. The following observations support this conclusion:

(1) No absorption was detected at room temperature in argon.

(2) Several shock tube runs were taken in pure argon and the absorption jumps which were observed at the shock front were of the correct order of magnitude to explain the discrepancies previously mentioned. The argon used was tested for oxygen content and was found to contain less than 0.1 per cent oxygen.

(3) Analysis of the records in connection with the separate investigation of the dissociation rate of oxygen revealed residual absorption of about the magnitude expected on those portions of the traces where oxygen was fully dissociated into atoms and was therefore not absorbing.

(4) Examination of the energy level diagram[84] for argon shows that room temperature argon does not absorb at wavelengths longer than 1048 A. Absorption at longer wavelengths is possible from the excited states.

(5) The observed extra absorption appears to be a continuum, since its intensity changes slowly with wavelength. This indicates that the mechanism responsible probably leads to ionization because jumps between discrete levels would necessarily lead to a discrete absorption spectrum.

f. Discussion of the oxygen results. The following observations about the oxygen results are based on an examination of figure 36:

(1) The distribution of the points agrees with the shape of the theoretical curves.

(2) Most of the points fall close to both the corrected and uncorrected IBM curves, although they seem to favor the corrected curves.

(3) The experimental scatter is about ±8 per cent, as judged from the points on figure 36(g).

At 1300 A and 1350 A the corrected curves depart markedly from the uncorrected curves in the direction of smaller $\hat{k}$ values. The oxygen points also depart sharply from the uncorrected curves at these wavelengths and in the same direction. However, the experimental points do not go as far toward smaller $\hat{k}$ as do the corrected curves.

As was pointed out in chapter I, the correction factor which appears on figure 17 is on uncertain ground below 1375 A due to the belief that the sudden change in slope which occurs there is caused by some other factor than the variation of the electronic transition probability with internuclear distance. Thus the method used to apply the correction factor to the excited vibrational states above 1375 A is not expected to apply below 1375 A.

Nevertheless, the effect is known to affect the absorption of molecules in the ground vibrational state, and these still make up the majority of the gas even at high temperature. The way in which the disturbance affects the higher vibrational states is simply not known.

g. Best estimate of $\hat{k}$ at high temperature. The following conclusions were reached on the basis of all available information:

(1) Above 1375 A the corrected IBM results were considered to be the best estimate of the high temperature absorption coefficient of oxygen.

(2) Below 1375 A empirically determined curves corresponding to $\hat{k}$ values intermediate between the corrected and uncorrected IBM curves were considered to be the best estimate.

The composite "best estimate" values of $\hat{k}$ as functions of temperature and wavelength are listed in table I. The "corrected" and "uncorrected" IBM results are also listed there.

4. Discussion of Experimental Errors

Each of the quantities affecting the experimental values of $\hat{k}$ will be considered in turn. Except for λ and T_{II} they are all contained in equation (14).

a. Error in wavelength measurements. On the basis of the experience gained in operating the monochromator, the wavelength settings were reproducible to ±6A. The band-pass width was 11A and maximum intensity occurred at the central wavelength. Since k varies slowly with wavelength the average absorption coefficient over the 11A band was believed to be a good approximation to the value at the central wavelength. The error in the wavelengths quoted for each run is believed to be no more than ±10A.

b. Error in temperature measurements. The high temperature, T_{II}, was obtained from the measured shock Mach number, M_I, using the plots shown on figure 32. The errors in the M_I values are discussed separately and lead to an uncertainty in M_I of 1.7 per cent. The corresponding maximum uncertainty in T_{II} as read from figure 32 is 2.5 per cent.

The plots on figure 32 are themselves subject to approximately 1 per cent uncertainty due to the use of a graphical solution of equations (19) and (22).

TABLE I

THE ABSORPTION COEFFICIENT OF OXYGEN AT SELECTED WAVELENGTHS AND TEMPERATURES

°K	(a) $\hat{k}$ (best estimate)									
T	1300	1350	1400	1450	1500	1550	1600	1660	1700	1750
300	0.090	0.500	0.985	0.995	0.822	0.583	0.335	0.135	0.060	0.018
1,000	.130	.480	.940	.906	.744	.550	.351	.180	.104	.053
2,000	.172	.435	.808	.718	.590	.471	.353	.229	.170	.112
3,000	.200	.371	.674	.580	.491	.407	.328	.242	.198	.143
4,000	.201	.304	.544	.472	.410	.348	.292	.230	.188	.148
5,000	.173	.251	.445	.385	.340	.300	.260	.210	.180	.147
6,000	.158	.210	.368	.320	.286	.253	.224	.190	.165	.137
7,000	.131	.185	.306	.268	.244	.220	.197	.168	.150	.130
8,000	.110	.161	.262	.230	.211	.192	.173	.150	.135	.117
9,000	.093	.142	.221	.200	.190	.172	.154	.134	.121	.107
10,000	.078	.122	.192	.172	.162	.152	.138	.121	.111	.098

TABLE I.- (Continued)

THE ABSORPTION COEFFICIENT OF OXYGEN AT SELECTED WAVELENGTHS AND TEMPERATURES

°K	(b) Corrected $\hat{k}$ values from IBM 704 calculations									
T	1300	1350	1400	1450	1500	1550	1600	1660	1700	1750
300	0	0.425	0.985	0.995	0.822	0.583	0.335	0.135	0.060	0.018
1,000		.420	.940	.906	.744	.550	.351	.180	.104	.053
2,000		.350	.808	.718	.590	.471	.353	.229	.170	.112
3,000		.280	.674	.580	.491	.407	.328	.242	.198	.143
4,000		.222	.544	.472	.410	.348	.292	.230	.188	.148
5,000		.185	.445	.385	.340	.300	.260	.210	.180	.147
6,000		.149	.368	.320	.286	.253	.224	.190	.165	.137
7,000		.124	.306	.268	.244	.220	.197	.168	.150	.130
8,000		.102	.262	.230	.211	.192	.173	.150	.135	.117
9,000		.089	.221	.200	.190	.172	.154	.134	.121	.107
10,000		.079	.192	.172	.162	.152	.138	.121	.111	.098

TABLE I.- (Concluded)

THE ABSORPTION COEFFICIENT OF OXYGEN AT SELECTED WAVELENGTHS AND TEMPERATURES

^{o}K	(c) Uncorrected $\hat{k}$ values from IBM 704 calculations									
T	1300	1350	1400	1450	1500	1550	1600	1660	1700	1750
300	0.216	0.545	0.862	1.00	0.870	0.625	0.370	0.158	0.075	0.028
1,000	.250	.557	.824	0.903	.781	.588	.387	.205	.124	.066
2,000	.297	.550	.706	.712	.621	.508	.387	.259	.200	.138
3,000	.335	.509	.594	.578	.510	.434	.358	.273	.222	.172
4,000	.328	.451	.498	.479	.426	.373	.319	.258	.219	.180
5,000	.304	.391	.422	.400	.361	.320	.280	.232	.204	.174
6,000	.271	.340	.360	.338	.306	.275	.245	.208	.187	.162
7,000	.245	.298	.306	.290	.263	.238	.215	.186	.168	.149
8,000	.219	.261	.268	.254	.230	.209	.190	.164	.152	.136
9,000	.199	.232	.234	.220	.204	.186	.170	.151	.138	.125
10,000	.180	.209	.207	.196	.180	.164	.150	.133	.125	.115

To evaluate the effect of the lack of precise knowledge of the enthalpy at high temperature the uncertainty produced in equation (19) by 3 per cent uncertainty in η was calculated[85] to be 0.67 per cent in a typical case. The enthalpy values used for temperatures below 5,000° K were good to 2.6 per cent[86]. The source[87] used for the higher temperatures did not state the precision of their results but the values given joined smoothly with the low temperature values.

The T_{II} values read from the plot were corrected in each case for variation of T_I from the standard value of 300° K used in preparing the plots. The T_I values were correct to 0.4 per cent.

The largest correction to T_{II} for the presence of dissociation behind the shock front was 2,932° K. The precision of this correction was difficult to estimate but was probably no worse than 10 per cent of the correction.

On the basis of the above discussion the uncertainty in T_{II} is believed to be about 4 per cent.

c. Error in measuring the Mach number. The shock Mach number, M_I, is a dimensionless velocity and was determined from the time required to go a distance of 10 inches ±0.1 inch. The test window was located at the center of the 10-inch distance. The shock speed decreased as the shock wave moved down the tube but at the window position the actual speed was the same as the average speed over the 10-inch distance. This statement is based on the assumption of constant deceleration.

Combining the error in distance measurement with the ±1 microsecond error in time measurement yielded an error of ±1.7 per cent in the shock Mach number if negligible error was assumed to exist in the value used for the sound speed.

d. Error in measurement of the density ratio across the shock front. Since the density ratio, σ, was found from the graphical solution of equations (19) and (22) the above discussion of the factors influencing the accuracy of the T_{II} values also apply for σ. However, as figure 33 shows, σ is less sensitive to error in M_I than is T_{II}. The σ values are believed to be correct to ±3 per cent.

e. Error in determining the value of $\hat{k}_I$. From figure 37(b) the uncertainty in $\hat{k}_I$ was estimated to be of the order of 5 per cent, although it may be somewhat larger than this for wavelengths shorter than 1400 A.

f. Error in measuring the intensity ratio. The accuracy of the distance measurements made on the enlarged records varied a great deal but was typically 5 per cent.

g. Error in the value of the maximum absorption coefficient, k_0^m. The value of k_0^m was taken to be 400 cm^{-1} ±5 per cent.

h. Error in determining the value of l. As was stated in chapter III, l = 2.54 centimeters ±0.1 centimeter.

i. Error in determining the value of $\hat{\rho}$. The normalized gas density, $\hat{\rho}$, was defined by equation (23) as follows:

$$\hat{\rho} = (p_I/p_s)(T_s/T_I)g \qquad (23)$$

The pressure, p_I, was measured to ±0.02 millimeter. The temperature, T_I, was measured to ±1° K. The mole fraction of oxygen initially present was known to ±0.004. On the basis of these statements the value of $\hat{\rho}$ in equation (14) was correct to ±1 per cent.

j. Error in the experimental $\hat{k}_{II}$ values. The net effect of the experimental errors discussed in the preceding sections has to be evaluated in the light of equation (14), which was used to compute $\hat{k}_{II}$. The leading factor, $1/\sigma$, was uncertain by about 3 per cent. The first term inside the square brackets is $\hat{k}_I$ and was uncertain by about 5 per cent. The second term was correct to about 10 per cent. The uncertainty in the square bracket term depends on the relative sizes of the two terms, since neither was dominant in all cases. Taking the conservative point of view, the uncertainty in the square bracket term was assumed to be 10 per cent. Thus the uncertainty in $\hat{k}_{II}$ was found to be 10.5 per cent.

It is satisfying to note that the observed scatter of 6 to 8 per cent is within the estimated limits of error.

Concluding Remarks

A theoretical and experimental investigation of the absorption coefficient of molecular oxygen at high temperature is reported here. The wavelength range covered is in the vacuum ultraviolet region from 1300 A to 1750 A. The theoretical treatment covers all temperatures from 300° to 10,000° K. The experimental investigation was carried out in the temperature range of 4,000° to 10,000° K. All values of the absorption coefficient found apply only to oxygen for which the vibrational degree of freedom is fully excited.

The final results for the high temperature absorption coefficient as a function of temperature and wavelength are listed in table I. The experimental values found are plotted on figure 36. The estimated uncertainty of the experimental values is of the order of 10 per cent except for the oxygen-argon results, which give absorption coefficients up to 200 per cent larger than oxygen. The experimental scatter of the oxygen-argon results was shown to be within the limits of experimental error if allowance is made for observed extra absorption, which is believed to be due to the presence of excited argon atoms at high temperature.

BIBLIOGRAPHY

BIBLIOGRAPHY

1. (a) Watenabe, K., Zelikoff, M., and Inn, E. C. Y.: Absorption Coefficients of Several Atmospheric Gases. Geophysical Research Paper No. 21; Geophysics Research Directorate, Air Force Cambridge Research Center, Cambridge, Mass., (1953).

   (b) Ditchburn, R. W., and Heddle, D. W. O.: Absorption Cross-Sections in the Vacuum Ultraviolet. I. Continuous Absorption of Oxygen (1800 to 1300 A). Proc. Roy. Soc. (Lond.) A220, 61 (1953).

   (c) Watenabe, K., and Marmo, F. F.: Photoionization and Total Absorption Cross Section of Gases. II. O_2 and N_2 in the Region 850 - 1500 A. J. Chem. Phys. 25, 965 (1956).

   (d) Ladenburg, R., and Van Voorhis, C. C.: The Continuous Absorption of Oxygen Between 1750 and 1300 A and Its Bearing Upon the Dispersion. Phys. Rev. 43, 315 (1933).

   (e) Schneider, E. G.: An Estimate of the Absorption of Air in the Extreme Ultraviolet. J. Opt. Soc. Am. 30, 128 (1940).

   (f) Byram, E. T., Chubb, T. A., and Friedman, H.: Dissociation of Oxygen in the Upper Atmosphere. Phys. Rev. 98, 1594 (1955).

2. (a) Sulzer, P., and Wieland, K.: Intensitätsverteilung eines Kontinuierlichen Absorptionsspektrums in Abhängigkeit von Temperatur und Wellenzahl. Helv. Phys. Acta 25, 653 (1952).

   (b) Stueckelburg, E. C. G.: Theory of Continuous Absorption of Oxygen at 1450 A. Phys. Rev. 42, 518 (1932).

3. (a) Gibson, G. E., Rice, O. K., and Bayliss, N. S.: Variation With Temperature of the Continuous Absorption Spectrum of Diatomic Molecules. Part II. Theoretical. Phys. Rev. 44, 193 (1933).

   (b) Gibson, G. E., and Bayliss, N. S.: Variation With Temperature of the Continuous Absorption Spectrum of Diatomic Molecules. Part I. Experimental. Phys. Rev. 44, 188 (1933).

   (c) Acton, A. P., Aickin, R. G., and Bayliss, N. S.: The Continuous Absorption Spectrum of Bromine: A New Interpretation. J. Chem. Phys. 4, 474 (1936).

   (d) Britton, D., Davidson, N., and Schott, G.: Shock Waves in Chemical Kinetics: The Rate of Dissociation of Molecular Iodine. Disc. Faraday Soc. 17, 58 (1954).

(e) Britton, D., Davidson, N., Gehman, W., and Schott, G.: Shock Waves in Chemical Kinetics: Further Studies on the Rate of Dissociation on Molecular Iodine. J. Chem. Phys. 25, 804 (1956).

(f) Britton, D., and Davidson, N.: Shock Waves in Chemical Kinetics: Rate of Dissociation of Molecular Bromine. J. Chem. Phys. 25, 810 (1956).

(g) Palmer, H. B., and Hornig, D. F.: Rate of Dissociation of Bromine in Shock Waves. J. Chem. Phys. 26, 98 (1957).

4. Herzberg, G.: Molecular Spectra and Molecular Structure. Volume I: Spectra of Diatomic Molecules. D. Van Nostrand Company, Inc., New York, (1950), p. 446.

5. Ibid., p. 101.

6. Ibid., p. 560.

7. Brix, P., and Herzberg, G.: Fine Structure of the Schumann-Runge Bands Near the Convergence Limit and the Dissociation Energy of the Oxygen Molecule. Canadian J. Phys. 32, 110 (1954).

8. Ref. 4, p. 240.

9. Ibid., p. 447.

10. Ibid., p. 194.

11. Ibid., p. 119.

12. Ibid., p. 199.

13. Coolidge, A. S., James, H. M., and Present, R. D.: A Study of the Franck-Condon Principle. J. Chem. Phys. 4, 193 (1936).

14. Ibid., pp. 196 and 202.

15. (a) Ibid., p. 208.

(b) Nicholls, R. W., and Jarmain, W. R.: r-Centroids: Average Internuclear Separations Associated With Molecular Bands. Proc. Phys. Soc. A69, 253 (1956).

(c) Nicholls, R. W.: The Interpretation of Intensity Distributions in the CN Violet, C_2 Swan, OH Violet and O_2 Schumann-Runge Band Systems by Use of Their r-Centroids and Franck-Condon Factors. Proc. Phys. Soc. A69, 741 (1956).

16. Ref. 4, p. 394.

17. Ref. 3(a), p. 196.

18. Ref. 4, p. 426.

19. (a) Morse, P. M.: Diatomic Molecules According to the Wave Mechanics. II. Vibrational Levels. Phys. Rev. 34, 57 (1929).

(b) Wu, T. Y.: The Vibrational Overlap Integral and the Intensities in Band Systems of Diatomic Molecules. Proc. Phys. Soc. A65, 965 (1952).

20. Ref. 4, p. 76.

21. (a) Dunham, J. L.: Intensities in the Harmonic Band of Hydrogen Chloride. Phys. Rev. 34, 438 (1929).

(b) Dunham, J. L.: The Energy Levels of a Rotating Vibrator. Phys. Rev. 41, 721 (1932).

22. Hurlburt, H. M., and Hirschfelder, J. O.: Potential Energy Functions for Diatomic Molecules. J. Chem. Phys. 9, 61 (1941).

23. Ref. 4, p. 201.

24. (a) Klein, O.: Zur Berechnung von Potentialkurven für Zweiatomige Moleküle mit Hilfe von Spektraltermen. Zeit. f. Physik 76, 226 (1932).

(b) Rydberg, R.: Über einge Potentialkurven des Quecksilberhydrids. Zeit. f. Physik 80, 514 (1933).

25. Coolidge, A. S., James, H. M., and Vernon, E. L.: On the Determination of Molecular Potential Curves From Spectroscopic Data. Phys. Rev. 54, 726 (1938).

26. Ref. 7, p. 110.

27. Fraser, P. A., Jarmain, W. R., and Nicholls, R. W.: Vibrational Transition Probabilities of Diatomic Molecules; Collected Results II, N_2, CN, C_2, O_2, TiO. Astrophys. J. 119, 286 (1954).

28. Wurster, W. H., Treanor, C. E., and Glick, H. S.: Schumann-Runge Oxygen Absorption in Shock-Heated Air. J. Chem. Phys. 29, 250 (1958).

29. Golden, J. A., and Myerson, A. L.: Recombination of Atomic Oxygen Observed by Means of the Flash Spectroscopy of Molecular Oxygen in the Vacuum Ultraviolet. J. Chem. Phys. 28, 978 (1958).

30. Margenau, H., and Murphy, G. M.: The Mathematics of Physics and Chemistry. D. Van Nostrand Company, Inc., New York, (1943), p. 469.

31. Ref. 13, p. 200.

32. Schiff, L. I.: Quantum Mechanics. McGraw-Hill Book Co., Inc., New York, (1949), p. 182.

33. Ref. 2(a), p. 664.

34. Ref. 32, p. 64.

35. (a) Ref. 2(a), p. 661.

(b) Ref. 4, p. 203.

36. Ref. 1(a), p. 26.

37. (a) Flory, P. J.: Predissociation of the Oxygen Molecule. J. Chem. Phys. 4, 23 (1936).

(b) Volman, D. H.: Photochemical Evidence Relative to the Excited States of Oxygen. J. Chem. Phys. 24, 122 (1956).

(c) Wilkinson, P. G., and Mulliken, R. S.: Dissociation Processes in Oxygen Above 1750 A. Astrophys. J. 125, 594 (1957).

38. Ref. 4, p. 240.

39. Ref. 37(a).

40. Ref. 37(b).

41. Ref. 37(c).

42. Ref. 15(c), p. 750.

43. Ref. 1(b).

44. Ref. 1(a), p. 25.

45. (a) Glick, H. S., and Wurster, W. H.: Shock Tube Study of Dissociation Relaxation in Oxygen. J. Chem. Phys. 27, 1224 (1957).

(b) Camac, M., Camm, J., Keck, J., and Petty, C.: Relaxation Phenomena in Air Between 3,000° and 8,000° K. Research Report 22, Avco Research Lab., Everett, Mass., (1958).

46. Gilles, A., and Vodar, B.: Variation With Temperature of the Transparency of Some Optical Materials in the Schumann Region. J. Opt. Soc. Am. 42, 783 (1952).

47. (a) Stockbarger, D. C.: The Production of Large Single Crystals of Lithium Fluoride. Rev. Sci. Instr. 7, 133 (1936).

(b) Stockbarger, D. C.: Artificial Fluorite. J. Opt. Soc. Am. 39, 731 (1949).

48. Courant, R., and Friedrichs, K. O.: Supersonic Flow and Shock Waves. Interscience Publishers, Inc., New York (1948).

49. Ferri, A.: Elements of Aerodynamics and of Supersonic Flows. The Macmillan Company, New York (1948).

50. Evans, J. S.: Method for Calculating Effects of Dissociation on Flow Variables in the Relaxation Zone Behind Normal Shock Waves. NACA TN 3860, National Aeronautics and Space Administration, Langley Field, Va., (1956).

51. (a) Bleakney, W., Weimer, D. K., and Fletcher, C. H.: The Shock Tube: A Facility for Investigations in Fluid Dynamics. Rev. Sci. Instr. 20, 807 (1949).

(b) Resler, E. L., Lin, S. C., and Kantrowitz, A.: The Production of High Temperature Gases in Shock Tubes. J. App. Phys. 23, 1390 (1952).

(c) Hertzberg, A., and Smith, W. E.: A Method for Generating Strong Shock Waves. J. App. Phys. 25, 130 (1954).

(d) Glass, I. I., and Patterson, G. N.: A Theoretical and Experimental Study of Shock-Tube Flows. J. Aero. Sci. 22, 73 (1955).

52. Ref. 51(b), p. 1391.

53. Ref. 51(b), pp. 1391 and 1392.

54. (a) Ref. 51(b), p. 1395.

(b) Russo, A. L., and Hertzberg, A.: Modifications of the Basic Shock Tube to Improve Its Performance. Report AD-1052-A-7, Cornell Aeronautical Laboratory, Buffalo, New York, (1958).

55. Duff, R. E.: Shock Tube Performance at Low Initial Pressure. Phys. Fluids 2, 207 (1959).

56. Chubb, T. A.: Transmission of Barium Fluoride Crystal in the Ultraviolet. J. Opt. Soc. Am. 46, 362 (1956).

57. Ref. 47(b), p. 740.

58. (a) Purcell, J. D.: Reflectance Measurements From 1140 A to 1190 A by a Simple Open Air Method. J. Opt. Soc. Am. 43, 1166 (1953).

(b) Hass, G., Hunter, W. R., and Tousey, R.: Reflectance of Evaporated Aluminum in the Vacuum Ultraviolet. J. Opt. Soc. Am. 46, 1009 (1956).

59. (a) Johnson, P. D.: Vacuum Ultraviolet Monochromator. J. Opt. Soc. Am. 42, 278 (1952).

(b) Hartman, P. L., and Nelson, J. R.: Hydrogen Lamp of Good Intensity and Reliability for the Vacuum Ultraviolet. J. Opt. Soc. Am. 47, 646 (1957).

60. (a) Wilkinson, P. G., and Tanaka, Y.: New Xenon Light Source for the Vacuum Ultraviolet. J. Opt. Soc. Am. 45, 344 (1955).

(b) Wilkinson, P. G.: A New Krypton Light Source for the Vacuum Ultraviolet. J. Opt. Soc. Am. 45, 1044 (1955).

61. (a) Lyman, T.: The Reversal of the Hydrogen Series in the Extreme Ultraviolet. Science 64, 89 (1926).

(b) Worley, R. E.: An Improved Source for the Lyman Continuum in the Vacuum Ultraviolet. Rev. Sci. Instr. 13, 67 (1942).

(c) Ref. 60(a), p. 344.

62. (a) Malmberg, J. H.: Millimicrosecond Duration Light Source. Rev. Sci. Instr. 28, 1027 (1957).

(b) Weeks, R. F.: A Simple Pulsed Ultraviolet Light Source. Technical Note 15, Institute of Optics, Rochester University (1958). Also obtainable as Office of Scientific Research TN 58-615.

(c) Brody, S. S.: Instrument to Measure Fluorescence Lifetimes in the Millisecond Region. Rev. Sci. Instr. 28, 1021 (1957).

(d) Carpenter, R. O'B.: Radiation Sources for the Vacuum Ultraviolet. Final Technical Report on Contract AF19(122)-432, Baird Associates, Inc., Cambridge, Mass. (1952).

(e) Dieke, G. H., and Cunningham, S. P.: A New Type of Hydrogen Discharge Tube. J. Opt. Soc. Am. 42, 187 (1952).

63. (a) Ref. 1(a), p. 17.

(b) Thurnau, D. H.: Quantum Efficiency Measurements on Several Phosphors Under Excitation in the Extreme Ultraviolet. J. Opt. Soc. Am. 46, 346 (1956).

64. Ref. 45(b), p. 3.

65. Martinson, O., Isaacs, P., Brown, H., and Ruderman, I. W.: Rise Times of Voltage Pulses From Photomultipliers. Phys. Rev. 79, 178 (1950).

66. Ref. 62(e).

67. Golden, J. A., and Myerson, A. L.: Improved, Single Flash, Continuum Source for Use Below 2000 A. J. Opt. Soc. Am. 48, 548 (1958).

68. Schexnayder, C. J.: On the Performance of a Double-Diaphragm Shock Tube Using the Reflected-Shock Method and a Light-Gas Buffer. J. Aero/Space Sci. 25, 527 (1958).

69. Jones, J. J.: Experimental Investigation of Attenuation of Strong Shock Waves in a Shock Tube With Hydrogen and Helium as Driver Gases. NACA TN 4072, National Aeronautics and Space Administration, Langley Field, Va., (1957).

70. Lundquist, G. A.: The NOL 8- by 8-Inch Shock Tube: Instrumentation and Operation. NAVORD Report 2449, Naval Ordnance Laboratory, White Oak, Md., (1952).

71. Parkinson, W. W., and Williams, F. E.: A Vacuum Ultraviolet Monochromator for Absorption and Photoconductivity Measurements on Luminescent Solids. J. Opt. Soc. Am. 39, 705 (1949).

72. Anonymous: DuMont Multiplier Phototubes, 2nd Edition. Allen B. DuMont Laboratories, Inc., Clifton, N. J., (1959).

73. Ref. 45(b).

74. (a) Byron, S. R.: Interferometric Measurement of the Rate of Dissociation of Oxygen Heated by Strong Shock Waves. Cornell University Graduate School of Aeronautical Engineering Report to Office of Naval Research on contract N401(25), (No date was on the report. The latest reference used was January, 1957).

(b) Girffith, W. C., and Kenny, A.: States of Partial Equilibrium Behind Shock Waves in O_2, N_2, CO, CO_2, and N_2O. Technical Report II-23, Princeton University Department of Physics (1957).

75. Hilsenrath, J., Beckett, C. W., Benedict, W. S., Fano, L., Hoge, H. J., Masi, J. F., Nuttall, R. L., Touloukian, Y. S., and Wooley, H. W.: Tables of Thermal Properties of Gases. National Bureau of Standards Circular 564 (1955), p. 430.

76. Fickett, W., and Cowan, R. D.: Values of Thermodynamic Functions to 12,000° K for Several Substances. J. Chem. Phys. 23, 1349 (1955).

77. Blackman, V. H.: Vibrational Relaxation in O_2 and N_2. Technical Report II-20, Princeton University Department of Physics (1955).

78. Ref. 74(a), p. 42.

79. Ref. 45(b), p. 11.

80. Ref. 45(b), p. 9.

81. Camac, M., Camm, J., Feldman, S., Keck, J., and Petty, C.: Chemical Relaxation in Air, Oxygen, and Nitrogen. IAS Preprint No. 802, Institute of Aeronautical Sciences, New York (Jan. 27, 1958), p. 10.

82. Ref. 74(a), p. 42.

83. Mathews, D. L.: Interferometric Measurement in the Shock Tube of the Dissociation Rate of Oxygen. Phys. Fluids 2, 170 (1959).

84. Gray, D. E. (Editor): American Institute of Physics Handbook. McGraw-Hill Book Co., Inc., New York (1957), p. 7-33.

85. Ref. 30, p. 498.

86. Ref. 75, pp. 12 and 435.

87. Ref. 76.

88. Ref. 1(a), p. 71ff.

89. Ref. 1(b), p. 67.

90. Ref. 13, p. 203ff.

91. Ref. 32, p. 178.

92. Staff of the Harvard Computation Laboratory. Tables of the Modified Hankel Functions of Order One-Third and of Their Derivatives. Annals of the Computation Laboratory of Harvard University, Volume II, Cambridge University Press, Cambridge, Mass., (1945).

93. Ref. 32, p. 183.

APPENDICES

APPENDIX A

PROCEDURE USED IN CALCULATING THE POTENTIAL CURVE FOR THE $B(^3\Sigma_u^-)$ STATE

Equation (8) shows that k/E^* is proportional to $a^{-1/3}\phi_{v''}^2$. Since k and E^* are known as functions of λ from room temperature data and $\phi_{v''}$ was calculated as a function of r from the Morse potential, a relation between λ and r_s was found by comparing properly normalized plots of k/E^* against $\tilde{\nu}$ and $a^{-1/3}\phi_{v''}^2$ against r_s. The following procedure describes how this was done:

(1) Two plots of $k\lambda/(k\lambda)_{max}$ against $\tilde{\nu}$ were prepared. One was based on the data of Watenabe, Zelikoff, and Inn[88] and the other on the experimentally determined absorption curve given by Ditchburn and Heddle[89]. The curves found in this way are shown on figure 38.

(2) A plot of $C_3 a^{-1/3}\phi_0^2$ against r_s is shown on figure 39*. C_3 was chosen to make the maximum ordinate unity.

(3) Corresponding λ, r_s pairs were tabulated by picking off $\tilde{\nu}$ and r_s for $k\lambda/(k\lambda)_{max} = C_3 a^{-1/3}\phi_0^2$. A separate tabulation was prepared for each of the experimental absorption curves of figure 38.

(4) By adding to $\tilde{\nu}$ the energy of the initial state as calculated from the Morse potential the points shown on figures 12 and 13

---

*As is shown in Appendix B, the use of a delta-function for the upper state eigenfunction requires that the integral in equation (3) vanish except for $r = r_s$. Thus r_s was used for the plot on figure 39 rather than r.

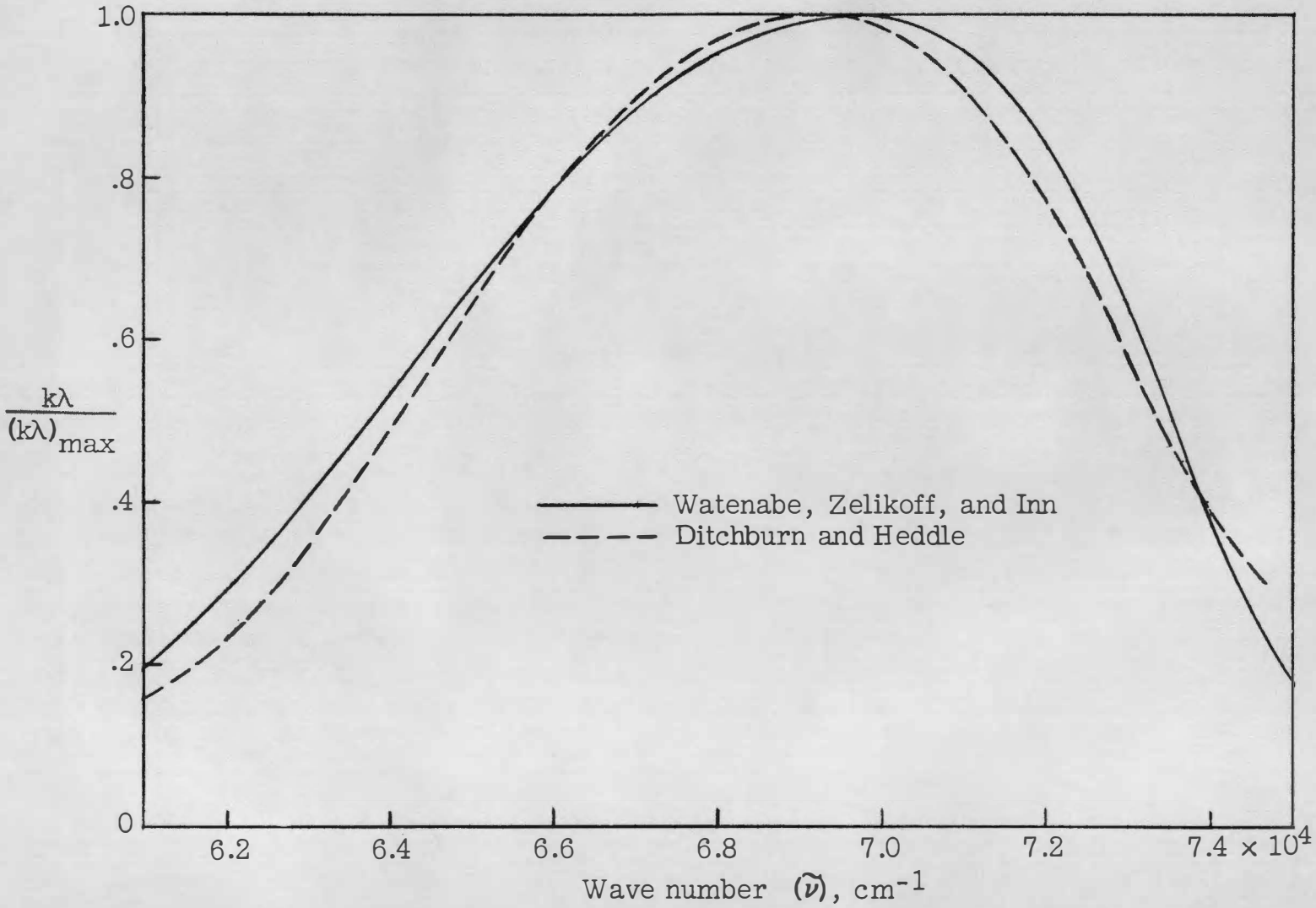

Figure 38.- The ratio $k\lambda/(k\lambda)_{max}$ as a function of $\tilde{\nu}$.

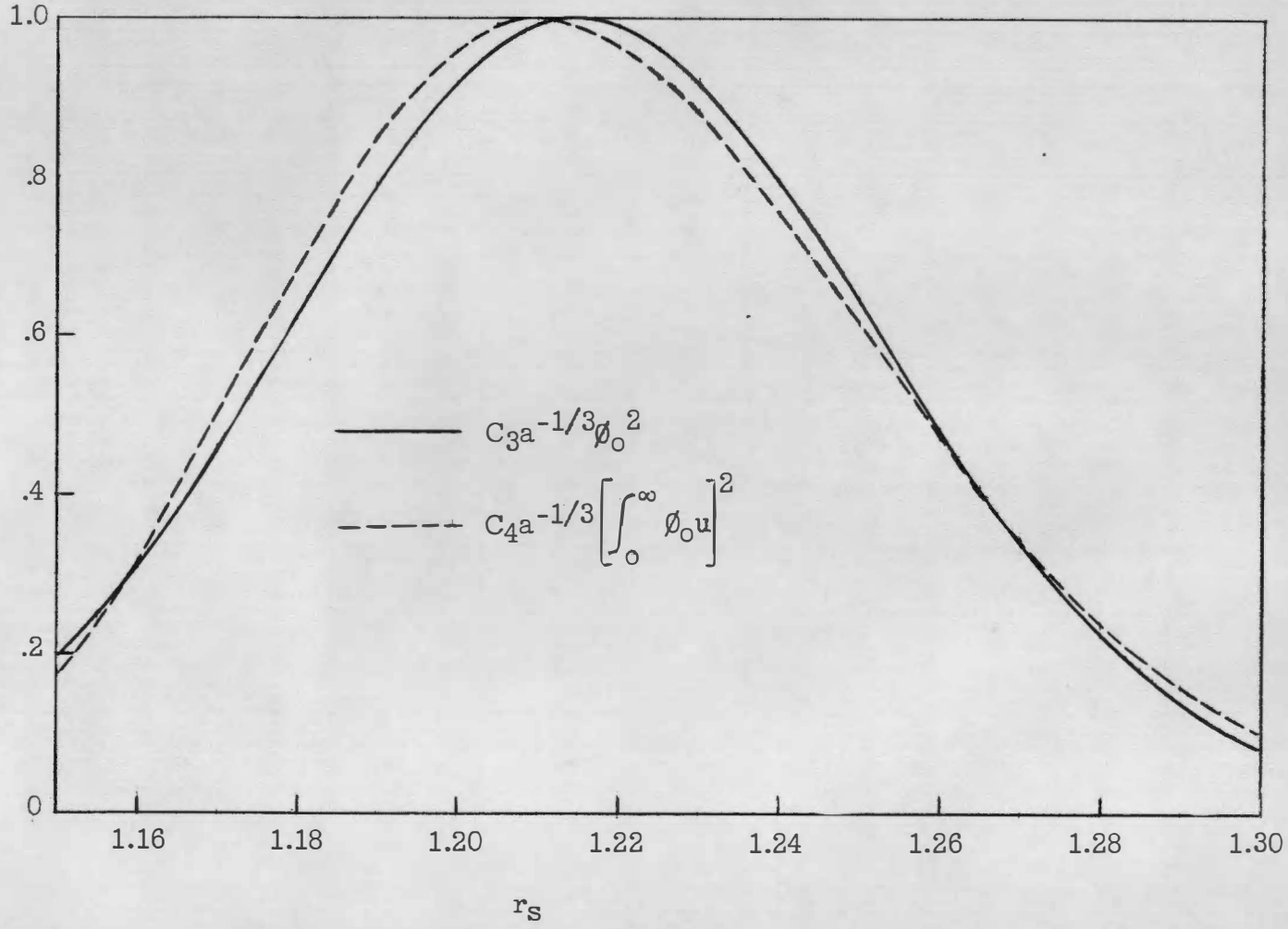

Figure 39.- The expressions $C_3a^{-\frac{1}{3}}\phi_o^2$ and $C_4a^{-\frac{1}{3}}\left[\int_0^\infty \phi_o u\right]^2$ as functions of r_s.

were found. The B state potential curve shown on figure 13 was determined by drawing the most reasonable appearing curve through all available points.

Note that this procedure assumes that $k_o(\lambda)$ can be correctly calculated from a knowledge of the initial state wave functions and the upper state potential curve by using the "reflection" method. Coolidge, James and Present[90] point out that this is not so, although it is a good approximation for $v'' = 0$. (See their fig. 6, page 204.) The most obvious error is a shift of the peak of the distribution curve toward longer wavelengths and is caused by the fact that maximum absorption occurs when the relative orientation of the initial and final state wave functions is such that the overlap integral, $\int_o^\infty \phi_{v''} u dr$, is maximized rather than when the turning point of the upper state wave function occurs at the same value of internuclear distance as the peak of the lower state wave function.

Upon completion of the IBM calculations based on the potential found as described a plot of $C_4 a^{-1/3} \int_o^\infty \phi_o u dr^2$ against r_s was added to figure 39. As before, the constant was chosen to make the maximum ordinate unity. The agreement with the plot of $C_3 a^{-1/3} \phi_o^2$ is remarkably good.

The two curves of figure 39 were used together with the Watenabe, Zelikoff and Inn curve of figure 38 to plot the points shown on figure 14. The E^*, r_s curve shown on figure 14 was derived from the B state potential used in all the calculations and it is satisfying to observe that the set of points based on the IBM calculations agrees with this

curve better than the "reflection" points, even though the difference is in most cases quite small.

APPENDIX B

DERIVATION OF EQUATION (8)

As was stated in equation (3), the absorption coefficient $k_{v''}(\lambda)$ is proportional to certain factors. The most important of these is the vibrational overlap integral, $\int_0^\infty \phi_{v''} u dr$. Replacing the u function by a delta function located at the turning point permits the integral to be evaluated, that is, $\int_0^\infty \phi_{v''} u dr = \phi_{v''}(r_s)$, where r_s is the value of r at the turning point of the B state.

Normalized Morse functions were used for $\phi_{v''}$. It was not necessary to normalize the delta functions used to replace u because the normalization factor $F^{1/2}$ for the u function appears explicitly in equation (3). The derivation of the factor, $F^{1/2}$, is given in Appendix C. Substitution of $F = (241.89\ E^{1/4} a^{-1/6})^2$ and $\int_0^\infty \phi_{v''} u dr = \phi_{v''}(r_s)$ into equation (3) gives the following result:

$$\hat{k}_{v''}(\lambda) = \text{constant}\ E^{*} a^{-1/3} \phi^2_{v''}$$

where $(241.89)^2$ has been absorbed into the proportionality constant and the whole equation has been divided by k_o^m.

APPENDIX C

DERIVATION OF THE NORMALIZATION FACTOR FOR THE u WAVE FUNCTION

The fact that Hankel functions satisfy the Schroedinger equation when V is linear has already been mentioned. The normalization factor was derived by suitably comparing the Hankel function solution for u, which is a good approximation near the turning point, to the WBK solution[91], which is a good approximation everywhere except near the turning point. The reasoning goes as follows:

(1) Except for a constant factor the asymptotic Hankel amplitude is identical to the WBK amplitude for the same potential. Let the potential used for the WBK function depart from a straight line at some point distant from the turning point and let it approach the dissociation energy of the B state as $r \to \infty$. Normalize the WBK amplitude to unity at infinity.

(2) The desired normalization factor is the factor required to make the Hankel amplitude coincide with the normalized WBK amplitude in the region where both are derived from a straight line potential.

(3) The value of the Hankel function at the turning point is given as 1.074 in the tables[92] used and this value was always used for the value of u at the starting point for the integration of equation (10) on the IBM 704 computer.

(4) The value of u at the turning point of a Hankel function is[93]

$$u(r_s) = A(2/3)^{1/2}(3)^{1/3}(2\mu a/\hbar^2)^{-1/6}/\Gamma(2/3)$$

where a is the slope of the B state potential curve at the turning point.

(5) Setting this equal to 1.074 gives

$$A = 2.09226 \times 10^5\, a^{1/6}$$

(6) The asymptotic Hankel amplitude* is

$$f_H = 1.7318A(\pi b/2)^{-1/2} = (1/2.4189)\mu^{1/6}/a^{1/4}(r - r_s)^{1/4}$$

where

$$b = \left\{(1/\hbar)\left[2\mu(E - V')\right]^{1/2}\right\}_{r \to r_s} = (1/\hbar)\left[2 \times 10^{-8}\mu a(r - r_s)\right]^{1/2}$$

(7) The corresponding normalized WBK amplitude is

$$f_{WBK} = 1.7318A(\pi b/2)^{-1/2}/1.7318A(\pi b_\infty/2)^{-1/2} = b/b_\infty)^{-1/2}$$

where

$$b_\infty = \left\{1/\hbar\left[2\mu(E - V')\right]^{1/2}\right\}_{r \to \infty} = (1/\hbar)(2\mu E)^{1/2}$$

$$f_{WBK} = (b/b_\infty)^{-1/2} = 10^{2}\mu^{1/4}/a^{1/4}(r - r_s)^{1/4}$$

---

*See Schiff's equations (28.16) and (28.17). The Hankel function used is $u^+ + u^-$ in Schiff's notation. The factor 1.7318 is the sum of $\exp(-\pi i/6)$ and $\exp(-5\pi i/6)$.

(8) The desired normalization factor is

$$F^{1/2} = f_{WBK}/f_H = 241.89\tilde{E}^{1/4}a^{-1/6}$$

(9) Substitution of F into equation (3) gives

$$k_{v''}(\lambda) = Ca^{-1/3}E^{*}\left[\int_{0}^{\infty} \phi_{v''}u\,dr\right]^2$$

where $(241.89)^2$ has been absorbed into the constant, C.